Effects of Fuel Properties, Injector Conditions and Impingement on the Sprays of Direct Injection Engines

by

Sebastian Henkel

Department of Mechanical Engineering
Imperial College London
Exhibition Road
London SW7 2AZ

A thesis submitted for the degree of Doctor of Philosophy

October 2015

Abstract

The concept of gasoline direct injection engines is at the forefront of modern research. Two major concerns with the design are the incomplete evaporation of the injected fuel that leads to increased engine-out emissions and the process of injector fouling caused by the direct exposure of the injector to the flame. The latter also reduces the lifetime of this component and also increases emissions at the same time. These are critical issues for OEMs as emissions legislations around the world demand increasingly stricter thresholds.

The research presented is split into two separate parts, to tackle both concerns. First, a series of fuel blends and operating conditions and their effect towards spray shape, droplet size and velocity as well as wall wetting will be investigated in a dedicated injection chamber. In order to quantify the amount of fuel that forms a liquid deposit on the surface a novel measurement technique is presented. The data gathered in these measurements is then used to show trends between the blends investigated and to give suggestions for potential improvements of future engine designs and modified engine operating conditions to reduce the amount of particulate emissions.

In the second part of the research a series of injectors that were previously fouled are investigated. The fouling caused a significant increase of particulate emissions in test engines and the focus here is to provide possible explanations for this drift. Additionally, some of the injectors were treated with a detergent fuel which reverted the change in emissions. A comparison of these injectors shall provide information about potential applications of such blends and how they would benefit the longevity of modern engines.

Declaration of Originality

I hereby declare that this thesis, and the research to which it refers, are entirely my own work and has not been submitted for any other award. Where other sources of information have been used they have been acknowledged and fully referenced.

Copyright Declaration

The copyright of this thesis rests with the author and is made available under a Creative Commons Attribution Non-Commercial No Derivatives licence. Researchers are free to copy, distribute or transmit the thesis on the condition that they attribute it, that they do not use it for commercial purposes and that they do not alter, transform or build upon it. For any reuse or redistribution, researchers must make clear to others the licence terms of this work.

Acknowledgements

The research presented was carried out in the Thermofluids Division at the Mechanical Engineering Department of Imperial College London as part of a research project to obtain the degree of Doctor of Philosophy.

First, I would like to thank my supervisors Professor Frank Beyrau, Professor Yannis Hardalupas and Professor Alexander Taylor for their continuous support and encouragement over the past four years. They were always open for discussion and provided constructive feedback throughout all stages of this PhD. At the same time they gave me the necessary creative freedom to develop my own experimental methodologies and procedures. This made for an inspiring research environment to work in. In addition, they ensured that personal matters were not left behind and provided support even beyond their professional responsibility.

I would also like to thank the partners of the collaborative projects at Shell Global Solutions and Nissan Motor Company Limited. Their support made it possible to conduct this research and I hope that similar efforts will be made to continue this productive relationship.

My close colleagues and friends at Imperial were instrumental in my progress. First and foremost I would like to thank Antonis and Thomas. Both have become very important friends to me. They helped me through all stages of this PhD and supported me during one of the toughest times of my life. I would also like to say thank you to Benoit, Carlos, Chris, Dimitris, Fabian, George (C.), George (V.), Guru, Johannes, Konstantinos, Kostis, Koulis and Nikos.

I also owe a big thank you to the remaining members of the Thermofluids Division that supported me and my work throughout the years. Many people have come and gone but the spirit was always positive and the intellectual input high. I would also like to thank the technical and administrative staff of the department, Mr Guljar Singh, Mr Asanka Munasinghe, Mr Edward Benbow, Mr Ian Wright and Ms Serena Dalrymple. Without their support it would have been impossible to build, modify and operate the experimental setups.

I would like to thank my friends back in Germany. Without them I would probably not have made it this far. Especially to Barbara, Benjamin, Eva, Esther, Martin and Michael, who I have the fortune to know since the last years of secondary school.

Lastly, I would like to say thank you to my parents. Their tireless support cannot be emphasised enough and without them it would not have been possible to come to Imperial College in the first place. The last two years were very tough, and I would like to especially thank my mother for making it possible for me to finish my research.

Contents

Abstract 2

Declaration of Originality 3

Copyright Declaration 4

Acknowledgements 5

Contents 7

List of Figures 10

List of Tables 19

Nomenclature 21

1 Introduction 25

2 Literature review 29

2.1 The concept of gasoline direct injection engines and their challenges 29

2.2 Liquid deposit formed by fuel sprays in direct injection engines 33

2.2.1 Liquid film formation and its relation to the generation of pollutants 40

2.2.2 Techniques to analyse soot particles and emissions 50

2.2.3 Parameters of the injection setup to influence the liquid deposit and pollutant emissions 53

2.3 Overview and evaluation of common measurement techniques to analyse thin liquid films 70

2.4 Refractive Index Matching 77
2.5 Pattern and droplet analysis of gasoline direct injection sprays 80
2.6 Influencing factors on injector fouling and the impact on injector and engine performance 86
2.7 Motivation and outline of the research 93

3 Experimental setup and methodology 97
3.1 Design of the injection chamber for the investigation of fuel deposits 97
3.1.1 Basic setup for the spray pattern and film thickness analysis 98
3.1.2 Recording setup of the spray pattern and film thickness analysis 104
3.1.3 Phase Doppler Anemometry principle and setup 106
3.1.4 Investigated fuel blends and experimental procedures 111
3.2 Experimental setup to investigate sprays of fouled injectors 117
3.2.1 Modified setup to record spray patterns of multi hole injectors 117
3.2.2 Optical setup for spray pattern analysis 119
3.2.3 Investigated injectors and fouling process 121

4 Development of a measurement technique to quantify liquid deposits on a rough metal surface 124
4.1 Principle of the measurement technique 125
4.2 Calibration method and data processing 126
4.3 Comparison to the Refractive Index Matching method 133
4.4 Measurement uncertainty 135
4.5 Application of the technique to investigate single component fuels 137
4.6 Summary and Conclusions 149

5 Characterisation of impinging fuel sprays 151
5.1 Qualitative spray analysis using High Speed imaging 152
5.2 Size and Velocity Analysis of the spray droplets 173
5.3 Analysis of the liquid deposit formed by the impinging spray in the injection chamber 187
5.4 Summary and conclusions 204

6 Effect of injector fouling on spray characteristics 212

6.1 Formation of injector fouling and its impact on particulate emissions during the run in test engines 213

6.2 Analysis of the spray pattern of clean and fouled injectors 223

6.3 Summary and conclusions 236

7 Conclusions and suggestions for future work 240

Bibliography 251

List of Figures

2.1 *Schematic comparison of the concept of gasoline direct injection (GDI) (a) and port fuel injection (PFI) (b)* [34]. *30*

2.2 *The concept of wall-guided (left side) and spray-guided (right side) direct injection engines* [37]. *31*

2.3 *Interaction between the spray and the wall, showing different influencing parameters on the liquid film formation* [52]. *34*

2.4 *Simplified classification regimes of droplets interacting with a solid surface* [57]. *35*

2.5 *Incident angle of the impinging droplet, leading to secondary droplet formation* [58]. *38*

2.6 *Schematic description of pool fires and their contributions to engine-out emissions* [69]. *40*

2.7 *Relation between measured particulate emissions and wall film mass for a multi hole injector ( ) and a swirl-type injector (•) by Drake et al.* [73]. *43*

2.8 *Fundamentals of RIM: In case of a smooth surface (a) light gets reflected specularly and refracted, whereas the rough surface (b) scatters incident light in all directions. With liquid on the rough surface (c) all phenomena occur.* *78*

2.9 Recordings produced with Refractive Index Matching [9]. *78*

2.10 Example of a calibration derived for Refractive Index Matching [9]. *79*

3.1 Experimental setup (a), close-up view of the injection chamber (b) and fuel preparation section (c). *100*

3.2 Photograph of the assembled impingement plate used in the spray visualisation experiments (a) and schematic of the impingement plate frame that was covered with a glass plate and a stainless steel sheet. *101*

3.3 The brass cap providing a press fit connection to the fuel line (a); the injector mount (b) and the whole assembly with the injector on top of the injection chamber (c). *101*

3.4 Injector tip (a) and illustration of the spray angle (b) of the single hole model injector. *102*

3.5 Recordings setup for spray analysis (a) and film thickness measurements (b). ..*106*

3.6 Principle setup of the Laser Doppler Anemometer with two intersecting laser beams creating a fringe pattern inside the probe volume [196]. *107*

3.7 Schematic of the optical arrangement used in PDA measurements (Dantec Dynamics). *108*

3.8 Schematic of the measurement location for the PDA spray analysis. *110*

3.9 Physical matrix (a) and chemical matrix (b) comprising 11 blends that were investigated during this study. *112*

3.10 Redesigned impingement plate that was used for the injector fouling studies. ...*118*

3.11 Electrical injector profile from IAV Automotive Engineering which was used as the basis for the electronics of the experimental setup (dark blue line). *119*

3.12 Optical arrangement of the injector fouling setup as an elevation view (a) and plan view (b). *120*

3.13 Multi-hole injector used in the injector fouling study with a close-up view of the injector tip and labels of the holes. 121

4.1 Physical principle of the measurement technique. The scattering behaviour of a rough metal surface (a) is changed once liquid is present (b). The deposit gradually reduces the apparent surface roughness and causes incident light to be reflected specularly. 125

4.2 Image processing to derive the calibration function. 129

4.3 Calibration correlation used for the film thickness experiments. Points (∗) obtained during the calibration procedure are shown with a double exponential fit (—), error approximation (- - -) and the calibration equation. ...130

4.4 Example image showing the processing used to analyse liquid films: dewarped images before (a) and after (b) the impingement of the spray, the calculated local intensity ratio with values between zero and one (c) and the actual 2D film thickness calculated with the calibration function (d). 131

4.5 Example of a time series of one recorded injection with the raw footage on the left-hand side and the processed image showing the 2D local film thickness on the right-hand side. 132

4.6 Comparison of the area averaged normalised intensity of a roughened metal (—) and a roughened glass plate (– ·). 134

4.7 Mean liquid volume of wall deposit of hexane (—), heptane (·····) and octane (– ·) fuels as a function of time after triggering the injector and a plate temperature of 100°C (a) and the individual mean time signal (—) for hexane (b), heptane (c) and octane (d) including the respective standard deviation (·····). 141

4.8 Mean liquid volume of wall deposit of ethanol (—), propanol (·····) and butanol (– ·) fuels as a function of time after triggering the injector and a plate temperature of 100°C (a) and the individual mean time signal (—) for

ethanol (b), propanol (c) and butanol (d) including the respective standard deviation (.....). 142

4.9 Example of the differences in the evaporation behaviour of alcohols (a) and alkanes (b). Bubbles were formed in case of alcohols, while alkanes did not show any signs of boiling. 143

4.10 Mean liquid volume of wall deposit of hexane (—), heptane (.....) and octane (– ..) fuels as a function of time after triggering the injector, with the plate temperature matching the boiling temperature of each liquid and the individual mean time signal (—) for hexane (b), heptane (c) and octane (d) including the respective standard deviation (.....). 147

4.11 Mean liquid volume of wall deposit of ethanol (—), propanol (.....) and butanol (– ..) fuels as a function of time after triggering the injector, with the plate temperature matching the boiling temperature of each liquid (a) and the individual mean time signal (—) for ethanol (b), propanol (c) and butanol (d) including the respective standard deviation (.....). 148

5.1 Extracted frames of a recorded time series of a free spray injection (blend PM1) at a rail pressure of 150 bar. 153

5.2 Extracted frames of a recorded time series of an impinging spray (blend PM1) at a rail pressure of 150 bar. The plate was at ambient temperature. 154

5.3 Visible start of injection (VSOI, lhs) which corresponds to the first frame with liquid present the nozzle of the injector and visible end of injection (VEOI, rhs), the first frame where the spray is separating from the injector tip. 156

5.4 Normalised mean spray image intensities of each fuel blend at 1.2 ms after VSOI for the case of 150 bar and 2 ms after VSOI for 50 bar injection pressure in false colours. This information provides a measure of the relative droplet number density in the resulting sprays. 161

5.5 Normalised mean standard deviation images of each fuel blend at 1.2 ms after

VSOI in the case of 150 bar and 2 ms after VSOI for 50 bar injection pressure in false colours. This information provides a measure of the relative fluctuations of droplet number density in the resulting sprays. 162

5.6 Extraction of the intensity profile of a horizontal line of the recorded spray image and the corresponding normalised intensity profile. 164

5.7 Example of the downstream mean spray width (—) and standard deviation (—) of its fluctuations calculated from the individual recordings of fuel blend PM6 for 50 bar (left side) and 150 bar (right side) injection pressure. 165

5.8 Measured mean spray width at 45 mm downstream of the injector tip for 150 bar rail pressure and 80 °C air temperature (—) and for 150 bar rail pressure at ambient air temperature (—) for different fuel blends. 166

5.9 Measured mean spray width at 45 mm downstream of the injector tip for 50 bar rail pressure and 80 °C air temperature, for different fuel blends. 167

5.10 Normalised mean images with the impingement plate installed at 0.534 ms after VEOI, for an air temperature of 80 °C and ambient plate temperature in false colours (normalisation by the largest spray intensity). The injection pressure was 150 bar. 171

5.11 Normalised mean images with the impingement plate installed at 5 ms after VEOI, for an air temperature of 80 °C and ambient plate temperature in false colours (normalisation by the largest spray intensity). The injection pressure was 150 bar. 172

5.12 Superimposed time series of 10 complete injections of fuel blend PM1 (injection width 1.51ms) with absolute timing. The injector triggering was performed through the PDA controller. 173

5.13 Radial profile showing the mean droplet velocity (∗), arithmetic mean droplet diameter AMD (∗), the calculated Sauter mean diameter SMD (∗), the standard deviation of the velocity (∆) and the standard deviation of the droplet

diameter (o), with corresponding Gaussian fits (solid lines of the same colour) of the spray generated by blend PM1, 45 mm downstream of the injector tip. ...175

5.14 Radial cross profile showing the mean droplet velocity (∗), arithmetic mean droplet diameter AMD (∗), the calculated Sauter mean diameter SMD (∗), the standard deviation of the velocity (△) and the standard deviation of the droplet diameter (o), with corresponding Gaussian fits (solid lines of the same colour), of all the investigated fuel blend, 45 mm downstream of the injector tip at ambient temperature and 150 bar rail pressure. 178

5.15 Illustration of the three windows that were extracted from each time series corresponding to the droplet distributions at the beginning, the mid and the end of the injection. The three windows are highlighted in green. 181

5.16 Scatter plots of the correlation between the droplet size and velocity of the three extracted windows for the centreline point of fuel blend PM1 at ambient temperature and 150 bar rail pressure. 183

5.17 Scatter plots of the correlation between the droplet size and velocity for the centreline point of all fuel blends at ambient temperature and 150 bar rail pressure. 184

5.18 Scatter plots of the correlation between the droplet size and Weber Number of the centreline point for all fuel blends at ambient temperature and 150 bar rail pressure. 185

5.19 Scatter plots of the correlation between the droplet size and Weber Number based on the approximated slip velocity between the air and the spray droplets of the centreline point for all fuel blends at ambient temperature and 150 bar rail pressure. 186

5.20 Extracted frames of the processed recording of the fuel deposit on the rough metal impingement plate for blend PM2 with a time stamp showing the time after the visible end of injection. The images represent the calculated mean from five repeated recordings for the measurements with a plate temperature

of 120 °C and 150 bar rail pressure. *189*

5.21 Maximum mean fuel deposit of each blend for a plate temperature of 120 °C and 150 bar rail pressure, with the corresponding time after VEOI. Note that the time is different for each fuel blend. *190*

5.22 Partially evaporated mean fuel deposit of each blend for a plate temperature of 120 °C and 150 bar rail pressure, with the corresponding time after VEOI. .. *192*

5.23 Maximum mean fuel deposit of each blend for a plate temperature of 160 °C and 150 bar rail pressure, with the corresponding time after VEOI. *193*

5.24 Mean fuel deposit over time, calculated from the image time series of all seven blends for the plate temperature 120 °C and 150 bar rail pressure, for PM2 (—), PM3 (—), PM5 (—), PM6 (—), PM7 (—), A (—) and E (—). *194*

5.25 Mean fuel deposit over time, calculated from the image time series of all seven blends for the plate temperature 160 °C and 150 bar rail pressure, for PM2 (—), PM3 (—), PM5 (—), PM6 (—), PM7 (—), A (—) and E (—). *196*

5.26 Mean deposit and standard deviation of each fuel blend for a plate temperature of 120 °C and 150 bar rail pressure as a function of time. The axes are scaled separately for each blend. *197*

5.27 Mean deposit and standard deviation of each fuel blend for a plate temperature of 160 °C and 150 bar rail pressure as a function of time. The axes are scaled separately for each blend. *198*

5.28 Example of a time plot and representation of the decay time $t_{3\tau}$ and coefficient 3τ. *199*

5.29 Mean fuel deposit over time for PM1 (—), PM2 (—) and PM3 (—) that is based on a second set of measurements with the plate temperature 120 °C and 150 bar rail pressure. *202*

5.30 Mean fuel deposit over time for PM1 (—), PM2 (—) and PM3 (—) that is based on a second set of measurements with the plate temperature 160 °C and

150 bar rail pressure. 203

5.31 Summary of the trends found during the film thickness measurements of the impinging sprays on a rough metal plate. 211

6.1 Relative drift of engine out particulate numbers during the dirty-up phase for blends Fuel A (●), Fuel B (●), Fuel C (●), Fuel D (●) and Fuel E (●,●). The latter fuel was run twice in this phase. Zero PN equals to the basic emissions level of new injectors. The blue bands correspond to start-up and shutdown phases of the test. This data was provided by Shell Global Solutions. 214

6.2 Relative drift of engine out particulate numbers during the clean-up phase for injectors previously fouled with blends Fuel A (●), Fuel B (●), Fuel C (●), Fuel D (●) and Fuel E (●,●). All injectors were run with Fuel C during this part, with the exception of one set of Fuel E that was exposed to Fuel F (●) here. Zero PN equals to the basic emissions level of new injectors. The blue bands correspond to start-up and shutdown phases of the test. This data was provided by Shell Global Solutions. 215

6.3 Comparison of micrographs from an injector that was run with Fuel A (a1-d1) in the dirty-up phase and a clean injector (a2-d2), with detailed pictures of both injector tips (a1, a2), all injector nozzles (b1, b2), a single injector nozzle close-up view (c1, c2) and the side views (d1,d2). The photographs were provided by IAV Automotive Engineering. 217

6.4 Comparison of micrographs from an injector that was run with Fuel A (a1-d1) in the dirty-up phase and an injector that was run with Fuel D (a2-d2), with detailed pictures of both injector tips (a1, a2), all injector nozzles (b1, b2), a single injector nozzle close-up view (c1, c2) and the side views (d1,d2). The photographs were provided by IAV Automotive Engineering. 218

6.5 Comparison of micrographs from an injector that was run with Fuel D (a1-d1) in the dirty-up phase and an injector that was run with Fuel C (a2-d2), with detailed pictures of both injector tips (a1, a2), all injector nozzles (b1, b2), a

single injector nozzle close-up view (c1, c2) and the side views (d1, d2). The photographs were provided by IAV Automotive Engineering. 220

6.6 *Comparison of micrographs from an injector that was run with Fuel A (a1-d1) in the dirty-up phase and one with Fuel C afterwards (a2-d2), with detailed pictures of both injector tips (a1, a2), all injector nozzles (b1, b2), a single injector nozzle close-up view (c1, c2) and the side views (d1,d2). The photographs were provided by IAV Automotive Engineering*. 222

6.7 *Mean images of the spray from the clean injector based on 5, 10, 15, 20 and 50 injections.* 224

6.8 *Extracted frames from the mean scattering intensity time series of the clean injector. The timestamp corresponds to the time after triggering the injector.* ...228

6.9 *Comparison of the spray pattern between the clean, the fouled (Fuel A) and the cleaned-up (Fuel C) injector. The top row shows the extracted mean image and the bottom row the corresponding standard deviation*. 229

6.10 *Comparison of mean scattering intensity images calculated from the first 50 (left column) and the last 50 (right column) injections of a 500 injection series*. 230

6.11 *Relative differences between the dirty and the cleaned-up injector sprays (left side) and the dirty and clean injector sprays (right side). Black corresponds to the same local intensity in both images, green to higher and red to lower intensities in the mean spray image of the dirty injector.* 231

6.12 *Second eigenmode (top row) and third eigenmode (bottom row) of the sprays generated by the three injectors*. 234

6.13 *Comparison between the cleaned-up injector (left) and the second clean injector (right).* 235

List of Tables

2.1 *Overview of important factors of the liquid influencing single droplet spray impingement* [55]. *35*

2.2 *Overview of parameters investigated to minimise liquid deposits in engines*. *53*

3.1 *Overview of investigated blends of the physical matrix*. *113*

3.2 *Overview of investigated blends of the chemical matrix*. *113*

3.3 *Calculated ratio factors and injection pulse widths for all fuel blends based on the reference blend PM4 at 150 bar injection pressure*. *114*

3.4 *Surface tension and viscosity data of the investigated fuel blends*. *115*

3.5 *Boundary conditions of the spray pattern analysis experiments*. *116*

3.6 *Available injectors and injector dirt-up and cleaning cycles, which were performed by IAV Automotive Engineering*. *123*

4.1 *Physical properties of the liquids used to test the measurement technique* [201]. *138*

4.2 *Calculated evaporation energy for each fuel based on a theoretical deposit volume and for the measured volume*. *145*

5.1 *Visible start of injection (VSOI), visible end of injection (VEOI) and visible injection time (VIT) of each fuel blend and rail pressure*. *157*

5.2 Measured temperatures of the air inside the injection chamber for the different plate temperatures and fuel blends investigated. 159

5.3 Quantities calculated from the Gaussian fits that were applied to the mean velocity, AMD and SMD profiles. 176

5.4 Overview of the quantities calculated from the Gaussian fits of all fuel blends investigated. 177

5.5 Comparison of the spray width based on the Gaussian velocity fits and the values calculated from the intensity analysis in chapter 5.1. 180

5.6 Respective decay time $t_{3\tau}$, fuel injection mass, maximum deposit mass, and percentage of deposited fuel for all fuel blends. 200

Nomenclature

Latin Symbols, uppercase

A	area
D	diameter
E	fuel deposit over time
E_0	maximum fuel deposit
N	number of droplets with diameter D
Oh	Ohnesorge Number
R_a	arithmetic mean of the surface roughness
R_z	vertical surface roughness
Re	Reynolds Number
ΔT	intensity ratio (RIM)
T	temperature
T_{inj}	injection temperature
R	ratio
$V_{\ln}$	normal velocity of incident droplet
We	Weber Number

Latin Symbols, lowercase

d	diameter or thickness
h	lower heating value

Latin Symbols, lowercase

i_0	intensity of the rough metal surface
i_{inj}	intensity with liquid film
i_{liq}	intensity of the rough metal surface covered by liquid
i_{ref}	intensity without liquid film
p	pressure
p_{inj}	injection pressure
$\dot{q}_e$	heat transfer rate from the environment
u_I	incident velocity
u_R	reflected velocity
t	time
v	velocity
x	x-coordinate
y	y-coordinate

Greek Symbols

α	incident angle
β	reflection angle
φ	horizontal detector angle
ρ	density
ρ_d	density of the droplet
σ	surface tension
θ	beam angle
ψ	vertical detector angle
τ	decay time

Abbreviations

Abbreviations

AC	alternating current
AMD	arithmetic mean diameter
APM	aerosol particle mass analyser
ASCII	American Standard Code for Information Interchange
BET	Brunauer, Emmett and Teller
bTDC	before top dead centre
CCD	charged-coupled device
CFD	computational fluid dynamics
CMOS	complementary metal–oxide–semiconductor
CPC	condensation particle counter
CPMA	centrifugal particle mass analyser
DMF	2,5-dimehtylfuran
DC	direct current
ELPI	electrical low-pressure impactor
EtOH	ethanol
FWHM	full width half maximum
GDI	Gasoline direct injection
IR	infrared
LCI	low-coherence interferometry
LDA	Laser Doppler Anemometry
LED	light emitting diode
LEV	low emissions vehicle
LIF	laser induced fluorescence
LII	laser induced incandescence
LPG	liquefied petroleum gas
NIR	near-infrared
NLD	non-linear diffusion
NO_x	nitrogen oxides

Abbreviations

OEM	original equipment manufacturer
PDA	Phase Doppler Anemometry
PFI	port fuel injection
PM	particulate mass
PN	particulate number
POD	proper orthogonal decomposition
PTFE	polytetrafluoroethylene
RIM	refractive index matching
RON	research octane number
SEM	scanning electron microscope
SMD	Sauter mean diameter
SMPS	scanning mobility particle sizer
T90	temperature at which 90% of the liquid has evaporated
TEM	transmission electron microscope
UBHC	Unburnt hydrocarbon
UV	ultra violet
VEOI	visible start of injection
VIT	visible injection time
VSOI	visible start of injection

Chapter 1

Introduction

The interaction between the spray and a solid wall is a widely observed phenomenon internal combustion engines. Most of the time this process is unwanted and can cause great challenges from an optimization stand point. One of these issues is wall or piston wetting observed in direct injection gasoline (GDI) engines [1], [2]. This concept describes the formation of a thin liquid film on the surface of the cylinder, usually as a consequence of the collisions between the fuel spray and the liner or piston during injection [3]–[8]. Although, this process is not only limited to the direct injection concept in engines, it has been shown that the created liquid films lead to diffusion type flames during the combustion phase which result in significantly increased emissions in unburnt hydrocarbons and particulates compared to regular in-cylinder combustion [4], [9]–[15]. Because of this, understanding the mechanism behind pool fires and minimizing their occurrence is of increasing interest for the automotive industry with regards to the strict targets of current emissions regulations EURO 6 in Europe and LEV III (Low Emissions Vehicle Program) in the US [16], [17].

The particulates formed during the combustion process in a GDI engine can also be a significant health hazard [18]–[21]. Literature shows that the direct injection concept can lead to significantly increased particle numbers, also in sizes, which are considered to be

very hazardous [16], [22]–[24]. This means that aside from the governmental legislation regarding the number and mass of particulate emissions, it is also of interest to further reduce possible health risks caused by of automotive emissions [25].

Several concepts have been tested to minimize the effect of particulate emissions caused by wall wetting in GDI engines. Aside from changing the engine design or layout which cannot be adopted for existing engine platforms as easily, there are other approaches that could be applied. One such idea is to modify the injection timing relative to the crank angle [26]–[28]. Also the concept of multi-stage injection has been tested, mainly to accommodate the increasing charge necessary due to downsizing and to avoid auto-ignition under certain load conditions [12].

Another approach is to change the surface temperature of the cylinder liner and the piston. There are investigations that show that, with increasing surface temperature in the engine the amount of liquid deposit and consequently the particulate emissions are notably reduced [29]. In combination with the increased emissions for cold start conditions, especially in the case of colder ambient temperatures certainly shows the potential impact of this property on engine performance and emissions reduction [30]. Additionally, increased fuel temperature and low cylinder pressure can also have a positive effect on the evaporation behavior of the liquid [31].

Because the process of liquid deposition and subsequent evaporation is happening in the order of milliseconds, it is necessary to establish a measurement setup that is capable to capture information at a large temporal resolution. There are several established measurement techniques applied in this research area. Most of them suffer from drawbacks leading to tradeoffs which might not be desirable for a given application. Usually, it is possible to achieve either a fast data recording rate or a good spatial resolution. After an intensive review, these concerns lead to the development of a novel measurement technique to investigate impinging gasoline sprays at different engine conditions.

An additional effect that leads to increased particulate emissions is the buildup of combustion products residue after each cycle; more specifically the deposits that lead to injector fouling can have a significant impact on the engine performance [32]. Although there is a clear link between injector performance reduction and injector deposits [33], this

problem has not been researched as much as the wall wetting phenomenon. Furthermore, it is not completely clear if the fouling behavior can be transferred between injector designs.

This work is split into two sections. The first and main part is investigating the effect of fuel composition on the formation of liquid deposits and the second part looks at injector fouling and the reasons for the observed drift in engine emissions. The research was derived and conducted as part of a joint collaboration between Shell Global Solutions, Nissan Motor Company Limited and Imperial College London. The test procedures were selected with the focus on minimizing particulate emissions of a current engine design in order to meet future emissions regulations.

As part of the first section the development of the experimental setup will be described and how it was used to recreate and vary certain engine conditions at a more approachable scale. The rig provided a time and cost effective alternative to similar research in an engine. Additionally, flexible optical access of the injection chamber was far superior to that of an optical engine and provided options for different measurement techniques. With the setup a series of gasoline blends were investigated regarding the spray patterns, velocity- and droplet size distributions and wall films. The experiments involved high speed spray visualizations, Phase-Doppler analyses of droplet velocities and sizes, as well as measuring the volume of thin liquid films generated by the spray. The latter was done with a novel measurement technique that was developed as part of this work and will also be described in detail. All measurements were performed with different temperatures and injection pressures to investigate influences on the spray in free and impinging configurations.

The second part of the work presented focuses on the spray pattern and penetration depth of injectors that were deliberately fouled in test engines as part of a collaboration between Shell Global Solutions and Imperial College London. Some of these injectors were subsequently cleaned with a special type of fuel which lead to emission levels that were comparable to new and unused injectors. This investigation is intended to yield an explanation of the change in engine performance and increase in particulate emissions caused by injector fouling.

Combining the results of both parts, an insight into the process of wall wetting and liquid deposition in gasoline engines shall be given, with possible recommendations for future engine development and management on how to minimize these problems.

Chapter 2

Literature review

2.1 The concept of gasoline direct injection engines and their challenges

For the majority of its lifetime, a modern automotive engine on the road is operated under partial load. This is a term which describes an engine running under less than full power. For the classical gasoline powered engine, this means that the throttle controlling the intake of air and fuel through the suction flange is almost closed. Naturally, the result is a large pressure drop and as such a very small engine efficiency. To overcome this issue and following the concept of Diesel engines, where the power is controlled by the amount of fuel that gets injected into the engine, the concept of the gasoline direct injection has been established [2]. Mitsubishi was the first OEM that introduced the modernised design of GDI engines into the market in 1996. In the following years it continued to be adopted by other car manufacturers [2], [8].

The key difference between a gasoline direct injection engine and a port fuel injection engine (PFI) is how fuel is mixed with air before the combustion. Figure 2.1 shows a schematic of the two principles [1], [12].

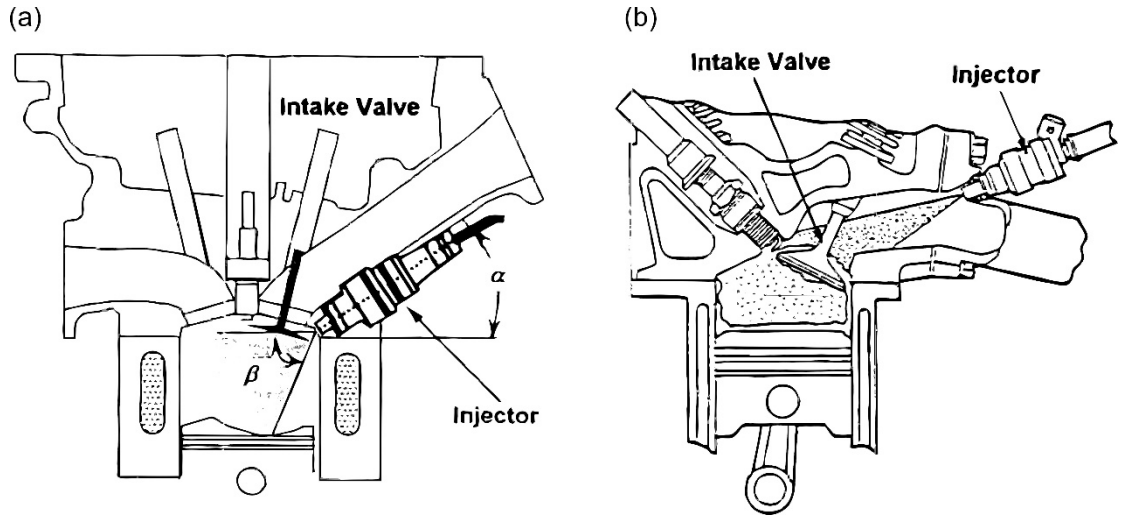


Fig. 2.1 *Schematic comparison of the concept of gasoline direct injection (GDI) (a) and port fuel injection (PFI) (b)* [34].

In the case of GDI, the fuel is injected directly into the combustion chamber, which opens the system up for many different injection strategies that were previously not possible. Also, this means that the principle of throttling the air flow to control the engines load is no longer necessary, which improves part-load operation efficiency substantially and thus reduces fuel consumption at the same time [1], [2], [35].

The concept of GDI was split into different designs over time. The major groups of GDI engine designs are air-guided, wall-guided and spray-guided. These concepts of direct injection engines are presented in Figure 2.2. Air-guided GDI engines use a tumbling motion of the inducted air to direct the spray droplets, injected at the centre of the chamber, towards the spark plug. In wall-guided injection concepts, the fuel spray gets injected from the side of the cylinder towards a shaped piston bowl, which guides the spray towards the tip of the spark plug and ensures a stable combustible mixture is created once the spark is created. In spray-guided engines, the injector sits very close to the spark plug to create ignitable mixture around it during combustion.

In general, a GDI engine can be operated as a so-called stratified-charge engine. This concept combines the features of a spark ignition engine and a compression ignition engine. Stratification allows for adjusting, for example, the injection and ignition timings

in order to avoid knocking, which is similar to Diesel engines, but the actual combustion is controlled by the spark ignition timing [36].

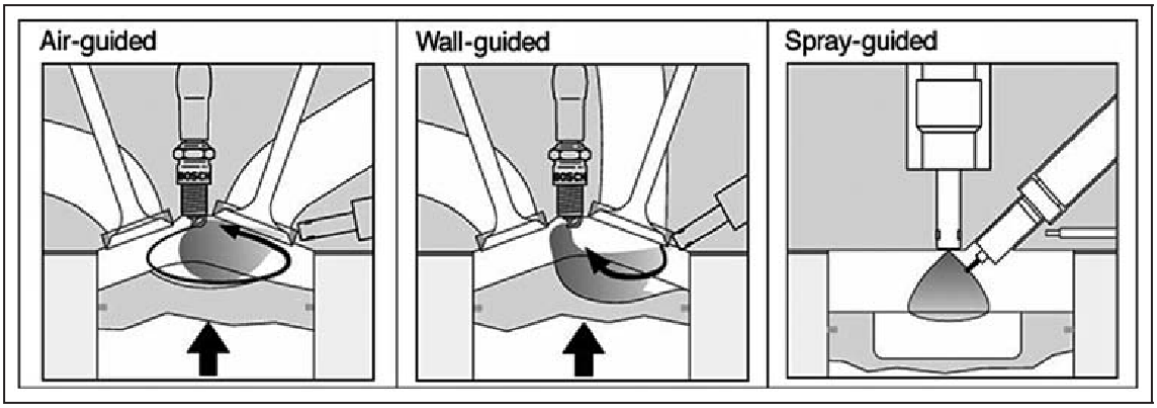


Fig. 2.2 *The concept of air-guided (left side), wall-guided (middle) and spray-guided (right side) direct injection engines* [37].

Another benefit is that with direct injection it is possible to achieve higher compression ratios, supported through charge cooling during the injection process. This is very important for the ongoing pursuit of downsized engines, which requires higher in-engine pressures [38]–[40]. Using different fuel blends, it is also possible to further enhance charge cooling, for example, with ethanol, and its large heat of evaporation [41].

Additionally, without fuel inside the manifold, it is possible to completely cut-off supply during deceleration, which further benefits fuel economy and reduces the amount of unburnt hydrocarbon (UBHC) emissions under these conditions. Overall, the fact that the injection of fuel is taking place inside the cylinder enhances the options for engine efficiency optimisations and emissions control dramatically and opens up engine design to completely new concepts [12].

Also the fuel consumption during cold start can be optimised by direct injection. Additionally, fewer heat losses and higher compression ratios are associated with GDI compared to PFI [34], [42]–[44].

However, aside from the advantages, there are also drawbacks and new challenges associated with the concept of GDI that are not an issue of the same magnitude with port fuel injection.

The topic of combustion instabilities in engine development regained interest in recent years, because of the increasing demand for downsized engines. Because the market would not accept a reduction in engine power to further reduce emissions, it is necessary to increase the cylinder pressure before combustion to yield similar performance in smaller displacement volumes. Usually, this increases the risk of knocking and other combustion instabilities significantly. The afore-mentioned idea of charge cooling by fuel injection is one concept to overcome some of these problems, but might not be sufficient in all engine operating conditions [37], [45].

Because fuel is atomising directly inside the cylinder, mixing with air can be greatly reduced, compared to PFI where mixing of air and fuel is promoted during the suction stroke. This can lead to droplets of fuel either not having evaporated fully or the existence of regions of rich and lean mixtures, which contribute to an increased formation of emissions. Brehob *et al.* [35] saw an increase of hydrocarbon emissions of up to 25% in a direct injection engine compared to a port injection engine at the same operating condition. Kaiser *et. al* [46] observed an increase of engine-out hydrocarbons by a factor of 3.5, promoted by increased stratification in their direct injection engine. Observations like these raise the concerns associated with the GDI concept and potentially create hurdles that cannot be overcome without substantial optimisation of the engine design.

The worst case scenario is the phenomenon of piston and wall wetting, caused by the impingement of the fuel spray, which can lead to wall film formation. Even though in some circumstances spray impingement can be desirable in wall guided engines to create a rich region around the spark plug, the presence of a liquid deposit, or film, during combustion usually creates several significant drawbacks. The literature shows that this film formation can lead to a significant increase in unburnt hydrocarbons and particulate emissions [3], [14]. The extent of those emissions can be much larger than for an optimised PFI engine [35], [47]. So large in fact, that it is of serious concern for car manufacturers to minimize the occurrence, since governmental regulations such as EURO 6 and LEV III

demand a low threshold of emissions from modern cars, which cannot be met in these cases [48].

The overall change in the emission profile of a direct injection engine compared to port fuel injection engines, and the increased tightening of emissions regulations with the development of more realistic driving emissions standards, are the main concern associated with the GDI design [49], [50].

In the following chapter a look at the interaction between spays and the walls of the combustion chamber in engines shall be presented. The overview includes research that links the deposit with the formation of pollutants in gasoline direct injection engines. Additionally, the various parameters that have shown an effect on the deposit formation will be presented and discussed.

2.2 Liquid deposit formed by fuel sprays in direct injection engines

Because of the underlying design of the GDI engine, an interaction between the fuel spray and the walls of the combustion chamber cannot be avoided completely. This interaction can cause fuel deposits of the surface that have a very long lifetime, which exceeds the evaporation time of regular fuel droplet clouds significantly. The presence of a liquid film on the piston surface or the cylinder liner during, and sometimes even after, the combustion phase is not at all desired. Many different parameters can have an influence in the actual film formation of an impinging fuel spray and need to be considered in order to optimise the engine design (Figure 2.3) [51], [52].

The spray itself depends heavily on the injector design (pinhole vs. swirl-type injector and multi-hole injector), the injection pressure and the temperature as well as the physical properties of the fuel such as surface tension and viscosity. Also the spray cone angle is very important. The droplets are characterised by their velocity, diameter, temperature and the incident angle, once they impinge on the plate. Ambient conditions, such as the air temperature, air flow (stagnant air continuum or momentum of flowing air)

and pressure all influence the formation of the liquid film, also. Finally, the conditions of the solid wall influence this phenomenon. The choice of surface material and *e.g.* its thermal conductivity, surface roughness and temperature has an impact on the extent and shape of the liquid film. The liquid film itself is usually characterised by its area, height and temperature, as well as by the thermal conductivity and surface tension of the liquid and by the velocity of the film (which will affect the effective heat transfer coefficient). Area and height are usually used to quantify the extent of the liquid film and evaluate how the change of a parameter is impacting the film formation.

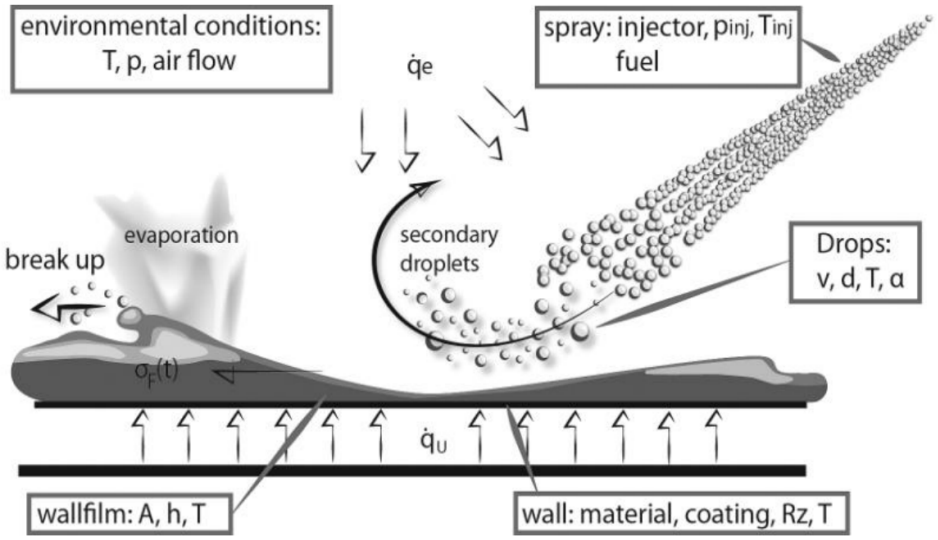


Fig. 2.3 *Interaction between the spray and the wall, showing different influencing parameters on the liquid film formation* [52].

The impact of these influential factors on spray impingement is mostly derived from single droplet experiments and models. A summary of the factors that promote droplet breakup on a solid surface can be found in Table 2.1.

The importance of investigating spray impingement inside the cylinder started already early in the development of the modern direct injection engine. Salters *et al.* [54] demonstrated with experiments carried out in an optical engine that, depending on the injection timing, a significant amount of liquid can be deposited on the piston surface. The

increase of deposit during later injection timings has been previously reported for Diesel engines, also [55].

Table 2.1: *Overview of important factors of the liquid influencing single droplet spray impingement* [53].

factor	effect
impact velocity	larger values promote breakup and wetting
droplet diameter	larger droplets increase wetting
surface tension	small values benefit breakup
viscosity	high viscosity reduces wetting
surface roughness	can increase wetting
wetting angle	large values reduce wetting

Over the years, a model of the mechanisms behind droplet impingement has been established by Bai *et al.* [56] amongst others, which focuses on the behaviour of individual droplets and how they interact with the wall. This model has also been applied to gasoline sprays, specifically in [51], [57], [58]. An overview of the different mechanisms is shown in Figure 2.4.

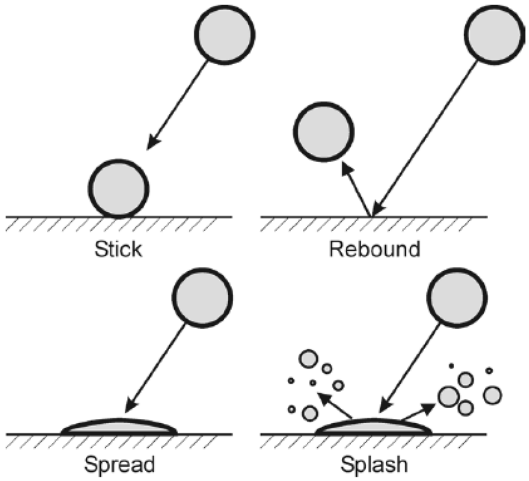


Fig. 2.4 *Simplified classification regimes of droplets interacting with a solid surface* [57].

In general seven different classification regimes are considered [56]:

1. **Stick**: The droplet adheres to the surface and remains almost completely spherical, which can occur at low impact velocities and lower surface temperatures.
2. **Rebound**: The droplet bounces off the wall after impact with a smaller velocity than the initial, but the size of the droplet remains unchanged. This can happen if the wall temperature is very high and a vapour layer is preventing direct contact between the droplet and the wall. In the case of lower temperatures, air can also be entrapped between the droplet and the wall.
3. **Spread**: Moderate impact velocities on dry or wetted walls usually lead to the spread of the droplet into a thin wall film, which can also happen if the droplet merges with an existing liquid deposit.
4. **Boiling-induced break-up**: At very high surface temperatures the droplet disintegrates because of instant boiling.
5. **Rebound with breakup**: Similar behaviour of the droplet to rebound, except that the droplet breaks up into smaller secondary droplets after impact.
6. **Break-up**: The droplet deforms after impingement and forms temperature induced instabilities on the hot surface, which cause it to break-up randomly.
7. **Splash**: If a droplet of high impact energy is colliding with the surface (with or without a present liquid film), usually a crown is formed which breaks up into smaller secondary droplets.

The regimes can be related to each other with the use of the Droplet Weber Number, which represents the ratio between the kinetic energy of the droplet and the surface tension [56]:

$$We = \frac{\rho_d V_{\ln}^2 d}{\sigma} \tag{2.1}$$

where ρ_d is the density of the liquid, $V_{\ln}$ is the normal velocity component of the incident droplet, d is the droplet diameter and σ is the surface tension. With increasing Droplet Weber Number, the impingement regimes are organised as Stick, Rebound, Spread and Splash. Note, however, that these models assume single isolated droplets: in a gasoline

spray, the distance between individual droplets is not large enough to neglect interaction between each other either before or after impingement. However, the mentioned characterisation provides a guideline to interpret the behaviour of different sprays as they impinge.

In addition to the Droplet Weber Number the Ohnesorge Number (Oh) is used to characterise droplets. It is defined as the ratio between the viscous forces and the forces due to the surface tension [59]:

$$Oh = \frac{\mu}{\sqrt{\rho_d \, \sigma \, d}} \tag{2.2}$$

where μ is the dynamic viscosity of the liquid. Large values of Oh mean that the viscosity of the liquid is dominating over the surface tension.

The Weber Number can be used to express the Ohnesorge Number with the help of the Reynolds Number [59]

$$\mathrm{Re} = \frac{\rho_d \, d \, V_{\mathrm{ln}}}{\mu} \tag{2.3}$$

leading to the following relation

$$Oh = \frac{\sqrt{We}}{\mathrm{Re}} \tag{2.4}$$

For a given liquid, droplet velocity can be controlled through the rail pressure and droplet diameter through the nozzle design and injection pressure. Both quantities directly affect the wetting behavior during impingement [53].

Over the years the droplet models were further developed and refined. Bai *et. al* [60] modified the original model to include the influence of surface roughness and impact angle. Other models consider the effect of wet surfaces combined with roughness. More detailed description of these refined models can be found in [51], [57], [61], [62].

One important aspect of the surface temperature in relation to the physical properties of the droplets is the Leidenfrost temperature [63]. The Leidenfrost effect

happens if the temperature of the solid exceeds the boiling temperature significantly, which leads to a vapour layer of the liquid almost immediately upon impact [64]. This layer then acts as an insulator, which hinders subsequent heat transfer greatly and as such reduces the evaporation rate of the droplets [65].

Aside from the surface temperature the incident angle also has a significant role on droplet impingement. If the droplet angle is not 90° to the impingement plane a tangential velocity component is introduced, which destabilises the spreading droplet upon impingement and helps to form secondary droplets due to fragmentation of the liquid film [61], [66]. A schematic overview of the influence of the incident angle is shown in Figure 2.5.

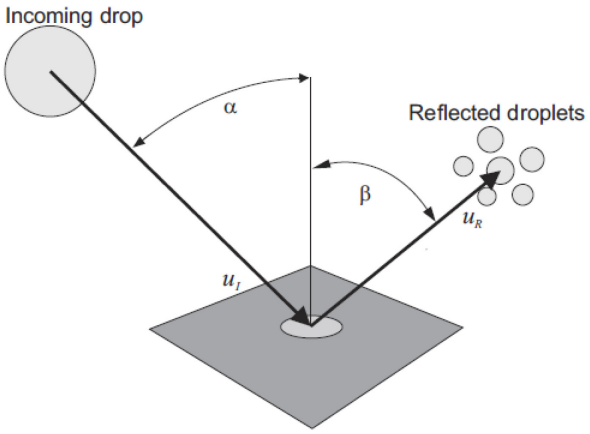


Fig. 2.5 *Incident angle of the impinging droplet, leading to secondary droplet formation* [58].

The value of the incident angle α, directly correlates with the reflection angle β, which means that a large angle of the original droplet relative to the impingement plane leads to large angles of the reflected droplets. Additionally, the droplet size does not affect the angles before and after impingement.

Furthermore, the incident angle also influences the liquid film on the surface if the spray as a whole is considered and not only individual droplets. Literature shows that liquid deposits generated by sprays perpendicular to the surface have a larger thickness

than those formed by angled sprays. Early investigations by Naber *et al.* [67] show that increasing the angle from the normal lead to significantly reduced sheet thicknesses of the liquid deposit. Also, the pattern of the liquid deposit changes from a circular to a more oval shape with increasing angles. A possible explanation is that angled sprays promote a slip motion of primary and secondary droplets, caused by the longitudinal velocity component, which means that fewer droplets contribute to the local film thickness.

More advanced models to describe the interaction between the fuel spray and the wall were developed by Han *et al.* [68] in an effort to describe the underlying process. This study also considered the influence of surface roughness and formation of secondary droplets after impingement, which led to a more comprehensive description of the real system.

A more critical view of single droplet research and its link to real sprays found in internal combustion engines was presented by Moreira *et al.* [53]. According to them single droplet models usually neglect the interaction between the droplets which plays a large role in the behaviour of real sprays. They concluded that it can be misleading to apply conclusions from single droplet measurements to complete sprays.

Looking at the physical properties of the fuel, it is important to consider that gasoline is a multi-component liquid. As such the different parts that form the blend have different evaporating behaviours. Zhao *et al.* [8] found that the most volatile components of the fuel evaporate first, leading to an increasing concentration of the less volatile parts. This can very much affect the mixture formation in the engine and the combustion behaviour. With that in mind it is important to also investigate real (*i.e.* commercially available) fuels in such scenarios.

The consequences of liquid fuel films, caused by impinging droplets, are so-called pool fires. These describe a diffusion flame that is created during the combustion phase of the engine once the flame front reaches the wetted surface of the piston. These fires have a very long lifetime which can exceed the expected combustion duration of a regular engine cycle [69]. Because of this, pool fires are associated with a drastic increase in unburnt hydrocarbons and soot emissions [3], [14]. A schematic explanation of the pool fire concept is shown in Figure 2.6.

Once the fuel film on the piston surface is created, it begins to evaporate and forms a vapour plume above it. Following the diffusivity of the fuel vapour, the mixing with air increases with the distance from the actual film and a combustible mixture is formed at the outer layer of the plume. Once the flame front reaches this mixture a diffusion flame is formed which is leading to the formation of carbon particulates. After the flame front has passed, a rich mixture of fuel and air in the area above the film remains, which is now surrounded by very hot burnt gas. Because of this, strong heat flux from the burnt side is initiated which causes pyrolysis of the fuel plume with drastic soot formation. The additional heat release by the pyrolysis and incandescence from the soot particles further aids in the stabilisation of the pool fire and promotes the evaporation of the remaining fuel film on the surface at the same time. At this stage, a growth of the pool fire is observed, which is caused by the ongoing diffusion of the flame. It is also promoted by the expansion stroke of the piston, which reduces the cylinder pressure.

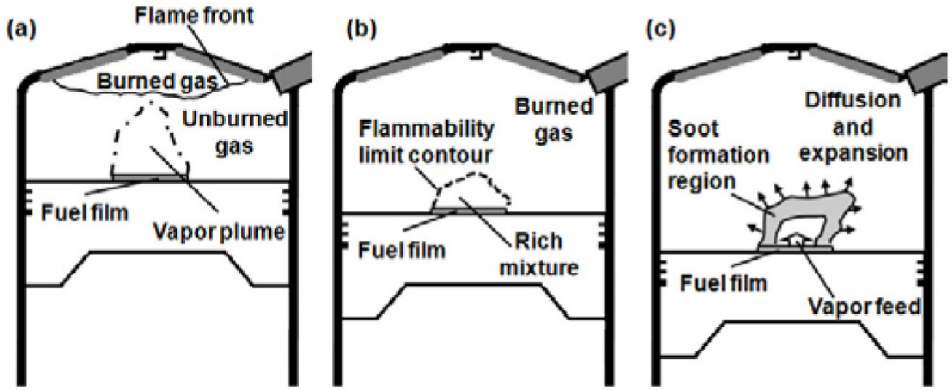


Fig. 2.6 *Schematic description of pool fires and their contributions to engine-out emissions* [69].

2.2.1 Liquid film formation and its relation to the generation of pollutants

Wall wetting and the formation of a liquid film on the liner surface or the piston bowl is considered to have a strong negative effect on engine-out emissions. Early research done

by Stovell *et al.* [70], in cooperation with Toyota already showed the first indication of the connection between wall wetting and the formation of soot and unburnt hydrocarbons in 1998, shortly after the release of the modern gasoline direct injection engine.

Research by Sandquist *et al.* [71] in a stratified-charge direct injection engine also showed that soot formation is significantly increased under stratified conditions. Although there was no direct investigation between the fuel deposit volume and emission formation, they suspected poor mixing and evaporation to be the reason. With a later injection time and higher level of stratification the amount of emissions was increasing, which supports the assumption that insufficient fuel evaporation is the main reason for increased emissions.

Stevens *et al.* [72] used a variety optical techniques to study the connection between fuel impingement, pool fires and soot emissions. They used laser induced fluorescence to quantify the film deposition process, direct flame imaging to visualise the pool fires and laser elastic scattering to capture the soot generated by these flames. The investigations were done in a single-cylinder optical direct injection engine. The data gathered through laser induced fluorescence showed the formation of the liquid film which was caused by impinging fuel sprays. These films persisted throughout the compression stroke and the time of ignition. After the flame arrival these films caused rich diffusion flames that followed the motion of the piston very clearly. Also, they persisted through the expansion stroke until the middle of the exhaust stroke in some cases. Towards the end of the exhaust stroke, they saw a lift-off of the flame, which was then extinguished. With their exhaust analysis they observed a clear correlation between the existence pool fires and soot formation. Even after the pool fire was extinguished, late in the cycle, there was still soot detected at the exhaust which (according to them) means that there are still particles accumulated in the cylinder top, even after the complete combustion of the liquid film. After many cycles they also observed a black carbon residue on the surface of the transparent piston caused by the pool fires, which illustrates the problem of engine fouling due to pool fires, an additional concern in gasoline direct injection engines aside from the increased particulate emissions.

Drake *et al.* [73] published very comprehensive results about the effect of fuel films on the formation of particulate emissions. They ran their tests in a wall-guided direct injection engine, operated at warmed-up and stratified conditions (at 2000 rpm), using a swirl-type injector and experimenting at optimised injection and spark timings. According to them, only a small fraction of the injected fuel actually contributed to the liquid film on the piston surface (about 1%) under these conditions. Their tests with iso-octane showed much smaller deposits (about 0.1%) which, according to them supports the idea, that heavy and less volatile components in the fuel are the main contributors to the liquid deposits [8]. Pool fires began once the flame reached the liquid deposit on the piston surface and started at the outside of the fuel film. They observed that the fire continues to burn as a rich diffusion flame fed by the liquid film until the entire film was gone or the in-cylinder temperatures became too low during the expansion stroke and extinguished the flame.

This process has also been investigated and modelled by Oliveira *et al.* [74]. They found that fuel condensation and deposit occur especially if the fuel vapour pressure is high enough and that the fuel vaporisation is promoted by the incoming flame. The fuel vapour then reacts with the surrounding oxygen forming a transient diffusion flame. The radiation generated by this flame was large enough to be detected as a second heat release peak, which illustrates the significance of pool fires to the overall combustion behaviour in direct injection engines.

The observed and visualised pool fires by Drake *et al.* [73], [75], [76] based on sprays with gasoline show a widespread occurrence over various engine operating conditions. They found that during these pool fires, hydrocarbon emissions and soot is created. According to them, the latter is less likely to oxidise before it exits the engine, which is different from soot formed in rich regions inside the cylinder. This is because of its formation close to the expansions stroke, which reduces the temperature too much for the reaction to continue to completion, combined with reduced mixing effects. For the investigated swirl injector under optimum engine conditions and for an injection mass of 10 mg per cycle, the relation between mass smoke emissions and liquid film mass was about 10^{-1} [73]. By replacing the swirl-type injector with a multi-hole design they were able to reduce the deposited fuel mass by an order of magnitude, which led to a reduction

of particulate emissions to almost zero. The correlation between the wall film mass and the measured particulate emissions can be seen in Figure 2.7.

Even though the amount of emissions in the case of the multi-hole injector were very small, the measurements with the swirl-type injector showed, very clearly, the direct link between the amount of liquid deposit and the soot formation.

Their research also pointed out that the soot formed either by not fully evaporated fuel droplets or over rich pockets was being oxidised for the most part during the combustion cycle of the engine [76]. This supports the assumption that the emissions level of particulate is significantly raised by the occurrence of pool fires.

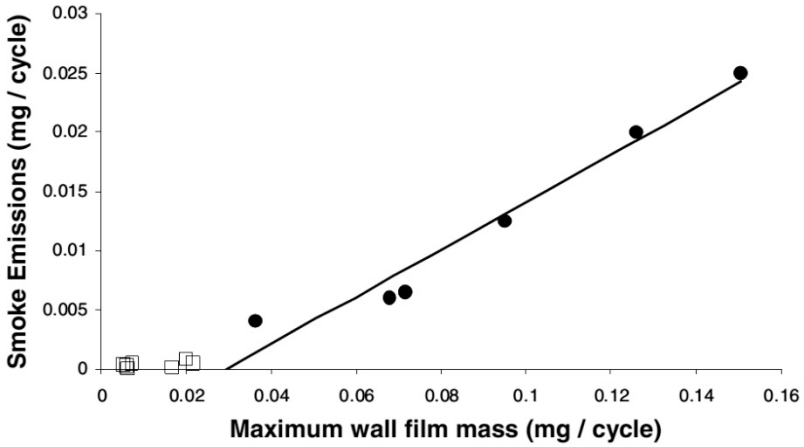


Fig. 2.7 *Relation between measured particulate emissions and wall film mass for a multi hole injector ( ) and a swirl-type injector (•) by Drake et al.* [73].

Similar findings regarding the correlation between the fuel deposit and the soot emissions were also reported by Ortmann *et al.* [77]. They compared different injectors in a modular engine, which was run with optical access, to measure the wall film and as a metal engine for analysing the corresponding soot formation under different operating conditions. The use of their wall guided injector configuration lead to a direct correlation between the detected fluorescent intensity, which is a function of the fuel film volume, and the emissions detected at the exhaust. Running an air-guided direct injection concept showed a

similar trend, but the overall amount of liquid on the piston was reduced and as such, also the emitted soot.

In a recent study about particulate emissions on GDI engines, Jiao *et al.* [78] developed a model that shows how wall wetting contributes to the amount of soot generated in the cylinder with different single- and multi-component fuels, injection timings and wall temperatures. They observed a direct correlation between the soot formation and the wall film mass in their model in the case of multi-component fuels in the single cylinder engine with single-hole and multi-hole injectors. They also found, that lighter components of the fuel film do not contribute to the particulate emissions as much as the heavier ones, because of the reduced volatility of the latter. Overall, these findings support the conclusions from other research groups, which were mentioned earlier.

Stojkovic *et al.* [15] looked at the formation of soot in rich zones inside the cylinder and pool fires by using high speed imaging of hydroxyl radicals. They combined data from previous research with the results obtained in this work and concluded that pool fires are the dominant source of particulate emissions, especially under warmed-up stratified conditions. Also, the mass of engine-out emissions did indeed correlate with the extent of the liquid film. Compared to the soot generated in rich zones in the cylinder volume the particles generated in pool fires seemed less likely to oxidise before they leave the engine, because these persisted over a very long time scale, according to them. This observation was verified by the measurement of the soot temperature, which showed significantly lower values for the soot generated by late pool fires. The values observed were too low for subsequent oxidisation of the particles generated.

In their work, Szybist *et al.* [79] investigated a series of fuel blends with different ethanol content regarding the generated particulate emissions. They concluded that the presence of liquid fuel on the piston resulted in the formation of large numbers of particles in pool fires, even though the ethanol content seemed to be beneficial.

Sabathil *et al.* [80] investigated particle formation during cold start and transient operation on an engine dynamometer, while varying fuel to air ratio and injection timing. The latter caused spray impingement under different conditions resulting in significantly increased soot formation.

Velji *et al.* [81] investigated soot formation and oxidisation in an optical GDI engine at different injection timings. They used a combination of Rayleigh scattering and laser induced incandescence to receive temporally and spatially resolved soot concentrations, particle sizes and particle number densities. According to them, the main source of soot inside a direct injection engine are pool fires, when the engine is operated in a homogeneous mode, without stratification. When run under stratified conditions soot is also generated in rich regions in the combustion chamber volume, complementing the pool fires. Overall, the generated soot could not be sufficiently oxidised during combustion, despite increased oxygen concentration, mainly because of the long lasting nature of these flames and the low residence time of the particles in the engine.

In a more recent study, Koepple *et al.* [29] developed a CFD model to describe the soot formation mechanisms inside an engine with a focus on the underlying process of spray-wall interaction as the most significant source of particulates. To validate the computational results they used data from experimental measurements performed in an optical single-cylinder engine with multi-component fuels. Their numerical results showed good agreement with the empirical data and emphasised, that with increasing liquid deposit on the piston surface, the amount of soot increases, especially for high rail pressures which lead to an increase in spray penetration and therefore larger wall films masses. This was further enhanced by changing the injection timing to earlier values, which caused more fuel to be deposited on the piston. These factors not only caused bigger film masses but also delayed film evaporation and as such poor mixing in the cylinder. They concluded that these locally very rich zones correspond to the increased number of particulate emissions and need to be avoided to meet the requirements of emissions regulations.

Johansen *et al.* [82] investigated the combustion and soot formation in a single-cylinder engine with optical access using fuel blends containing high ethanol content. The injection configuration was spray guided. Varying different conditions, such as engine speed, amount of injected fuel, injection sequence and timings, they investigated soot formation and oxidisation through high speed imaging, chemiluminescence and soot incandescence. During their experiments, they ran single and multi-injections per cycle and measured the soot formation under different conditions. The phenomenon of wall wetting

and pool fires was observed under several conditions, but especially during their single injection process. Once fuel impingement happened they saw significantly increased particulate emissions. They also saw pool fires to persist to very late times in the engine cycle at which point the temperature inside the cylinder was no longer sufficient to oxidise the particles, and they concluded that the pool fires were the primary source of soot in their single injection experiments.

The combustion behaviour of gasoline regarding its emission levels was also investigated by Oh *et al.* [83] in a single-cylinder direct injection engine in comparison with liquefied petroleum gas (LPG). The latter has a significantly better evaporation rate inside the cylinder, which lead to reduced emissions by a factor of three compared to gasoline. Even though the actual particle size distribution was the same with both fuels under different operating conditions, the overall particle numbers were lower across the spectrum in the case of LPG. Even though they did not specifically investigate pool fires, they concluded that higher emissions were caused by poorer mixing and insufficient evaporation of gasoline.

Aside from soot formation, the generation of unburnt hydrocarbons caused by wall wetting and pool fire has also been of concern. Giovanetti *et al.* [84] already pointed out in the 1980s that large droplets of a fuel spray can impinge on the piston surface before they evaporate and contribute to the formation of hydrocarbons. Early investigations with modern direct injection engines also showed a drastic increase of hydrocarbon emissions compared to related engines with port fuel injection under similar conditions.

Kaiser *et al.* [46] detected an increase of hydrocarbons by a factor of up to 3.5 overall in their experiments. Although they were not able to investigate the reason for this, they suspected a much degraded evaporation behaviour of the direct injection engine in stratified conditions, which promoted liquid fuel to be present during combustion.

The research by Sandquist *et al.* [71] also showed increased emissions of hydrocarbons for stratified direct injection engines. In their single-cylinder setup they showed that overmixing at the air and fuel boundaries and undermixing at the spray centre and on the surface of the piston are most significant factors leading to hydrocarbon emissions. Fuels that are less volatile seem to promote the emissions level, and according

to them it is necessary to investigate real fuel blends rather than fuel substitutes (*e.g.* iso-octane), because of their drastically different evaporation behaviour.

Li *et al.* [4] designed an in-cylinder injection probe to deliberately deposit fuel on the cylinder wall and investigated the connection between the deposit volume and engine-out hydrocarbon emissions under different operating conditions. With their apparatus they were also able to test the effect of wetting different surfaces inside the cylinder on the extent of hydrocarbon emissions. Overall, they found that the wetting of any surface inside the cylinder leads to strongly elevated hydrocarbon emissions, also under part load conditions. They observed a difference between wetting the cylinder liner and the piston surface, because the temperature of the former is more affected by the coolant performance. The amount of hydrocarbon emissions was directly proportional to the amount of liquid deposit. Under part load condition there was an increase of up to 70% when depositing around 10% of the injected fuel on the surface. They also saw an increased hydrocarbon level throughout the entire exhaust process after depositing 1.5 mg of liquid fuel inside the cylinder. In general, they concluded that the process of fuel film evaporation is slow compared to the combustion phase of the engine. Proposed reasons were the limitation of the heat transfer and the increased overall cylinder pressures during the compressions and expansions stroke. Later work from Li *et al.* [85] also showed that wetting of the exhaust side of the liner is especially detrimental regarding emissions and they also pointed out that liner impingement could have an effect on the oil-layer performance of the engine.

The connection between in-cylinder wall wetting and hydrocarbon emissions was also investigated by Stanglmaier *et al.* [13], with similar findings to Li *et al.* [4]. They also used an injection probe to impinge fuel on different sections of the cylinder and at different times relative to the crank angle of the engine. They agreed that the occurrence of wall wetting in general leads to increased hydrocarbon emissions. By varying the start of injection relative to the engine cycle they could investigate the effect of residence time of the liquid deposit on the amount of emissions. Overall, they saw very little change, which implied that the process of vaporisation was much slower than the engine cycle and was mainly controlled by the surface temperature and the cylinder pressure. It also meant that

impingement happened late in the cycle where the oxidisation of the hydrocarbons was less likely. The worst case scenario was wetting the liner under the exhaust ports and the piston top, which was according to them a likely area that is affected in the investigated engine design and they proposed a change in the location of the injector.

Huang *et al.* [86] continued the research with the injection probe and used a series of pure hydrocarbon liquids to investigate the influence of fuel volatility and structure on the exhaust hydrocarbons. They concluded that volatility has a non-linear effect on hydrocarbon emissions in the case of wetting of the piston surface and that the relation between the surface temperature and the boiling temperature of the liquid is very important. One fuel with a boiling temperature far below the surface temperature produced very high hydrocarbon emissions, which was due to the Leidenfrost effect according to them. In another study, they investigated engine load and speed and how these affect the hydrocarbon formation [87]. They found that, in their setup, the amount of unburnt hydrocarbons was up to an order of magnitude larger in the case of fuel impingement compared to homogeneous charge and that a larger deposited volume led to more emissions.

The extent of hydrocarbon emissions due to wall wetting was also investigated by Pierre *et al.* [88]. They were operating a single cylinder direct injection engine in transient conditions. During the experiments they used a mixture of four different single component fuels and observed increased hydrocarbon formation in the case of spray impingement, especially in cold start conditions. During engine warm-up injection timing and engine temperature seem to have a critical influence on the emissions.

Chin *et al.* [43] designed a multicomponent fuel combustion model to simulate the hydrocarbon emissions caused by wall wetting at different locations within the cylinder chamber. The results were verified by comparing them to experimental data. The computational data agreed with the experimental results and showed significant increase in hydrocarbon emissions in the case of wall wetting near the exhaust valves and on the piston surface. Overall, the emissions increased more the closer the wall wetting happened to the exhaust port of the cylinder. They also observed preferential evaporation of the lighter components of the liquid deposit in the case of long lasting films that survived the

expansion and exhaust stroke. The remaining heavy components in the film hindered the evaporation behaviour as previously seen.

In a more recent study, Costanzo *et al.* [89] investigated fuel films regarding hydrocarbon emissions in a direct injection engine at warm-up conditions. They were able to observe the liquid film in the firing engine, while recording the temperatures of the liquid and correlating the results with corresponding exhaust gas measurements. The imaging was done with a high speed camera and the surface temperature was recorded through thermocouples in the combustion chamber. Most of the injected fuel was delivered in vapour form and well defined volumes of liquid fuel were deposited at different locations inside the cylinder. Using several assumptions they were able to extract hydrocarbon emissions that were originating from the liquid film and ignore those that were created in the gas phase of the cylinder. Overall, they agreed with previous findings that the presence of any liquid film inside the engine causes an increase in hydrocarbon emissions and that with increased film mass the amount of hydrocarbons also increases. It was possible to collapse most of their data when taking the surface temperature and the initial amount of liquid deposit into account. The results showed that 10% of the deposited fuel mass is detected as hydrocarbons at the exhaust of the engine. The overall amount of hydrocarbon emission was reduced with increasing wall film temperature.

Parallel to their experiments about particulate emissions, Drake *et al.* [9] also looked at the hydrocarbon emissions caused by liquid deposits in the cylinder. In the comparison between the multi-hole and the swirl-type injector they saw more similar results in the engine-out hydrocarbon emissions, then in the case of the particulates. For both injectors they saw increased hydrocarbon emissions caused by the liquid deposit. However, the clear trend between the fuel film mass and the engine-out hydrocarbon mass was not as evident. This was in contrast to the findings of other groups, which predominantly saw a direct link. Drake *et al.* concluded that their investigated engine condition might have been the cause of that. In their case they estimated that about 10-15% of the wall film mass gets converted to unburnt hydrocarbons that are emitted by the engine, which resulted in a contribution of 2-15% of the cumulative hydrocarbon emissions in the case of their swirl-type injector and about 1% in the case of the multi-hole

injector, which produced almost no liquid film on the piston top. Aside from wall films, they also saw that lean regions in the cylinder volume, below the flammability limits, also caused hydrocarbon emissions.

In addition to particulates and hydrocarbons, other emissions have also been investigated. In Particular, carbon monoxide, carbon dioxide and NO_x are of interest as they are also heavily regulated by the vehicle emissions legislations EURO 6 and LEV III. There are studies available trying to link these emissions to the occurrence and extent of fuel wall deposit. However, the trend is not as clear in this case, which is why there will be no detailed overview given. Publications about this matter can be found in [46].

2.2.2 Techniques to analyse soot particles and emissions

Different measurement techniques are applied in the context of pollutants produced by gasoline direct injections engines. One of the main concerns in this context are particulate emissions, which are also the focus of this research. To provide some background a brief overview of common techniques to analyse soot particles are presented in this section.

A number of quantities are used to characterise and compare particulate emissions of internal combustion engines. These are particle mass, particle number concentration, size distribution, composition, shape and structure. Depending on the quantity relevant, different techniques are applied.

The measurement of the particulate mass is most commonly done through gravimetric analysis. Usually, a diluted sample of the exhaust gas is cooled down and filtered. The filter itself is weighed before and after the sampling to measure the total mass of the collected particles. A particular concern of this method is organic vapour adsorption that can occur during the sampling process. This creates a bias of the measurement, in particular if the accumulated particle mass is small. Different filter media are being used to minimise this effect, but the creation of artefacts cannot be eliminated completely [90].

An alternative method to determine particle mass is the aerosol particle mass analyser (APM). It utilises two rotating coaxial electrodes that form a cylindrical channel

through which pre-charged particles are flowing. The particles are exposed to electrostatic forces on the inside and centrifugal forces on the outside of this channel, which means that particles below a certain mass-to-charge ratio get collected on the inside wall and particles above it get collected on the outside wall. Effectively, only a small range of particles pass through the apparatus. By knowing the charge of these particle, the mass can be inferred [91]. The downside of this method is that particles that collide with either wall and adhere are lost in the analysis.

An advancement of the APM is the so called centrifugal particle mass analyser (CPMA), which uses the same two cylinders, but also introduces a force gradient over the gap. This is done either by rotating the inner cylinder at a larger speed than the outer or by changing the geometry of the electrodes. Because of this it is possible to force the particles to the centre of the channel rather than to the wall and as such increase the efficiency of the analyser [92].

Particle number concentrations are usually measured with a condensation particle counter (CPC). To detect fine particles the aerosol is saturated with water vapour. Once the sample is cooled down, the particles act as condensation nuclei and droplets are formed around them. These can then be detected through optical methods from which the particle number concentration can be inferred [93]. One main concern of this technique is the formation of agglomerates during the condensation process that affect the final particle number. This can be avoided if the sample is diluted appropriately. Furthermore, the lower detection limit of this technique is commonly between 3 to 10 nm, which means if a significant number of particles in that region is to be expected, the reliability of the produced data is compromised [93], [94].

Particle size distribution is frequently measured with scanning mobility particle sizers (SMPS). The technique uses two concentrically cylinders, which impose an electric field on the particles. For a given intensity of this electric field the time required for a particle to travel to the inner rod depends on its size. The different particle sizes are then extracted through collection slots positioned around the inner cylinder. Unique with SMPS is that the electric field intensity varies over time by changing the applied voltage [95]. The

benefit of this technology it its large measurement range. However, its sampling time in the order of minutes can be insufficient to investigate highly transient phenomena [96] [97].

An alternative to the SMPS is the electrical low-pressure impactor (ELPI) [98], [99]. It uses a diode charger to charge the sampling particles to a defined level. These particles are then separated in a so called cascade impactor which consists of a number of insulated stages with different electric fields collecting different sizes of particles. Once a particle impacts on the surface of a stage its charge is transferred and detected by an electrometer. This way it is possible to obtain the number concentration and size distribution of the sampled particles.

In some cases scanning electron microscope (SEM) and transmission electron microscope (TEM) imaging are also used to analyse size distributions in combination with automated imaging analysis. Examples of this can be found in [100] and [101].

The soot particles produced by GDI engines mainly consist of elemental carbon (sometimes also referred to as black carbon) and organic carbon. Commonly, the actual composition of soot is done by coulometry. In this process a sample is oxygenated in a heated flow and converted to CO_2. The amount of carbon dioxide is then determined in a coulometer. The distinction between the different carbon types is done by extraction beforehand [102].

An optical method to analyse the particle size is laser induced incandescence (LII). Particles are heated with a short laser pulse and begin to radiate in the visible spectrum as a consequence. The emitted light can then be related to the concentration and the radiation decay of a particle to its size [103], [104]. The benefit of this method is its large temporal resolution and sensitivity, which makes them useful for measuring transient effects of internal combustion engines. Also, it does not require a specific dilution of the sample [105].

The surface of soot particles is characterised in the literature as BET surface, active surface or its equivalent surface, which are all relevant in the context of engine emissions and their potential health hazard. BET (named after Brunauer, Emmett and Teller) quantifies a particle by the amount of nitrogen it can adsorb on its surface [106]. The active surface is determined through the adsorption kinetics of ions or radioactively labelled

atoms on the particle surface [107]. The equivalent surface is calculated from the particle size distribution assuming all particles are spherical; one example of this is the Sauter mean diameter [108].

Commercial exhaust gas analysers usually combine several of the techniques presented in this chapter to fully characterise particulate emissions. In addition to the mentioned quantities and techniques, it can also be of interest to determine further particle characteristics, such as density and shape of particles as well as agglomerates, which is also done by a combination of the methods presented here [93], [94], [109].

2.2.3 Parameters of the injection setup to influence the liquid deposit and pollutant emissions

As shown in chapter 2.2.1, the fuel deposit on the cylinder wall and piston bowl is a significant contributor to the formation of emissions, both in particulate form and hydrocarbons. In the literature, a series of parameters have been pointed out and studied that have an effect on the level of emissions caused by fuel deposit. This is why it is necessary to further optimise the engine design and combustion concept. Ideally the phenomenon of wall wetting is eliminated, or at least minimised as much as possible, once the combustion cycle begins and the flame front reaches the walls.

Parameters that are most relevant to this research and that will be discussed in this chapter in more detail are listed in Table 2.2.

Table 2.2: *Overview of parameters investigated to minimise liquid deposits in engines.*

parameters discussed	
injector design	injection pressure
injection timing	engine load and speed
spark timing	surface temperature
multi-injections	fuel composition

The first concept for minimising engine emissions is the design of the injector or the injector type. Drake *et al.* [9] compared in their extensive study of soot and hydrocarbon formation, caused by fuel films, the effect of the injector design on the extent of the liquid deposit This was done by comparing a six-hole with a swirl-type injector. The former had a spray angle of 50° and the latter a cone angle of 70°. Both were operated with the same maximum pressure and yielded the same flow rate, which corresponded to 10 mg per injection. In their direct measurements of the fuel film they saw an increase of the wall film area by a factor of more than four in the case of the swirl-type injector. The calculated average film height was also about five times larger. Both values are reflected in the film area, which was about 20 times larger in total and in the measured engine-out emissions. In the worst case the swirl-type injector produced around 10 times as much soot as the multi-hole design. Even though, they observed a change in the difference between injectors depending on the injection timing, the swirl injector was always significantly worse than its counterpart. The captured differences in hydrocarbon emissions were not as drastic, but the swirl design produced up to twice as many emissions. However, for later injection timings they saw that the six-hole injector could result in more hydrocarbons and, for very late injections, both injectors produced about the same amount of engine-out hydrocarbons. This led them to the conclusions that the contribution of wall film to the hydrocarbon emissions was not as dominant as expected, since the deposit volume was significantly larger for the swirl injector.

Ortmann *et al.* [77] investigated different concepts of fuel injection combined with different injector designs to minimise the formation of wall films end engine-out emissions. They used a combination of an optical engine and a single-cylinder metal engine in different configurations to gather a large amount of data. One injector had a swirl design, the other was of a multi-hole type. At injection pressures larger than 80 bar, both injector designs showed similar mean droplet sizes. For smaller pressures, however, the multi-hole design produced droplets that were larger on average. During the wall film measurements they saw consistently larger fuel films in the case of the swirl-injector in a wall-guided configuration, which agrees with the findings of Drake *et al.* [73]. These observations were also reflected in the measured soot at the exhaust. The swirl type

injector produced significantly higher particulate emissions by a factor of almost three compared to the multi-hole design. Only for low injection pressures of 65 bar did the swirl injector seem to be beneficial. This was most likely due to the larger droplet size produced by the multi-hole injector. In the case of the air-guided configuration the differences in soot were not large and both injector designs produced a similar amount of emissions, due to the complete avoidance of spray impingement. Similar to the wall guided experiments, low injection pressures seemed to cause a notable increase in particulates in the case of the multi-hole injector due to poor atomisation. Hydrocarbon emissions were at the same level between the two injector designs for both wall and air guided configurations, respectively.

Another approach to optimise engine behaviour regarding emissions is engine management or injection timing. This parameter is one of the key advantages of the direct injection concept over port fuel injection engines and allows not only for stratified operation, but also for charge cooling through multiple injections [2].

Drake *et al.* [9] looked at the effect of injection timing on the formation of hydrocarbon and soot. In the case of particulates, either a very early or a very late injection timing seems to be preferable. When fuel was injected very early, the spray impinged on the piston surface and a large fuel film was formed. However, the associated longer residence time on the surface led to an almost complete evaporation by the time the flame reached the location of the residual film during combustion. They also saw no persisting film during the exhaust stroke. For very late injections, the distance between injector and piston was maximised, which lead to a reduction of the fuel film and consequently of the particulate emissions. For an end of injection at around 50-55° bTDC they observed the largest amount of soot during their tests. The hydrocarbon emissions showed the opposite trend: very early and very late injections led to large amounts of unburnt hydrocarbon emissions. This means that under their engine conditions, the wall film was not the main source, but rather insufficient mixing and the formation of overly rich regions in the engine volume were the main contributor to unburnt hydrocarbons.

Szybist *et al.* [79] also looked at soot and hydrocarbon formation at different at different injection timings in their turbocharged four-cylinder direct injection engine. In the case of late injections, the hydrocarbon emissions increased due to a reduced mixing time.

Soot formation was elevated for very early and very late injection timings. Intermediate injections led to rather small amounts of soot. Their results agree with other publications, in that early injection promotes piston wetting because of the short distance to the injector and very late injection reduces the evaporation time of the liquid film significantly.

Koepple *et al.* [28] saw a similar connection between injection timing in their part numerical, part experimental study. Early injection timings led to increased wall wetting, due to the reduced distance between injector and piston. As such, the measured particulate emissions also increased by more than an order of magnitude for these cases.

Kaiser *et al.* [46] looked at engine emissions while changing the injection timing, amongst other parameters. They looked both at individual hydrocarbon classes and the cumulative emissions as a function of the end of injection. According to them, there was a strong change in the quantity of hydrocarbons when changing this parameter, but there was no monotonic trend, which is similar to other publications. At very advanced injection timings the overall hydrocarbon emission was relatively low, because of the homogeneous operation of the engine. With retarded end of injection, hydrocarbons seemed to decrease slightly, but showed relatively little variation. Once the operating condition switched to stratified at late injection timings, the hydrocarbon emissions increased manifold, most likely due to insufficient mixing of fuel and air.

Hochgreb [7] experimented in a stratified single-cylinder optical engine and investigated fuel impingement on the piston with laser induced fluorescence. The intensity of the fluorescence signal was a function of the wall film extent. The start of injection was varied, and she saw a reduction of the remaining fuel on the piston surface with earlier injections, although liquid was present in all cases. A visual inspection of the transparent piston also supported the fluorescence measurements in that the amount of soot deposit was increasing with retarded injections timings.

A fairly comprehensive study on engine operating conditions and how it changes particulate emissions was reported by Farron *et al.* [110]. In the case of early injections they saw much increased levels of particulate emissions, which was reduced by switching to later timings. They also saw that richer operation of the engine was particularly bad in the case of late injections. Even though they did not specifically look at spray

impingement, it is fair to assume that the interaction between the spray and the wall could be the reason for these observations. It is also interesting, that their measured particle size spectrum showed a unimodal distribution in all cases.

Aside from the injection timing, the spark timing can also be used as an optimisation parameter for engine-out emissions. Daniel *et al.* [111] looked at the changes caused by this parameter in combination with biofuel and gasoline. Different blends showed different sensitivity to this parameter, with methanol being the most sensitive and unleaded gasoline the least sensitive. In general, later ignition timing had a positive effect on the total concentration of particulates.

This parameter was also investigated by Farron *et al.* [110]. Overall, they saw that advancing the ignition timing relative to the end of injection promotes particulate emissions because of insufficient time to achieve good mixing in the cylinder. These findings do agree with Daniel *et al.* [111].

Oh *et al.* [112] investigated the effect of multiple injection on the formation of hydrocarbon emissions. They used a single cylinder engine in a spray guided configuration, which was operated in lean stratified condition. By running the engine with two injections instead of a single one they saw a drastic reduction in hydrocarbons, which could be further improved by injecting three times.

Szybist *et al.* [79] also looked at soot formation at different injection strategies. Their idea was to minimise spray penetration and wall impingement by increasing the number of injections from one to two. Multiple injections helped to reduce soot formation, mainly for early injection timings. For later timings, this setup actually generated more soot compared to the single injection. This is because the improvement in spray penetration and impingement is overshadowed by the reduced mixing time in the cylinder volume for the last of the multiple injections. As a consequence, the number of particles is elevated. Other engine-out emissions were not impacted by this multi-injection strategy.

Johansen *et al.* [82] investigated soot formation in a single-cylinder optical engine while also varying the number of injections. The basis was a single injection with a given injection mass, which was split into up to four injections during their tests. In the case of the single injection they observed increased wall wetting caused by the long injection time,

subsequent impingement duration and the large penetration depth. With a multi injection strategy, they were able to almost eliminate all pool fire occurrences on the piston bowl.

Another parameter that can be controlled to further reduce engine emissions is the rail or injection pressure. Oh *et al.* [112] saw a reduction of particulate and hydrocarbon emissions for large injection pressures. In the case of sprays generated at 200 bar, hydrocarbons could be reduced by a factor of two and the particulates by a factor of up to four in their single-cylinder spray guided direct injection engine at low loads.

Johansson *et. al* [113] looked at the impact of injection pressure on the formation of particle number and particle size distribution in their spray guided GDI engine. Increasing the injection pressure from 100 to 200 bar led to a reduction of particulate emissions overall. The biggest effect was observed for large particles, although the overall shape of the particle size distribution was not changed. In conclusion they saw that the trend of decreasing particle numbers with increasing fuel pressures was not as pronounced for low loads in their tests.

Ortmann *et al.* [77] showed in their experiments with different injectors and engine configurations that a larger injection pressure can lead to increased spray penetration and therefore to an increased wall film, in the case of a wall guided system. The increase in the fuel film also resulted in elevated soot levels at the exhaust. Only for very high pressures of 110 bar did the fuel film volume decrease, alongside the particulates. They assume that this happened because of superior atomisation and consequently much improved evaporation of the droplets before they managed to impinge on the wall. In the case of the air guided injection, the fuel film was avoided for all injection pressures and hence the soot levels were relatively small in all cases. As such, the soot emissions were mainly influenced by atomisation, which improved with increasing injection pressure due to a decreased gasoline droplet diameter. The hydrocarbon emissions followed a similar trend, both for wall and air guided injection configuration, which also implies that the main source of hydrocarbon might not be the fuel film under the presented engine conditions.

In their numerical study, Koepple *et al.* [28] compared experimental data with their computational results to look at the influence of rail pressure on wall wetting and pollutant formation. An early start of injection with increased rail pressure caused more soot to be

formed, which was explained by the increased wall film mass due to the larger spray penetration. The particulate number was around an order of magnitude larger in the case of 150 bar rail pressure compared to 50 bar. For retarded injections, however, the increased fuel pressure resulted in an improvement, because of superior atomisation and droplet evaporation behaviour.

An additional parameter that can be adjusted to reduce emissions levels is engine load and speed. Johansson *et al.* [113] investigated the influence of engine speed on particle number and size distributions in their experiments. Overall, the largest size of particles was reduced with increasing engine speed. Smaller sizes of particles did not seem to be affected as much by engine speed, although the overall number of particles increased significantly with engine load.

Kaiser *et al.* [46] saw that by increasing engine speed from 750 to 3000 rpm under lean stratified conditions, the hydrocarbon emissions increased 3.5 fold in an almost linear correlation.

Huang *et al.* [87] investigated the effects of engine load and speed on the formation of hydrocarbon emissions, while separating them between their source of origin. This means they were able to distinguish if they were produced in the cylinder volume or the fuel film. They concluded that hydrocarbons emissions are increasing significantly due to fuel films. With increasing engine speed and load, the engine out total hydrocarbons decrease slightly, because of increased oxidisation mainly due to larger cylinder temperatures. The overall change, however, varied with the volatility of the fuel, with higher amounts of hydrocarbon emissions produced in the case of the more volatile liquids.

Li *et al.* [4] and Alger *et al.* [114] on the other hand saw in their investigations with an optical engine that with increased engine speed and load the amount of hydrocarbons are higher compared to idle or low load engine conditions. Their explanation was that, because of the reduced residence times for the liquid film, the evaporation was reduced together with the oxidisation time in the gas phase.

Because of the close correlation between fuel films and pollutant formation, the evaporation behaviour of impinging droplets on hot surfaces is also of high interest, particularly as to how it is influenced by the surface temperature.

Stanglmaier *et al.* [65] performed a study to investigate the evaporation of deposited wall films generated by single component liquids, binary mixtures and multicomponent fuels at wall temperatures between 50 and 300 °C and varying ambient pressures (50-1270 kPa). The experiments were carried out in a specially designed pressure vessel with an aluminium block mimicking the piston bowl. The uniform droplets were generated with a special syringe, which was connected to a stainless steel tube and produced droplet sizes of about 2 mm in diameter. The droplets impinged on the heated surfaced and their evaporation behaviour was timed through manual visualisation. During evaporation the surface temperature was also recorded via an embedded thermocouple. In the case of their single-component fuels, they observed similar evaporation behaviour for all liquids. At wall temperatures lower than the boiling temperature the lifetime of the droplet on the wall was decreasing almost monotonically with increasing surface temperature. Once the surface temperature matched or slightly exceeded the individual boiling temperature of the liquid, the evaporation time reached its minimum. After that, the lifetime increased again because of the Leidenfrost effect, which creates a vapour layer between the surface and the liquid, reducing the effective heat transfer significantly. Binary and multi-component fuels showed an overall similar evaporation curve with increasing surface temperature, but because of the overlapping characteristics of the individual components the actual behaviour could not be predicted as easily. The regions of decreasing lifetime and the influence of Leidenfrost were broader and merging into each other. Increasing the ambient pressure for their tested fuel yielded two different results. If the temperature is lower or around the boiling temperature or distillation range, increasing pressure suppressed the evaporation rate of the liquid. Once the Leidenfrost region was reached this effect reversed, which meant evaporation was promoted with increasing pressure. The reason for this was the compression of the vapour layer shielding the droplet from the hot surface, and as such heat transfer was promoted. Further results showed that the maximum evaporation rate of gasoline is shifted towards larger temperatures (by more than 100 °C) with increasing ambient pressures when going from 50 kPa to 1100 kPa. This means that the Leidenfrost effect observed here should be reduced in magnitude for real engine pressures.

Hochgreb [7] also looked at the influence of the piston surface temperature on fuel deposits in her optical direct injection engine. The temperature was varied between 30 °C, in the case of a cold engine, and up to 170 °C when running the engine over a longer period of time. Even for the largest temperatures, a fuel film was still observed at a time, which corresponds to ignition under fired conditions, although the extent of the liquid film was decreasing with the temperature, notably. According to her, this might be because of limited heat transfer inside the film.

In another work, Oliveira and Hochgreb [74] developed a 1D model to calculate the energy and mass transfer in thin liquid fuel films on the cylinder wall. Parameters were the wall temperature, the boiling temperature of the liquid and the latent heat of evaporation. Their model showed that fuel condensation is happening in a warmed-up engine if the vapour pressure of the liquid is large enough. In the case of a cold wall they saw a rapid increase in vaporisation rate once the flame reached the liquid film due to peaking heat transfer. For wall temperatures that were smaller than the boiling temperature of the liquid, the calculated evaporation rates were relatively low. Once the wall exceeded the boiling temperature, the rate increased significantly. Their model, however, did not include Leidenfrost effects, which might change the evaporation rate at very high temperatures as observed in other studies. In the case of increasing heat of evaporation, the vaporisation rate of the liquid decreased for constant vapour pressure, with a non-linear relation. The overall rate of evaporation was increasing with wall temperature, but the amount of oxidisation did not change notably at the same time. Their explanation for the latter is that the location of the diffusion flame and the peak energy release rate were not affected by the surface temperature. As expected, the evaporation rate was also promoted by a decreasing boiling temperature and decreasing film thickness. Overall, their calculations showed that increased volatility of the liquid leads to larger evaporation rates, which increased the amount of fuel in the gas phase.

Serras-Pereira *et al.* [115] investigated the effect of spray impingement on the heat flux from the cylinder liner of a multi-hole injector in an optical engine. They placed sensors around the liner close to the top dead centre of the piston. The engine was operated at 1500 rpm and 0.5 bar intake pressure with engine temperatures of 20 °C and 90 °C.

They also ran on either gasoline or iso-octane, both injected at 150 bar. The heat flux measurements were correlated with image visualisation through the transparent piston. From their imaging they saw that the gasoline sprays were affected by the engine temperatures in shape, once the temperature was larger than the boiling point of the lighter components in the blends. This effect was not observed for iso-octane, because the engine temperatures in their experiments never exceeded its boiling temperature. Using the various heat flux sensors they could pinpoint the location and extent of the spray impingement during their measurements. In the case of 20 °C engine temperature, they did not observe a difference in the impingement behaviour of both fuel types. At 90 °C, however the heat flux was reduced by up to 85% in the case of gasoline and by only about 15% for iso-octane. According to them this was due to the collapsing spray of the former once it was exposed to the high temperatures. They also found that, at higher temperatures, there were notable fluctuations of the signal in the area around the intake valve, which meant that impingement was unstable and changing between cycles. In order to further minimise wall wetting they assessed a three injection pulses strategy. At 20 °C engine temperature they saw a reduction in the heat flux signal of up to 80% which corresponded to a drastic reduction in impingement. The magnitude of the change was comparable to the difference between the lower and higher temperature experiments and according to them could prove useful under cold start conditions in a real engine.

Schultz *et al.* [116] used an infrared thermography method to study the effect of fuel deposits on the cylinder surface. They used a heated plate to simulate the piston under homogenous charge conditions of a gasoline direct injection engine. With a multi-hole injector, n-heptane was sprayed on the plate and the change in temperature was recorded from the bottom of the plate with an infrared camera. During their measurements they varied wall temperature, rail pressure, injector distance and injector angle. An increasing surface temperature of the impingement plate had a positive effect on the wall film area. From 80 °C to 160 °C the cumulative film area was reduced by more than 35%. The other varied quantities only had a small impact on the film, which illustrates the significance of the surface temperature as a parameter to optimise wall wetting in direct injection engines.

A parameter that has gained increasing interest in recent years is fuel composition. In particular, the increasing amount of ethanol (sometimes also methanol or other alcohols) in gasoline blends has been researched, and in particular as to how it affects emissions in direct injection engine. The main reason is that these components can be used as a biofuel supplement or substitute for gasoline [50].

A feasibility study of ethanol as a gasoline supplement or substitute was done by Taniguchi *et. al.* [117]. They were looking at engine performance, injector fouling and emissions with different blends containing increasing amounts of ethanol. In their engine tests they found a beneficial effect of ethanol on engine performance and reduction of knocking, as well as on particulate emissions and on accumulation of solid combustion products. However, they experienced an increase of hydrocarbon emissions under full load at low engine speeds, most likely caused by insufficient evaporation of the fuel during these conditions. Overall, they came to the conclusion that ethanol can have a positive impact on engine performance.

Price *et al.* [118] investigated a series of fuel blends containing ethanol and how it impacts the formation of hydrocarbon and soot emissions in their spray guided direct injection engine. They compared a blend of unleaded gasoline with gasoline containing 30% and 85% of ethanol by volume. When operating the engine under stoichiometric conditions there was a clear connection between ethanol content and particulate emissions. With increasing ethanol, the soot formation was reduced, especially in the case of the blend containing 85% ethanol. The soot levels of the unleaded gasoline and the blend with 30% were more similar. The blend with the highest amount of ethanol was also the least sensitive towards air/fuel ratio changes regarding particulate emissions. The amount of particulates was consistently lower, with an increasing gap between the blends in the rich region. They traced this back to oxygen that is being carried in the ethanol molecule, which according to them reduces the concentration of soot precursors formed during combustion. They also measured the temperature and saw that the increased evaporation rate of ethanol reduced the amount of fuel on the piston wall during the compression stroke. The hydrocarbon emissions were reduced in the case of the high ethanol blends when the engine was running at low load. With increasing load this trend was reversed with the

highest emission levels generated by the 85% ethanol blend and the pure gasoline emitting the lowest. According to them, this was caused by the oversaturation of the charge, due to larger volume of fuel necessary with the large ethanol content to achieve the same air to fuel ratio. They assume that fuel was unable to evaporate completely and as such this significantly contributed to the exhausted hydrocarbons.

Szybist *et al.* [79] compared blends with 20% ethanol and 85% ethanol in a port fuel injection and a direct injection engine, while looking at particulate emissions. Overall, they saw that by using the direct injection concept, the particulate emissions were increasing notably, up to two times compared to port fuel injection. According to them, this was caused by wall wetting on the piston surface. Within the direct injection tests, however, they were able to reduce particulates by an order of magnitude when switching from the blend with 20% ethanol to the one with 85%. The particle numbers were approaching the level of the PFI tests, even though the injection mass was increasing with the ethanol content, to maintain the same fuel to air ratio. As such an increased wall film was to be expected in combination with the increased latent heat of evaporation of ethanol. However, oxygenated fuels seemed to produce less particulate emissions in general, which seemed to be compensating for the increased liquid deposit.

Storey *et al.* [119] expanded this research and analysed the effect of air to fuel ratio of gasoline and ethanol blends on particulate emissions in a GDI scenario. They compared blends with 10%, 20% and pure gasoline at stoichiometric and lean fuel to air rations. In the case of stoichiometric operation they observed a significant decrease of particulate emissions with increasing ethanol: however, this trend was not as pronounced in the case of lean mixtures. The presence of ethanol did in fact halve the particulate emissions, but the difference between 10 and 20% ethanol was almost not existing. These observations were also made at cold start conditions, where a lean mixture could not benefit from the larger amount of ethanol as much. These findings agree with their earlier work [120].

Fatouraie *et al.* [26] tested two blends of 50% and 85% ethanol mixed with indolene, a type of standardised gasoline. Their experiments were carried out in an optical single-cylinder direct injection engine. It was run at a constant 1500 rpm with medium load. To investigate the soot formation, a high speed camera operated at 9000 fps was used

to capture the incandescence signal during combustion. When evaluating the recordings, they saw that soot was starting to form from the piston surface in the case of pure indolene and more from the top side of the cylinder in the case of 50% ethanol. The amount of soot was reduced in the case of the latter and the blend with 85% did produce the least amount. By integrating the captured incandescence signals for each run and averaging those over 15 cycles they saw that the signal from the pure indolene fuel was more than an order of magnitude larger than for the blend with 50% ethanol. The blend with 85% did not produce a detectable signal at all. These observations remained fairly insensitive towards changes in the coolant temperature. Retarded fuel injection timings lead to increased fuel impingement in all cases and as such to increased particulate emissions. However, the ethanol blends seemed to be more sensitive to this parameter and showed a larger relative increase. According to them, this could indicate, that the changes of soot emissions due to ethanol might also be caused by changes in the spray characteristics.

Catapano *et al.* [121] did an intensive parametric study of ethanol blends on the soot and hydrocarbon formation in direct injection engines. The single cylinder optical engine was operated at 2000 rpm at full load and also at 4000 rpm with partial load. In their experiments they investigated blends of pure gasoline, mixtures of gasoline with 20, 50, 85% ethanol and pure ethanol regarding the particulate emissions at the exhaust. The first data was based on the integral luminosity of two colour pyrometry inside the combustion chamber, which is directly related to the soot incandescence. For the case of 2000 rpm and full load they saw a clear trend between increasing ethanol content and the reduction of soot. When running the engine at 4000 rpm partial load, however, a similar trend was not observable. In this case, the fuels with 50 and 85% ethanol produced significantly larger cumulative intensities. These findings were supported by engine out particulate number measurements. The number of particles in the lower speed setup was more than an order of magnitude smaller for pure ethanol than for pure gasoline with a quasi-logarithmic relation in-between. Also, the size distribution became narrower with decreasing mean diameter. The 4000 rpm experiments produced the largest number of particles in the case of 50% ethanol, with lower numbers for smaller and larger concentrations. According to their observations, this is explained by increased wall wetting

and the occurrence of pool fires. In the case of large ethanol concentration, the injection timing had to be increased also, which lead to larger spray penetration and therefore increased wall wetting on the piston. The evaporation rate of ethanol, on the other hand, has an opposing effect. At the temperatures inside the cylinder at 4000 rpm, ethanol seemed to evaporate faster than gasoline and as such reduced the amount of soot caused by the rich diffusion flames on the surface. They also noted, that ethanol and gasoline can form an azeotropic mixture, which can additionally hinder evaporation of wall film. This is especially the case for the 50% and 85% ethanol blends in these experiments. The trends observed for the particulate numbers were also reflected in the particulate mass. In the case of hydrocarbon emissions, both operating conditions of the engine yielded the same results. Overall, the emissions increase slightly with the ethanol content, but remain very similar in magnitude.

Sobotowski *et al.* [122] looked at the influence of fuel composition on particulate emissions. They were varying the ethanol content from 0 to 15% while also looking at different aromatic contents (14-38%) of fuels with different PM (particulate mass) indices. The latter is a quantity that describes the probability of a blend to form particulate emissions inside a direct injection engine and was established by Honda [123]. The different blends were tested in vehicles with port fuel and direct injection engines. In general, they saw larger amounts of soot being produced by the vehicle with a GDI engine. By increasing the aromatic content the particulate emissions also increased. Increasing the ethanol content also leads to larger amounts of soot in the case of blends with higher PM indices. According to them ethanol can have an amplifying effect on the PM index. This could be caused by the increased latent heat of evaporation of ethanol for their blends of up to 15% ethanol.

Sementa *et al.* [124] also looked at the influence of bio-ethanol on the performance and emissions of GDI engines. They compared gasoline blends with pure ethanol fuel at different injection timings and 1000 rpm speed at idle conditions as well as 1500 rpm medium load in an optical four cylinder engine. The overall particles number measured at the exhaust was slightly smaller for the ethanol fuel in the case of higher engine speed and early injection, but the mean particle diameter was reduced significantly at the same time.

This was explained with the particle size distribution that was more bimodal in the case of ethanol with a clear shift towards smaller diameters. In the case of late injection, the particle number was slightly larger for ethanol, but with a similar size distribution and mean diameter. Combining these two means that the emitted particle mass was significantly smaller for the ethanol fuel.

Costagliola *et al.* [125] investigated the engine efficiency alongside the emissions in relation to the ethanol content in gasoline fuel. They also found a very beneficial effect of ethanol on particulate emissions, with a reduction of up to 90%. However, aside from particulates they also found that, for fuels with higher ethanol content a drastic increase of carbonylic compounds was emitted, at a level of up to 3.5 times higher for 85% ethanol compared to the regular gasoline blends. The largest amount detected was acetaldehyde.

He *et al.* [126] agreed with the emissions reducing effect of ethanol in gasoline and compared these findings with iso-butanol blends over different engine operating conditions in a 2 litre turbocharged direct injection engine. The measured particle emissions were reduced under all investigated engine conditions in the case of the blend with 20% ethanol and 12% iso-butanol. A maximum reduction of particles with 20% for the former and 30% for the latter could be achieved at best. The measured particle sizes followed a bimodal distribution in all measurements with peaks at 10 nm and 70 nm. For advanced injection timings they saw an increase in particulate emissions across the board, because of the enhanced spray impingement. They also observed a strong sensitivity towards engine load, which raised the overall relative particulate emissions by about 50% if the load was increased by only 10%.

Daniel *et al.* [127] investigated bio-fuel blends in GDI and PFI engines regarding their production of particulates and other emissions. Aside from ethanol they were also looking at 2,5-dimethylfuran (DMF) as a potential gasoline supplement. The analysis of the particulate emissions showed a reduction in size with increasing ethanol content up to 75%. For larger ethanol fractions no further improvement was observed. Overall, the trends observed for the direct injection test were not repeated with the PFI design, which also showed larger amounts of particulate emissions across the tested blends.

Wang *et al.* [128] compared gasoline and ethanol blends in a spray guided direct injection engine at 1500 rpm and stoichiometric air to fuel ratio regarding particulate emissions. In their experiments they saw that ethanol has a strongly positive effect on the particle mass reduction because of its oxygen content compared to gasoline. In addition to that, they saw that soot generated from ethanol got oxidised faster than its gasoline counterpart. Particle numbers did increase for both fuel types with engine pressures up to 6.5 bar IMEP (indicated mean effective pressure) and decreased again for larger values than that. In all cases ethanol produced slightly higher particle numbers. The particle mass, on the other hand, showed significantly smaller values for ethanol compared to gasoline, with the largest differences being more than an order of magnitude at high engines pressures. Additionally, the cumulative particle mass decreased with engine pressure for ethanol, in contrast to gasoline.

Chen *et al.* [129], [130] observed a different relation between ethanol in gasoline blends and particulate emissions. Their research was focused on how the enthalpy changes with increasing ethanol content and how it affects the performance of their single-cylinder optical engine. For a given temperature of 25 °C the latent heat of evaporation is increasing with the ethanol content, since pure gasoline fuel (or in their case iso-octane) has a lower specific heat of evaporation. Running the engine at 1500 rpm and under part load they saw a significant increase of particulate numbers and mass with increasing ethanol content. In the case of the 85% ethanol blend, the total mass of soot was about 8 times higher compared to the blend with 10% ethanol. This relation was valid both for cold and warm engine conditions. These observations do not agree with findings of most groups and might have been caused by the particularities of their setup and engine conditions.

Aside from mixing ethanol with gasoline to change the formation of particulate emissions, Zhao *et al.* [131] also investigated hydrogen-gasoline mixtures. They added small quantities of hydrogen directly to the engine that was operated with a mixture of 65% iso-octane and 35% toluene. At high engine load they observed that smaller particles are reduced by the addition of hydrogen. In the case of 10% hydrogen (from the stoichiometric air to fuel ratio) a reduction of up to 85% in particulate numbers was achieved and the total mass was reduced by 17% when the engine was operated in rich

conditions. For stoichiometric injections, hydrogen had a slightly negative effect on the particulate mass. When the engine was run under low load, the total mass of soot was reduced significantly by adding hydrogen with a decrease of 97% for 10% hydrogen.

Leach *et al.* [132] also looked at changing fuel compositions and how they affect particulate numbers, in particular the aromatic content. They tested different blends in a single-cylinder optical engine to derive a particulate emissions index for direct injection engines. Parameters varied were the vapour pressure and the so called double bond equivalent of the fuels by increasing the toluene content. In their measurements the particulate emissions did increase notably with the amount of aromatics, with pure toluene producing very high levels. Looking at the vapour pressure, they observed a significant increase in emissions with decreasing vapour pressure. Overall, their results showed that the used emissions index is a reliable quantity to predict the particulate emissions in relative terms.

Wang *et al.* [133] looked at the issue of soot emissions from a different point of view. They investigated the composition of particulate matter generated by a spray guided direct injection engine and its oxidisation to gain a better understanding of the physical processes behind this phenomenon. A thermogravimetric analysis method was applied in a single-cylinder spray-guided direct injection engine run with gasoline, ethanol and blends of 25% ethanol in gasoline. The experiments were performed at 1500 rpm and slightly rich fuel to air ratios. In their comparisons they found that soot generated by oxygenated blends were easier to oxidise. Analysing the underlying mechanism it seemed that less energy is required to oxidise the soot formed with ethanol compared to that originating from gasoline. Also for the latter, the oxidisation process was more sensitive towards engine load. The energy and temperatures necessary were larger for higher engine loads.

The complex mechanism of soot formation in a direct injection scenario was also investigated Sukegawa *et al.* [134], who derived two 3D models to predict particulates generated from spark ignition engines. The numerical results were compared and verified with experiments from a single-cylinder direct injection engine. The first model was based on a 0D self-ignition elementary reaction and the second on a 1D propagation elementary reaction. Comparing the numerical data with experimental results, they found that the

second model produced reliable results. According to them, the first model was insufficient, because it did not include the temperature distribution in the flame.

Naik *et al.* [135] also modelled the mechanism of soot formation by looking at the reaction mechanism in a GDI engine. Their findings were compared to previously obtained empirical data. The blend, which was used to calculate the reaction mechanism with 230 species, was a 7-component surrogate fuel. This was then combined with a pseudo-gas soot model specifically developed for the research. It included nucleation, growth and oxidisation of the particles. Data was gathered for different injection timings and inlet temperatures. After comparing the numerical results with the empirical they saw good agreement of their model with the experiments. Retarded injections led to more than an order of magnitude higher particulate emission, where the change of the inlet temperature only had very insignificant effects on the soot formation.

In addition to the minimisation of wall wetting through fuel or engine properties, the influence of injector location can also be considered. However, unlike the aforementioned parameters this cannot be applied to a production engine since it requires a substantial change of the design. For that reason this parameter shall only be mentioned briefly. Seimle *et al.* [136] investigated different injector designs in a side mounted and central location inside the cylinder of a pre-development six cylinder flat engine. Under the same operating conditions they saw a significant reduction in particulate emissions in the tailpipe measurements with the side-mounted injector producing more than an order of magnitude larger particle numbers and this shows the potential of this engine design parameter.

2.3 Overview and evaluation of common measurement techniques to analyse thin liquid films

The investigation of thin liquid films on solid surfaces is a widely researched phenomenon, not only limited to the wall wetting process found in direct injection engines. There are numerous techniques published focusing on this type of investigation. Usually, they all

have their own advantages and compromised, which makes them more suitable for special applications. Because the nature of thin liquid films in gasoline engines is that of a very fast transient process, a measurement technique for this work has its own requirements. Ideally one wants to collect data with a high spatial and temporal resolution (the process of film deposition and evaporation happens in the order of milliseconds), while not changing the physical and chemical properties of the fuel blends investigated. Additionally, the technique should be non-intrusive and not interfere with the deposit directly. In this chapter a number of techniques, commonly used to investigate such thin films, will be presented and evaluated regarding its applicability towards this research. The overview is mainly focused on optical methods given the background of this work.

One family of techniques for liquid film thickness measurements is based on interferometry, whereby light from a source is split equally into two beams by a beam splitter. One of the beams travels a fixed distance and is reflected towards the detector. The other beam passes through the liquid film getting reflected at its interface and is travelling back to the detector from there. Combining the two beams creates an interference pattern recorded by the detector. From these patterns, information of the film thickness can be calculated. The liquid film to forms a spatial interference fringe pattern that is different from the pure summation of the individual waves [137].

This interference pattern can yield information about the thickness of transparent liquid films [138], [139]. There are several different iterations of interferometry used to investigate thin liquid films. Borgetto *et al.* [140] used low-coherence interferometry (LCI) to measure liquid film thickness of linear alkanes. In their case, a super luminescent LED (light emitting diode) was used as a light source to illuminate the film and create interference patterns. From the spacing between individual maxima in the interferogram, it was possible to measure the film thickness. Gao *et al.* [141] used wavelength scanning interferometry to investigate transparent films. Combining a white light interferometer with a near-infrared super luminescent light-emitting diode interferometer, it was possible to measure the liquid film thickness, while compensating for noise and vibrations introduced by the experimental setup at the same time [141], [142]. Debnath *et al.* [143] used spectrally resolved phase-shifting interferometry to investigate thin transparent films.

This technique uses a white light source. By analysing the phase shift in spectrally resolved interferograms, they were able to measure the thickness of a thin transparent film on a reflecting substrate. All presented methods of interferometry have a common limitation that they can only measure along a line. Also, the temporal resolution of the technique is somewhat limited. This means that, for investigations of highly unsteady liquid deposits, this technique might not be reliable enough.

Similar to the interferometry method is the so called fringe method. This technique is often used to measure the thickness of liquid films in capillaries or investigate two phase flows inside small diameter tubes [144]. Kariyasaki *et al.* [145] showed that this technique can also be used to measure the film thickness of thin transparent films on top of a solid surface. By using collimated illumination of the liquid film with a coherent light source (laser) at a fixed angle, it is possible to create fringe patterns [146], [147]. The reason for this is the fact that the liquid film is not perfectly uniform across the surface. Therefore, the parallel light gets refracted and reflected at different locations of the film. The reflected and refracted light can interfere at the surface of the liquid film and create a fringe pattern that changes with the local film thickness. Since the fringe pattern is formed at the surface of the liquid film, precise focusing of the optical system is necessary. Kariyasaki *et al.* [145] were using a microscope with a CCD camera to generate and record the fringe patterns. Kariyasaki *et al.* [145] presented thickness profiles across the liquid film. In another set of experiments, they showed that it is possible to track a shrinking hexane film over time by using shorter exposure times and higher recording frequencies. The advantage of the fringe method is its high sensitivity to the local film thickness, even in multi-phase flows [145]. With the presented technique, however, it is only possible to measure along a line and not in 2D. Furthermore, the temporal resolution illustrated with a volatile liquid at room temperature might not be sufficient at larger temperatures, especially if the boiling point of the liquid is exceeded. Additionally, the rather complex optical alignment might limit the *in-situ* application of this technique to an injection chamber or pressure vessel, where the angle of illumination is fixed and the optical distance to the specimen may be large.

Another technique based on the fringe pattern formation was used by Ozdemir and Whitelaw [148]. They derived an analytical correlation between the interferometric fringe pattern and the thickness of an unsteady liquid film. Solving for the optical transformation function of their optical setup, the intensity fluctuations created by the fringes could be linked to the film thickness without the need for a separate calibration. Using a photodiode to detect the signal, they were able to achieve a high temporal resolution. However, the recordings only yielded time-dependent liquid film thickness measurements at a point, similar to the techniques presented earlier.

Probably the most common technique to investigate liquid deposit on solid surfaces is based on Laser Induced Fluorescence (LIF) [149]. Fluorescence describes the spontaneous emission of radiation from an electronically excited molecule. In the case of LIF, this excitation is generated by the laser light source [150]. This method requires a fluorescent tracer to be present in the liquid. This can be either one of the components of the liquid itself or a fluorescent dye added to the liquid. In both cases a laser is used to excite the tracer molecule, which then emits a fluorescent signal. If the laser intensity and the concentration of the tracer in the liquid are constant, it is possible to relate the recorded fluorescent intensity signal to the amount of liquid on the surface [149]. Also, with the use of appropriate optical components, it is possible to form a light sheet, which can illuminate the entire liquid film. In this way, the emitted fluorescent intensity from the entire area of the liquid deposit can be captured, usually with a CCD camera, which includes information on the local film thickness. With such a setup it is possible to obtain spatially and temporally resolved information. However, the selection of the tracer can be challenging for this kind of application [151]. Ideally the tracer should yield a strong fluorescent intensity signal, while remaining proportional to the concentration of the tracer and insensitive to changes, such as pressure and temperature. Also, the tracer should show the same physical behaviour as the investigated fuel. This means properties like evaporation rate, diffusivity, convection, surface tension and viscosity should be the same. In practical applications it is usually not possible to find a tracer which meets all of these requirements [151]. For investigations that involve multi-component liquids, like gasoline, it is common to replace the original fuel with a mixture of a fluorescent tracer and non-fluorescent fuel

substitute. This can be 3-pentanone, which is excitable with a UV laser and iso-octane, the main component of gasoline. In this way, it is possible to create a traceable liquid with similar properties as gasoline [151]–[153]. In a scenario where a set of real gasoline blends needs to be investigated, such substitution of a fuel component is not an option. Alternatively, it is possible to add a fluorescent dye to the liquid, which acts as the tracer substance. These dyes have a very high fluorescent yield, which means only extremely small amounts need to be added to the fuel [154]. This way the physical properties of the liquid remain largely unchanged, usually without any effect on the measurement. However, care should be taken to ensure that the absorption of the incident light within thick liquid films does not lead to a non-linear dependence of the fluorescent intensity on the fluorescent dye concentration [155]. The downside of these tracer substances is that they do not evaporate with the liquid [156]. This means, over time, the number of tracer molecules does not change and therefore it is not possible to obtain a reliable time-dependent signal of the evaporating liquid deposit. As a consequence, only deposits, which are not significantly affected by evaporation, can be investigated in order to minimize this error. Both approaches, with an added dye or the liquid tracer, have the disadvantage that by illuminating the liquid film it is very likely that the region above the liquid film is also illuminated. This means that the fluorescent intensity signal not only corresponds to the actual liquid film but also to the areas above it. Alonso *et al.* [151], Greszik *et al.* [157] and Kabadin *et al.* [158] developed a method to overcome this issue. By coupling the light source into the glass plate where the liquid deposit is formed, it is possible to receive total internal reflection between the glass plate and the surrounding air. Consequently only the tracer molecules inside the liquid deposit get excited and produce fluorescence signal. As such, an accurate measurement of the film thickness is possible. In order to calibrate the setup to be able to correlate a fluorescence signal to a certain film thickness, different liquid films have to be generated. Commonly, a liquid film is formed in the gap between two parallel glass plates. Knowing the distance between the plates it is possible to link the signal to the film thickness.

To further improve the LIF technique, Hidrovo *et al.* [159] presented a method called reemission reabsorption laser induced fluorescence. Essentially, the physical

fundamentals are based on LIF, however, it uses emission and subsequent re-absorption of two different dyes instead of pure fluorescence of a single tracer. The absorption and emission spectra were selected in a way that the fluorescent wavelength of the first dye overlapped with the absorption wavelength of the second. The latter then fluoresced at a third wavelength. By calculating the ratio between the two signals, it was possible to very accurately determine the actual film thickness, because effects such as reflection and changes in illumination intensity got cancelled out. The detection of two wavelengths, however, makes the optical setup more complex compared to ordinary LIF. Hidrovo *et al.* [24] used two CCD cameras equipped with optical filters and mounted on the same lens with an optical-path-splitting module. In this way, it was possible to ensure good overlap between the two images and achieve very high accuracy during their measurements. Furthermore, using the fluorescent intensity ratio makes the calibration independent of the optical characteristics of a particular setup. The downside of the re-absorption method is the limited range of film thicknesses it can be applied to. The main factor is the necessity of an optically thick medium with enough re-absorption to be able to accurately quantify the thickness. In combination with the non-evaporative behaviour of the dyes, this technique might not be reliable enough for investigations of evaporating fuel deposits.

An additional laser based technique to measure liquid film thicknesses is the laser light absorption method. Mouza *et al.* [160] used the absorption of light from a diode laser passing through a thin liquid film which contained a dye. Using the law of Beer and Lambert, it is possible to determine the film thickness by measuring the absorption ratio in a calibrated system [161]. The light source used in these experiments was a low power diode laser. The signal was recorded with a silicon photodiode at a fixed distance from the light source. This setup yielded 1D measurements. In the case of a steady film, it would be possible to move the laser and detector along a line across the film. Consequently, spatial information of the liquid deposit would be available. Generally, this particular method is very similar to the dye based LIF technique, only the physical principle is different. This means that the advantages and disadvantages also apply here. Dye based absorption measurements yield a good signal with very little tracer concentration. The dye used by Mouza *et al.* [160] was methylene blue, which does not co-evaporate and hence is only

suitable for non-evaporating deposits or measurements with no temporal resolution, similar to the dyes used in LIF. Yang *et al.* [162] used a near-infrared (NIR) diode laser to measure the thickness of liquid water films. In these experiments, the addition of a tracer is not necessary, since liquid water shows broad band absorption for infrared light [163]. In order to further separate the absorption signal from any background noise, they used two diode laser of different IR wavelength, both being absorbed by water. Since the absorption wavelength of water changes with temperature, it was also possible to obtain temperature information of the vapour. In order to calibrate the setup they used a calibration tool to accurately generate different film thicknesses. They used it to measure thicknesses of 5-1000 µm with a good resolution. A later work by Greszik *et al.* [157] compared this method to LIF and spontaneous Raman scattering. As a result they were able to show that both the spontaneous Raman and the NIR based techniques can capture the evaporation behaviour of water films very well. However, not all liquids, such as gasoline, absorb NIR. This would mean that in such an application a tracer chemical would be necessary. This fact causes the same dilemma for this type of investigations as the LIF based methods.

Apart from optical methods presented here, there are also acoustic techniques used to investigate liquid films. Commonly, these are utilising ultrasonic waves, which are attenuated and reflected due to discontinuities created by liquid/gas interfaces. The application of different iterations of acoustic techniques can be found in [164] and [165].

As a final class, electrical techniques shall be mentioned. These are split into conductance-based and capacitance-based methods. The former uses electrodes to generate an electrical potential difference. The resulting current between the electrodes can be related to the liquid film thickness. Applications are presented in [166], [167] and [168]. The capacitance method uses two parallel metal plates to form a capacitor by applying electrical current to them. The capacitance is then changed if a liquid film is present. This change can be linked to the thickness of the deposit. Further details can be found in [169] and [170].

A rather novel optical technique used to investigate liquid deposits is Refractive Index Matching (RIM). This forms the methodological basis of the work presented and as

such, a deeper explanation of the fundamentals and an overview of the application will be given in the following chapter.

2.4 Refractive Index Matching

The Refractive Index Matching method was developed by Drake *et al.* and first presented in 2002 [9], [75], [171]. The method was developed to quantitatively analyze liquid deposit on the piston surface of a gasoline direct injection engines. Due to the temperature changes during the cycles of the engine, the use of an LIF based method was not favored, because of the temperature dependence of the fluorescence signal. Refractive Index Matching provides quantitative information about the fuel deposit with large temporal and spatial resolution while remaining insensitive to temperature and pressure variations. Also, this method works for single and multi-component fuels [9].

The physical basis of RIM is that light is reflected at the interface of two media with different refractive indices, such as air and glass. If the interface is smooth and if the angles are chosen carefully, incident light gets reflected predominantly towards one direction. This is categorized as specular reflection [137]. Note that part of the light gets also refracted. In the case of a homogeneously roughened interface, the incident light gets scattered diffusely in all directions. If a liquid film is present on the solid material, the apparent roughness is being decreased and as such the scattering behavior changes. Part of the incident light gets reflected specularly and also refracted, similar to the smooth surface. This change of the scattering behavior can be related to the thickness of the liquid film. All three cases are illustrated in Figure 2.8.

In their experiments Drake *et al.* replaced the clear quartz piston by a quartz window with a uniformly roughened surface. Using a white light source to illuminate the windows at a fixed angle and looking at the piston with a CCD camera from below, the dry surface appears as a white region in the recording as shown in Figure 2.9. With a liquid deposit on the piston more light is transmitted through the glass. The reason being that the refractive index of the liquid is closer to the one of glass and also that the liquid film is

decreasing the local roughness of the surface [9]. Because of the larger fraction of transmission, only a smaller part of the incident light gets scattered towards the camera. This results in a darker spot in the recording (see Figure 2.9a). If the thickness of the liquid film is too large in relation to the surface roughness, however, the detected light intensity becomes insensitive towards the liquid film thickness.

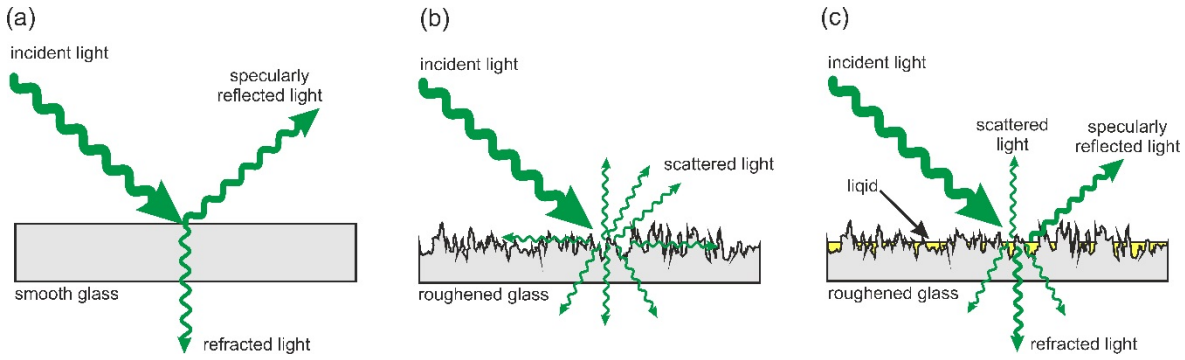


Fig. 2.8 *Fundamentals of RIM: In the case of a smooth surface (a) light gets reflected specularly and refracted, whereas the rough surface (b) scatters incident light in all directions. With liquid on the rough surface (c) all phenomena occur.*

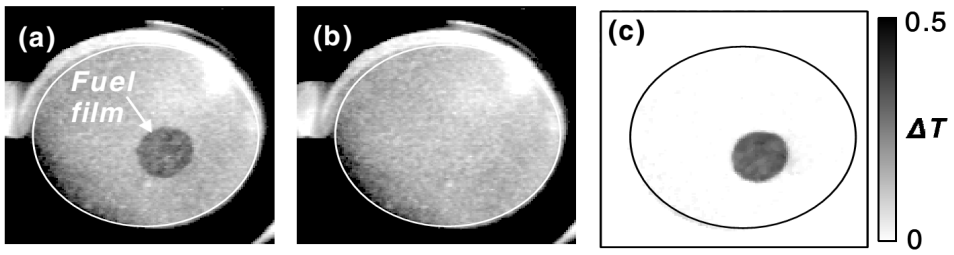


Fig. 2.9 *Recordings produced with Refractive Index Matching* [9].

Because of the dependence of the scattered light intensity on the physical configuration of the individual measurement setup, *in-situ* calibrations are essential [9]. They applied known volumes of a non-volatile hydrocarbon to the rough glass windows while constantly recording the glass window. The local intensity change $\Delta T(x, y)$ is evaluated pixel by pixel following the relation

$$\Delta T(x,y) = 1 - \frac{i_{inj}(x,y)}{i_{ref}(x,y)} \tag{2.5}$$

where i_{ref} is the local intensity without any liquid present, i_{inj} the respective intensity with a liquid film covering the surface and x and y are the local coordinates. By definition, the intensity ratio $\Delta T(x,y)$ becomes zero with no film on top and larger than zero with liquid. A 2D representation of the intensity ratio is shown in Figure 2.9c. By relating the measured intensity ratio to an area averaged film thickness, calculated from the known volume of applied liquid, it is possible to derive a calibration [9]. An example of this calibration relation with a polynomial fit is Figure 2.10.

The strong non-linearity is explained by the geometry of the asperities of the glass window. For small volumes the area covered by liquid changes almost linearly with the amount of applied. As the apparent asperity is reduced more liquid is necessary to evoke a change in the intensity ratio [9].

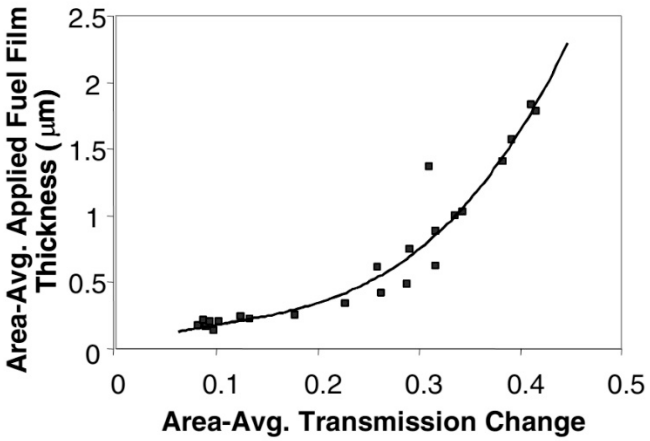


Fig. 2.10 *Example of a calibration derived for Refractive Index Matching* [9].

With the RIM method, Drake *et al.* [9] were able to compare fuel film thicknesses to smoke and hydrocarbon emissions of a direct injection engine running at various engine conditions. They were also comparing the effect of different injector types on these quantities. As a result they were able to state that the liquid fuel film is not the main source of unburned hydrocarbons detected at the exhaust of the engine.

Yang *et al.* [172] were using RIM to investigate impinging diesel sprays in a heated test chamber. The thickness of the diesel films created were in the range of 3-5 μm and they were able to show that the maximum thickness was decreasing with larger ambient temperatures. The use of a larger injector nozzle, however, did not show a significant effect on the fraction of the deposit compared to the total injected volume.

Maligne *et al.* [173] were using the Refractive Index Matching technique to conduct time resolved measurements of fuel deposit formed by an impinging gasoline spray. They were showing that even at engine conditions that involve high surface temperatures it was possible to observe the formation of a liquid film. To further evaluate the reliability of their results they also performed LIF measurements at the same conditions. Overall they found very good agreement between the two techniques regarding the evaporation behaviour of the liquid deposit.

2.5 Pattern and droplet analysis of gasoline direct injection sprays

With the ongoing optimisation in the design of direct injection engines, one focus lays on the spay structure and atomization process of injectors. Usually, two main injector designs are used in this type of engine, the swirl and the multi-hole design. The latter has gained more and more interest because it provides a more stable injection profile over a wider range of operating conditions [174]. Additionally, there is an indication that the multi-hole design reduces the extent of wall wetting caused by spray impingement and as such the amount of generated engine-out emissions [73]. For this reason and because of the injector designs used in this work, the literature presented here will focus on multi-hole injectors only.

Mitroglou *et al.* [175] did a very extensive investigation on a series of multi-hole injectors for GDI engines. They were looking at three different six-hole designs with symmetric and non-symmetric nozzle arrangements and a non-symmetric eleven-hole injector. The experiments were carried out in a dedicated constant volume injection

chamber, with controlled ambient conditions. The chamber pressure was varied between atmospheric and 12 bar, the rail pressure was adjusted between 80 and 200 bar. The electronic injection windows were set up to 1.5 ms. The spray structure was recorded through high speed Mie-scattering and the droplets were analysed with a Phase Doppler Anemometer. The results of the spray imaging showed that the increase of the injection pressure mainly affects spray penetration and not so much the spray angle and cone size. This was the case for both center and side holes of the injectors. Overall, the central spray showed the largest penetration compared to the side sprays. When increasing the chamber pressure the spray characteristics changed significantly. In the case of the symmetric six-hole injector, the penetration depth was less than halved in the case of 12 bar inside the chamber compared to atmospheric pressure. The other injector designs showed a similar trend, but the change was not as drastic. The overall spray angle was little affected by changes of the ambient pressure. The investigations of the droplet velocity distributions through the Phase Doppler measurements showed that the mean centerline droplet speed is increasing with injection pressure, as expected. However, they did not observe a linear relation between the two parameters. The largest velocities of around 180 ms^{-1} were observed for the symmetric six-hole injector at 200 bar rail pressure when measuring 10 mm downstream of the nozzle. For the same injector, the mean droplet velocity was reduced by the factor of eight when increasing the vessel pressure from ambient to 12 bar. This illustrates how much the spray penetration is hindered if the ambient pressure is significantly larger than atmospheric. During these measurements they also varied the injection duration, which showed that for injections shorter than 1.5 ms the spray is not fully developed and does not reach a steady state droplet velocity. Once 1.5 ms of injection duration is reached, a prolonged timing did not change the achieved mean centerline velocity. With increasing the downstream distance from the injector, the recorded velocity profiles were decreasing slightly. Similar results arose from the statistical analysis of the mean droplet diameter which was decreasing only slightly when moving away from of the injector. However, the droplet sizes were affected by the ambient pressure quite notably with increasing diameters for larger vessel pressures of up to 55%, especially for the off-centerline locations of the spray. Changing the rail pressure did not have as much of an

impact. When switching from 80 to 200 bar the mean droplet size was reduced by 25%. Overall, the droplet sizes ranged roughly between 10 and 20 µm.

Matchitto *et al.* [176] looked at the spray pattern and atomization of different fuel blends from a six-hole GDI engine injector. They used gasoline and n-butanol, which were injected at 50 and 100 bar into a pressure vessel. The surrounding air was set to ambient temperature and pressure. To analyse the spray structure they applied Phase Doppler Anemometry and obtained droplet velocity and size distributions under different test conditions. The injection width was set to larger values for the smaller rail pressure and increased overall in the case of n-butanol to account for the lower calorific value of this type of fuel when the same fuel to air ration is considered. The measurement distance was varied from 5 to 20 mm downstream of the nozzle. Analyzing the droplet data for the centerline at each location they saw a decrease in the mean droplet size and velocity with increasing distance. According to them the droplet size change is not due to evaporation of the liquid but mainly because very close to the nozzle the flow and spray is very unstable, which might skew the results. When looking at the temporal signal of each measurement location it shows that it requires about 500 ms from triggering the injector to reach a stable diameter for all distances and both pressures. The initial droplet sizes are much bigger when the spray is forming during needle lift, but rapidly decreasing in magnitude until these reached a stable value. The velocity signal showed the opposite behavior where it required around the same time to go from a low initial value to the steady droplet speed. Overall, they observed that for increased pressure the droplets reached the probe volume slightly earlier, which was also represented in the larger velocity values for this operating condition. The mean droplet diameter of the centerline was only increased very slightly over the distance of the spray for both rail pressures. Only the measured diameters at the spray edge were increasing quite notably with distance. The values were between 7 µm in the case of 100 bar rail pressure, centerline and 5 mm distance from the injector and 14 µm for the spray edge, 20 mm downstream of the nozzle at 50 bar fuel pressure. The mean velocities were increasing with the distance for all test conditions, both at the centerline and spray edge. The core velocities were between two to three times larger than at the spray edge. The values varied between 20 ms^{-1} at the outside of the spray and far away

from the nozzle and the lower rail pressure and 100 ms^{-1} at the centerline, close to the injector with high fuel pressure. Changing the fuel from gasoline to n-butanol produced consistently larger spray core droplet sizes in all test conditions. This was explained by the increased viscosity and surface tensions of n-butanol compared to gasoline. The centerline velocities of n-butanol droplets were slightly higher than its gasoline counterpart for the large injection pressure due to the decreased atomization properties, creating bigger droplets with larger momentum. Contrasting that, the droplet sizes were smaller in the case of n-butanol at the boundary of the spray for the lower pressures. The velocities at larger distances on the other hand were very similar for both fuel types.

Aleiferis *et al.* [177] did a spray study with a multi-hole injector on gasoline and other fuel substitutes in an injection chamber. They investigated spray penetration, cone angles and droplet size and velocity distributions, while varying the injector body temperature and the ambient pressure. To generate data a combination of high speed imaging, Phase Doppler Anemometry and laser diffraction was used. Their results showed that spay penetration was very similar for all fuels at ambient conditions. Also, the change of the injector body temperature had only little effect on this variable. When operating at 90 °C there was an increased penetration of about 10%. By decreasing the chamber pressure from 1 bar to 0.5 bar the penetration was also increasing about 10% for most sprays. The captured plume tip velocities from the high speed recordings were in the range of 80 to 90 ms^{-1} for all fuel types. At the operating condition of 120 °C and 1 bar chamber pressure, they saw that the spray of n-pentane was collapsing. For the reduced chamber pressure at the same temperature, however, they saw larger differences of the spray plume between the blends. Similar to the penetration depth, the overall spray cone angle was not changing significantly between the fuel types. Ethanol and gasoline showed a reduction of the angle with increasing injector body temperature, probably due to their high volatility compared to the heavier fuels investigated. In general, they observed that the spray was collapsing when the chamber pressure was lower than the vapor pressure of the fuel. The findings of the high speed imaging were confirmed by the droplet measurements, with recorded sizes between 10 and 17 µm for all fuels. Increasing the injector body temperature led to a decrease of the diameter of the gasoline sprays and the n-pentane

sprays, while the iso-octane sprays remained more stable over a wider range. Decreasing the chamber pressure led to a reduction of the mean droplet size at the same time, again with iso-octane being the most stable. The captured droplet velocities for iso-octane were not directly correlating with its droplet sizes. Decreasing the chamber pressure at ambient temperature resulted in a notable increase of the droplet speed, due to reduced drag forces, according to the authors. For an injector temperature of 120 °C this trend was not as pronounced, however. Overall, the largest recorded velocities were around 80 ms^{-1} which is the same magnitude as the spray drip velocities from the high speed imaging.

A rather recent computational and empirical study on the spray structure of gasoline and 2,5-dimehtylfuran (DMF) were done by Li *et al.* [178]. Spray penetration, droplet velocity and droplet size distributions were investigated with a combination of shadowgraph imaging and Phase Doppler measurements. The results were used to evaluate the spray structure differences of gasoline and DMF. Additionally, the data was the basis to review different atomization and spray models. The experiments were carried out with a multi-hole injector and the injection width was set to 2 ms with a rail pressure of 100 bar. The spray analysis was done at on one of the central spray plumes as a function of downstream distances from the injector tip. After analyzing the temporal velocity time signal they saw that the initial measured droplet velocity was immediately decreasing as the spray front was passing the probe volume. According to them, this was caused by drag forces that were affecting the first droplets. After this observed dip, the velocity stabilized at slightly larger temperature conditions until the values trailed off rapidly after the end of injection. This evolution of the temporal velocity signal was observed for all measurement locations, but decreasing with increasing downstream distance. The value of the steady droplet velocities of the fully developed spray was between 60 and 40 ms^{-1} depending on the distance from the injector, with DMF producing slightly larger velocities. The corresponding mean droplet diameters also started from a large value that was rapidly decreasing to a stable value once the initial spray front passed the probe volume. However, there was no increase of the diameter after the initial measured decrease, as opposed to the velocity time signal. The values did not change significantly for the different measurement locations and were around 25 μm. A trail-off similar to the velocities was not observed in

the size measurements immediately after the end of injection. Throughout the measurements, DMF produced slightly larger values than gasoline. This was explained by the larger surface tension of the former of around 25%. The observed spray penetration was marginally larger for DMF, caused by the differences in velocities and diameters creating a larger droplet momentum, according to the authors. This circumstance affected wall wetting during injection negatively especially with DMF showing a reduced evaporation rate compared to gasoline. The spray models that were compared with the experimental data were able to represent these spray characteristics with varying success and only one was able to cover the entire behavior reasonably well.

Behringer *et al.* [179] compared the atomization behavior of two multi-hole injectors, one with laser drilled and one with spark eroded nozzles, using different fuels. They tested gasoline, butanol and ethanol and analyzed them through spray imaging and Phase Doppler measurements. Spray penetration, spray tip velocities, spray cone angle and droplet size distributions were captured and evaluated. The experiments were performed in an injection chamber at 20 °C and 80 °C with ambient pressures of 0.5 and 1 bar. The rail pressure was fixed at 120 bar. At the lower temperature they saw a reduced spray penetration for the alcohols, with butanol producing the smallest value, which was explained by the larger viscosity compared to gasoline. At the higher temperature point, the differences between the fuels were notably reduced and they showed a more comparable penetration behavior. The spray angle measured between 0 and 25 mm distance from the injector was the smallest in the case of ethanol and the largest for gasoline with butanol in-between at 20 °C ambient temperature and 1 bar. When the pressure was reduced to 0.5 bar, the angle of the gasoline spray was affected the most and the values became smaller than those of the other two. Increasing the chamber temperature also produced the smallest spray angles with gasoline, while the two alcohols were very similar. At the reduced vessel pressure and 80 °C, butanol yielded the largest angles followed by ethanol and gasoline. Aside from the order of the fuels, the overall values were not affected too much by changing the ambient conditions. The droplet size measurements showed that the smallest droplets were produced by the gasoline spray at around 17 µm and the largest in the case of butanol with roughly 24 µm. By decreasing the

chamber pressure and maintaining 20 °C they observed only a slight reduction of the diameter observed. On the other hand, by increasing the ambient temperature, all values were reduced with the alcohols being affected the most. A further reduction of the pressure increased this trend to about 20% in the case of Butanol.

The specific relationship between injector deposits and how it affects the spray pattern was studied by Lindgren *et al.* [180]. Droplet size and velocity distributions of a swirl-type injector were measured with a Phase Doppler Anemometer. Measurements were done in an injection chamber at ambient conditions and a rail pressure of 50 bar. Between the clean and fouled injector they saw an increase of the droplet velocities by 30% and of the droplet sizes by 5%. According to them a change like this can have a significant impact on engine performance and emission levels.

Even though these measurements were done on a swirl injector, this issue also exists for multi-hole injectors and is the focus of the second part of this work. A more detailed overview of the impact of injector fouling on engine performance and emissions is given in the following chapter.

2.6 Influencing factors on injector fouling and the impact on injector and engine performance

The design of the gasoline direct injection engine and its shift of the injector from the air-port to inside the combustion chamber directly exposes the injector to the harsh conditions created by the combustion process. As such, it is possible that flame and combustion products are interacting with the injector in a negative way. This fact can lead to injector deposits and fouling or coking which then affects the fuel spray structure and can impact engine performance, fuel consumption and emissions as a consequence [181]–[183]. Additionally, cases of injector failure due to plugging caused by combustion deposits have been reported for road vehicles [184].

Aradi *et al.* [185] did a study on the phenomenon of injector deposits and how they are affected by different fuel blends and engine conditions. They carried out experiments in

a four cylinder engine which was run with rich fuel to air ratios to promote injector fouling. Additionally, the load of the engine was varied which affected the temperature of the injector tip. The latter was measured with a special thermocouple that was mounted inside the injector body. The cycle to dirty-up the injectors was 6 hours long, at an engine speed of 2500 rpm. During that time they recorded the fuel flow which they used as a measure of the quality of the injection. After their online measurements, they removed the injectors from the engine and scraped off the deposits. These were then analysed via infrared spectroscopy and electron microscopy. The deposits inside the holes were extracted by rinsing the injector with solvents, which were subsequently evaporated and the residue was also analysed. During their tests they observed a clear trend between the temperature increase and the flow loss of the injectors, which was calculated though the data of the air to fuel ratio sensors at the exhaust. For some of their blends the maximum loss was around 10%, which was achieved for temperatures between 170-180 °C of the injector tip. At temperatures close to 190 °C, however, they saw that the flow loss decreased again for all fuels. When looking at the flow loss over time for individual injectors, they found that there was a periodic loss and increase of the injector flow. At the beginning of their test cycle they observed a steady decrease of the fuel flow rate, but after a while a balance between build-up and removal of the deposits was established. They also observed that the extent of the deposit is affected by the boiling temperature (more specifically T90, the temperature that corresponds to 90% evaporation of a given fuel blend in a distillation process) of the fuel. With increasing volatility, the amount of the deposits seemed to increase and *vice versa*. In addition to the physical properties, they also observed that by increasing the olefin content, injector fouling was also increasing, although they observed some minor inconsistencies in that trend. By analyzing the external and internal injector deposits they saw that fouling on the injector exterior was formed by fuel components and elements of the cylinder lubrication. Fouling on the inside was only formed by fuel components.

In the later work of Aradi *et al.* [186], [187] they focused on how the formation of injector deposits can be controlled with the use of fuel additives and detergents. The experiments were carried out in the same engine as before with similar properties, but

focused on the temperatures that lead to the largest deposit formation and additionally the temperature that had a reducing effect on the deposits. They selected three types of fuel blends from the previous experiments and added a series of chemical detergents of two classes (so-called Mannich and polyetheramines). The fuel loss was again used as an indicator of injector performance. Overall, the addition of the detergents had a very positive effect on the reduction of injector deposits, with the group of Mannich detergents being superior to polyetheramines. A reduction from 10% flow loss to about 2% percent was achieved with the additives. It was also possible to reverse the effect of injector fouling by up to 70% created during an initial 6 hour cycle by adding a detergent for the same amount of time. Also, when running the engine with the additive from the beginning there was a notable reduction in injector flow, even at the most critical temperature condition, compared to the results without an additive. These observations were also verified in high speed imaging of the spray and a droplet analysis via Phase Doppler Anemometry. Both the spray pattern and the droplet size distribution were not changing with the addition of a detergent over time, while they observed significant changes in both cases for fuels without additives, once fouling had occurred. The spray shape looked distorted and the droplet sizes were skewed towards larger diameters across the spray profile.

Similar studies of the influence of fuel composition and fuel additives on the formation of injector deposits were also published by Kinoshita *et al.* [181], Arters *et al.* [182], Ashida *et al.* [188] and Noma *et al.* [189], all showing reduced injector performance in the case of deposits and a reduction of this effect by changing the fuel properties and adding detergents. Kinoshita *et al.* [181] additionally proposed that an injector temperature below the temperature that corresponds to T90 of the fuel is also contributing significantly to suppress injector fouling. In this context Dumont *et al.* [190] proposed a test cycle to assess the injector deposit of different blends with and without additives that can be applied to vehicle and dynamometer test runs.

A drastic change in the injector and engine performance due to fouling was also observed by Joedicke *et al.* [191]. They performed a dirty-up cycle in a four-cylinder turbo charged direct injection engine and a following run with fuel containing detergent. The

engine was operated under homogeneous conditions and low speeds during the experiment and the authors were monitoring injection duration and hydrocarbon, as well as carbon monoxide emissions. In the dirty-up cycle they observed an increase of the injector pulse width of up to 25% at the time of 55 hours. A switch to the detergent blend reverted this effect completely after a bit more than 10 hours. Carbon monoxide was increasing by about 120% at 35 hours into the cycle, but dipped down after that before increasing again at the end. The hydrocarbon emissions were increasing by more than 30% after 20 hours and maintained an elevated but slightly declining level throughout the dirty-up cycle. Towards the end a small increase was detected. Both observations could indicate that the injector fouling is a cyclic process which oscillates slightly around a mean value. After switching to the detergent containing fuel the carbon monoxide levels dropped back to their original value after about 8 hours. Hydrocarbon emissions also decreased in this part, but more slowly. The injector coking also affected the fuel consumption that was increased by around 2.5% during dirty-up and was following the same pattern as the other quantities. In addition, they also observed an increase in burning duration for the dirty injector.

One critical aspect of injector fouling is the change of engine out emissions. This was investigated by Arters *et al.* [33] in GDI engine equipped vehicles alongside tests in laboratory test engines. The authors ran a deposit accumulation cycle on all engines and compared the fouled injectors to unused counterparts. They tested different blends of fuel also with additives. Overall, their observations were similar to the previously mentioned literature data. The injectors of the GDI engine showed reduced flowrate after an 8000 km vehicle test, which was further decreased after 16000 km. Using two types of additives, they were able to reduce the injector fouling level overall and also partially clean previously fouled injectors in clean-up runs. When investigating the particulate emissions during their vehicle tests, the authors saw a very clear correlation between particulates and injector fouling. With increasing deposits and as such increasing injector nozzle restrictions or plugging, the amount of soot measured at the exhaust was also increasing. In the worst case they saw almost three times as much particulate mass for the fouled injector. A very similar trend was also observed for fuel consumption, which was also increased by up to 25% if injector fouling was occurring. Other emissions, such as hydrocarbons, carbon

monoxide and NO_x were also affected negatively but the trend was not as clear. With increasing flow rate restriction they observed a slight decrease in these emissions, which was then increasing again for larger values. In the case of the largest deposits, hydrocarbon emissions increased by more than 80% and carbon monoxide and NO_x emissions almost doubled.

Research published by Carlisle *et al.* [192] looked at particulate and hydrocarbon emission changes initiated through injector deposits with changing fuel composition and additive content. Measurements were done in a multi cylinder research engine that used a spray guided injection setup and provided optical access. The engine was operated both under homogeneous and stratified conditions between 1125 and 5250 rpm. Multiple temperature sensors were installed in the cylinder and injector to record temperature profiles during the tests. Hydrocarbon and soot emissions were measured with commercial exhaust gas analysers. During their tests they observed deposit build up at different levels for each fuel blend, with the exception of iso-octane, which did not produce any deposits in stratified or homogeneous mode. For all other fuels there was a steady increase of the hydrocarbon emissions and soot formation recorded over time. Under stratified conditions and large engine speeds, however, the emission increase was leveling out which could indicate a stabilization of the fouling process, according to them. Between the fuel blends they found that an increase in aromatic and olefin content led to more hydrocarbon and particulate emissions, while there was no clear trend observed for the influence of T90 in stratified engine mode. Under homogenous conditions there was also a trend for olefin and aromatic content to increase hydrocarbon and particulate emissions. However, unlike in the stratified mode, these measurements showed a correlation between emissions increase and increasing T90. Comparing the emission levels to measurements with a fuel containing additives they observed a significant reduction in hydrocarbon and particulates in stratified mode. Injector deposits were also significantly reduced. Contrasting that, the authors found an opposite effect for homogeneous operation, where the emissions were increased by adding detergents and the injector coking was also promoted. According to them, this illustrates the difference of the coking mechanism between the two operating conditions.

Berndorfer *et al.* [193] investigated the combustion processes in their direct injection engine and how it impacts particulate emissions. They observed rich diffusion flames on the injector tip that were covered by combustion deposits. According to them they were the main reason for increased particulate emissions. The measurements were performed in a single-cylinder engine that was configured with a large cylinder bore to minimise wall wetting and equipped with optical access through an endoscope. The engine speed was set to 2500 rpm with a pressure of 6 bar using stoichiometric fuel to air ratios. The injector diffusion flame was visualised through imaging of the flame radiation from which an integral intensity was calculated. In the measurements over time, they observed a rapid increase of the integral intensity within the first 10 minutes of the test run. After this point the cumulative flame intensity remained constant with fluctuations around a mean value. The latter were explained by cycle to cycle variations. This trend was also followed closely by the engine out particle number and mass measured at the same time. After about 35 minutes they saw a layer of deposit on the injector tip once they opened up the engine. After removing this layer the performance of the engine returned to its original level. In another test they compared a clean with a fouled injector that was coked for 10 hours. Their time resolved data showed a clear luminosity difference in the combustion cycle that was caused by the injector diffusion flame of the dirty injector. The observed change was also reflected in the soot formation. Microscopic investigations revealed that there were only very minor deposits in the injector bores and around the nozzle exits, but a very large layer of build-up on the tip. Because of this they did not observe notable changes in the spray cone angle, spray penetration and droplet size distributions between clean and fouled injectors. The fouled injector was also used to investigate the effect of rail pressure on the diffusion flame. From the time resolved measurements they found that increasing the injection pressure had a strongly positive effect with 200 bar almost eliminating the diffusion flame. At the same time, changing the operation to a double injection concept impaired this effect for all injection pressures. The test of different injector tip coatings showed only very miniscule improvement. Switching from the six-hole injector to a five-hole variant reduced the diffusion flame due to the increased static flow rate.

Bacho *et al.* [194] did a case study on engine parameters that enhance injector deposit formation. They used a four-cylinder direct injection engine operated in homogeneous charge with speeds between 1500 and 3000 rpm and a constant temperature of 110 °C. A central mounted injector position was also compared with a side mounted configuration. The change in static flow was used to quantify injector performance. The fouling process was based on previous work published by the authors [184], which showed that injector temperature and engine soak time were the most important contributors to coking. The former was also monitored during these experiments and reached a maximum of 118 °C for 1500 rpm and 40kPa engine pressure. Comparing the two injector locations, their results showed that a central mounted injector is much more exposed to fouling than the side mounted alternative. The former produced a relative mean flow reduction of almost 8% and the latter only about 2.5%. When running the engine with a lean mixture this difference was further increased. Rail pressure had a positive effect on injector deposits. A change from 50 bar to 100 bar almost halved the flow rate reduction. This was confirmed by a microscopic analysis of the injector tips, which showed much more pronounced deposits for the lower pressure case.

In their comprehensive publication on emissions of GDI engines, Wang *et al.* [128] also investigated the effect of injector fouling. Their single-cylinder engine with a spray guided injection setup showed a drift of the soot and hydrocarbon formation once deposits were present on the injector tips. The plugged injector with a flow rate loss of 8.5% at 150 bar rail pressure showed an increase in hydrocarbon emissions of almost 10% over a large range of tested engine pressures compared to the clean case. According to them, this was caused by promoted spray impingement from the longer injection width necessary to compensate for the reduced flow rate. In addition, the deposit absorbed fuel and caused a rich diffusion flame on the injector tip which was also reported by Berndorfer *et al.* [193], previously. These trends were also observed in the particle size and mass distributions of the soot emissions. Even though there was no change in the shape of the distributions, increasing levels of injector fouling yielded significantly larger levels of particle numbers and masses. This relationship was also found if the injection pressure was reduced to 50 bar. However, the overall level of emissions was increased by more than twice the

original numbers for all measurements. In addition to the increased release of emissions, a slight loss of the peak in-cylinder pressure and elongated combustion duration were observed for the fouled injectors. Experiments with ethanol substituting gasoline lead to fewer injector deposits and as such smaller flow rate losses. This was also affecting the hydrocarbon and particulate emissions less negatively, which were only marginally elevated. According to the authors, this was mainly attributed to the better evaporation rate of ethanol under engine conditions and the oxygen content, which was beneficial for soot oxidization.

Additional reports of the positive effect of ethanol on injector fouling minimization can be found in [117]. A significant reduction of the deposit with increasing ethanol content of the blend was shown. In the case of pure ethanol there was no real cocking of the nozzle observed.

A very recent and comprehensive review of the mechanism and effects of injector fouling in modern gasoline direct injection engines was published by Xu *et al.* [183]. Their report includes common techniques to quantify injector fouling, such as spray visualization, flow rate measurements and composition analyses of the deposits. The effects on injector and engine performance, some of which are mentioned in this chapter, are also presented. Different injection strategies and engine design parameters are also listed and discussed.

2.7 Motivation and outline of the research

Gasoline direct injection engines provide a lot of benefits to the manufacturer and consumer alike, but these benefits also come with significant drawbacks as the examples from the literature show. Two of these concerns are the focus of this research, the increase in particulate emissions related to wall wetting and the control of injector fouling and its associated drift in engine-out emissions.

Although research like this has been done before, it was usually limited to a small number of real fuel blends or only surrogate fuels were tested instead. With the presented

study a large series of potential gasoline blends that are relatively close to market are investigated. The aspect of distillation behavior, ethanol content as well as aromatic and olefin content are the key aspects.

Testing these blends under defined conditions can require a lot of resources, especially when carried out in laboratory engines. For this reason an alternative approach is chosen, by designing a dedicated injection chamber setup. With this it is possible to test a large number of different multi-hole injectors used in gasoline direct injection engines at numerous conditions and with a large variety of fuel blends, both in a time and cost efficient way. Additionally, a flexible chamber design allows for the application of many optical measurement techniques that can be tailored towards the subject of interest.

For the investigation of wall wetting phenomena, several optical techniques were used in the past, but as the evaluation in chapter 2.3 shows, these have drawbacks that cannot be neglected for 2D measurements of high spatial and temporal resolutions. In particular, the common need of proxies with these techniques would increase the list of challenges significantly, as a large number of fuel blends that span over a wide range of physical and chemical properties are investigated here. Finding a single, or even a small number of suitable additives that functions satisfactory in all cases would prove challenging. Furthermore, the signal generated by these proxies is usually pressure and temperature dependent. This makes them impractical for highly transient measurements, or if different temperature points will be investigated.

For these reasons it necessary to develop a novel technique that is independent of adding a dye or similar chemicals and is also suitable for tests under different engine-like conditions. The intention is, to design a measurement environment that produces a reliable signal that is only a function of the fuel and not skewed by boundary conditions enforced by the technique. Such a technique opens up this research for a large number of fuels and engine properties and provides extensive understanding on how these parameters affect wall wetting and as a consequence the level of particulate emissions.

In order to put the results in a better context, however, it is also necessary to characterize the spray itself as the atomization and evaporation affects engine performance even before the occurrence of spray impingement. For this reason extensive spray droplet

measurements are performed with the means of Phase Doppler Anemometry. This is also done in conjunction with high speed imaging of the spray itself and the interaction between the spray and a solid surface.

With the knowledge and experimental expertise gained during these investigations the setup is expanded towards the examination of the effect of atomizer deposits on the spray characteristics. The issue of injector fouling is a well-documented phenomenon and the associated problems, such as increased particulate emissions go hand in hand with wall wetting. So far there is a lack in fundamental understanding of the exact processes that lead to injector fouling, which is why the extended research is characterizing the spray pattern of deliberately fouled injectors in comparison to clean and unused injectors. Additionally, the potential application of detergent additives to revert or prohibit this mechanism is assessed.

Both parts of this research, linked by the challenge of particulate emissions reduction in gasoline direct injection engines, shall illustrate the underlying mechanisms and provide potential ideas on how to further improve engine design to remedy this dilemma.

The research presented is split into different parts. In the next chapter, the experimental rig and the recording setup that were used to analyse spray patterns and the fuel film thickness of impinging gasoline sprays is presented. Then, the Phase Doppler technique is explained alongside the used equipment, before the fuel blends and conditions that were part of the first set of experiments are listed. After this, the modifications of the rig to accommodate the injector fouling investigation shall be presented, which concludes the experimental setup and methodology section.

In chapter 4 the background of the newly developed measurement technique is explained, followed by the used calibration and post-processing methods. To validate its principle, the technique is then compared to RIM and used in a single component fuel study to investigate the potential influence of the boiling temperature in relation to the surface temperature of the impingement plate.

Chapter 5 presents the findings of the fuel study, which is split into the data from the high speed recordings, the PDA measurements, and the quantification of wall wetting with the technique that is discussed in chapter 4.

In the following chapter, the results of the injector fouling investigations are presented alongside analysis procedures that have not been used before in this context.

Finally, the research is summarized with conclusions as well as suggestions for future work.

Chapter 3

Experimental setup and methodology

In this chapter the design of the experimental rig and the recoding setup will be presented. This includes the development of the dedicated injection chamber, the arrangement of optical components and the fuel blends and conditions that were tested to assess the influence of fuel and engine properties on the sprays characteristics and wall wetting.

Then the modifications that were applied to the rig to investigate injector fouling will be explained including the new alignment of the camera and light source. The chapter is finished with an overview of the investigated injectors and conditions of this research.

3.1 Design of the injection chamber for the investigation of fuel deposits

A dedicated experimental setup was designed in order to investigate sprays that are found in gasoline direct injection engines. The basic intention was to create an abstract injection chamber which allows for recreating different temperature conditions found inside an engine at various operating points. The investigation was focusing on the spray pattern, both in an impinging and free spray scenario, with different fuel blends and boundary conditions. The research was split into three major parts. At the beginning a more

qualitative procedure was used to see the effect of changing physical and chemical properties on the spray cone and the interaction between the spray and a temperature controlled glass plate. Based on this data, a selection of fuel blends was made to analyse the spray structure with Phase Doppler Anemometry. In the last step, the liquid deposit of several characteristic blends was quantified via a specially developed technique. By combining the results, a deeper insight into the influencing parameters and fuel wall wetting will be provided. These results are to be correlated with engine data obtained by Nissan Motor Company Limited in parallel investigation, using identical fuel blends.

For each step of this research, the basic experimental setup was modified to accommodate the measurement equipment. An overview of the initial design and the modifications are given in this chapter, alongside an overview of the investigated fuel blends and experimental conditions.

3.1.1 Basic setup for the spray pattern and film thickness analysis

The basic experimental setup included a cube-like injection chamber with a specially designed injector mount, a temperature controlled impingement plate and an air heating system, as well as a fuel preparation section. The design was kept mostly modular to accommodate the different phases of this study, which required changes in the measurement components. An overview of the rig with close-up view of the injection chamber and the fuel preparation section are shown in Figure 3.1.

The central component of the experimental setup is the injection chamber. It consisted of a cubical aluminium frame made of 25 mm wide struts with a length of 300 mm. The entire frame was mounted on a 450x450 mm^2 steel base plate, which was raised by 130 mm from the optical table (Thorlabs Inc.) with additional aluminium struts. The bottom clearance was used to connect four flexible ducts (80 mm diameter, ERIKS Industrial Services Ltd.), which were connected to the laboratory extraction system. This way a steady low velocity air flow was ensured, to purge the injection chamber from

evaporated fuel. The bottom of the aluminium frame was sealed against the plate with adhesive rubber foaming. Each side of the chamber could be closed with either aluminium panels or polycarbonate windows depending on the configuration. Each side could also be sealed off with rubber sealings to achieve isolated stable conditions with different temperatures inside the injection chamber in combination with the rubber foaming at the bottom of the frame. The rear aluminium panel was either blank during spray analysis or supporting the temperature controlled impingement plates, when experiments of impinging sprays were performed. These plates were attached by aluminium brackets to the rear panel to maintain a stable alignment angle between the spray and the plate. The impingement plate used during the spray analysis measurements was machined from a solid block of aluminium with a surface of 100x120 mm^2. The top was covered with a 100x100 mm^2 glass plate that had a thickness of 3 mm (quartz glass, UQG Optics) and the bottom with a 1 mm stainless steel sheet of the same dimensions. Both were held in place with high temperature silicone adhesive (SILCOSET 153, ACC Silicones). The complete thickness of the assembled plate was 20 mm. At the rear side of the plate three 0.5 inch stainless steel pipes were mounted. One port was used as a supply and the other two as a return. The pipes were connected to a heat exchanger (Julabo ME-12, Julabo UK LTD) via flexible metal tubes. The heating liquid was silicone oil (Rhodorsil 47V100, Bentley Advanced Materials). The whole heating system of the impingement plate was specified to reach stable temperatures of up to 200 °C to recreate surface temperatures of the engine piston during different engine conditions. The temperature of the plate was set at the heat exchanger and controlled through a temperature gauge (PT100) that was mounted inside the plate. Additionally, the surface temperature was checked manually with a surface thermocouple (RS Temperature Probe k-type, RS Components). A schematic of the plate frame and picture of the impingement plate can be seen in Figure 3.2.

The top side of the injection chamber was closed with an aluminium panel, which also provided the structural support of the injector mount. The design of the aluminium injector holder was custom made to provide a seal with the injector tip PTFE gasket. The holder was mounted into a counter bracket at the bottom of the aluminium panel and screwed in with eight M6. The injector itself was mounted to the aluminium holder with a

brass cap that was fixed with two M6 screws. Figure 3.3 shows the brass cap, injector holder and the whole assembly on top of the injection chamber.

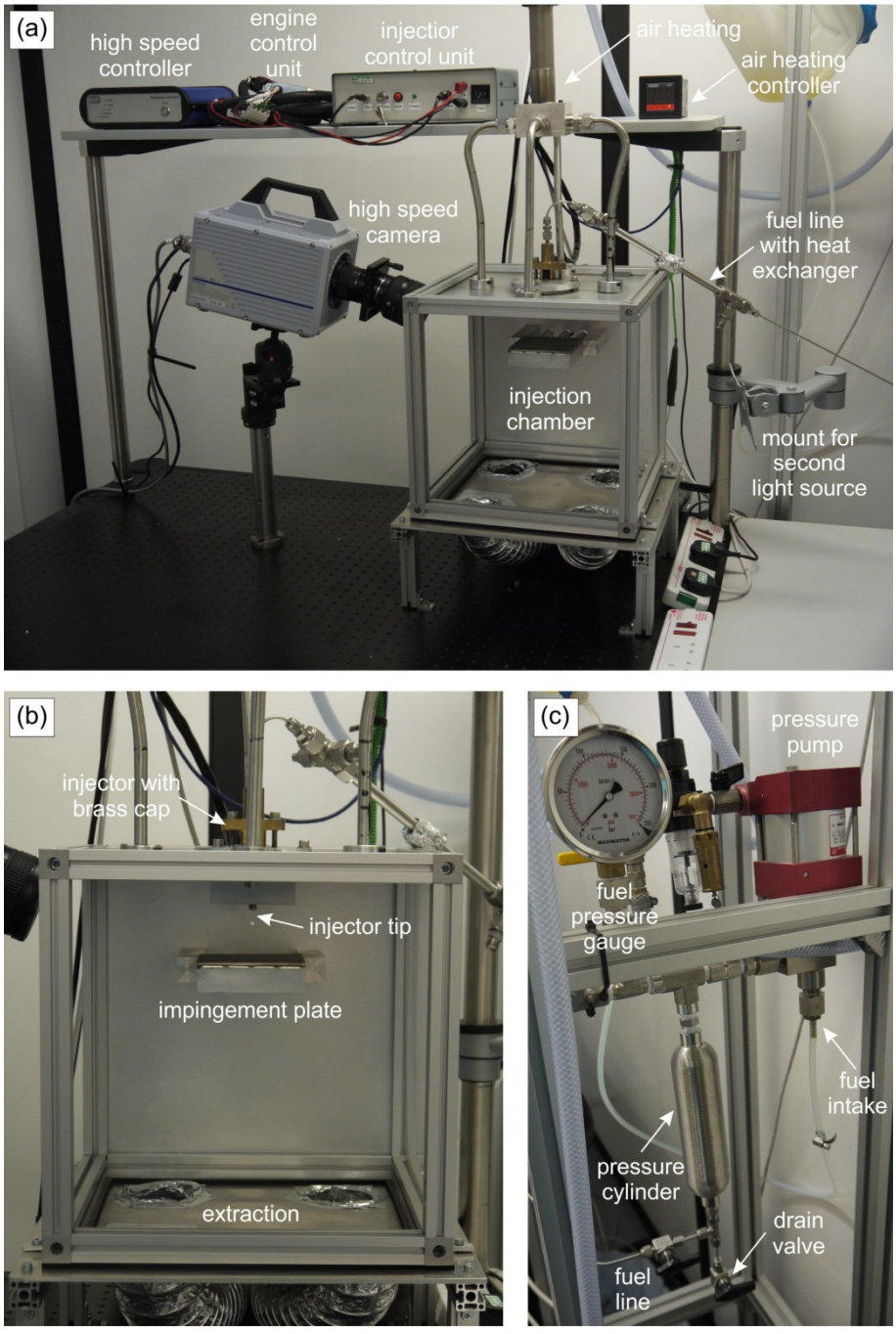


Fig. 3.1 *Experimental setup (a), close-up views of the injection chamber (b) and fuel preparation section (c).*

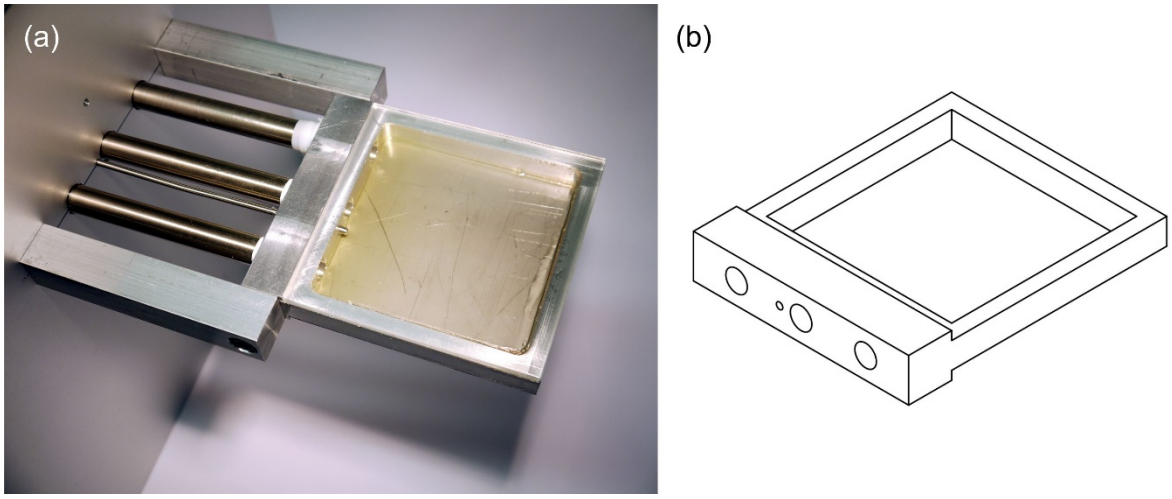


Fig. 3.2 *Photograph of the assembled impingement plate used in the spray visualisation experiments (a) and schematic of the impingement plate frame that was covered with a glass plate and a stainless steel sheet.*

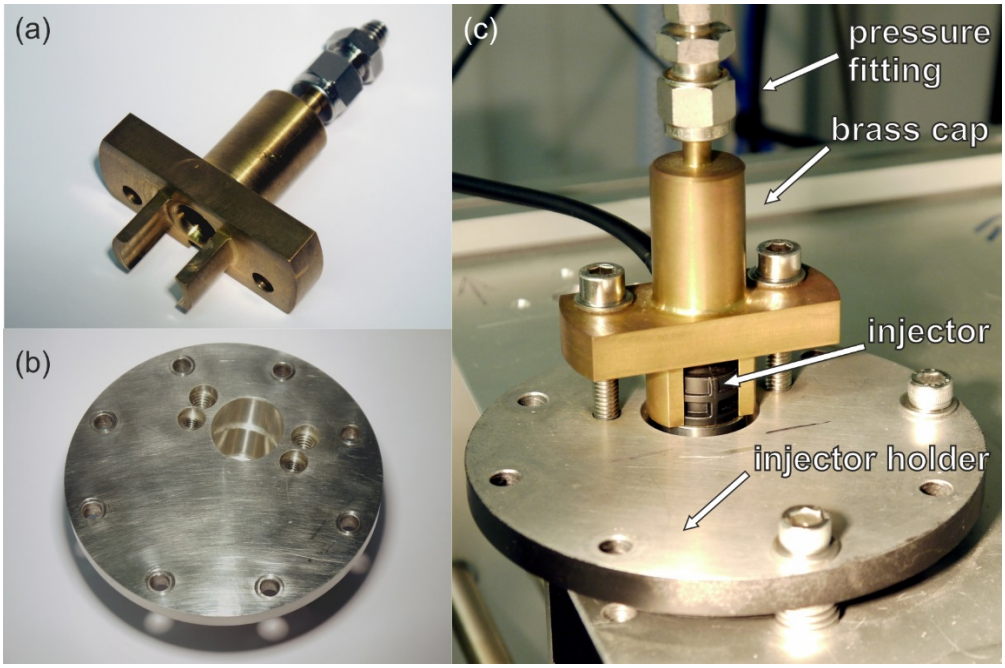


Fig. 3.3 *The brass cap providing a press fit connection to the fuel line (a); the injector mount (b) and the whole assembly with the injector on top of the injection chamber (c).*

The injector itself was a custom made by Bosch with a single hole design (Robert Bosch GmbH). The design of the hole corresponds to one of the side holes of the multi-hole injector that is used in the GDI engines from Nissan Motor Company Limited. The nozzle

diameter was about 200 µm. The spray angle of this single nozzle was 20° to the nominal axis of the injector body. The injector nozzle can be seen in Figure 3.4.

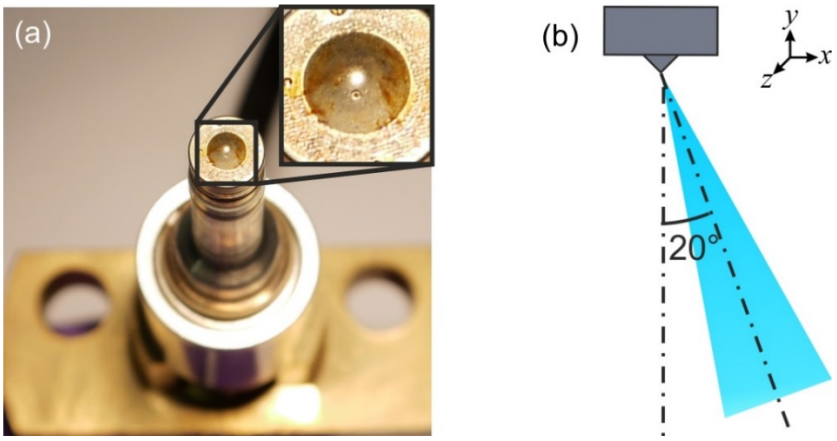


Fig. 3.4 *Injector tip (a) and illustration of the spray angle (b) of the single hole model injector.*

The injector body was mounted vertically in the chamber which meant the incident angle of the spray relative to plate normal equated to 20°. The distance between injector and impingement plate was chosen to be 45 mm, which resembles the distance between injector and piston surface inside the Nissan test engine during reference engine conditions. Actuation of the injector needle was done through a modified engine control unit from Nissan and programmed with a custom injector control unit provided by Shell Global Solutions.

The ambient temperature inside the injecting chamber was controlled with a high temperature heater (LHS 21L System, Leister AG). The heating cartridge was push fit to a manifold with four outlets that were connected to the top panel of the chamber. The distance of these outlets from the centre of the top panel was 120 mm. By choosing this distance and with a predominant flow in the same direction as the spray, the risk of affecting the spray flow was minimised. The flow rate of the air heater was adjusted manually, with a rotameter, and the set temperature was controlled automatically, with a thermocouple that was located about 30 mm above the impingement plate just outside the field of view of the camera during the measurements. During measurements the flowrate

was set to 200 $l min^{-1}$. This equates to about 10 ms^{-1} air velocity inside the pipe. To test whether there was any limitation caused by the use of the air supply, spray tests with significantly higher flow rates of 400 $l min^{-1}$ were performed, which did not show any change in the spray pattern. For this reason it is fair to assume that there is no significant momentum interaction between the air heater and the spray during measurements at the above mentioned flow rate.

The injected fuel was conditioned in the fuel preparation section. A pneumatically actuated pump was supplying fuel from a reservoir to the system at pressures up to 200 bar (MSF22, Maximartor GmbH). The fuel pressure was adjusted through the air supply pressure with a needle valve and controlled via a pressure gauge connected to the fuel line. A 155 ml pressure cylinder (Swagelok Ltd.) was connected to the pressure side of the pump to reduce fluctuations caused by the injector and movement of the piston of the pump. A drain valve at the bottom of the section allowed for purging the system and replacing the fuel with a different blend. Also bleed and pressure relief valves were installed, in order to remove air from inside the system and reduce the fuel pressure if necessary. The fuel line was equipped with an optional heat exchanger that could be used to temperature control the fuel supply to the injector. The counter flow double walled tube design was fed by a secondary heater using silicone oil (Julabo ME-12, Julabo UK Ltd.). The fuel line was connected to the brass cap that was holding the injector. All connections were secured with compressions fittings certified for high pressure applications (Swagelok Ltd.).

During the development of the measurement technique to quantify fuel deposits and for the investigation of the multi-component fuel blends, a modified impingement plate was used. The basic aluminium frame was the same but the top glass plate was replaced with a stainless steel cover that was held in place with screws and the bottom was closed. With this design it was possible to attach steel plates with different surface roughnesses (R_a, the arithmetic mean of the surface roughness values) to the top of the plate. Different R_a values were tested and a roughness of 60 µm was eventually selected for the final technique development steps and the later measurements to have enough headroom for potentially large liquid film thicknesses. All stainless steel plates were supplied by

Blackburns Metal Ltd. The plates were attached with a thin layer of thermal heat compound (RS Components) to maximise heat transfer and compensate for any inhomogeneities in the contact surfaces.

3.1.2 Recording setup of the spray pattern and film thickness analysis

All *in-situ* measurements inside the injection chamber were done with the 12 bit high speed CMOS camera HighSpeedStar 6 from LaVision GmbH. This includes the recordings of the spray pattern with and without the impingement plate and the film thickness analysis of fuel deposits generated by impinging sprays. All calibrations for the technique were also done with this setup.

For the spray pattern measurements the camera was angled downwards at about 10° in order to also capture the liquid film formed on the glass plate if the impingement plate was installed. The image of the camera was cropped to a size of 384x400 pixels^2 with a recording rate of 15000 fps and an exposure of 1 µs. The latter was the smallest setting available, which was chosen to minimise motion blur of the fast moving spray droplets. The lens used was a Nikon 50 mm f/1.4. The illumination was done with the light source placed behind the spray relative to the camera. This resulted in a bright background and a dark spray that resembled shadow image recordings. Compared to directly illuminating the spray with a high speed laser, which was also tested, this configuration yielded much better contrast and the spray pattern was more clearly visible. The light source was a 500 W halogen lamp, which was mounted on a flexible arm next to the injection chamber. To minimise the effect of unnecessary heating up of the injection chamber by the lamp, it was switched on only for a couple of seconds during the actual recording and thus no temperature change was detected during measurements by the thermocouples inside the chamber. The raw images were captured in Davis 7.2 (LaVision GmbH) and further analysed in Matlab 2013b.

The development of the measurement setup and the validation of the novel methodology to quantify thin liquid films were mostly done with a Pike F-032 CCD camera from Allied Vision Technologies. This is a 14 bit monochromatic camera with a resolution of 640x480 pixels. The recording rate was chosen between 10 and 120 fps with an exposure of 5 ms, depending on the volatility of the liquid and the ambient conditions. The images were recorded with Allied Vision's SmartView and stored as a bitmap series. Recordings were subsequently analysed in Matlab 2013b (MathWorks, Inc).

During the film thickness measurements with the high speed camera, the image resolution was 1024x1024 pixels^2. Images were recorded at a frame rate of 2000 fps and an exposure of .5 ms with a Nikon 85 mm f/1.4 lens. The camera was mounted with its viewing axis tilted downwards from the horizontal by 10º. Figure 3.5 shows schematics of the two described configurations. A Scheimpflug adapter was set to 20º to improve the depth of field (Figure 3.5b) [195]. The injection system was triggered by the high speed controller of the camera, in order to synchronise the recording with the injection. This ensured that during each recording sequence, only one injection was captured. The raw images were captured in Davis 7.2 (LaVision GmbH) and processed in Matlab 2013b using the same basic algorithms as for the images acquired during the methodology development phase. Additional analysis of results was also done in Excel 2010 (Microsoft Corporation).

In all cases a 50 W halogen light source was used which was placed close the camera lens at an angle of about 40°. The illumination cone of the light bulb had an angle of 48°. The bulb was powered by a 12 V DC power supply (IPS1810H, ISO-TECH) to avoid fluctuations in the illumination intensity.

During the development of the methodology several factors influencing the sensitivity and reliability of the results, were investigated. The angle of the optical setup (light source, camera) played a significant role. Additionally, the feasibility range of the measurements depends on the surface roughness of the plate, which needs to be selected according to the expected range of film thicknesses. In general, it was found that the light source positioned close to the camera was preferred for this application. This way the measurement range and signal was maximised.

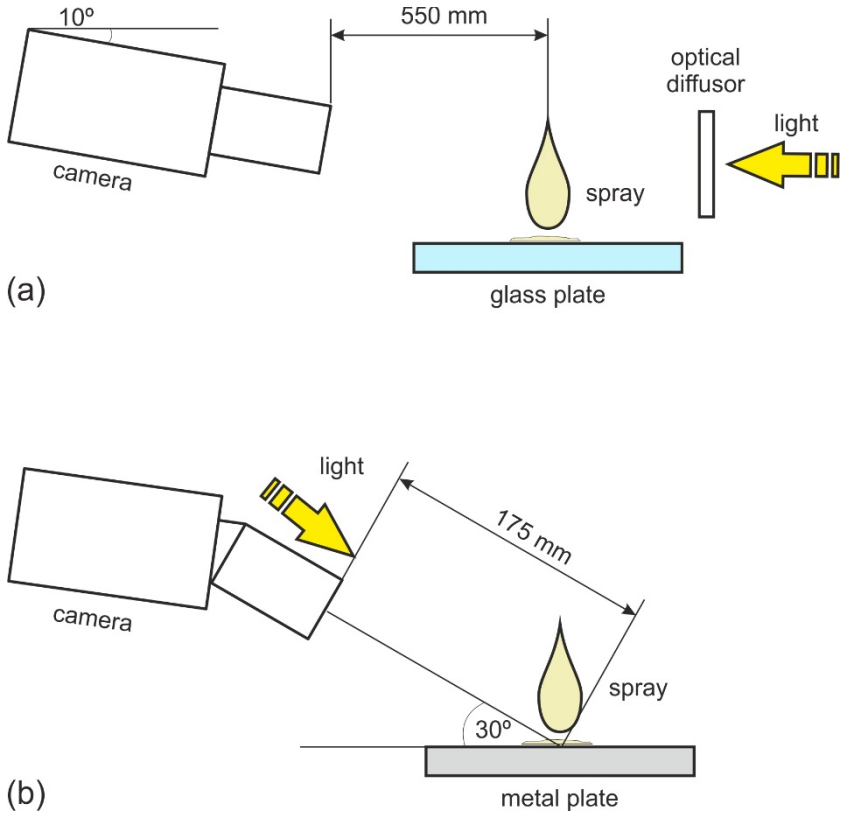


Fig. 3.5 *Recordings setup for spray analysis (a) and film thickness measurements (b).*

3.1.3 Phase Doppler Anemometry principle and setup

Based on the spray pattern analysis a more detailed droplet size and velocity analysis was done on a selection of fuel blends with the means of Phase Doppler Anemometry (PDA). Phase Doppler Anemometry is an enhanced iteration of Laser Doppler Anemometry (LDA), which is a highly established non-intrusive way to measure particle and droplet velocities [196], [197]. Additional benefits are the high accuracy and large spatial resolutions without the necessity of a calibration. LDA utilises two laser beams that are crossing at an angle and as such generate an interference or fringe pattern of known spatial intensity variations across the beam intersection. A schematic of the principle LDA setup is shown in Figure 3.6

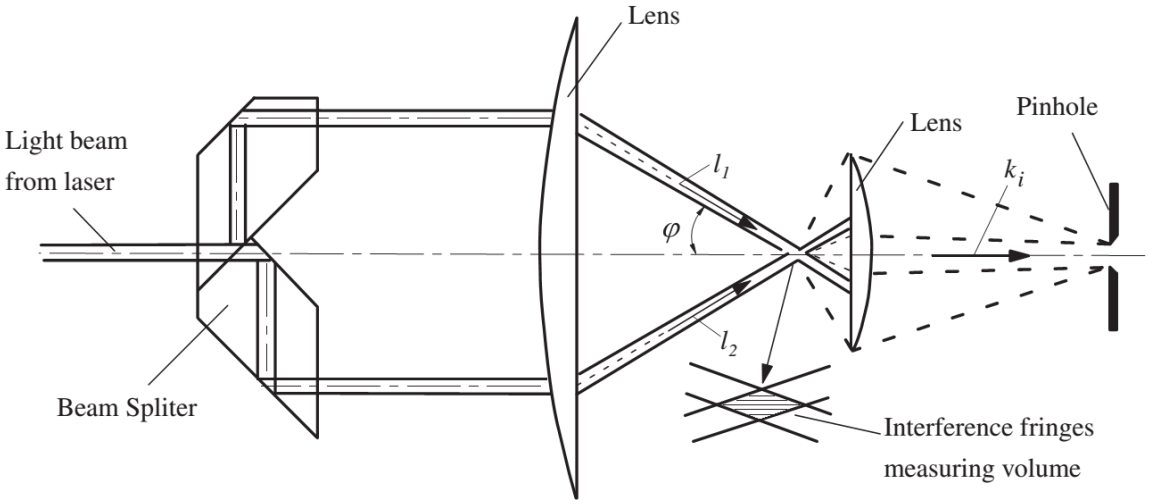


Fig. 3.6 *Principle setup of the Laser Doppler Anemometer with two intersecting laser beams creating a fringe pattern inside the probe volume* [196].

If a particle or droplet is moving through the probe volume it scatters light towards a detector. The intensity of the scattered light is fluctuating with a frequency that is depending on the component of velocity perpendicular to the fringes of the particle for a given fringe distance. Based on that frequency it is possible to calculate the velocity value. Because of the nature of this setup there exists a directional ambiguity of the particles detected, since the signal appears the same if the particle is crossing the probe volume in opposite directions. To overcome this drawback, usually a frequency shift of the laser beams is introduced which results in a fringe pattern that is no longer static but moving in one direction with a known velocity. With this it is possible to distinguish between opposite particle flow directions. Also, when using fringe movement opposite of the predominant particle direction it is possible to further extend the measurement range towards very low velocities [197].

Phase Doppler Anemometry is an extension of the LDA method. It allows for simultaneous measuring size and velocity of spherical particles, while maintaining the same advantages of LDA. The basic setup is similar, but Phase Doppler Anemometry utilises two detectors instead of a single one with a known angle between each other (Figure 3.7).

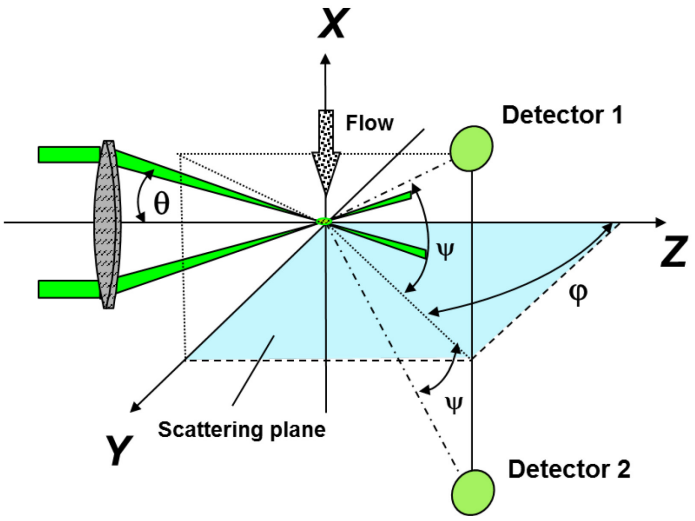


Fig. 3.7 *Schematic of the optical arrangement used in PDA measurements (Dantec Dynamics).*

Similar to LDA, the light of the interference pattern is scattered by a particle, but the scattering pattern is recorded by two detectors. The two intensity signals show a phase shift, which is proportional to the particle diameter and can be used to link velocity and size together. Because the signal is of a sinusoidal nature, the issue of a 2π-phase-shift ambiguity exists. In the of a particle size exceeding a critical value, the system is no longer able to quantify the diameter correctly, because it cannot differentiate the signal from a very small particle, which effectively gives the same relative phase shift. This issue is usually resolved by using a 3 detector setup [197].

The Phase Doppler system used in this work was a Fibre PDA system from Dantec Dynamics. It comprised a 58NN70 Detector unit with a BSA P80 Flow and Particle Processor. The laser light source was a Spectra Physics Laser Stabilite 2017 (model 2550 power source and model 2670 remote control) which provided a dual laser beam at 514.5 nm wavelength. The optional blue beam used for 3D velocity measurements was blocked off. The laser power was set to about 1 W total at the power supply. The intensity difference between the two beams was checked with a laser power meter and adjusted to be less than 10%. Additionally, the polarisation orientation of the beams was verified with a polarisation filter during set up. The transmitting and the receiving head used fixed lenses with a focal length of 310 mm. The aperture for all measurements was mask B. The heads

were aligned in a 30° forward scattering angle configuration. The injector was triggered through the PDA system for each recording. Data was collected with the Dantec programme BSA Flow Software (version 4.50.00.64). The data collection mode was set to burst with automatic calibration enabled. The frequency shift was induced by a Bragg cell with a 40 MHz frequency. The acquisition time was set to 3 ms for each recording, which accounted for triggering delays and the time for the spray to reach the probe volume. It also made sure that the entire spray duration was captured. The input centre velocity was determined by a small number of test measurements and set to 97.55 ms^{-1} with a velocity span of 195.10 ms^{-1}. The limits were chosen to be very broad to make sure the entire velocity range was captured. The detector sensitivity was set to 850V and the gain was 26 dB with an anode current limit of 1500 µA. The PDA detector settings were kept on auto with no additional manual input. The properties for both beams were the same, with a spacing of 38 mm between the two beams, a diameter of 2.2 mm and an expander ratio of 1.95. This resulted in a probe volume of approximately 1 mm^3. The collected time signal during each measurement was filtered with a lower limit of 0.8 ms and an upper limit of 2.1 ms. The injecting time was kept constant at 1.51 ms for all fuel blends to retain the comparability between the sprays and possible effects that occur over the course of the injection process. This way effects of the leading and the trailing edges of the spray cloud were removed, which would else skew the velocity and size distributions significantly.

For these experiments, the setup described in chapter 3.1.1 was modified to accommodate the PDA probes. The cubical injection chamber with the metal base plate was detached from the legs and mounted on a one-axis horizontal traverse system (EPX 40, Phoenix Mecano Ltd.). The traverse was mounted on a frame made out of aluminium struts (Bosch Rexroth AG), which also supported the emitting and receiving probes of the PDA system. The height and off axis distance of the injector relative to the probe volume was adjusted manually. This meant that during the measurements there was one degree of freedom along the traverse axis with a fixed downstream distance of 45 mm from the injector tip. This distance resembled the location of the injection plate to the injector, which was not installed during the PDA measurements. For all blends a horizontal profile crossing the centreline was recorded. Figure 3.8 provides an illustration on the

measurement locations during these experiments with a definition of the coordinate system.

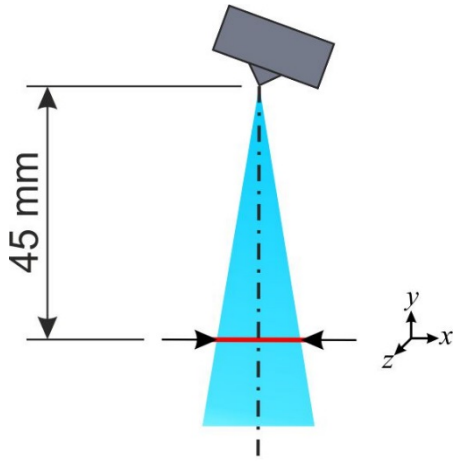


Fig. 3.8 *Schematic of the measurement location for the PDA spray analysis.*

The injector was mounted with its normal axis at an angle of 20° relative to the vertical direction, with a different injector holder, which provided a spray perpendicular to the measurement plane. Before each measurement, a brief scan of the spray profile was done to detect the centreline of the spray. Based on that, points of 0.5 mm increments up to an offset of 2 mm to both sides of the plane of symmetry were recorded. For each point a sample size of 20000 droplets were collected. The software stored size, velocity information and time of arrival (relative time after start of recording) for each droplet detected. This information was stored in ASCII files, which were imported and processed in MatLab 2013b.

The measurements uncertainties of this setup were either associated with the PDA method and algorithm or the experimental procedures [197]. Aligning the emitting and receiving probes was done with the help of a compressor nebuliser (Omron CompAir NE-C28P) that provided defined Gaussian droplet distributions. With this it was made sure that the probe volume was in focus, that the signal yield was maximised and that the values detected were correct. The actual uncertainty of the measurement electronics inside the PDA processor was not available through the software. However, the unit was equipped

with a self-calibrating light probe that was used in an automatic mode before each measurement. The overall values of droplet size and velocity will be displayed as mean and standard deviation values, based on the sample size of 20000, which were obtained from statistically independent recordings. Each injection yielded around 200 droplets, with lower numbers close to the centre of the spray. The detector phase ratio validation was set to 15%.

The relative alignment of the injector was the same for all measurements, only the horizontal position was adjusted with the traverse that was actuated with a manual hand wheel. The total travel length of the linear unit was 100 mm with an accuracy of 0.1 mm and was only moved in one direction during measurements to avoid hysteresis by the adjustment gears.

3.1.4 Investigated fuel blends and experimental procedures

The total of eleven blends investigated was split into two groups of fuels. One group was focusing on the change of the boiling behaviour (*i.e.* T90) and the ethanol content and was called the "physical matrix" consisting of seven blends. The second group used the olefin and aromatic content as varied parameters and was referred to as the "chemical matrix". An overview of these properties is shown in Figure 3.9.

In the case of the physical matrix fuel blends, PM4 was the basepoint for all calculations. Two main parameters were of interest. One was changing the distillation properties which are represented through T90 on the x-axis while maintaining the ethanol at 5% and in the other case of PM5, PM6 and PM7 the parameter was ethanol content while keeping T90 as constant as possible. Because of the reduced boiling temperature of ethanol compared to iso-octane it was not entirely possible to keep those two parameters independent of each other. This is evident in the case of PM6 an especially PM7 which showed a reduced T90. Blend PM2 is where the two axes intersect. A more detailed list of the blends and their properties can be seen in Table 3.1 and Table 3.2. All percentages are based on volume.

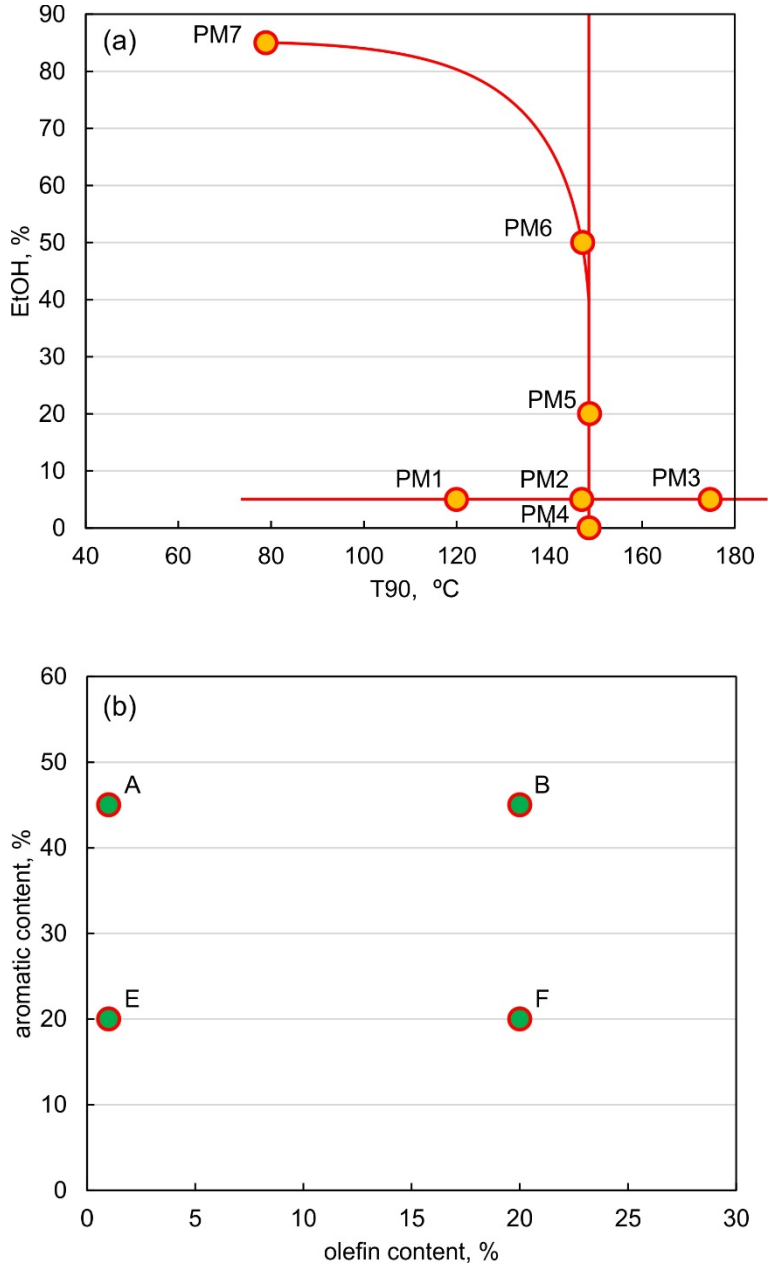


Fig. 3.9 *Physical matrix (a) and chemical matrix (b) comprising 11 blends that were investigated during this study.*

Table 3.1: *Overview of investigated blends of the physical matrix.*

fuel	T90, °C	EtOH, %	lower heating value, MJ/kg	density, g/cm^3
PM1	120.0	5	42.08	0.7252
PM2	147.0	5	41.46	0.7438
PM3	174.7	5	41.34	0.7535
PM4	148.6	5	42.06	0.7395
PM5	148.7	20	39.08	0.7536
PM6	147.2	50	33.16	0.7667
PM7	78.9	85	27.88	0.7750

Table 3.2: *Overview of investigated blends of the chemical matrix.*

fuel	T90, °C	olefin content, %	aromatic content, %	lower heating value, MJ/kg	density, g/cm^3
A	134.1	1	45	40.62	0.7604
B	134.7	20	45	41.42	0.7607
E	138.6	1	20	42.32	0.7580
F	142.6	20	20	42.88	0.7551

Based on the physical properties of blend PM4 (density, lower heating value and rail pressure) the injection pulse width for each blend was calculated. During the experiments of the spray pattern analysis, the rail pressure was set to either 50 bar or 150 bar. From the baseline of the 1.5 ms injection time, in the case of PM4, a ratio factor R was calculated.

$$R = \frac{\rho_{PM4}\sqrt{\frac{p_{PM4}}{\rho_{PM4}}}\,h_{PM4}}{\rho_i\sqrt{\frac{p_i}{\rho_i}}\,h_i} \tag{3.1}$$

where ρ is the density of the fuel, p the injection pressure and h the lower heating value. The index $PM4$ denotes the properties of the reference blend PM4 at 150 bar

injection pressure and the index i the properties of the compared blend at the respective injection pressure.

In order to calculate each injection width, the value of 1.5 ms was multiplied with the calculated ratio. A detailed overview of the injection pulse widths and the corresponding ratios are listed in Table 3.3.

Table 3.3: *Calculated ratio factors and injection pulse widths for all fuel blends based on the reference blend PM4 at 150 bar injection pressure.*

fuel	rail pressure, bar	ratio	injection duration, ms
PM1	50	1.009	1.514
	150	1.7482	2.622
PM2	50	1.012	1.517
	150	1.752	2.628
PM3	50	1.008	1.512
	150	1.746	2.619
PM4	50	-	1.500
	150	1.7458	2.598
PM5	50	1.066	1.599
	150	1.847	2.770
PM6	50	1.246	1.869
	150	2.158	3.236
PM7	50	1.474	2.210
	150	2.552	3.829
A	150	1.021	1.532
B	150	1.001	1.502
E	150	0.982	1.472
F	150	0.971	1.456

Most of the fuel blends have a similar value of the injection width at around 1.5 ms for 150 bar rail pressure and 2.6 ms for 50 bar rail pressure. Mainly, the blends with higher ethanol content, and as such decreasing lower heating value, required significantly longer

injection timings to achieve the same energy content per injection. The largest value was required for blend PM7.

Additionally, the surface tension and viscosity for all liquids were determined and are listed in Table 3.4.

Table 3.4: *Surface tension and viscosity data of the investigated fuel blends.*

fuel	surface tensions, N/m	viscosity, mm^2/s
PM1	0.023	0.594
PM2	0.023	0.596
PM3	0.025	0.578
PM4	0.022	0.596
PM5	0.024	0.691
PM6	0.022	1.003
PM7	0.025	2.300
A	0.024	0.543
B	0.024	0.504
E	0.025	0.652
F	0.023	0.609

Please note that all values and equations presented were provided by Shell Global Solutions for this work.

The experimental work to investigate the influence of different fuel blends and engine conditions on the spay characteristics and wall wetting behaviour was split into three different parts. The first phase was looking at the macroscopic pattern of free and impinging sprays, the second phase investigated spray droplet velocity and size distributions and the third phase the liquid deposits generated by impinging sprays.

The first set of measurements with the purpose of collecting spray pattern data comprised all fuel blends shown in Figure 3.9 and were carried out in the injection chamber with the optical arrangement shown in Figure 3.5. During the experiments the air temperature inside the injection chamber was varied, as well as the injection pressure, plate

temperature, for free and impinging sprays. The complete list of the varied parameters and boundary conditions are listed in Table 3.5.

Table 3.5: *Boundary conditions of the spray pattern analysis experiments.*

vessel temperature, °C	fuel pressure, bar	plate temperature, °C	distance plate injector, mm	fuel blends
80	50	-	no plate	PM1-PM7
80	150	-	no plate	all blends
80	50	ambient	45	PM1-PM7
80	150	ambient	45	all blends
ambient	150	80	45	all blends
ambient	150	200	45	all blends
ambient	150	T90	45	all blends

Based on the results of the high speed imaging data, a selection of operating conditions and fuel blends was made for the following experiments. The spray droplet size and velocity analysis with Phase Doppler was done for blends PM1, PM2, PM3, PM5 and PM7. None of the blends of the chemical matrix were investigated. The injection pressure was fixed at 150 bar and all temperatures were left at ambient conditions. For each of the listed blends, a cross profile was recorded as described in Chapter 3.1.3.

In the last phase, the liquid deposit generated by the impinging spray on a heated rough metal plate was investigated. In the same manner to the Phase Doppler measurements, the injection pressure was fixed at 150 bar. The temperature of the impingement plate set to 120 °C and 160 °C for each blend. The air temperature of the injection chamber was ambient, but monitored and recorded before the measurements, as it was affected by the set plate temperature due to convective heat transfer. The selected fuel blends were PM1, PM2, PM3, PM5, PM6, PM7 of the physical matrix and A and E of the chemical matrix, which is a total of 8 blends. A new measurement technique to quantify the liquid deposit volume was developed for this set of experiments. A detailed description of the measurement principle and how it was established can be found in chapter 4.

3.2 Experimental setup to investigate sprays of fouled injectors

The second project was investigating the impact of combustion product deposits on injector and engine performance. This was a parametric study comparing new, unused injectors with fouled and cleaned-up injectors. In a series of engine tests, a great impact on engine-out emissions was observed depending on the type of fuel that was used. After a treatment with fuel blends containing a specialised detergent these phenomena could be reversed. In this part of the work presented, the effect of injector fouling on the spray pattern was investigated to provide a possible explanation for the observed change in particulate emissions.

3.2.1 Modified setup to record spray patterns of multi hole injectors

The experimental setup used in these experiments was a modified version of the previously introduced rig of Chapter 3.1.1. The main fuel delivery system was kept the same and new injectors were mounted at the top of the injection chamber with the same injector holder and brass cap. Both were compatible with this type of injector. The impingement plate was replaced with a new design to accommodate optical access from underneath. The concept was similar to the original with an aluminium frame that used an inlet port at the rear centre and two outlet ports next to it. These ports were connected to the same heat exchanger. The overall dimensions of the plate were bigger compared to the first one with 150x170 mm^2, in order to be able to increase the field of view of the camera. The inner section of the plate was cut though completely. Both sides were covered by quartz glasses of 150x150 mm^2 with a thickness of 3 mm (UQG Optics). These were glued in with the same silicone adhesive as before (SILCOSET 153, ACC Silicones). This design led to a temperature controlled transparent impingement plate. Optionally, a surface roughened quartz glass plate could be placed on the top side of the plate for potential film thickness measurements. Figure 3.10 shows the new impingement plate design.

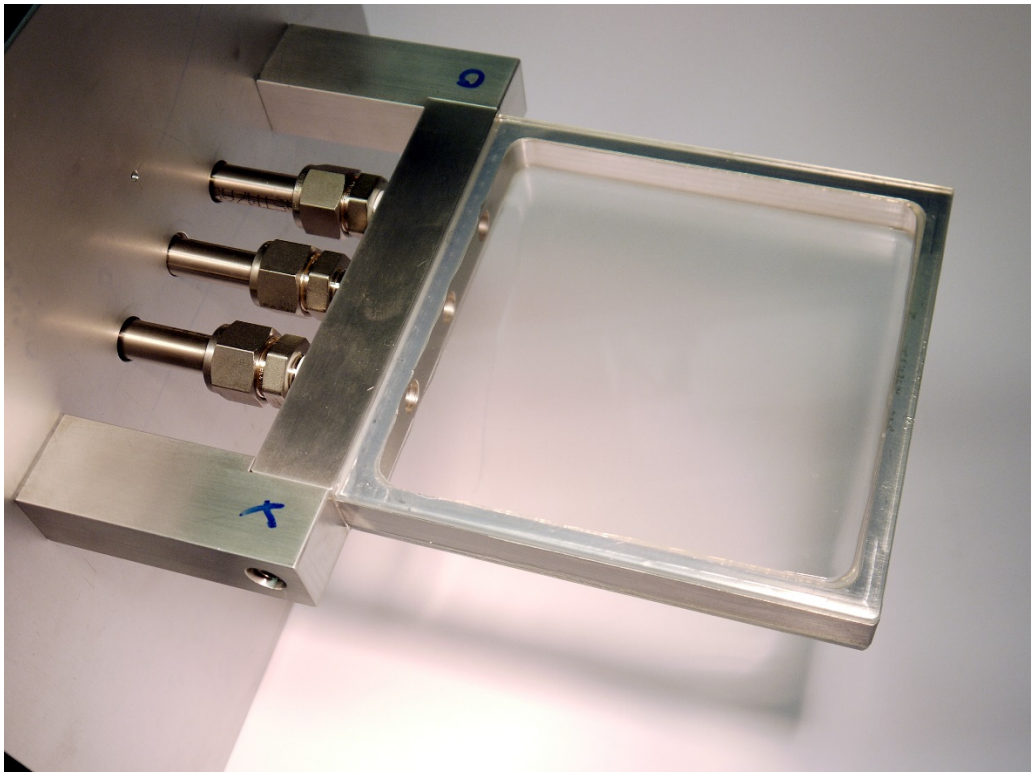


Fig. 3.10 *Redesigned impingement plate that was used for the injector fouling studies.*

The injectors were actuated with a dedicated control unit (GN068-00-230, Control Unit for HDEV 5.2 with PN2130 Driver Stage and Control Unit CJ840, Gantec GmbH), which also acted as a power supply. Additionally, this control device allowed to finely adjusting the injector profile to match the electronic triggering of the engine control unit used in a VW EA211 2.0 litre engine. The injector profile, which was used as a basis can be seen in Figure 3.11. It was provided by IAV Automotive Engineering, who performed tests with the injectors in the VW engines as part of this project.

For all measurements, the total injection time was set to 1.25 ms, which was split into a boosting phase where the needle was lifted, and a holding phase were the needle stayed fully open. All measurements were carried out with the same type of fuel and under the same conditions as will be presented in Chapter 3.2.3.

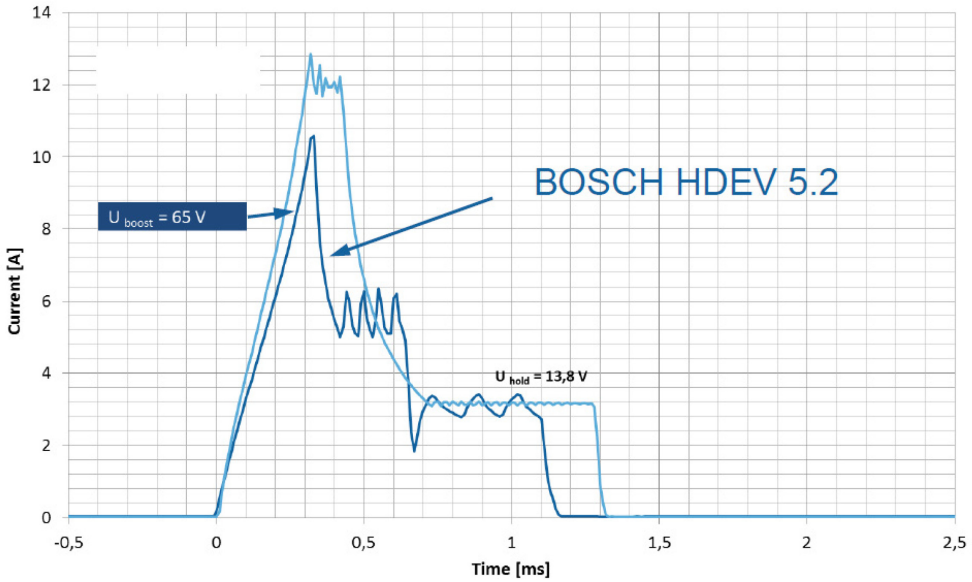


Fig. 3.11 *Electrical injector profile from IAV Automotive Engineering which was used as the basis for the electronics of the experimental setup (dark blue line).*

3.2.2 Optical setup for spray pattern analysis

The spray patterns were recorded with the same camera as before (HighSpeedStar 6 from LaVision GmbH) at a framerate of 20000 fps and an exposure time of 25 µs. The image was cropped to a size of 512x512 pixels^2 to achieve the desired framerate. The camera body was mounted horizontally on a lab jack to be height adjustable. The Nikon 85 mm f/1.4 lens was attached to the body with a 13 mm extension tube. The images were recorded with Davis 7.2 and processed in Matlab 2013b. A calibration of the setup was done with a dot target, which resulted in a magnification of 0.1194 mmpixel^{-1} at the plane of the injector.

The viewing direction of the camera was redirected with a 200x200 mm^2 mirror angled at 45°, which was mounted underneath the impingement plate inside the injection chamber. With this setup the entire jet ensemble generated by the injector was recorded from a bottom up view without any optical distortion. The camera was triggered with the injector electronics. The internal clock of the camera controller was set to a random reset upon receiving the TTL pule of the injector electronics to ensure repeatable synchronisation of the recording setup.

Illumination was done with the same 50 W halogen light source that was used before, which was powered by an AC to DC power supply at 12V (IPS1810H, ISO-TECH). The light source was located at a 90° angle from the camera axis, centred towards to impingement plate and the injector tip. The alignment of the bulb was perpendicular to the plate surface. A schematic illustrating the optical arrangement can be found in Figure 3.12.

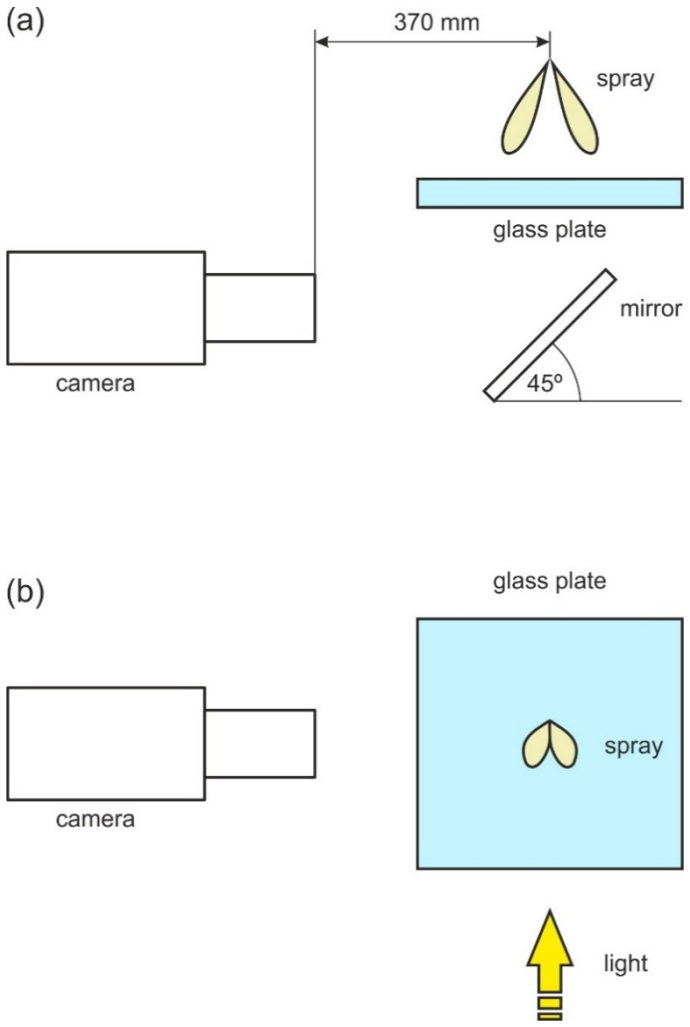


Fig. 3.12 *Optical arrangement of the injector fouling setup as an elevation view (a) and plan view (b).*

3.2.3 Investigated injectors and fouling process

A total of 50 injectors were provided to investigate the effect of fouling on the fuel spray. They were from the same multi-hole type (Bosch HDPE 5.2, VW part number 04E 906 036 E), with 5 holes in total, located around the centre of the injector tip. A photo of one injector with a close-up view of the injector tip and the hole numbering can be seen in Figure 3.13.

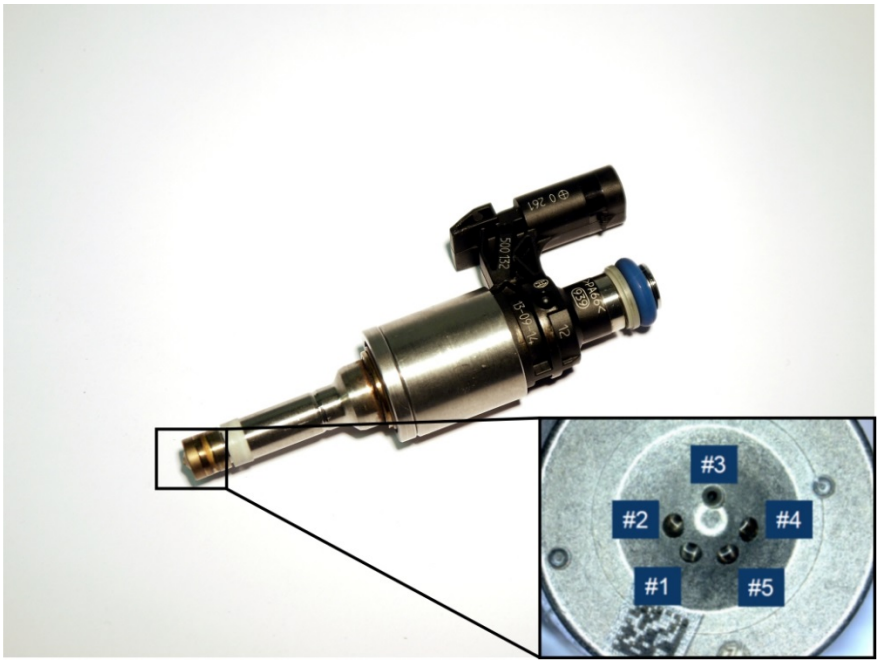


Fig. 3.13 *Multi-hole injector used in the injector fouling study with a close-up view of the injector tip and labels of the holes.*

Injector holes #1 and #2 as well as #4 and #5 create spays that are pointed slightly outwards at an angle. Hole #3 opens almost parallel to the injector axis. All holes had a similar diameter of about 200 µm which resulted in a static flow rate of 6.44 $mgms^{-1}$ for a rail pressure of 100 bar, 7.98 $mgms^{-1}$ for 150 bar and 9.23 $mgms^{-1}$ for 200 bar. These numbers were provided for this work by IAV Automotive Engineering. Interpolating these values for the afore mentioned 160 bar rail pressure and 1.25 ms injection width used in the experiments resulted in a fuel mass of 10.29 mg per injection.

For the dirty-up process 48 out of the 50 injectors were used in VW EA 211 four cylinder engines. A set of four injectors was exposed to one of the five types of E10 fuel blends (Fuel A, Fuel B, Fuel C, Fuel D, 2xFuel E) for a duration of 5 hours. After this period, all injectors were removed and replaced by a new set which were exposed to the same dirty-up cycle. Once the second set was completed, the fuel was switched to blend C in all engines and to blend F in the case of one set previously used with Fuel E. The second phase was run for an additional nine houses. Blend C was containing the detergent to counteract the fouling process. This resulted in a set of four dirty injectors that were used only in the dirty-up cycle and a set of corresponding injectors that were initially dirty but subsequently cleaned with the detergent fuel. Additionally, one set that was not treated with Fuel C at all, but used with Fuel E in the dirty-up cycle and Fuel F in the clean-up cycle. During all runs, the engine out emissions and fuel trim (*i.e.* the fuel to air ratio, managed by the engine control unit) were monitored. Two of the initial 50 injectors were not used during the engine experiments and functioned as the reference points for the spray pattern analysis. A complete overview of the injectors and the cycles that were performed are listed in Table 3.6. Please note that the injector set in bold was not treated with Fuel C in the clean-up cycle but with Fuel F instead.

After the engine cycles, all injectors underwent an analysis of the fouling with microscopic imaging. Based on these images and combined with the emissions data, one injector from the dirty-up cycle 1 was selected for further investigations. Also, the corresponding injector used in the same cylinder was investigated from the cleaning cycle. The findings were compared to the two unused injectors that functioned as the reference.

Each injector was mounted in the injection chamber and was operated with a rail pressure of 160 bar, which corresponded to the pressure used in the fuel system of the test engines.

Table 3.6: *Available injectors and injector dirt-up and cleaning cycles, which were performed by IAV Automotive Engineering.*

run	Fuel A	Fuel B	Fuel C	Fuel D	Fuel E	Fuel E
dirty-up 1 with each fuel	cyl 1	cyl 1	cyl 1	cyl 1	cyl 1	cyl 1
	cyl 2	cyl 2	cyl 2	cyl 2	cyl 2	cyl 2
	cyl 3	cyl 3	cyl 3	cyl 3	cyl 3	cyl 3
	cyl 4	cyl 4	cyl 4	cyl 4	cyl 4	cyl 4
dirty-up 2 with each fuel	cyl 1	cyl 1	cyl 1	cyl 1	cyl 1	cyl 1
	cyl 2	cyl 2	cyl 2	cyl 2	cyl 2	cyl 2
	cyl 3	cyl 3	cyl 3	cyl 3	cyl 3	cyl 3
	cyl 4	cyl 4	cyl 4	cyl 4	cyl 4	cyl 4
cleaning, switch to Fuel C from dirty-up 2	cyl 1	cyl 1	cyl 1	cyl 1	cyl 1	**cyl 1, Fuel F**
	cyl 2	cyl 2	cyl 2	cyl 2	cyl 2	**cyl 1, Fuel F**
	cyl 3	cyl 3	cyl 3	cyl 3	cyl 3	**cyl 1, Fuel F**
	cyl 4	cyl 4	cyl 4	cyl 4	cyl 4	**cyl 1, Fuel F**

With the experimental setup presented, that was specifically designed for the tasks that were investigated in this research it was possible to apply a number of measurement techniques and generate a large amount of data that forms the foundation of ideas and suggestions to further improve gasoline direct engine designs and operating parameters. The setup also allowed for the development of a new measurement concept to better investigate the pressing issue of wall wetting, under certain engine-like conditions and without the need of proxies. The data and results obtained with the rig and the methods will be presented and discussed in the following chapters.

Chapter 4

Development of a measurement technique to quantify liquid deposits on a rough metal surface

In order to obtain the liquid film thickness measurements, an important issue had to be overcome. This was the inability to use one fluorescent additive that can be dissolved in every fuel. This means that Laser Induced Fluorescence technique for liquid film thickness could not be used. Therefore, a novel technique was developed to investigate liquid deposits created by impinging sprays, similar to those found in direct injection engines. The new technique is similar to the Refractive Index Matching (RIM) technique presented in chapter 2.4. However, it relies on the change of the light scattering behaviour of a rough solid surface, once liquid is applied. In this case, however, a treated metal plate was used instead of a glass piston. With the use of a rough metal surface, it was possible to recreate the conditions found inside the cylinder of an engine more closely compared to other techniques. The temperature of the metal surface was adjustable, which allowed insight into the effect of the surface temperature on the liquid deposit.

Based on the measurement principle a calibration method was developed that allowed for the generation of stable thin liquid film of a defined thickness. At this stage a

suitable surface roughness of the plate was also selected from a variety of plates that were tested. In conjunction with the calibration method a post processing procedure was established that yielded the data points linking the film thickness and the change of the scattering behaviour. Also, this post processing was extended for the actual measurements. After that, the method was verified with a comparison to RIM and tested during the investigation of single component fuels. All steps of the technique development will be presented here.

4.1 Principle of the measurement technique

The basic principle of the technique for the measurement of liquid film thickness is the change of scattering patterns of a roughened surface exposed to liquid deposit of varying thickness. The fundamental mechanism underlying this technique is shown in Figure 4.1.

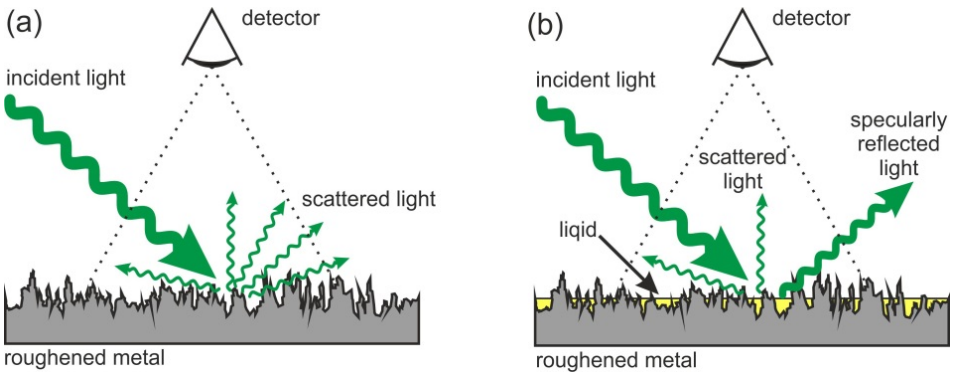


Fig. 4.1 *Physical principle of the measurement technique. The scattering behaviour of a rough metal surface (a) is changed once liquid is present (b). The deposit gradually reduces the apparent surface roughness and causes incident light to be reflected specularly.*

In the case of a homogeneously roughened metal surface incident light illuminating the plate at a defined angle is scattered diffusely in all directions. Part of the light is scattered

towards the detector, which is located well outside the specular reflection angle. When a liquid is deposited, a partially smooth surface is created as the liquid is reducing the asperity. For this reason the part of the incident light is reflected secularly and the amount of the light that is scattered towards the detector is reduced. The actual amount of specular reflection depends on the extent of the proportion of the smooth part of the surface, which increases with the amount of liquid on the plate until the thickness of the liquid layer is larger than the roughness. Selecting the angle of the incident light and the angle of detection relative to the metal plate carefully, it is possible to correlate this intensity change $R(x,y)$ to the actual thickness of the liquid deposit:

$$R(x,y) = 1 - \frac{i_{liq}(x,y)}{i_0(x,y)} \tag{4.1}$$

with

$$i_0(x,y), i_{liq}(x,y) = f(d(x,y)) \tag{4.2}$$

where i_0 is the local intensity without any liquid present, i_{liq} the respective intensity with a liquid film covering the surface, d the thickness of the film and x and y are the local coordinates.

4.2 Calibration method and data processing

Following the approach of Drake *et al.* [9], Yang *et al.* [172] and Maligne *et al.* [173], a calibration method was developed. In their case a micro syringe or microliter pipette was used to apply known volumes of liquid to the glass surface in their experimental setup, while recording images with a CCD camera. Due to capillary forces generated by the asperities the liquid spread immediately after getting in contact with the surface [172]. Knowing the optical magnification, it was possible to calculate the area of the liquid film, and knowing the volume an area averaged film thickness could be derived. In this way it

was possible to correlate the captured intensity ratio (cf. Equation 4.1) with the film thickness. By varying the amount of transferred liquid they were able to generate liquid films of different thicknesses, and as such different corresponding intensity ratios. From that, a calibration function was established.

Based on this procedure a calibration methodology was developed. As a calibration liquid dodecane was chosen, because of its low volatility, while being from same family of Hydrocarbons as octane, the major component of gasoline. Furthermore, the wettability on metal surfaces proved to be very good. Using this liquid it was possible to generate very thin films while minimising systematic errors caused by evaporation. In order to verify this, 1 µl of dodecane was dropped on the rough metal plate (cf. chapter 3.1.1), which was placed on a micro balance (R200D, Sartorius Research) at room temperature. Over the course of 10 minutes the change in mass was less than .5 %. Based on this, the amount of dodecane was considered to be stable for the duration of each calibration measurement. The liquid was applied with the help of a microliter pipette (Rainin Classic PR2 0.1-2µL, Anachem Ltd). In order to limit the area on the metal plate the liquid can cover, a circular paraffin boundary, approximately 15 mm in diameter was created with a paraffin pen (Marker PAP PEN Immunostaining, VWR). Thus, it was possible to not only generate very thin films but also create thicknesses significantly larger than 10 µm. As such, it was possible to not only generate very thin films, but also create homogeneous thicknesses significantly larger than for example 10 µm. An important advantage of the technique is that the calibration is independent of the liquid that is used. Therefore, the calibration with dodecane is valid for all liquids with a similar refractive index, which is the main factor that determines the observed change in scattering behaviour [73]. This is the case for the fuels investigated here.

In order to obtain a calibration function based on Equation 4.1, known volumes of dodecane were deposited on the roughened metal plate while recording images. The recorded images at the beginning with no liquid on the surface were used to calculate the initial intensity i_0 . Once the liquid film was spread evenly across the surface, series of images were obtained from which the intensity i_{liq} could be calculated. In both cases a mean image based on five frames was used. The standard deviation of these images was

below 2%. By repeating these steps with different amounts of liquid, it was possible to derive the relation between liquid film thickness d and the change of intensity ratio R.

After recording the images with the CCD camera, several processing steps were performed. These are shown in Figure 4.2. Both the reference image without liquid (Figure 4.2a) and the image with the liquid film (Figure 4.2b) were corrected for optical distortion using the dewarping feature provided by Davis software (results in Figure 4.2c and Figure 4.2d). This way, it was also possible to determine the magnification scale of the pixels. The two dewarped images essentially correspond to i_0 and i_{liq} of the intensity ratio equation. Therefore, it was possible to calculate a 2D intensity ratio based on Equation 4.1, when dividing each pixel of the two images by one another and subtracting the result from the value one. This step yielded Figure 4.2e, where the region, which was not covered by the liquid, had a value of approximately zero and appeared black and a region covered by the liquid with values between one and zero, corresponding to a certain film thickness. The next set of processing steps was aiming to detect the area that was covered by the liquid and its boundaries. In order to increase the contrast ratio between these two areas, a non-linear diffusion filter (NLD) was applied, following the guidelines from Weickert *et al.* [198], [199], and also a 3x3 median filter (Figure 4.2f) to reduce the noise introduced by the NLD filter. The result can be seen in Figure 4.2g where the area covered by liquid shows very high intensities while maintaining the initial boundary between liquid and non-liquid. As a last step, a modified binarisation algorithm based on an in-house code was applied [200]. An individual threshold was determined, based on a pixel by pixel intensity analysis of the image. Pixels with values larger than this threshold became unity, pixels with smaller values were set to zero. The algorithm also used a clean-up routine to remove the small black islands created in the previous steps. With the information on the physical extent of the liquid film contained in picture Figure 4.2h, the boundary of the liquid film could be calculated. Using this information, an area averaged intensity ratio was derived from Figure 4.2c. Knowing the volume that was deposited on the metal plate, the calculated intensity ratio could be linked to an area averaged liquid film thickness.

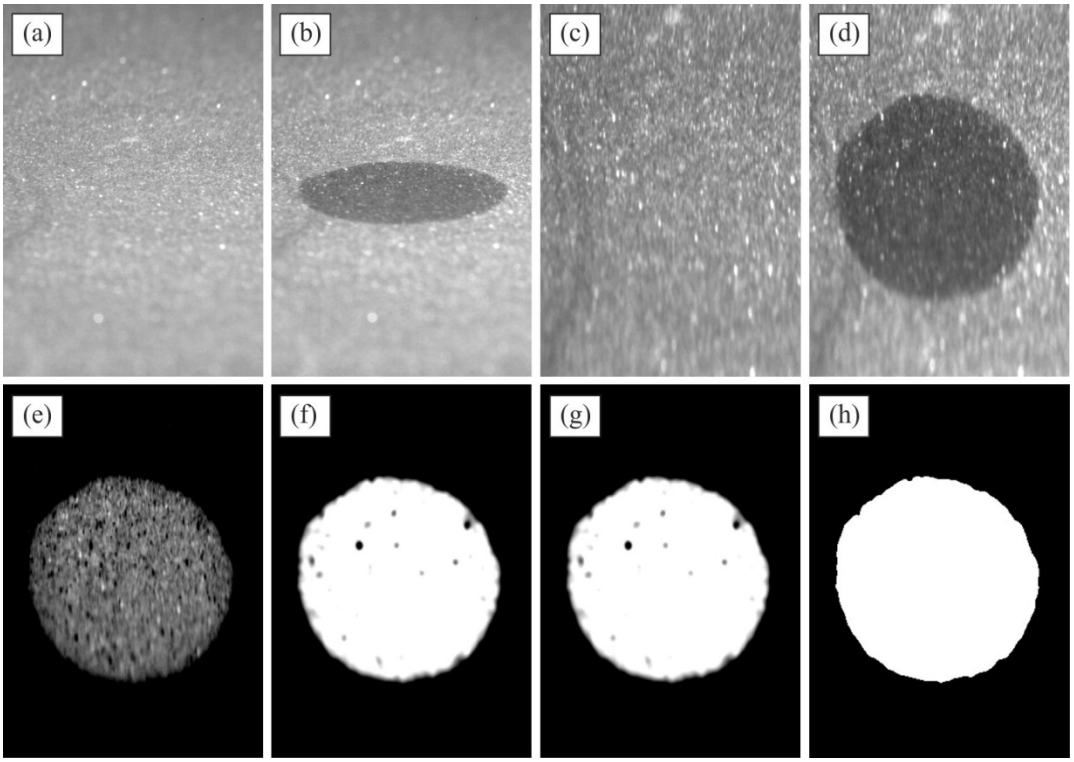


Fig. 4.2 *Image processing to derive the calibration function.*

The entire process was repeated many times with different volumes of liquid. As a result a correlation between the film thickness and the intensity ratio was derived and is shown in Figure 4.3.

The calibration correlation shown here was established for the exact setup described in Chapter 3.1.2. Because of the nature of this technique it shall be noted that this correlation is valid for this particular setup only. Any change in the experiment would require a recalibration of the system.

The calibration function was derived from a least squares fit method using a double exponential function in the form of

$$y = a \cdot e^{bx} + c \cdot e^{dx} + e \tag{3}$$

which was applied with the statistical toolbox of MatLab 2013b. The dashed lines indicate an uncertainty of 1.25 µm in film thickness, which corresponds to a volume of approximately 0.2 µl (10% of the pipette maximum) of liquid. With this approximation it

can be seen that the sensitivity of the method varies notably with the thickness of the liquid film. Basically, the plot can be split into two regions. Between zero and about 0.4 intensity ratio there is a high sensitivity towards changes in the film thickness. For intensity ratio values larger than 0.5 the calibration becomes very insensitive, which is why thicknesses larger than 0.25 mm cannot be captured reliably with this setup. A change in the optical arrangement or a different roughened metal plate would be necessary to further extend the measurement range towards larger values.

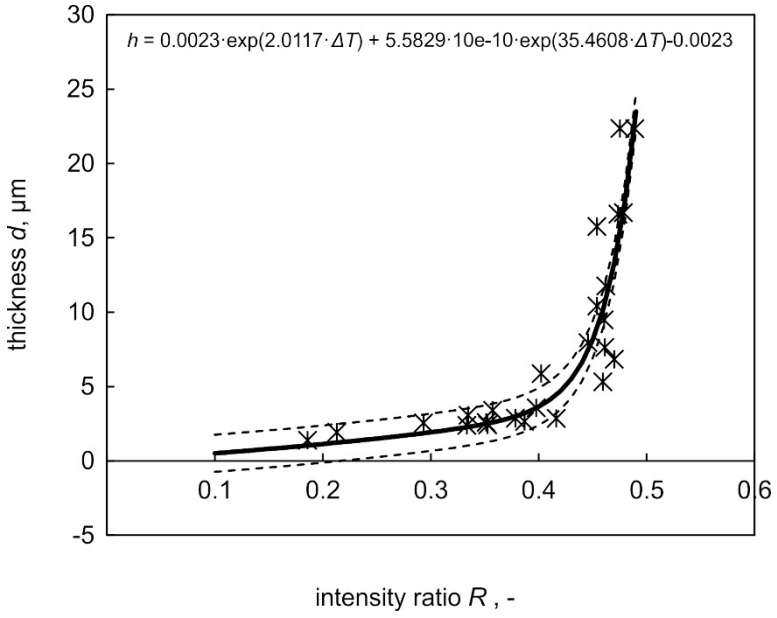


Fig. 4.3 *Calibration correlation used for the film thickness experiments. Points (∗) obtained during the calibration procedure are shown with a double exponential fit (—), error approximation (- - -) and the calibration equation.*

The data processing used for the actual measurements used similar steps to the calibration method. The injector was triggered by the camera and, because of the delay between triggering the injector and the spray impinging on the plate, a series of images without a liquid film were recorded. Once the injection process was completed the liquid film became visible in the recordings. The first step was correct the optical distortion in all images. Frame number 2 of each recording was used as the reference image. An example

of the reference image and a later frame of the same time series with a liquid deposit can be seen in Figure 4.4.

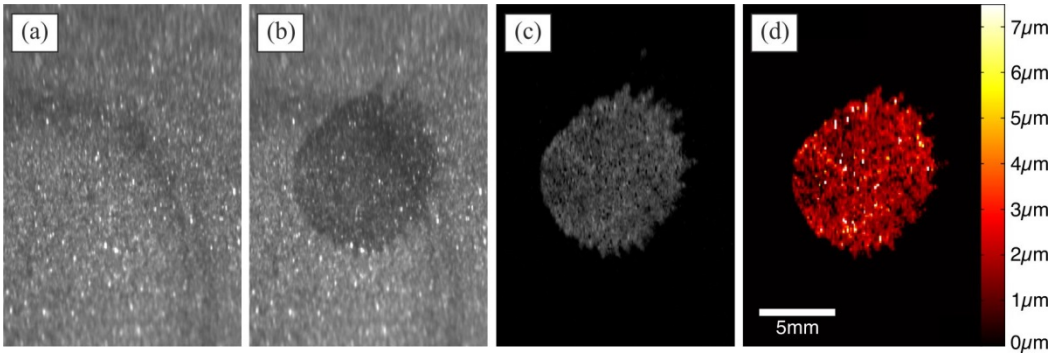


Fig. 4.4 *Example images showing the processing used to analyse liquid films: dewarped images before (a) and after (b) the impingement of the spray, the calculated local intensity ratio with values between zero and one (c) and the actual 2D film thickness calculated with the calibration function (d).*

By dividing the intensity field values in each of the two dewarped images (Figure 4.4a and Figure 4.4b) by each other, the local intensity ratio is calculated (Figure 4.4c) and with the use of the calibration function the final instantaneous 2D local film thickness is computed (Figure 4.4d). Extracted frames of a complete time series showing the raw image and the 2D final film thickness can be seen in Figure 4.5.

Please note that this is a line of sight measurement technique. Because of this it is not possible to reliably detect the liquid film during the impingement as the spray impedes direct view of the liquid film. Once the injection is complete and the spray itself is gone reliable data of the wall deposit can be obtained.

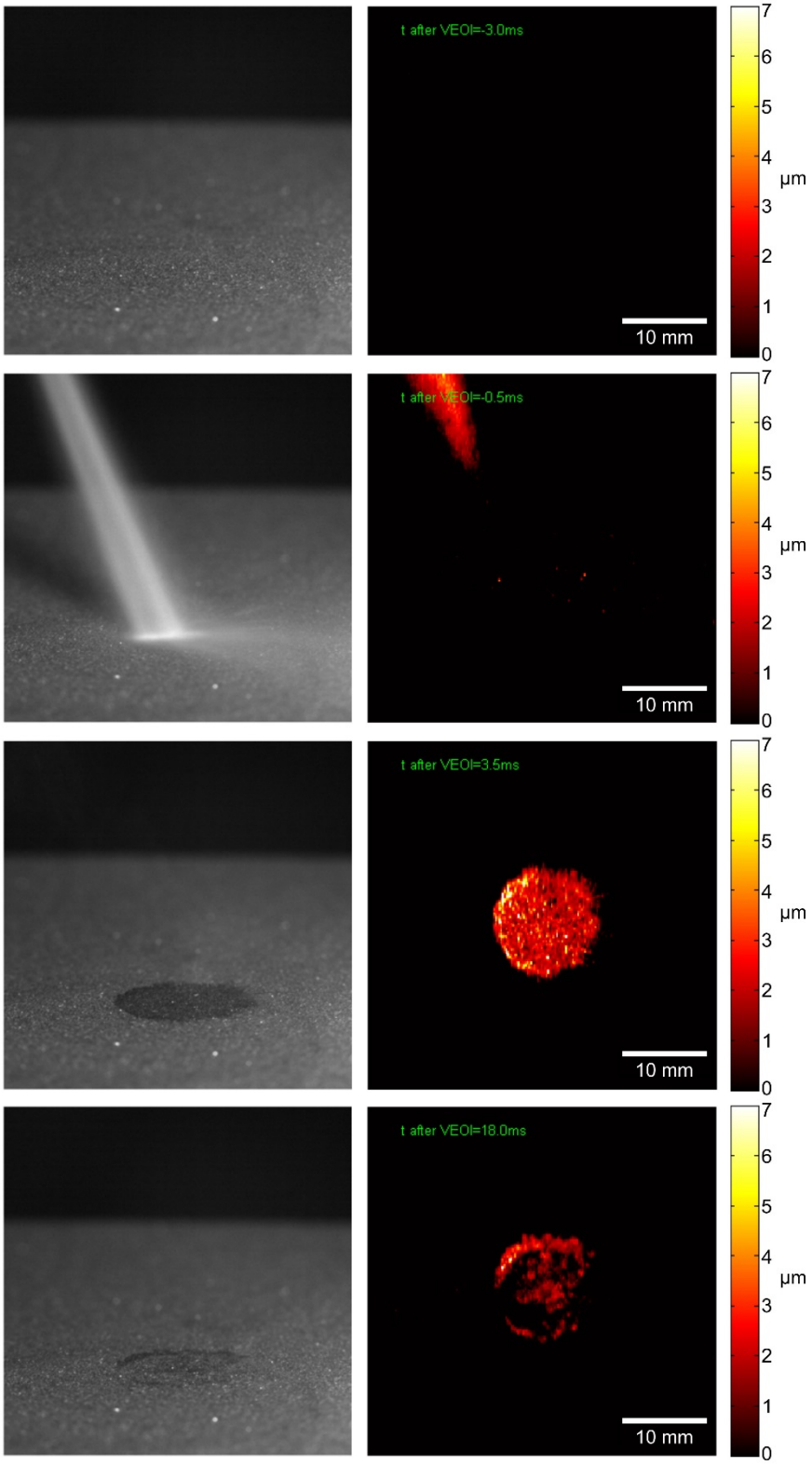


Fig. 4.5 *Example of a time series of one recorded injection with the raw footage on the left-hand side and the processed image showing the 2D local film thickness on the right-hand side.*

4.3 Comparison to the Refractive Index Matching method

In order to verify the assumptions made during the development of the measurement technique and the proposed intensity ratio, tests were performed where a rough metal plate is compared to a rough glass plate at ambient temperature, following the approach of the Refractive Index Matching method presented by Drake *et al.* [75]. For this purpose, both the metal and the glass plates were installed in the fuel injection chamber. The angles of the light source and the camera were kept constant during the comparison experiment. The injected fuel was a regular unleaded gasoline blend (RON95, Shell Global Solutions) in both cases. The injection was triggered by the initiation of recording by the camera, making sure to record the entire process, which included the surface before and after impingement. As mentioned before, the nature of these techniques is that they are based on line of sight recordings. For this reason it was not possible to record reliable data during the actual injection process, but only after the injection process was over and the actual spray had disappeared.

From the recorded images, the average normalised intensity i_{liq}/i_0 was calculated for an extracted area of 5x5 mm^2 at the centre of the liquid film. The selected area of each frame was divided by the exact same area of the reference frame without liquid. The values were then used to create a time signal for both plates which are presented in Figure 4.6.
The overall shape of both curves looks is with distinct changes of the evaporation rate resulting in changing slopes of the curves. Mainly the sensitivity (*i.e.* the change of the scattered light intensity) is different for the two plates, which causes an overall difference in the magnitude of the intensity values.

Before the fuel injection, the normalised intensities equal one in both cases. The impingement of the spray results in the formation of a liquid deposit which changes the scattering behaviour. Consequently, the values abruptly decrease to a minimum. Over time, the values gradually increase again and converge with the intensity ratios recorded before the injection, as the liquid is evaporating. Please note, that those images were not corrected

for noise which explains why the values of the normalised intensity do not become unity again.

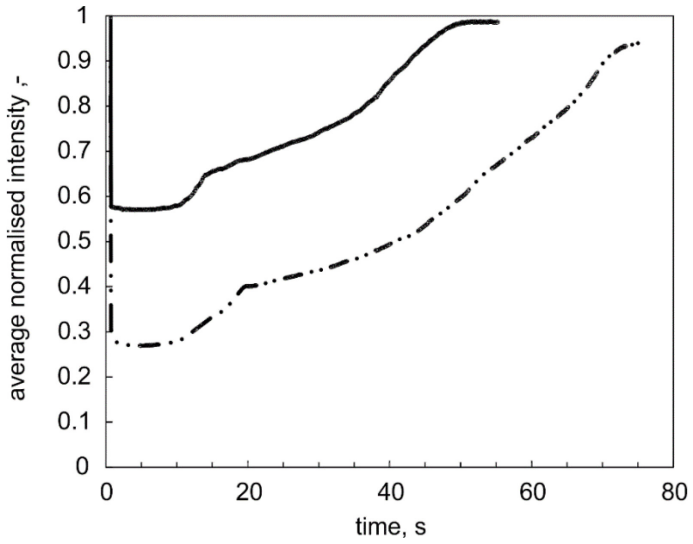


Fig. 4.6 *Comparison of the area averaged normalised intensity of a roughened metal (—) and a roughened glass plate (– ..).*

The curves of both materials are composed of segments with different slopes, which follow the same patterns. This is most likely caused by the multi-component nature of the used gasoline blend. It is fair to assume that the lighter components evaporate first with the heavier components remaining on the plate for a longer period. Additionally, this also shows that the use of metal plate does not alter the general evaporation behaviour of multi-component fuels.

However, it is noteworthy, that the evaporation process is significantly quicker with the metal plate, probably caused by the larger thermal conductivity of the material. The smallest value of the normalised intensity for the metal plate in this test is approximately twice as large as that for the glass plate (appr. 0.6 for metal and 0.3 for glass). This could be explained by the fact that metal is a non-transparent material, unlike glass, and as such the effect of light refraction is missing. Because of that, the entirety of the incident light gets reflected and scattered.

Despite the described differences, the data obtained in this chapter provides good evidence that it is possible to correlate the described intensity change to the actual film thickness of the deposit, similar to the Refractive Index Matching method.

4.4 Measurement uncertainty

As mentioned briefly during the description of the setup in chapter 3.1.2 the optical alignment angles of the camera and the light source relative to the impingement plate play a significant factor for the measurement technique. During the development of the technique it was found that a shallow angle leads to an oversensitive setup, where even very thin liquid films already lead to intensity ratios larger than 0.5. This also makes the technique very insensitive towards changes of thicker liquid films. At the other end of the spectrum are angles that cause direct reflections of the light source towards the camera. These need to be avoided completely. This issue might not be evident without a liquid film on the rough surface because the incident light gets scattered evenly and the surface appears grey. Once a deposit is partially smoothing the rough surface, regions of very high intensity are recorded. The intensity values associated with these areas are larger than those without a liquid which would result in a negative intensity ratio and makes the measurements invalid. The angles that were chosen for the present experimental setup were mainly determined by the compromise between sensitivity, measurement range and optical access of the setup. By using a different light source and recording optics (*e.g.* endoscope or fibre optics) it would be possible to extend the range of the alignment angles and thus broaden the applicability of the setup, especially in optical engines with limited access.

Other factors that contribute to measurement uncertainty can be split into two categories, errors that affect the calibration procedure and errors that occur during measurements. When calibrating the setup, the largest uncertainty comes from applying defined volumes of liquid on the plate with the microliter pipette. As shown in the calibration plot (cf. Figure 4.3) for the used setup the intensity ratio is quite sensitive

towards errors in the transferred volume of the liquid in the region between 0.1 and 0.4. For intensity ratios that are larger than 0.4, the error approximation is converging with the calibration line as the relationship becomes more insensitive with changes in the film thickness. The approximation of a constant error of 0.2 µl as shown in the figure was used to illustrate the two sensitivity regions of the calibration and is overestimating the error for smaller volumes that were applied to generate calibration thicknesses. An error of 10% relative to the actually applied liquid volume results in approximately 10% error of the film thickness for a given area. With that the intensity ratio is fluctuating by approximately ±0.03 in this range.

The image processing steps necessary to detect the boundaries of the liquid film and to determine the film area can induce a minor shift of the film front by two pixels in the worst case. For the given magnification of the setup this corresponds to a length of 0.116 mm. In relation to the circular area with a diameter of approximately 15 mm that was used during the calibration this equates to an error of less than 1.6%. Because of the small magnitude, this error will not be considered in the discussion of the results obtained with this method.

Noise introduced by the DC power supply will also be neglected for the discussion. The power supply was specified for fluctuations of 1 mVrms at 12V operating voltage. The cameras were left to warm up for at least 30 minutes until a stable operating temperature of the internal cooling system was achieved. In this way, the drift in the sensitivity of the chips during measurement was minimized. In addition, the noise calibration feature provided in the recording software was used to subtract the noise of the dark image, before each measurement. With this, the noise generated by the recording electronics was minimized and kept constant for all experiments.

During measurements the main uncertainty was introduced through fluctuations from injection to injection. It was observed, that the values of the maximum deposit volume measured could fluctuate by up to ±10%. To ensure reasonable significance of the data, measurements were repeated five times and the mean values as well as the standard deviations were calculated. A more detailed discussion of this matter will be provided in the following chapter.

4.5 Application of the technique to investigate single component fuels

In order to verify the concept of the described technique and to demonstrate potential applications, a selection of single component fuels with known physical properties were chosen and tested in the fuel injection chamber. The fuels were selected in a way that the effect of increasing boiling temperature of the liquid on the extent of the liquid deposit could be investigated. At the same, time potential gasoline supplements or substitutes were being investigated. With this in mind, the results could provide information on how to further minimise wall wetting and as such the formation of particulate emissions in direct injection engines.

The first set of single component fuels consisted of the linear alkanes hexane, heptane and octane (technical grade, VWR International UK). The properties of these chemicals are well defined and share some similarities with the hydrocarbon components found in regular gasoline blends. One feature of the three substances is that they all share similar physical properties. Quantities such as viscosity, surface tension are very comparable and density, specific heat capacity and specific heat of evaporation are virtually the same.

As a second set of single component fuels ethanol, propanol and butanol, was chosen, which are single linear alcohols (technical grade, VWR International UK). Unlike the alkanes, these chemicals show more differences in their physical properties. This includes viscosity, heat capacity and heat of evaporation. Exceptions are density and surface tension, which do not change significantly, similar to the investigated alkanes. An overview of the mentioned physical properties of all substances tested can be seen in Table 4.1.

From this overview it is evident, that in the case of the alkanes, only the boiling temperature varies significantly between the substances. From hexane to octane the temperature increases by 57 °C. Because of this isolated dominant change of the boiling temperature within this group of liquids, experiments will mainly show the influence of the boiling temperature of a liquid on the liquid deposits of impinging sprays. The group of

alcohols cover a smaller range of 37 °C with their boiling temperature, but show a comparable increase with increasing chain length of the molecule. A comparison of these fuels with the alkanes shall provide more insight on how liquids with different properties aside from the boiling temperature behave when compared to similar liquid, which show differences in only one physical property.

Table 4.1: *Physical properties of the liquids used to test the measurement technique* [201].

fuel	boiling temperature, °C	density, g/cm^3	viscosity, m Pa s	surface tension, N/m	heat capacity, J/(K kg)	heat of evaporation kJ/kg
hexane	69	0.659	0.326	0.018	2293.69	334.78
heptane	98	0.684	0.386	0.020	2241.87	364.26
octane	126	0.703	0.542	0.022	2238.32	362.01
ethanol	78	0.789	1.144	0.022	2420.96	837.02
propanol	97	0.803	1.938	0.024	2406.19	689.57
butanol	117	0.810	2.544	0.024	2386.08	584.04

In the first set of experiments, the plate temperature was set to a constant 100 °C for all fuels presented. The injection duration was kept constant at 1.50 ms with a rail pressure of 150 bar and the air temperature inside the test chamber was ambient. Please note that the temperature above the plate was depending on the set plate temperature as it was heating up the surrounding air. A total of five measurements were performed for each type of fuel. From the recorded high speed images, an instantaneous cumulative liquid volume on the plate was calculated and from that a volume over time was extracted as described in Chapter 4.2.This data can be seen in Figure 4.7 in the case of the three alkanes and in Figure 4.8 for the alcohols. The x-axis scale corresponds to the time after triggering the injector.

In the case of the alkanes it is evident that with increasing boiling temperature, the volume of the liquid deposit increases significantly (Figure 4.7a). Hexane, with the lowest

boiling temperature of the three liquids, generates almost no liquid film compared to the other two. The deposit produced by the octane spray shows about twice the value for the initial volume compared to hexane. In addition, it also takes about an order of magnitude longer to evaporate compared to heptane. For heptane, the time scale is also relatively small and the deposit was completely evaporated within a 40 ms. These observations illustrate clearly how the boiling temperature in relation to the wall temperature affects the liquid deposit. In the case of hexane, with a boiling temperature that is much lower than the 100 °C, the spay deposit is almost non-existent after the end of injection. If the boiling temperature increases and is much closer to the surface temperature the deposit volume also increases. Once this property exceeds the wall temperature, wall wetting becomes drastically more pronounced as this is the case for octane. Similar observation of the wall temperature in relation to the boiling temperature and how it affects liquid films were previously mentioned [65], [87]. In general, for single component liquids the evaporation rate increases with increasing wall temperature with its maximum at its boiling temperature and slightly above. Once the boiling temperature is exceeded by several tens of degrees the evaporation rate decreases again because of the Leidenfrost effect shielding the liquid from the plate with a vapour layer. For single component fuels this is to be expected between 50 and 80 °C above the boiling temperature to have an effect, which is not the case for hexane [114]. This means that the evaporation rate for hexane is still to be expected to be very large for a plate temperature of 100 °C. In the case of heptane the boiling temperature is very slightly exceeded which means that the evaporation rate should be a bit under its maximum. Octane has a boiling temperature which is 26 °C higher than the surface, which moves it away from the potential maximum evaporation rate. This explains both the initial volume of the deposit and the long evaporation time of this fuel. The trends in the deposit volume are also reflected in the observed film thicknesses which were around 2 µm in the case of hexane, 8 µm for heptane and 12 µm for octane.

Looking at the individual plots of the liquid deposit volume (Figure 4.7b, c and d) it can be seen that the standard deviation shows a similar characteristic for the alkanes. Only in the case of hexane do the fluctuations between the recordings seem to be less

pronounced. Overall it can also be seen that the standard deviation becomes smaller as the liquid film evaporates completely and converges with the mean value.

Similar observations can also be made in the case of the three linear alcohols. Looking solely at the boiling temperature as the most influential property, the order of the liquid fuel deposit volume follows the same trend as for the alkanes. Ethanol, with the smallest boiling temperature, produces the smallest deposit, followed by propanol and butanol. The latter takes almost an order of magnitude longer to evaporate compared to propanol, which is similar to the relative behaviour observed with the alkanes. In addition, the observed film thicknesses were of the same magnitude as the ones for the alkanes and followed the same trend in relation to the boiling temperature. Focusing on the latter relative to the plate temperature, similar conclusions as with the alkanes can be drawn. Once the boiling temperature of a liquid is exceeded by several tens of degrees, the evaporation rate reaches a maximum, which should be the case for ethanol. If the boiling temperature is larger than the wall temperature the rate decreases significantly. Such is the case for butanol. Propanol, with a boiling temperature in-between the other two also shows a deposit volume which is intermediate.

The separate plots of each alcohol (Figure 4.8b,c and d) show that the standard deviation increases from ethanol to propanol and butanol. Fluctuations between the ethanol injections are very small and the standard deviation follows the mean value very closely. The other two fuels have more variances between injections, especially at the beginning of the recording in the region close to the initial deposit volume. Over time, the standard deviation lines are also converging with the mean, similar to the alkanes.

When comparing the two plots of Figure 4.7 and Figure 4.8, some differences are apparent. Most notably, the time scale for all alcohols seems to be longer compared to the respective alkane. Overall, there is a factor of two between them. In the case of ethanol this might be explained because of the higher boiling temperature by almost ten degrees. But in the case of butanol this is not valid as its boiling temperature is in fact smaller than of octane. The initial volume is also much larger for ethanol than for hexane. Propanol and heptane produce a very comparable initial volume, although the evaporation of the former takes twice as long. Looking at the physical properties it is apparent that the three alcohols

have the larger heat of evaporation. However, the fuel with the smallest heat of evaporation of the alcohols, butanol, takes the longest to evaporate of all tested fuels. This could be a first indication that the different behaviour alcohols vs. alkanes might not only be connected to the heat of evaporation, but be in fact more complex than that.

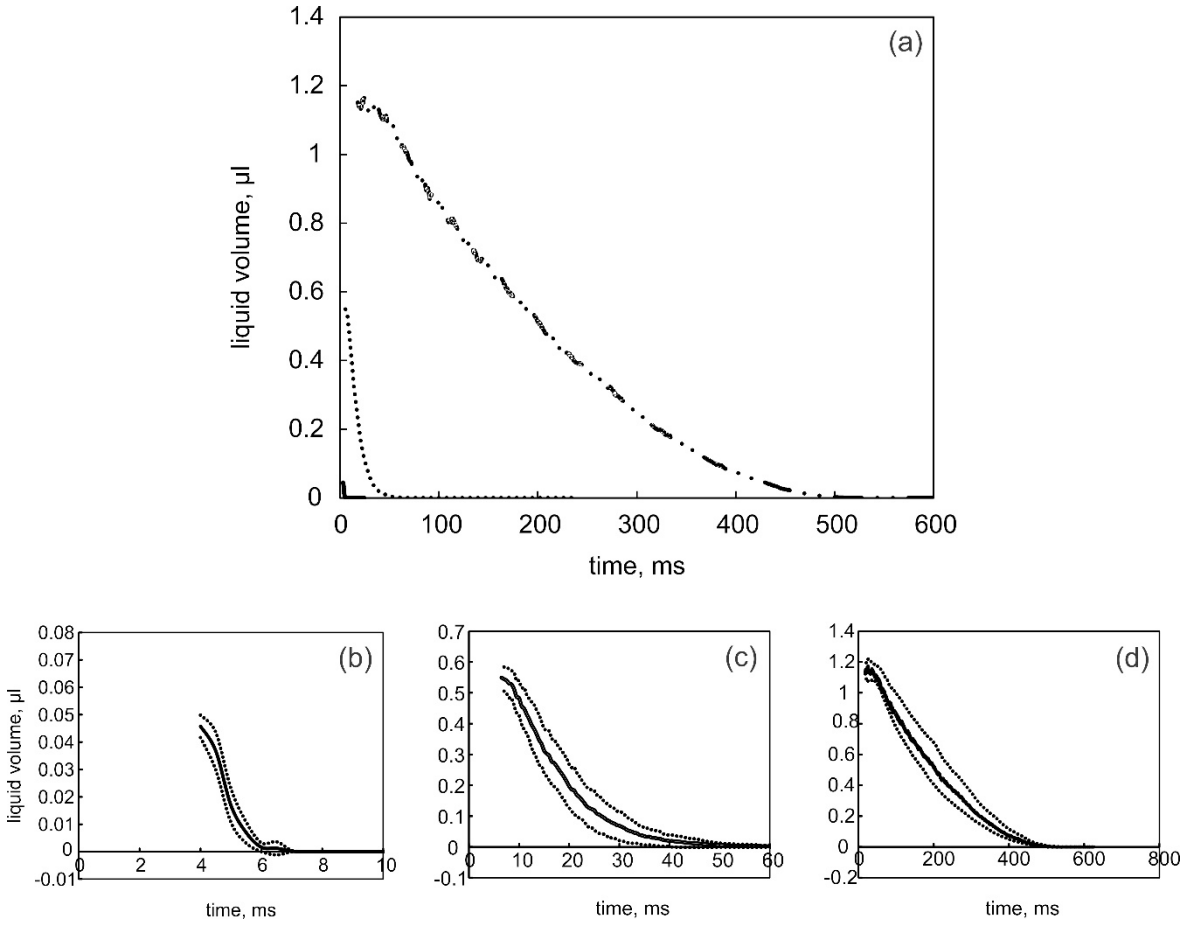


Fig. 4.7 *Mean liquid volume of wall deposit of hexane (—), heptane (.....) and octane (– ..) fuels as a function of time after triggering the injector and a plate temperature of 100°C (a) and the individual mean time signal (—) for hexane (b), heptane (c) and octane (d) including the respective standard deviation (.....).*

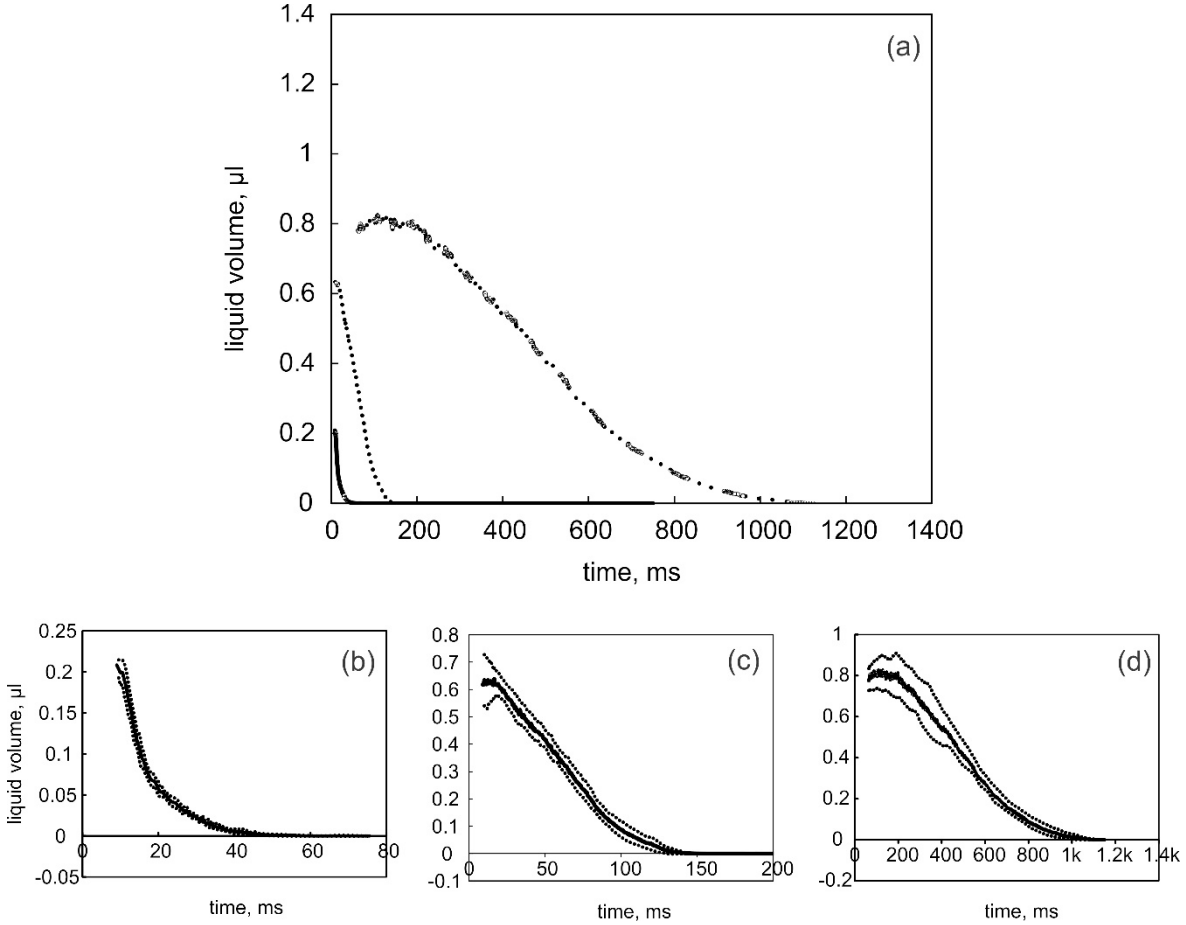


Fig. 4.8 *Mean liquid volume of wall deposit of ethanol (—), propanol (.....) and butanol (– ..) fuels as a function of time after triggering the injector and a plate temperature of 100°C (a) and the individual mean time signal (—) for ethanol (b), propanol (c) and butanol (d) including the respective standard deviation (.....).*

In the case of butanol the shape of curve is different from all of the other ones recorded, with its maximum value not at the beginning but rather a bit later at around 150 ms. This can be explained by the evaporation behaviour of this liquid. During the recordings it was evident that the liquid film was boiling and formed bubbles during the first couple of images. This was also the case for propanol and ethanol, but it had much less of an impact on the measurements. Because of the bubble formation, specular reflections created large intensities in those images which lead to local film thicknesses skewed towards smaller

values. This behaviour becomes more pronounced when the film thickness becomes larger, since the relative intensity fluctuations caused by bubbles increase. Because of that phenomenon it can be assumed that the real initial deposit volume should be closer to the value of octane given the similar shape of the two curves at larger times. This is also supported by the values of the standard deviation. These are much larger during the initial phase of the measurements, where boiling was observed. A comparison between a liquid film of the alkanes and an alcohol to illustrate the different evaporation behaviour can be seen in Figure 4.9.

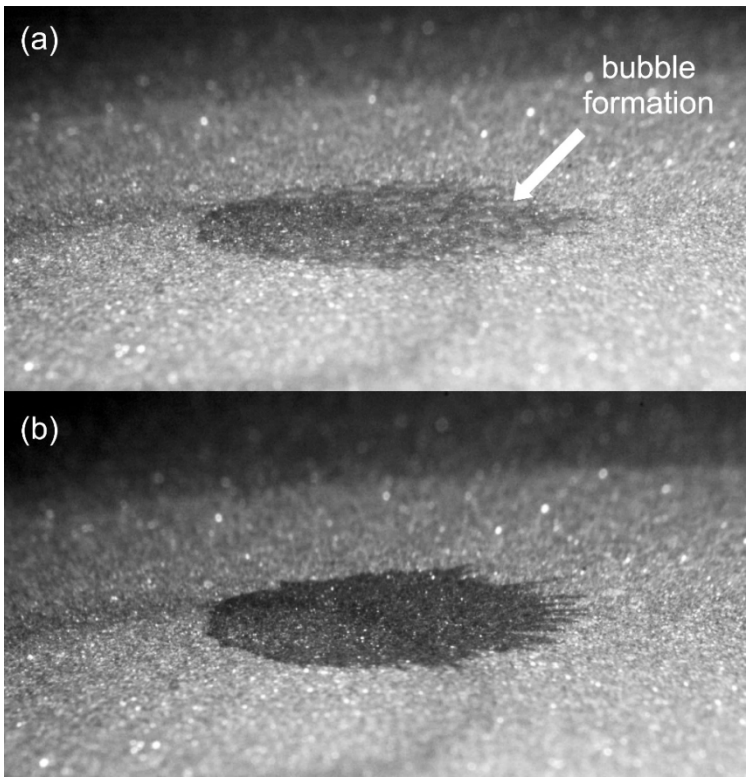


Fig. 4.9 *Example of the differences in the evaporation behaviour of alcohols (a) and alkanes (b). Bubbles were formed in the case of alcohols, while alkanes did not show any signs of boiling.*

Despite the different evaporation behaviour, it appears that if the boiling temperature is smaller than the plate temperature then the deposit is small, and the opposite if the boiling

temperature is higher. Essentially, the same liquid film behaviour is observed with the alcohols as with the alkanes.

To further analyse the effect of physical properties of a liquid on the formation of liquid deposits, an estimated total energy to evaporate the fuel film was calculated for each liquid. These were based on the physical properties shown in Table 4.1 and the results can be seen in Table 4.2. During these calculations a theoretical deposit volume was assumed, which is the basis to calculate the total energy required to evaporate the respective liquid on the impingement plate. The assumption was made that the entire spray volume gets deposited during the injection process. The resulting fuel film volume is 15 µl, which is based on flow rate data provided by the manufacturer of the injector and correlated engine data. This assumption neglects any real interaction between the spray droplets and the surface, which would lead to much smaller liquid deposits in reality. In fact this boundary condition can be seen as a worst case scenario without knowing the wettability behaviour of individual fuels. Based on the deposit volume, the energy required to heat up each liquid from room temperature (20 °C) to boiling temperature can be calculated. Once the film reaches boiling temperature, the energy to evaporate the liquid was calculated using the latent heat of evaporation from Table 4.1. A theoretical estimate of the total energy to evaporate the liquid was then calculated by combining the two values. Please note that this energy also ignores the mass transfer from the liquid to the vapour phase that exists during all conditions and especially during heating up the deposit. Additionally, any convective effects are also ignored.

Within the group of alkanes the total energy based on this theoretical deposit volume increases as the boiling temperature becomes larger. The reason for this is that the latent heat of evaporation is almost identical between the three fuels, and as such the total energy is only affected by the energy that is required to heat up the liquid to boiling temperature. Ultimately, these calculations yield a trend which agrees with the results found in the experiments an increase in the boiling temperature results in larger deposits and longer evaporation times.

In the case of the alcohols, however, the same trend cannot be observed. Similar to the alkanes, the energy required to reach boiling temperature increases from ethanol to

butanol, even though the specific latent heat of evaporation decreases significantly at the same time for these liquids. So much so in fact, that the energy required to evaporate the respective alcohol compensates for the increasing energy required to reach boiling temperature of the fuels completely. In the end, the total energy necessary to evaporate each alcohol does not increase with the boiling temperature, but stays almost the same for the three fuels.

Table 4.2: *Calculated evaporation energy for each fuel based on a theoretical deposit volume and for the measured volume.*

fuel	energy to reach boiling temperature, J	energy to evaporate, J	total energy based on the theoretical volume, J	total energy based on the measured volume, J
hexane	1.11	3.31	4.42	0.13
heptane	1.79	3.74	5.53	0.20
octane	2.50	3.82	6.32	0.49
ethanol	1.66	9.91	11.57	0.16
propanol	2.23	8.31	10.54	0.44
butanol	2.81	7.10	9.91	0.54

Using this knowledge similar, calculations of the total evaporation energy were undertaken based on the maximum volume that was measured with the methodology presented. Please note, that although this is a more realistic estimation, it neglects the temperature change of the liquid deposit during injection and assumes that the measured film is still at 20 °C after the end of injection. Nevertheless, if the total evaporation energy is calculated in the same way as before, but based on the maximum volume measured in each experiment, one can see the same trend as observed in the experiments for both groups of fuels. With increasing boiling temperature of the single component fuel, the total energy to evaporate the measured deposit increases, also. Furthermore, if an alkane is compared to an alcohol with a similar boiling temperature one can see, that the required energy is higher for the latter. This could provide a first explanation as to why the initial deposit volume is higher in the

case of the alcohols, again with the exception of butanol, and why the evaporation time is roughly twice as large for all alcohols as compared with the respective alkane.

A second set of experiments was conducted to further investigate the phenomenon of wall wetting and how it is affected by the wall temperature in relation to the boiling temperature of the liquid. The above mentioned tests were repeated under the same conditions with the exception of the wall temperature. This time, the surface temperature was adjusted to match each individual boiling temperature of the liquid. The high speed recordings were analysed in the same way and mean the volume time series of each fuel was extracted from the five recording of each fuel. The results are presented in Figure 4.10 for the alkanes and in Figure 4.11 for the alcohols.

The two plots illustrate that the evaporation behaviour as a function of time within the two families of single component fuels overlap nearly perfectly. Focusing on the three alkanes in Figure 4.10a, with the boiling temperature being the only physical property that is changing, the significance of this property in relation to the surface temperature is very clearly demonstrated. It is apparent, that adjusting the plate temperature to match the boiling temperature of the fuel has a drastic effect, not only in the initial deposit volume but also in the evaporation time of the liquid. In the case of octane the maximum deposit volumes was halved and the evaporation time was reduced by more than an order of magnitude. On the other hand the hexane volume was increased by over an order of magnitude, as was the evaporation time. Heptane with a boiling temperature very close to the original 100 °C surface temperature during the first set of experiments remained largely unchanged.

Interestingly, the three alcohols behaved in a similar way as the alkenes during these experiments even though their physical properties are more different from each other. The volume and evaporation duration of ethanol was increased by a factor of 3-4 and the time of butanol was reduced to one fifth. The extent of the propanol deposit became slightly larger during the second series of experiments. Please note, that all alcohols also showed minor boiling inside the film, similar to the first set of experiments, which was most pronounced in the case of butanol. This could explain why the initial deposit volume of butanol appears to be smaller compared to ethanol and propanol. Similar to the 100 C

case, the scattering behaviour could be affected by bubble formation which reflects more light towards the camera, and therefore skewed the results of the calculated film thickness towards smaller values. Again this is supported by the standard deviations of the butanol measurements shown in Figure 4.10c, which are much more pronounced compared to the other two alcohols.

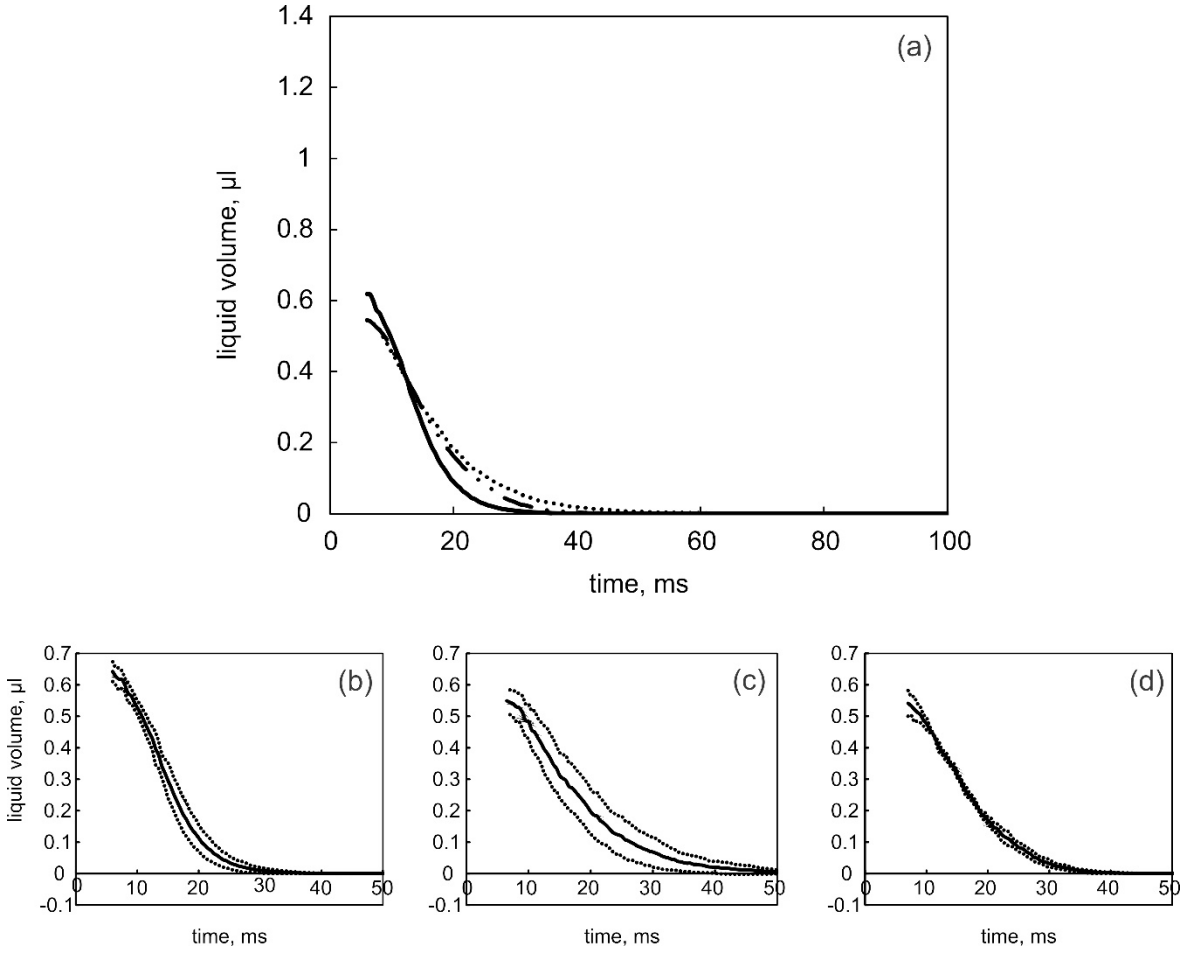


Fig. 4.10 *Mean liquid volume of wall deposit of hexane (—), heptane (.....) and octane (– ..) fuels as a function of time after triggering the injector, with the plate temperature matching the boiling temperature of each liquid and the individual mean time signal (—) for hexane (b), heptane (c) and octane (d) including the respective standard deviation (.....).*

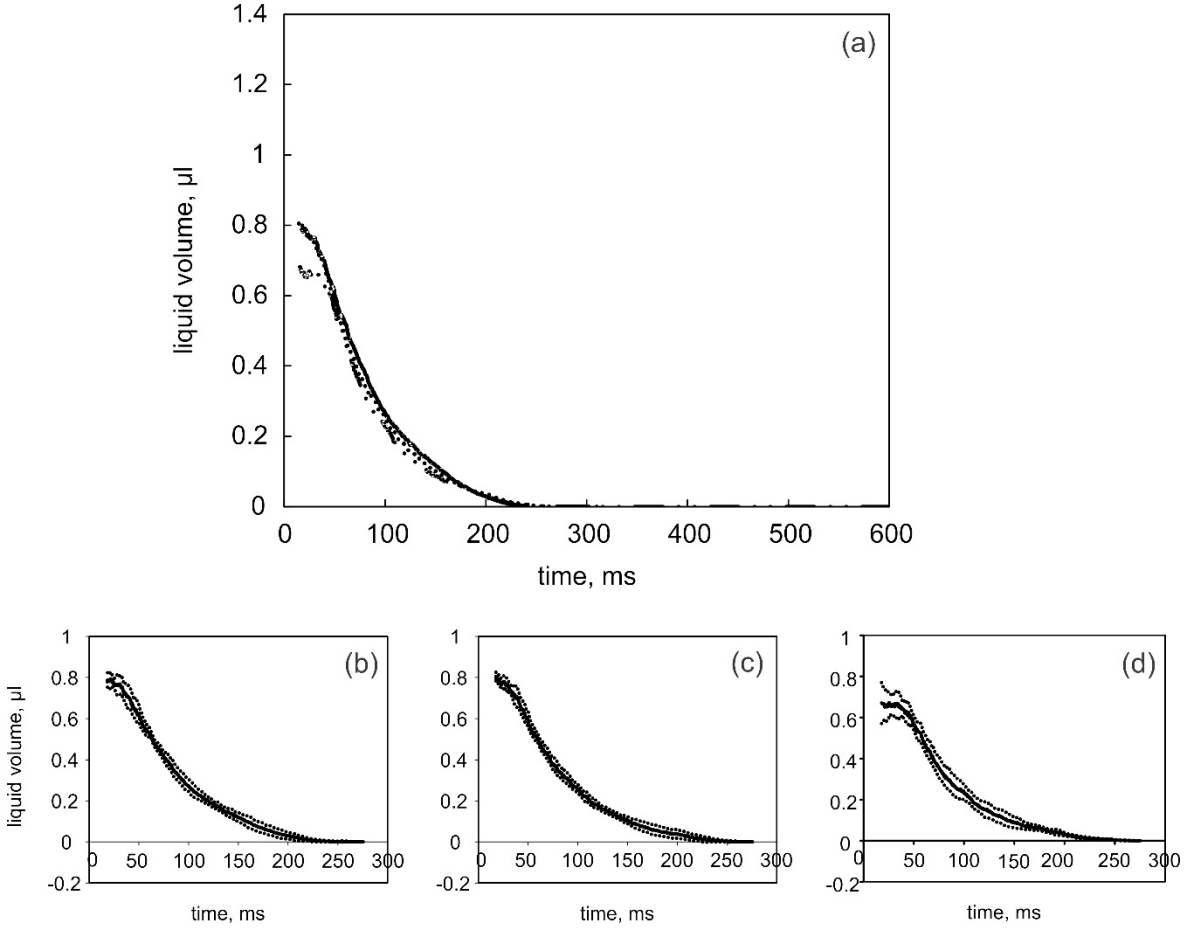


Fig. 4.11 *Mean liquid volume of wall deposit of ethanol (—), propanol (.....) and butanol (– ..) fuels as a function of time after triggering the injector, with the plate temperature matching the boiling temperature of each liquid (a) and the individual mean time signal (—) for ethanol (b), propanol (c) and butanol (d) including the respective standard deviation (.....).*

Between the two families of fuels, a difference in the time scale remains with the alcohols taking 5-6 times as long as the alkanes to evaporate, although the initial deposit volume is similar. This could be explained by the latent heat of evaporation which is up 2.5 times larger for the alcohols.

Overall, the findings of these experiments mean that adjusting the surface temperature to match the boiling temperature of the liquid has a dramatic impact on deposit formation and evaporation as reported previously [116], [202], [203]. Surprisingly, the

three alcohols seem to behave in the same way, despite their fewer similarities in their physical properties than the alkanes. This would mean that the boiling temperature of the liquid is the most influential property for the liquid deposit formation and evaporation, which is remarkable. If this observation is applied to the cylinder wall and piston wetting inside a direct injection engine, this would mean that by increasing the wall and piston surface temperature inside an engine to match or exceed the boiling temperature of the fuel, the amount of liquid deposit will be reduced significantly. This could potentially be achieved by modifying the coolant temperature or performance to raise the steady-state operating temperature of the engine. With that, a potential to reduce the amount of particulate emissions from modern gasoline engines is given, since the exhaust particulate emissions are linked to the liquid film formation during the injection process [1].

4.6 Summary and Conclusions

A novel method to investigate the physics of liquid fuel deposits and evaporation, created by a spray of a fuel injector impinging on a piston or wall surface, was developed. The technique makes use of the change of the liquid scattering intensity emitted from a metal surface with known roughness, when liquid is deposited. Important advantages of the technique over previously established methods are the ability to measure time-dependent spatial distribution of liquid film thickness without a need to add a fluorescent tracer in the liquid, while the measurement principle is not influenced by changes of the pressure and temperature of the liquid or the surrounding gas and liquid properties. However, an *in-situ* calibration of the dependence of signal intensity on liquid film thickness is required for each optical setup. Therefore, the developed method can be applied to measure the time-dependent and 2D distribution of the liquid film within the environment of gasoline direct injection engines. However, the technique can also be applied to numerous applications, where liquid film deposits on a solid non-transparent surface are important. The main findings of the paper are presented below.

- The principle of the technique, the data processing approach and the calibration procedure were presented and demonstrated. A comparison of the evaporation behaviour of liquid fuel deposited on a metal and a glass plate was also performed, to further demonstrate the applicability of the technique.
- The application of the technique was demonstrated by selecting linear alkanes and alcohols with changing boiling temperature and studying the behaviour of the liquid film thickness on a metal impingement plate with variable temperatures. When keeping the surface temperature constant at 100 °C, an increase in the liquid film thickness was observed with increasing boiling temperature, both with the alkanes and the alcohols. By adjusting the plate temperature from 100 °C to match the boiling temperature of each individual fuel, it was possible to overlap the evaporation curve of all alkanes and alcohols respectively. This means that not only the time scale until complete evaporation was similar within each group of fuels, but also the initial volume of the liquid film . Overall, this shows the strong influence of the boiling temperature of the fuel on the behaviour of the liquid film thickness, which suggests that control of the wall temperature in the cylinder of a gasoline direct injection engine may reduce the liquid fuel deposit, which may assist the reduction of particulate emissions at the exhaust.
- Future work is required to further develop the technique and make it more independent towards the effects of the angle of illumination and detection. This would broaden the applicability and open it up for numerous investigations.
- The necessity of an *in-situ* calibration might prove obstructive for the transfer of the technique to metal test engine. By further understanding the effect of the light source and optics positioning it could be possible to abstract this step outside of the actual chamber and apply it inside the cylinder during later measurements. In combination with endoscopic optical excess this would make the technique viable in real engines.
- Finally, the effect of surface roughness on the evaporation rate of thin liquid films should be evaluated, which may assist the reduction of wall wetting in IC engines.

Chapter 5

Characterisation of impinging fuel sprays

The study presented in this chapter is focusing on how changing physical and chemical properties of the fuel is affecting the pattern, structure and wall wetting behaviour of gasoline sprays found in modern direct injection engines.

In the first set of experiments the shape of the spray without the presence of the impinging plate was analysed. Then, the spray interaction during the impingement on a glass plate was investigated at different conditions. All the blends mentioned in chapter 3.1.4 were tested here and the results were used as a basis for the other experiments.

The findings of the spray pattern analysis guided the selection of fuel blends in order to characterise the spatial distribution of the droplet size and velocity in the spray using Phase Doppler Anemometry. This provided a deeper look into spray structure with possible explanations on why these fuels behave differently.

In the final part the actual wall wetting was quantified with the measurement technique presented in chapter 4 for a selection of fuels. Because of the apparent link between liquid deposits and engine-out emissions, the intention was to investigate how this process can be controlled through the properties of the fuel blend and the operating conditions of the engine.

The results of each part of the study will be presented and discussed separately with a concluding section that is summarising the observed trends and providing suggestions for possible improvements to minimise wall wetting in a direct injection engine.

5.1 Qualitative spray analysis using High Speed imaging

This part of the study was intended to yield general data on the spray shape and interaction between the spray and a solid surface through high speed visualisations. The results were meant as the foundation for the following more quantitative experiments to decide which blends require more detailed investigations.

The spray for every individual blend was recorded five times for each condition, which included the free spray and sprays that were impinging on a heated glass plate. An example of a high speed recording with and without the plate can be seen in Figure 5.1 and Figure 5.2. Both show extracted frames of time series with the timestamp representing the time after starting the recording and triggering the injector electronics.

The field of view was selected in such a way that the injector tip appears at the top left corner of the image (Figure 5.1). Because of the placement of the light source behind the chamber relative to the camera, the background appears white and the objects and the spray as darker shades. As such, the silhouette of the non-transparent injector tip appears black with the bottom part of the injector mount that surrounds it. Because the focal plane was adjusted to be in the centre of the injector, the injector mount contours do not appear sharp, but slightly blurred in the recordings. The glass plate used to investigate impinging sprays (Figure 5.2) can be seen at the bottom of the image and appears darker than the background, but not as dark as the spray and the liquid deposit. The area right underneath the glass plate is covered by the non-transparent aluminium frame which provided the support of the glass plate and was flushed with the heated silicone oil.

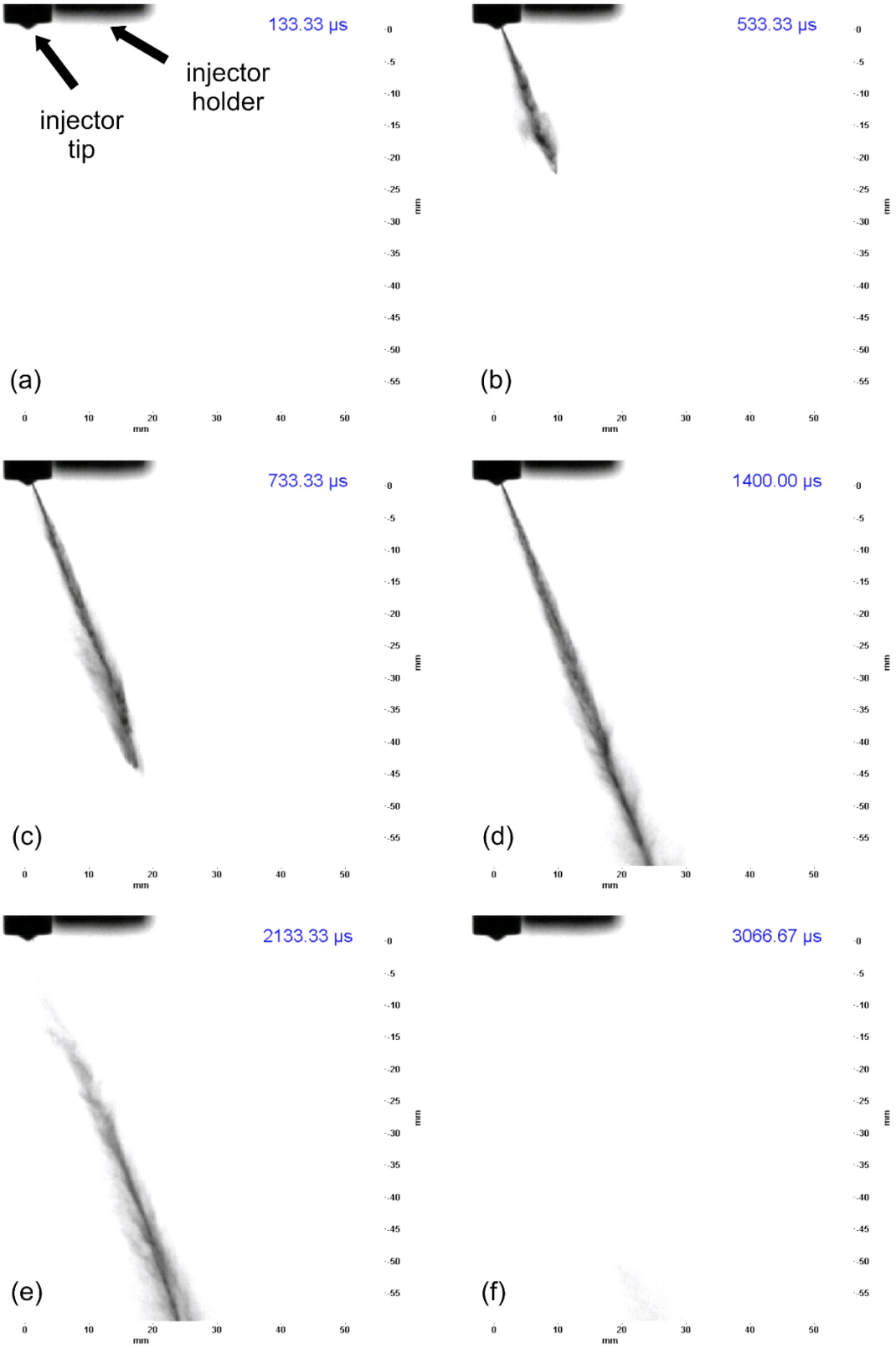


Fig. 5.1 *Extracted frames of a recorded time series of a free spray injection (blend PM1) at a rail pressure of 150 bar.*

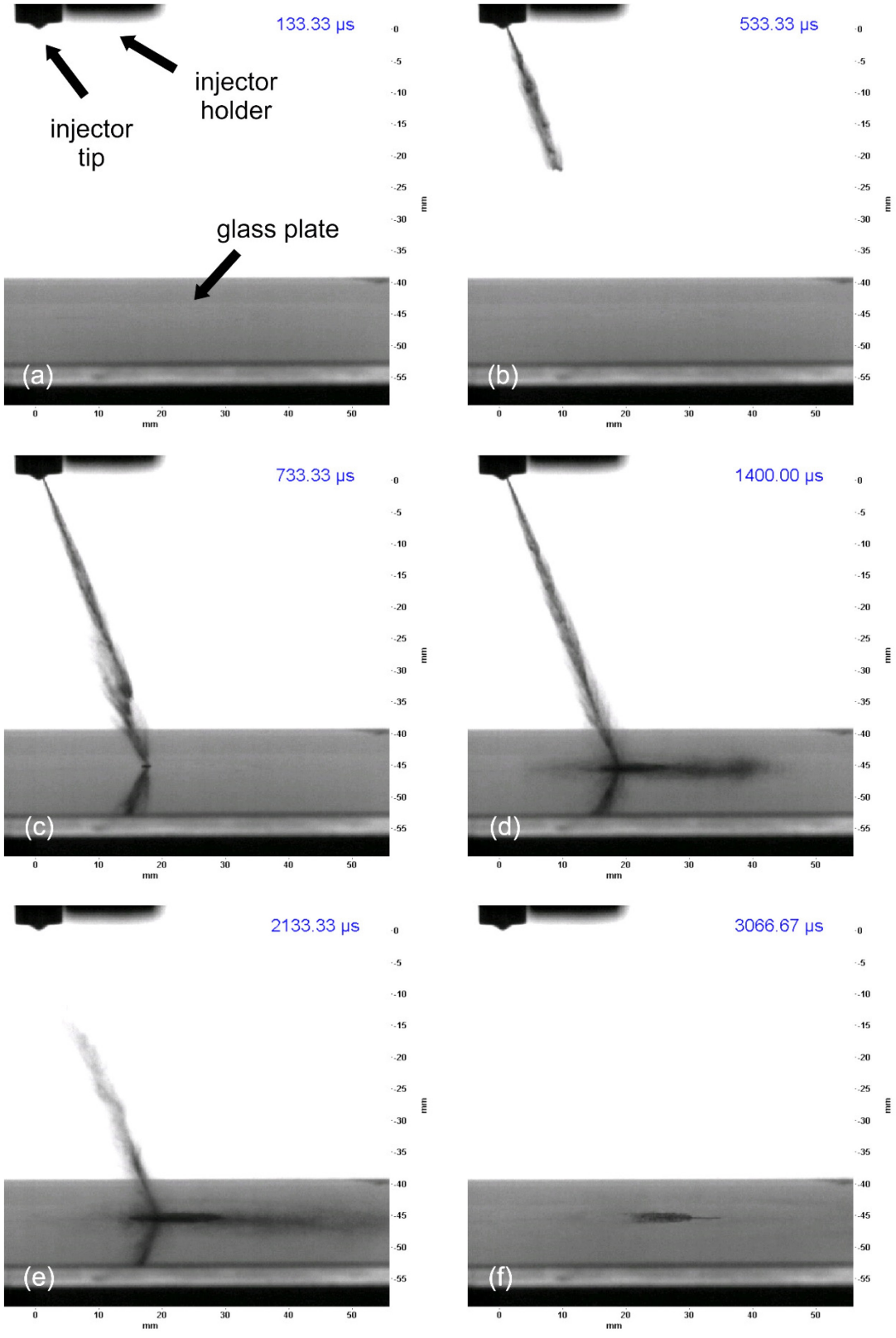


Fig. 5.2 *Extracted frames of a recorded time series of an impinging spray (blend PM1) at a rail pressure of 150 bar. The plate was at ambient temperature.*

Usually, several frames into the recording the spray starts to form (Figure 5.1b), as the liquid jet breaks up into droplets. The leading edge shows notable deformations caused by the momentum transfer of the fast moving droplets to the surrounding air continuum. As the spray propagates the shape becomes more regular and stabilises to a quasi-steady state (Figure 5.1c and Figure 5.1d). It can be seen that around the very dense core of the spray, a droplet cloud is formed with a slightly irregular shape. Once the injection window is passed, the needle of the injector is closing and the spray separates from the nozzle (Figure 5.1e). The trailing edge of the spray is much less dense than the spray core which results in a less dark appearance. After the injection is complete, smaller droplets remain suspended in the air for a period of time and form fuel a mist that slowly evaporates.

The steps described can also be observed in the impinging spray (Figure 5.2). Before a steady state is reached, the leading edge of the spray is impinging on the glass plate, which was mounted at a distance of 45 mm downstream of the injector tip (Figure 5.2c). Once impact of the leading edge happens, a liquid fuel film is formed on the surface. Above this film, secondary droplets appear very close to the surface that move from the spray centre outwards. Even though the impingement happens at a relatively steep angle, the cloud of secondary droplets remains very close to the surface. The predominant motion of the droplets was in conjunction with the spray direction (towards the right hand side in the recordings). Once the injection process was completed, there are also droplets that remain suspended in air, just above the plate (Figure 5.2f). Additionally, a distinct liquid film can be seen, which remains on the surface of the plate for a much longer time scale than the injection process. The observed motion of the droplets also affects the shape of the liquid deposit which appears much more noticeable towards the right side and appears very thin in the area where the spray impinges, further to the left. This indicates that the horizontal component of momentum of the angled spray results in pushing the liquid film along the surface.

The first step of evaluating the recordings was to analyse each series and to derive a synchronisation criterion of the measurements. For this reason, a visible start of recording (VSOI) and a visible end of injection (VEOI) were determined. The appearance of fuel at the nozzle of the injector cannot be synchronous with the trigger point of the electronics

because of small electronic delays and mostly because of injector needle and liquid inertia in the idle injection system. During inspection of each time series, the first frame and its corresponding timestamp that showed a fuel spray was defined as the VSOI and the first image that showed a separation of the spray from the injector corresponded to VEOI. An example of both instances can be seen in Figure 5.3.

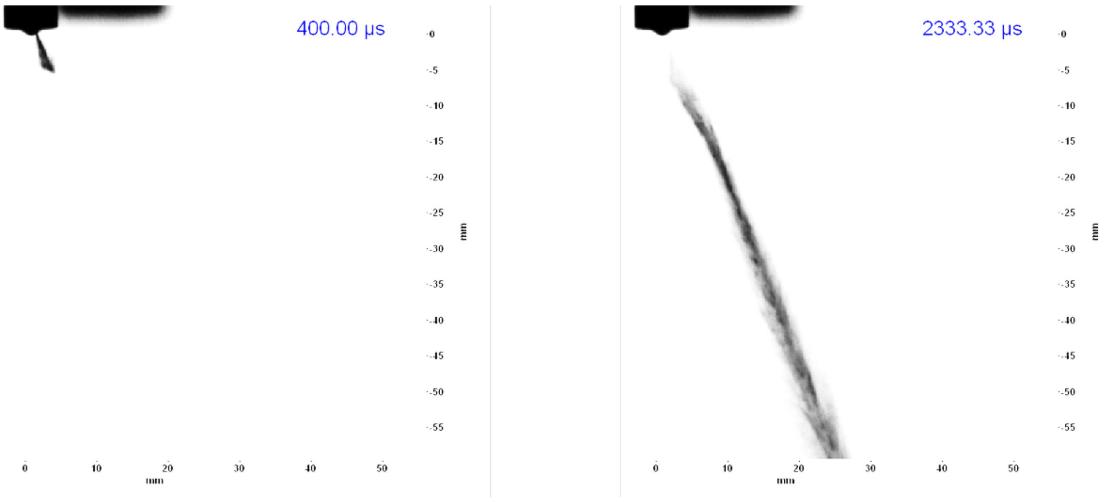


Fig. 5.3 *Visible start of injection (VSOI, lhs) which corresponds to the first frame with liquid present at the nozzle of the injector and visible end of injection (VEOI, rhs), the first frame where the spray is separating from the injector tip.*

From the difference of these two numbers a visible injection time (VIT) was also calculated. These synchronisation criteria were established for all blends, pressures and corresponding injection timings. It will be referred to in all subsequent calculations and analyses of this study. An overview of all frames and time stamps of the VSOI, VEOI and VIT for all fuels and conditions can be seen in Table 5.1.

The first observation that can be drawn from this overview is that the VSOI is the same for every fuel and condition. As it turns out, the rail pressure difference between 50 bar and 150 bar does not have a detectable effect on this delay. Most likely, the temporal resolution of the recoding frequency of 15 kHz is not high enough to capture the differences between the two pressures. Assuming a constant electronic delay, the time

between two frames equates to 13.33 µs which could be much longer than the difference in liquid acceleration inside the nozzle once the needle gets lifted. On the other hand, the reduced delay could also be compensated to some degree by a longer needle lift time caused by the larger back pressure.

Table 5.1: *Visible start of injection (VSOI), visible end of injection (VEOI) and visible injection time (VIT) of each fuel blend and rail pressure.*

fuel	injection pressure, bar	VSOI, frame #	VSOI, ms	VEOI, frame #	VEOI, ms	VIT, ms	inj. time, ms	diff*, %
PM1	50	7	0.400	48	3.134	2.734	2.622	4.27
	150	7	0.400	31	2.000	1.600	1.514	5.68
PM2	50	7	0.400	48	3.134	2.734	2.628	4.03
	150	7	0.400	31	2.000	1.600	1.517	5.47
PM3	50	7	0.400	48	3.134	2.734	2.619	4.39
	150	7	0.400	31	2.000	1.600	1.512	5.82
PM4	50	7	0.400	48	3.134	2.734	2.598	5.23
	150	7	0.400	31	2.000	1.600	1.500	6.67
PM5	50	7	0.400	50	3.267	2.867	2.770	3.50
	150	7	0.400	32	2.067	1.667	1.599	4.25
PM6	50	7	0.400	56	3.667	3.267	3.236	0.96
	150	7	0.400	36	2.334	1.934	1.869	3.48
PM7	50	7	0.400	66	4.334	3.934	3.829	2.74
	150	7	0.400	42	2.734	2.334	2.210	5.61
A	50	7	0.400	31	2.000	1.600	1.532	4.44
B	50	7	0.400	31	2.000	1.600	1.502	6.52
E	50	7	0.400	30	1.934	1.534	1.472	4.21
F	150	7	0.400	30	1.934	1.534	1.456	5.36

*) relative to the VIT

With all measurements having the same visible start of injection, the VEOI is only influenced by the injection width, which was calculated through the lower calorific value of each blend for a given injection pressure. As expected, the visible end of injection is

increasing with the injection time. Fuel blends PM1, PM2, PM3 and PM4 from the physical matrix have very similar values for both rail pressures. Once the ethanol content reached 20% the injection duration was increased to maintain the same calculated fuel to air ratio and as such the timing of the VEOI is increasing by several frames. In the case of PM7 with 85% ethanol the largest injection width was required which results in a VEOI of 2.734 ms in the case of 150 bar rail pressure and 3.934 ms for 50 bar.

Looking at the visible injection time in comparison to the set injection duration it can be seen that the former is always larger than the latter. The relative difference based on the set injection time varies between about 4% and 7% in the case of 150 bar rail with no obvious trend. In general, the difference between the visible and the set injection time is most likely explained by the closing time of the needle inside the injector, which is not taken into account by the injector electronics, and the remaining liquid in the nozzle that travels through the nozzle until the needle is closed completely. It is fair to assume that this process is independent of the set injection time which is why the values are of the same magnitude. Additionally, similar to the VSOI the temporal resolution might not be high enough to resolve fine differences between the injection times that are very small.

For the 50 bar rail pressure measurements, differences between the visible and the set injection time were slightly smaller (between 3 to 5%). Because the lower pressure cases use a much longer set injection width compared to their high pressure counterpart, a constant closing time of the injector needle contributes less to the visible injection, in relative terms. One exception is the observed injection time of PM6 at 50 bar, which only differs by about 1% from the set injection time. It is possible that this particular injection time coincides very well with the recording frequency of the camera, wherefore the error remains this small.

As mentioned in the description of the experimental procedure (chapter 3.1.4) the air temperature inside the chamber was set to 80 °C during measurements of the free spray as well as with the impingement plate which was at ambient temperature. Because heat transfer occurred from the warm air into the cold plate the system was left until stable temperatures were recorded inside the plate before each measurement. The temperatures inside the plate varied between 33 and 35 °C during these measurements.

Additionally, the plate temperature was set to 80 °C, 200 °C and the specific T90 of the blend with ambient air temperature. The latter was recorded as it was depending on the actual plate temperature due to the heat transfer. The values are listed in Table 5.2.

Table 5.2: *Measured temperatures of the air inside the injection chamber for the different plate temperatures and fuel blends investigated.*

fuel	plate at 80 °C, °C	plate at 200 °C, °C	plate at T90, °C
PM1	50	90	68
PM2	50	90	72
PM3	49	90	85
PM4	49	92	75
PM5	48	94	78
PM6	48	93	74
PM7	48	90	48
A	50	92	74
B	50	91	74
E	50	92	78
F	50	92	79

The recorded temperatures for the plate temperatures of 80 °C and 200 °C were very close at each measurement. The air temperature for the T90 points was between 48 °C in the case of PM7 with the lowest T90 value and 85 °C for PM3 with the highest T90. The air temperature was also used to assure that a stable operating condition was reached before the actual recordings. The numbers presented illustrate that the evaporation of the liquid would not only be promoted by the increased heat transfer from the solid surface to the liquid at higher temperatures, but also due to the partial pressure in the gas phase. In addition it is to be expected, that the latter also enhances the evaporation of the spray droplets before the impingement.

Furthermore, heating the air and the impingement plate increased the injector body temperature slightly. The recorded values were between 22 and 24 °C during all

measurements. The temperature of the injector tip was presumed to be higher but with the given setup it was not possible to obtain reliable temperature measurements at this location. Previous research by other groups used embedded temperature sensors in the injector tip to determine the local temperature [177], [185], which was incorporated in the design of the model injector.

The first step was to evaluate the impact of the different operating conditions and fuel compositions on the shape of the gasoline spray. Therefore mean and standard deviation of the image intensities were calculated from each measurement series. This was done by inverting the intensity scale used during the recording, which resulted in a bright spray in front of a black background. The individual images were then averaged and normalised by the largest intensity detected in the spray. This was usually in the area closest to the injector tip, where the droplet density reached its maximum. In the scale, a large intensity corresponds effectively to a large droplet density which leads to more light being scattered. The same procedure was applied to the standard deviation of the image intensities. Figure 5.4 shows the mean spray intensity at 1.2 ms after VSOI for the case of 150 bar rail pressure and 2 ms after VSOI for the case of 50 bar. The corresponding standard deviation of the image intensity can be seen in Figure 5.5.

The spray shape depicted in the mean images of PM1, PM2 and PM3 looks very similar with a rather narrow spray cone with a core of large intensity (function of the droplet number density). This means that these sprays are relatively compact with a high droplet density. The surface tensions of PM1 and PM2 are identical, only PM3 has a slightly higher value. Additionally, between these three blends the T90 is increasing by almost 60 °C, which does not seem to have a noticeable impact on the spray pattern. Looking at the additional fuel properties it becomes apparent that these fuel blends all have similar properties. They have the same ethanol content, a similar viscosity and about the same injection duration. Because of these similarities the sprays share a strong resemblance. In comparison, the spray of PM4 is a little wider and less compact than these three. The blend has a slightly smaller ethanol concentration, but the surface tension and the viscosity are very similar. Also, the T90 is the same magnitude as PM2.

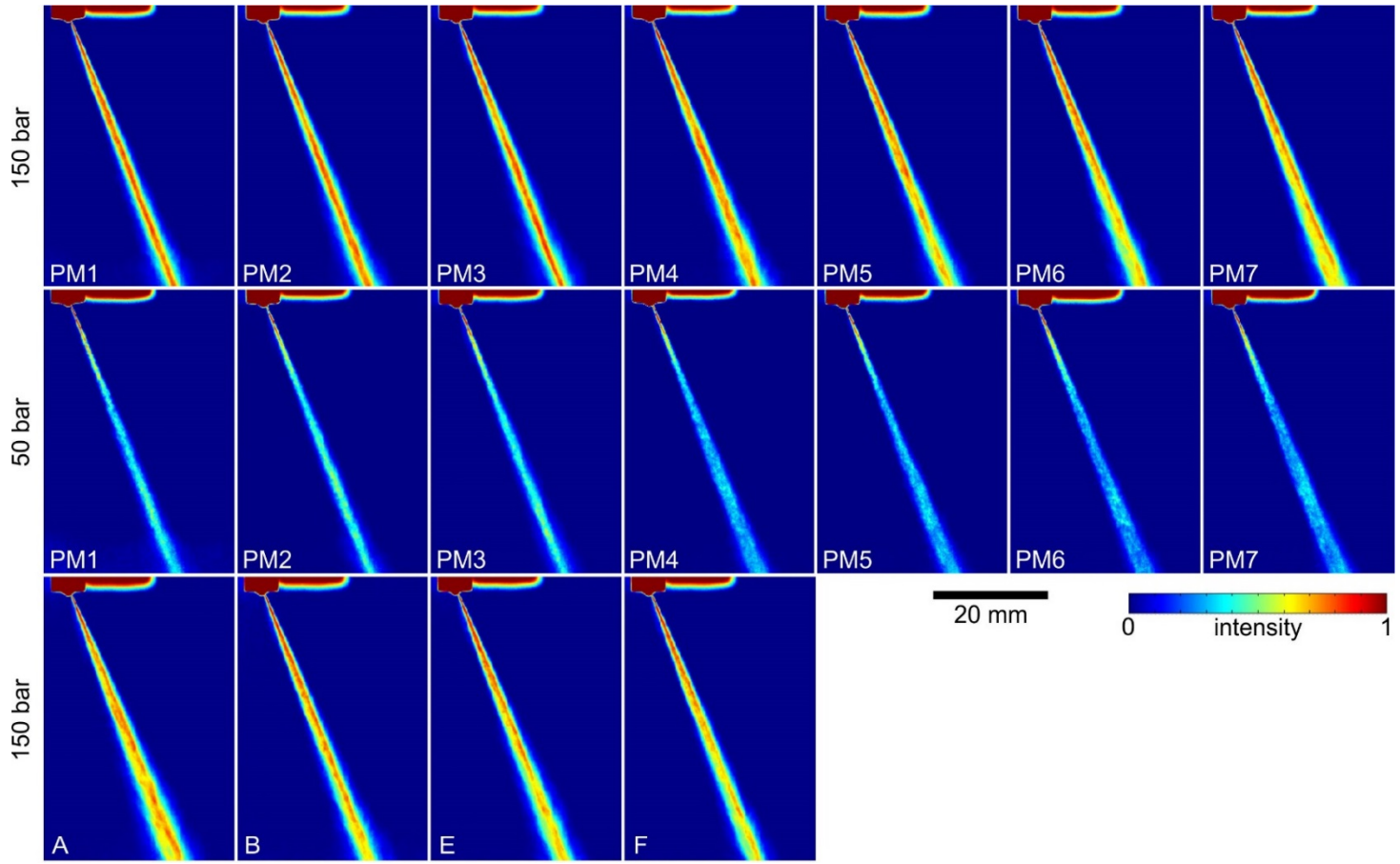


Fig. 5.4 *Normalised mean spray image intensities of each fuel blend at 1.2 ms after VSOI for the case of 150 bar and 2 ms after VSOI for 50 bar injection pressure in false colours. This information provides a measure of the relative droplet number density in the resulting sprays.*

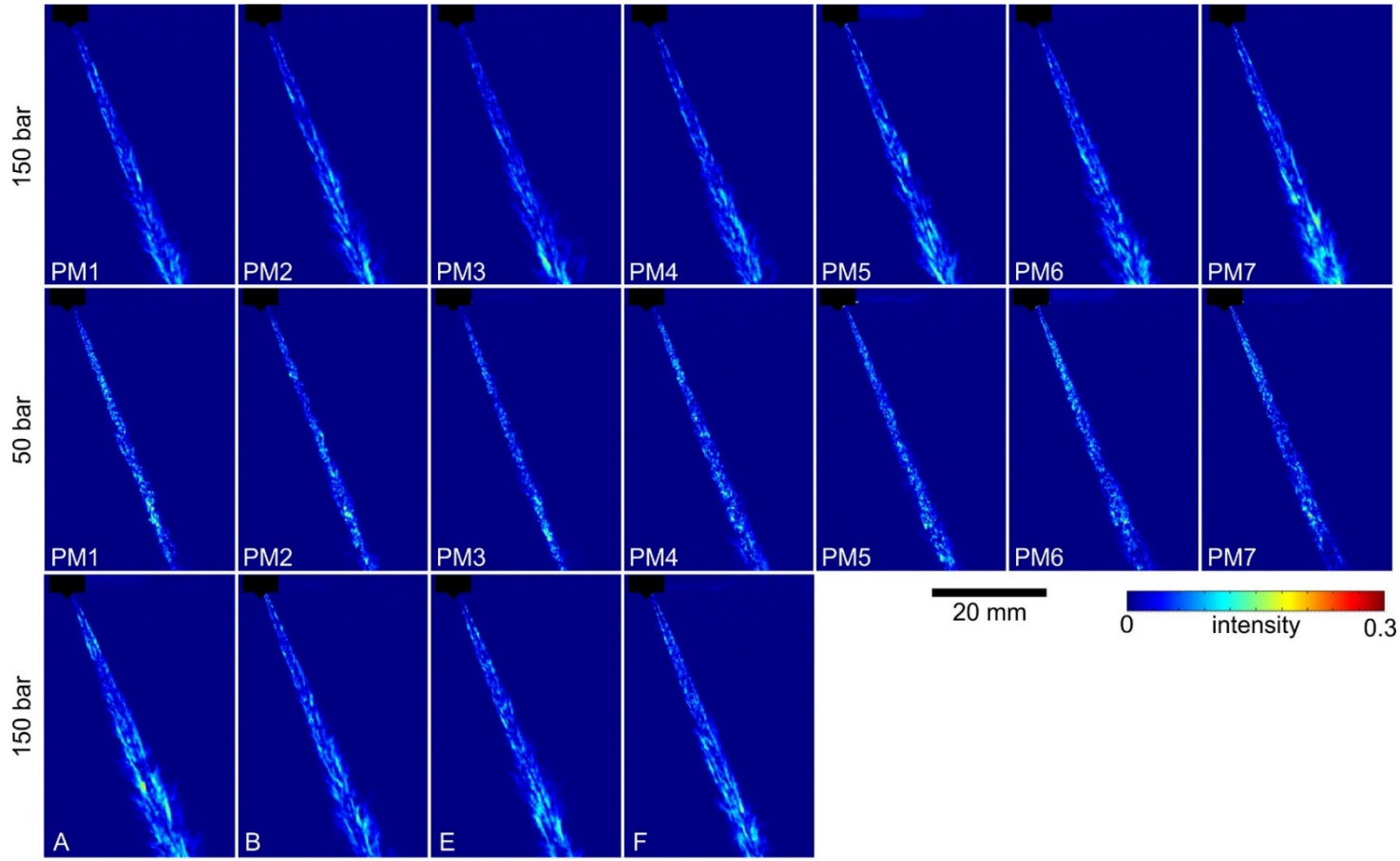


Fig. 5.5 *Normalised mean standard deviation images of each fuel blend at 1.2 ms after VSOI in the case of 150 bar and 2 ms after VSOI for 50 bar injection pressure in false colours. This information provides a measure of the relative fluctuations of droplet number density in the resulting sprays.*

Focusing on the fuel blends PM5, PM6 and PM7 with increasing ethanol content, the spray shape changes notably. Between them, the cone becomes wider and the measured intensities decrease along the spray axis. This means these sprays fan out more with a lower droplet density further downstream compared to the other sprays. It is also apparent that these observations become more dominant with increasing ethanol content. The fraction of ethanol is increasing by a factor of more than four between them. The blend PM7 with 85% ethanol produces the widest spray cone of all blends from the physical matrix. Additionally, the viscosity of the liquid is increasing more than three times from PM5 to PM7. The surface tensions remain at a comparable level, with PM6 having a slightly smaller value. Such an effect on the spray cone angle was reported by Aleiferis *et al.* [177] when they compared gasoline sprays with ethanol sprays injected by a multi-hole injector.

Similar observation can be made for the results of the measurements with 50 bar rail pressure. PM1, PM2 and PM3 are almost identical and with increasing ethanol content the spray becomes wider (PM5-PM7). As expected, all sprays at the lower injection pressure are much less dense than their high pressure counter-part. A lower injection pressure usually leads to inferior atomisation with larger droplets sizes and lower droplet number density [28]. This results in less light scattering during the recordings and as such lower intensity values in the image analysis.

Within the group of fuel blends from the chemical matrix no clear trend is obvious. The surface tensions and viscosities are quite similar between those fuels. Blend A produces the widest spray overall, even when compared to the blends from the physical matrix. Blend F shows the most compact spray of the chemical matrix. However, none of the sprays are as narrow as the ones generated by blends PM1-PM3.

The corresponding standard deviation of the fluctuations of droplet number density, obtained from all measurements (Figure 5.5), lie between 0 and 0.15 on the same scale. In general, the observed fluctuations between the individual repetitions are relatively small on the centreline of the cone, especially close to the injector tip. The boundary of the spray is more influenced by the interaction between the droplets and the surrounding continuum of air. Additionally, the mixing between spray and air is increasing with the length of the

spray which results in the largest fluctuations at the bottom of the recording. Overall the largest fluctuations of droplet number density are produced by fuels PM7 and A, which also have the widest spray cone.

To further describe the differences of the spray patterns in a quantitative way, the downstream spray width was determined analytically for each fuel blend in the free spray configuration without the impingement plate. For this analysis frame 25 (1.134 ms after VSOI) was selected for all measurements at 150 bar rail pressure and frame 31 (1.600 ms after VSOI) for the measurements at a rail pressure of 50 bar. At both points in time the respective spray was fully developed and the spray width was perceived stable. From each of the recordings of each fuel blend, horizontal image lines were extracted from which normalised intensity profiles were calculated. This process is illustrated in Figure 5.6 with an example.

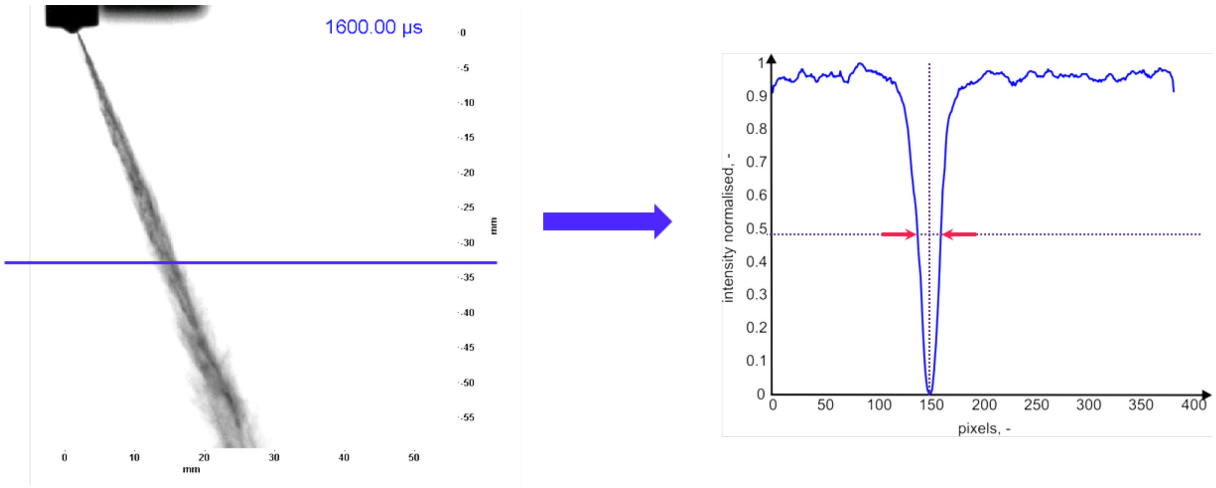


Fig. 5.6 *Extraction of the intensity profile of a horizontal line of the recorded spray image and the corresponding normalised intensity profile.*

The extracted values were normalised by their maxima detected along the respective horizontal line. From the calculated intensity profile, the location of the centre and the width of the spray can be calculated. This was achieved by using the full width half maximum method. The results were then corrected for the 20° spray inclination to obtain

the actual spray width perpendicular to the spray axis. The process was repeated for all horizontal lines from 8 mm to 56 mm downstream of the injector tip, in 1.6 mm increments. From the results of each individual recording, a mean spray width and the standard deviation were calculated for each downstream location. Both values were collected and plotted as a function of the downstream location (Figure 5.7).

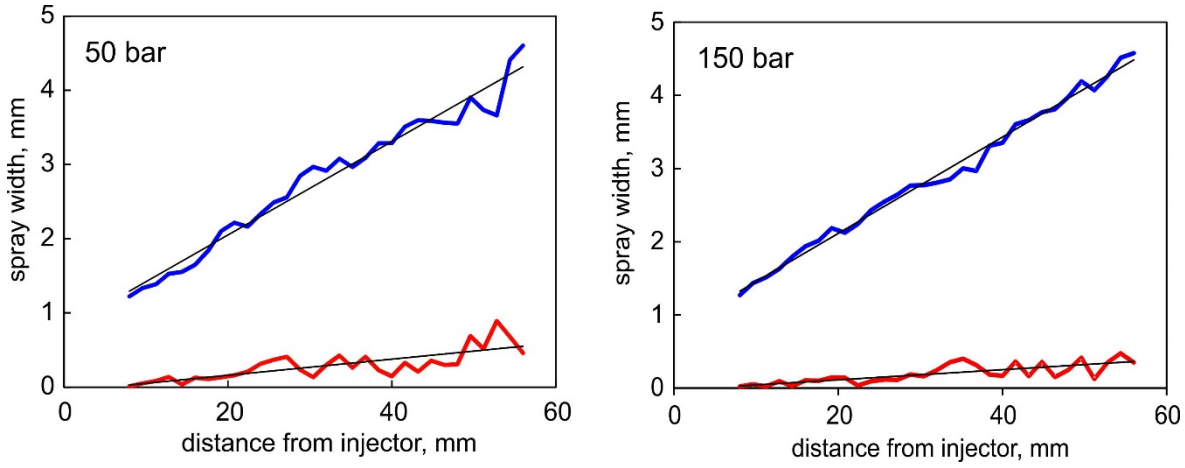


Fig. 5.7 *Example of the downstream mean spray width (—) and standard deviation (—) of its fluctuations calculated from the individual recordings of fuel blend PM6 for 50 bar (left side) and 150 bar (right side) injection pressure.*

A linear fit (least squares) was then applied to both data series to even out the remaining fluctuations between the recordings and the extracted intensity profiles with the assumption of a linear increase of the spray width with the distance from the nozzle. The inclination of the spray width does not change notably between the two rail pressures. However, the fluctuations around the linear fit, both for the average spray width and the standard deviation are much smaller when the pressure increases. This could be caused by the higher momentum of the droplets in the case of 150 bar injection pressure.

The linear fits were then used to calculate the spray width at 45 mm downstream of the injector and the corresponding standard deviation. This distance corresponds to the location of the impingement plate when it was installed in the chamber. The results of the 150 bar and 50 bar measurements are presented in Figure 5.8 and Figure 5.9, respectively.

In addition, the influence of the air temperature inside the injection chamber was also evaluated. For this evaluation, the same processing steps were applied to the 150 bar injection pressure case with ambient air temperature and the lowest plate. Please note that during these measurements the air temperature directly above the plate was around 50 °C with lower temperatures further away. Strictly speaking this does not represent a case with the air at room temperature, but because the only heat source was the plate itself, it was used to determine a qualitative impact of the air temperature on the spray width. Because the impingement plate was installed during these measurements, the spray width was analysed between 8 mm and 40 mm downstream of the nozzle. This provided enough clearance from the surface to avoid the influence of secondary droplets on the results. The values calculated from this series can be found in Figure 5.8.

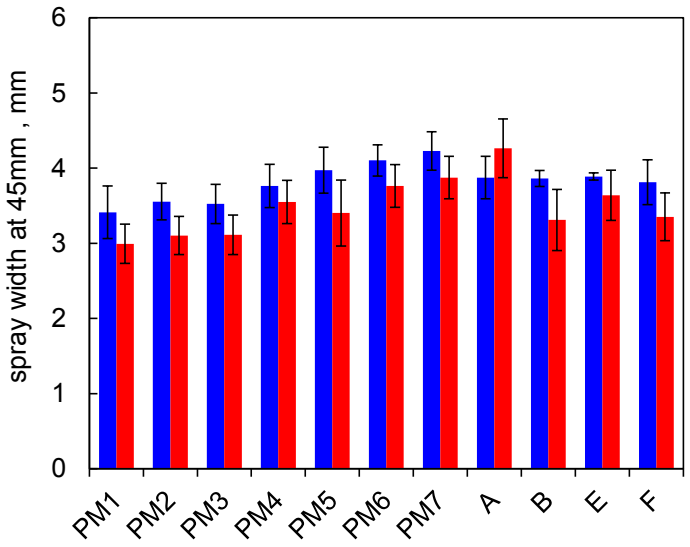


Fig. 5.8 *Measured mean spray width at 45 mm downstream of the injector tip for 150 bar rail pressure and 80 °C air temperature (—) and for 150 bar rail pressure at ambient air temperature (—) for different fuel blends.*

Similarly to the observations made for the mean spray images, the spray widths of fuels PM1, PM2 and PM3 are very close with values slightly higher than 3 mm. In the case of PM5-PM7 and the increasing ethanol content, the width increases to almost 4 mm.

Extending the results to the chemical matrix, it can be seen that blend A generated the widest sprays at over 4.2 mm, and B the most narrow. Again, there is no discernible trend visible between those four fuels. The standard deviation of the spray fluctuations has the same magnitude for all blends, which shows that the fluctuations between individual injections are not significantly affected by the investigated fuel properties.

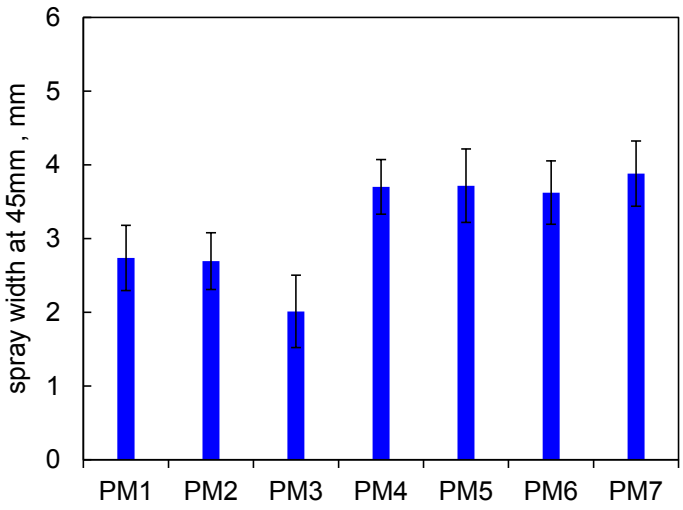


Fig. 5.9 *Measured mean spray width at 45 mm downstream of the injector tip for 50 bar rail pressure and 80 °C air temperature, for different fuel blends.*

When the sprays widths of the physical matrix blends with an air temperature of 80 °C are compared to the ambient cases it can be seen that all values are larger (cf. Figure 5.8). However, the overall trend relative to each other remains the same. The absolute differences are most likely explained by the reduced evaporation rate due to the smaller air temperature. It is fair to assume that this results in a hindered heat transfer and as such a poorer evaporation rate of the droplets in the spray and especially at its border.

Overall, the results of the spray width agree very well with the observation made during the mean spray image analysis. This behaviour was also observed by Aleiferis *et al.* [177] albeit at a larger scale with a wider temperature range.

The widths of the 50 bar sprays are slightly narrower than for their 150 bar counterpart, although the differences are very small. PM1 to PM3 produce relatively narrow sprays of the same magnitude at around 2.8 mm with the only exception being PM3 which has a slightly smaller value. The rest of the blends produce wider sprays close to 4 mm and the trend of increasing spray cones with increasing ethanol content is not as evident. The standard deviation of the spray width fluctuations for all measurements at the lower operating pressure is larger compared to the 150 bar case. This would mean that the fluctuations between the sprays of individual injections are larger here, and the spray itself is less repeatable and stable. This could also explain why the trends, which were observed for the 150 bar measurements are not as pronounced.

Aside from the spray structure, the interaction between the spray and the heated (glass) surface was also of major interest in this experiment. Similar to the sprays without the plate, mean images were generated for all series and each condition. The focus of this analysis was the shape of the liquid deposit on the glass, which is why only frames after the visible end of injection were analysed. Please note that this analysis has a qualitative nature and the depicted intensity cannot be directly related to the film thickness as it cannot be correlated with the light scattering behaviour, but it can be used to investigate differences in the size and shape of the deposits. Figure 5.10 shows mean images of each blend at time 0.534 ms after VEOI for an air temperature of 80 °C and ambient plate temperature. The apparent differences of the liquid film between the investigated blends are more subtle than the spray patterns. However, some of the trends are also reflected here. The liquid deposit of PM1, PM2 and PM3 also look very similar and the extent of the liquid film slightly increases with the ethanol content for PM5, PM6 and PM7. This is the case, even though the injection time is much larger, for PM7 compared to the rest. From the chemical matrix blends, the deposit of fuel A is slightly larger than the deposit of fuel F. Lowering the injection pressure to 50 bar results in a smaller film area with higher intensities for all blends. However, all deposits at the lower operating pressure share a great deal of resemblance and no consistent differences can be observed.

Looking at the same images at a later point in time differences in the evaporation rate behaviour can be assessed. Figure 5.11 shows the respective recordings at time 5 ms after VEOI.

In all cases a large part of the liquid deposit has evaporated at 5 ms after the visible end of injection. The trends observed previously are also reflected in this analysis. The liquid deposits of fuel blends PM1, PM2 and PM3 look very similar after this time which indicates that their evaporation rate behaviour is comparable for this operating condition. A large ethanol content seem to be very beneficial and accelerates the evaporation rate for the case of PM7. Fuels PM5 and PM6 look more similar to the other blends at this point. The same observation can be made for the lower injection pressure case, where only PM7 differs significantly from the rest and seems to be evaporating faster. From the chemical matrix blends, A and F look quite similar after this time and differ from B and E that show higher intensities.

In all images it becomes apparent that the liquid deposit is not formed homogeneously but rather that the right side of it usually takes longer to evaporate. This indicates that the local liquid film thickness is larger in that region compared to the area where the spray impacts on the plate. An explanation would be the increased slip motion by the droplets due to the angled alignment of the spray relative to the plate compared to a perpendicular impingement, which enhances a lateral motion of the liquid on the surface away from the injector [67].

Repeating these analysis steps for the experiments with ambient air temperature and heated impingement plate yielded that, with increasing plate temperature, the liquids begin to form droplets on the surface and that the blends that previously showed good evaporation rate (PM7, A and F) produce more pronounced films than before. Adjusting the plate temperature to the T90 of each droplet did result in a more even evaporation rate behaviour, but the differences were not eliminated completely. These two observations indicate that the evaporation behaviour of multi-component liquids cannot be scaled with a single parameter, *i.e.* T90, but is in fact more complex and requires a more in depth characterisation, an observation that was also made by Stanglmaier *et al.* [65]. Choosing a plate temperature of 200 °C, which exceeds the T90 of all liquids, greatly increased the

evaporation rate and the differences between the blends became no longer visible. This demonstrates the importance of the piston temperature during engine operation. The trends presented here were used as a basis for subsequent experiments analysing the spray structure and a quantitative analysis of the fuel deposit on a metal impingement plate.

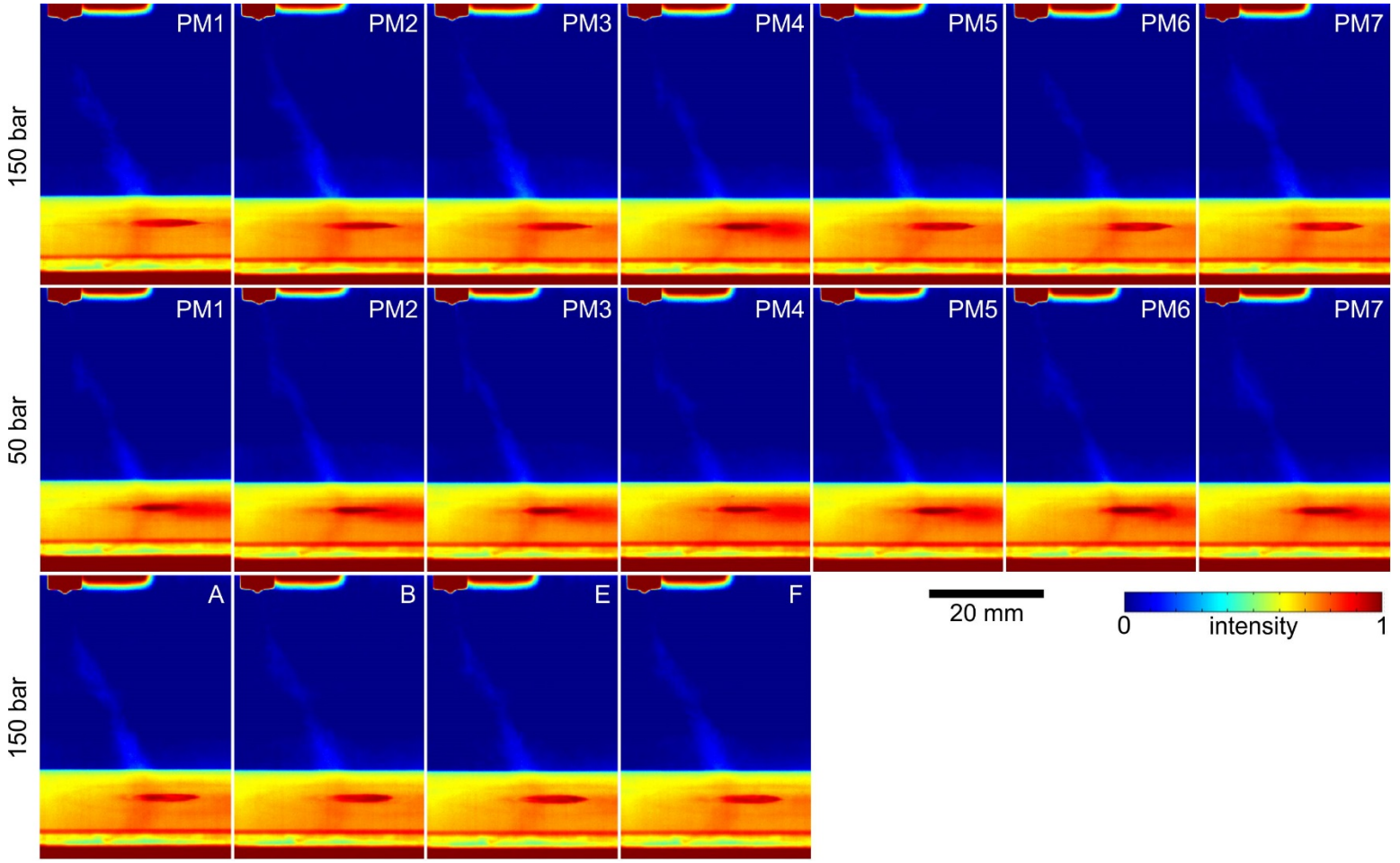


Fig. 5.10 *Normalised mean images with the impingement plate installed at 0.534 ms after VEOI, for an air temperature of 80 °C and ambient plate temperature in false colours (normalisation by the largest spray intensity). The injection pressure was 150 bar.*

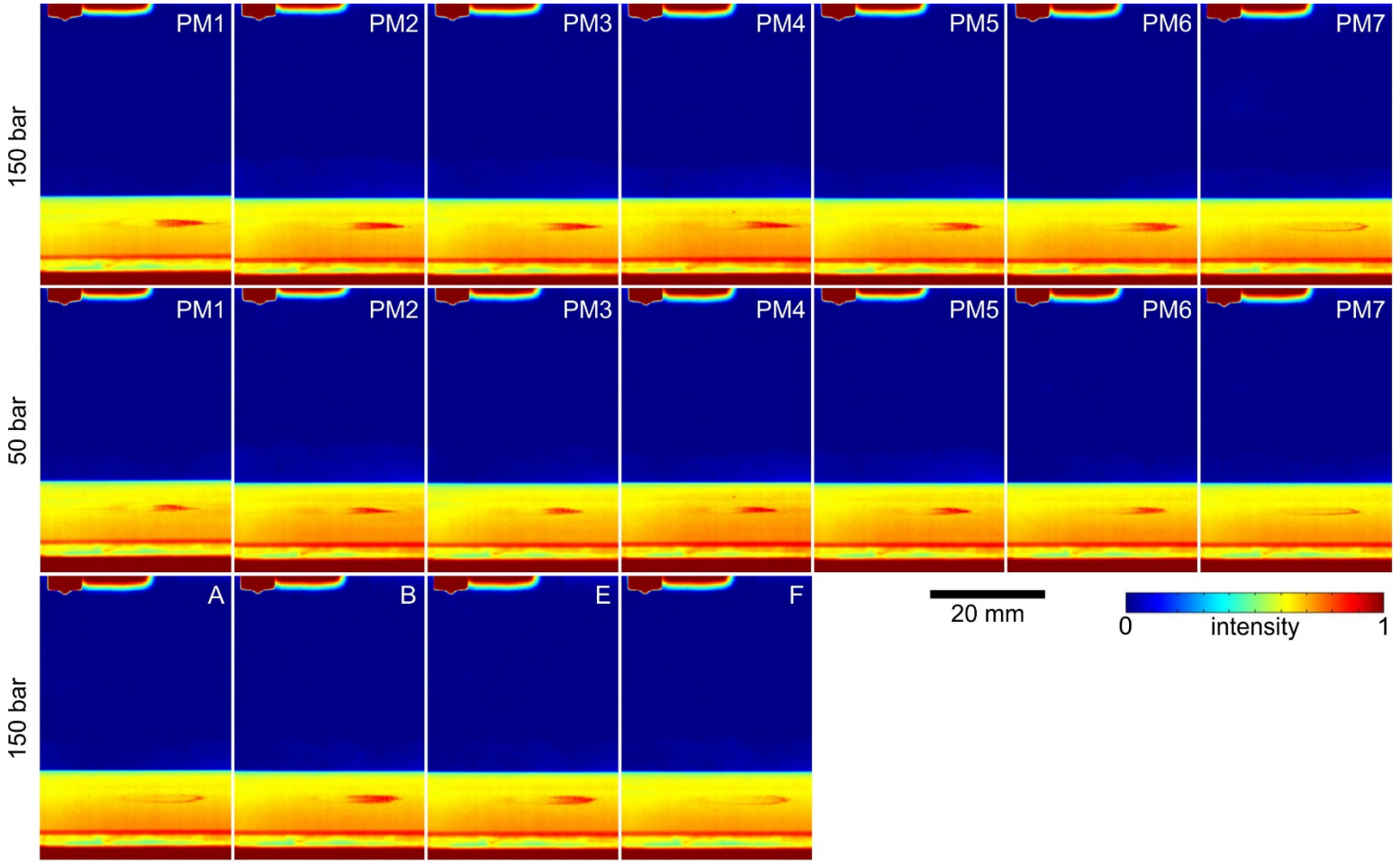


Fig. 5.11 *Normalised mean images with the impingement plate installed at 5 ms after VEOI, for an air temperature of 80 °C and ambient plate temperature in false colours (normalisation by the largest spray intensity). The injection pressure was 150 bar.*

5.2 Size and Velocity Analysis of the spray droplets

Based on the results of the spray pattern analysis fuel blends PM1, PM2, PM3, PM5 and PM7 were selected for the droplet size and droplet velocity measurements. This was done through Phase Doppler Anemometry. The intention was to analyse the differences observed in the previous chapter in a more detailed way to examine how much effect the increased ethanol content, the changing viscosity and surface tension have on the spray.

Before the actual data acquisition, the time signal of the droplet velocity of a series of injections for each fuel blend was evaluated. This was used to assess the velocity as the spray edge was approaching the probe volume and how it changed after the injection was completed. An example of such a time signal can be seen in Figure 5.12.

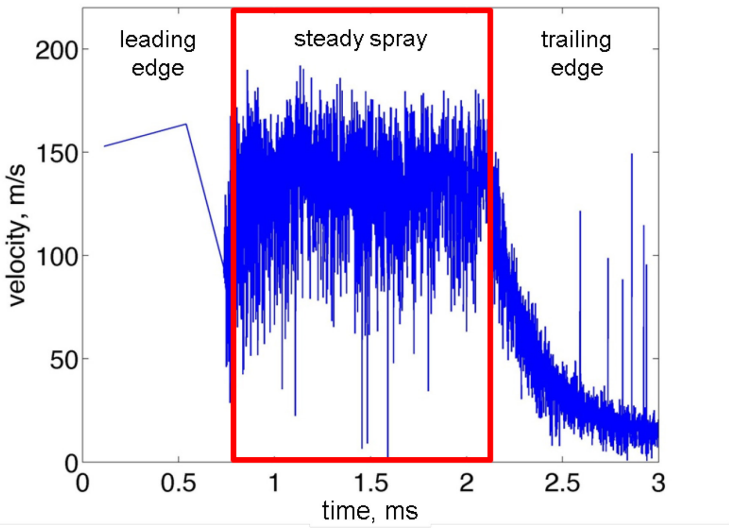


Fig. 5.12 *Superimposed time series of 10 complete injections of fuel blend PM1 (injection width 1.51ms) with absolute timing. The injector triggering was performed through the PDA controller.*

It was made sure that no droplets remained in the injection chamber before each measurement. As such, there is no signal detected immediately at the start of the recording. The injector was triggered at the same time and about 0.7 ms after the leading edge of the spray was approaching the probe volume. Because of compression effects of the spray, the velocity is affected and as such lower than the average of the steady spray. From 0.8 ms onwards, the signal stabilises and becomes steady, with a large yield of valid droplet velocities. This period lasts as long as the set injection time on the injector electronics. Once the injection is completed, and the trailing edge of the spray reached the probe volume (2.1 ms into the recording) the velocities are decreasing rapidly and converge to around 0 ms^{-1} velocity. In this example the signal between 0.8 ms and 2.1 ms is considered to be representing the steady spray and equates to the extracted signal of each recording. These limits were kept constant for all fuels and measurement locations inside the spray. This method assured that the comparability of the results was available.

During each measurement, the probe volume of the Phase Doppler instrument was moved from one side of the spray to the other in a single direction to avoid spatial hysteresis caused by the traverse. For each location 20000 data points were collected and, from this, the arithmetic mean droplet velocity and droplet diameter (AMD) were calculated with the corresponding values of standard deviation values. Additionally, the Sauter mean diameter (SMD) was calculated. It equates to the diameter of a single droplet with the same volume to surface ratio as the cumulative volume of all spray droplets over the cumulative surface area [197], [204]. It is defined as

$$SMD = \frac{\int_0^\infty D^3 dN}{\int_0^\infty D^2 dN_i} \tag{5.1}$$

where D is the droplet diameter and dN is the number of droplets with the diameter D. Small values of the SMD mean that the spray produced a small volume to surface ratio, which corresponds to a large interface that enhances the evaporation rate of the spray. This would be preferred in a gasoline direct injection engine in order to minimize residual liquid fuel and wall wetting during the combustion phase.

Figure 5.13 shows the radial profile of the mean droplet velocity and droplet diameters (AMD) as well as the calculated SMD for fuel blend PM1. The distance from the injector tip was 45 mm.

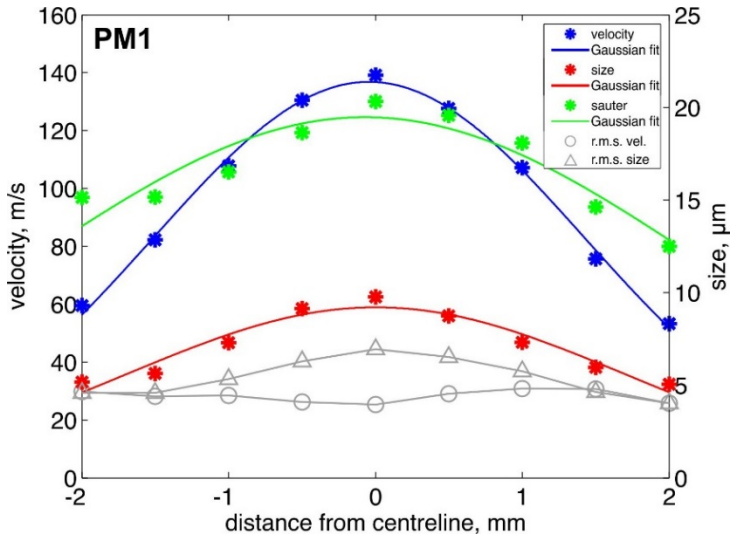


Fig. 5.13 *Radial profile showing the mean droplet velocity (✳), arithmetic mean droplet diameter AMD (✳), the calculated Sauter mean diameter SMD (✳), the standard deviation of the velocity (△) and the standard deviation of the droplet diameter (○), with corresponding Gaussian fits (solid lines of the same colour) of the spray generated by blend PM1, 45 mm downstream of the injector tip.*

The radial profiles of all three quantities are symmetrical with their maxima at the centerline of the spray. Mean velocity reaches a maximum value close to 140 ms^{-1} at the centre and about 60 ms^{-1} close to the border of the spray at distances ±2 mm from the centre. This means that the velocity decay is more than 50% of its maximum over the half-width of the spray. Such an observation was also made by Mitroglou *et al.* [175] and Behringer *et al*. [179] and is quite characteristic for sprays of multi-hole injectors as the droplets at the centre are shielded from the momentum loss between the fast moving liquid and the air continuum. The AMD of the droplets also show a decay from the centre

outwards, but the magnitude of the gradient is reduced compared to the velocities. The measured maximum is close to 10 µm and the minimum about 5 µm, which also means a difference of 50%. The SMD is about 20 µm in the centre and 13 µm at the edge. Compared to the velocities, which decay almost linearly for distances equal or greater than ±1 mm from the centerline, the mean diameter profiles resemble more a stretched bell curve. The corresponding standard deviation of the velocity remains fairly constant across the spray with values around 30 ms^{-1}. The standard deviation of the AMD is shaped similarly to the mean diameter profile, but it does not decay by the same relative amount with a maximum of almost 6 µm at the centre and about 4 µm at the outside.

In order to examine the location of the maximum and the distribution of the mean velocities, AMDs and SMDs, Gaussian fits were applied to each profile with a least square method. From these fits the magnitude and location of the respective maxima and widths (FWHM, full width half maximum) of the profiles were calculated. These values for fuel blend PM1 are shown in Table 5.3, which also includes the coefficient of determination R^2 of each Gaussian fit.

Table 5.3: *Quantities calculated from the Gaussian fits that were applied to the mean velocity, AMD and SMD profiles.*

quantity	mean velocity	AMD	SMD
maximum	136.73 ms^{-1}	9.21 µm	19.47 µm
FWHM	4.89 mm	5.57 mm	7.57 mm
position of maximum	-0.04 mm	0 mm	-0.07 mm
R^2 of the fit	0.9953	0.9301	0.8608

The maximum values determined through the Gaussian fit are slightly smaller in all cases, as can also be seen in Figure 5.13. The width of the spray (FWHM) is increasing from the fit of the velocity to the SMD fit, which is due to the flatter shapes of the size plots and the larger values of the SMD. The position of the maximum coincides almost perfectly with the indicated centerline of the plot, which is a result of symmetrical shape of the

measurement data. The coefficient of determination (R^2) of the Gaussian fit is very high for the mean velocity and slightly smaller for the AMD and SMD points. Looking at Figure 5.13 it becomes clear that the droplet sizes follow more an s-shaped curve towards the outside of the spray cone which results in a less accurate fit. Overall, the values and distributions presented have the same magnitude shown by other groups for similar conditions [58], [179].

The above analysis steps were also repeated for the fuel blends PM2, PM3, PM5 and PM7. A comparative overview of these plots can be seen in Figure 5.14 and a summary of the quantities calculated from the Gaussian fits is presented in Table 5.4. The latter also includes the surface tension and the viscosity of each liquid.

Table 5.4: *Overview of the quantities calculated from the Gaussian fits of all fuel blends investigated.*

quantity	PM1	PM2	PM3	PM5	PM7
maximum velocity, ms^{-1}	136.7	139.5	138.9	138.4	132.0
maximum AMD, µm	9.2	9.1	9.3	9.3	10.1
maximum SMD, µm	19.5	19.7	19.8	19.9	20.4
FWHM of velocity fit, mm	5.0	4.7	4.7	4.8	5.5
Surface tension, $N\ m^{-1}$	0.023	0.023	0.025	0.024	0.025
viscosity, mm^2s^{-1}	0.594	0.596	0.578	0.691	2.300

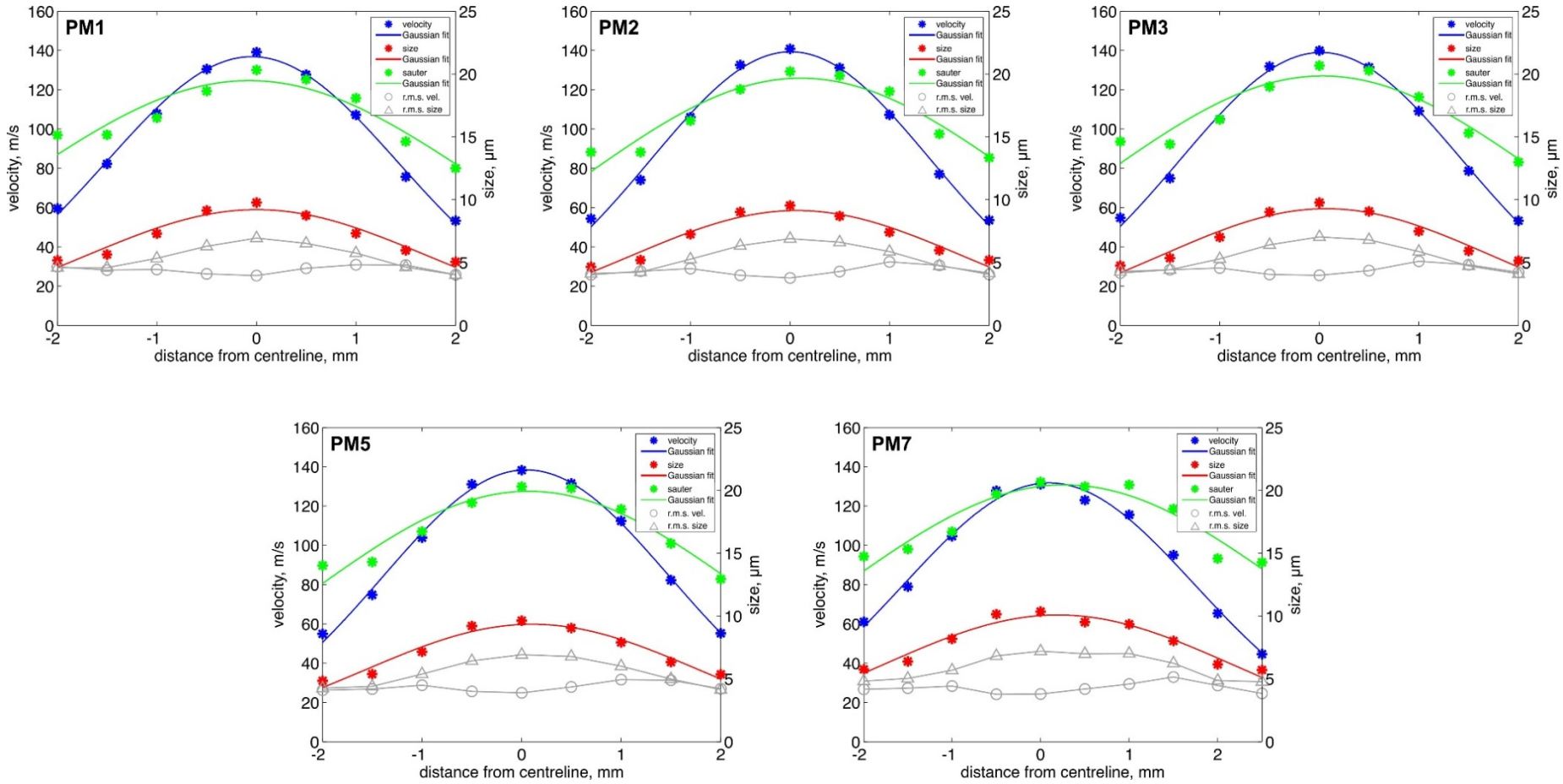


Fig. 5.14 *Radial cross profile showing the mean droplet velocity (✳), arithmetic mean droplet diameter AMD (✳), the calculated Sauter mean diameter SMD (✳), the standard deviation of the velocity (Δ) and the standard deviation of the droplet diameter (o), with corresponding Gaussian fits (solid lines of the same colour), of all the investigated fuel blend, 45 mm downstream of the injector tip at ambient temperature and 150 bar rail pressure.*

The droplet distributions across all sprays are almost identical, both in velocity and size. Both the magnitude of the maxima and the decay from the centerline outwards show the same behavior, with fuel PM7 being the only exception. The spray of the latter produces centerline velocities that are slightly smaller than the rest with minimally larger values for the AMD and SMD. Additionally, the radial profiles are not completely symmetrical. For this reason, data at an additional position 2.5 mm away from the plane of nominal symmetry was recorded. The physical properties of PM7 are significantly different from PM-PM3 with a surface tension about 10% larger and a viscosity almost four times as high. This relation is in contrast to the findings by Marchitto *et al.* [176] who observed increased velocities and diameters for liquids with higher viscosity and surface tension. However, in their experiments the difference of the latter was larger than here.

A possible explanation could be a higher evaporation rate of ethanol, which would lead to smaller droplets with lower momentum and, as such, lower velocities at the probe volume. However, despite the large difference in viscosity of fuel PM7, the differences are still very minor.

Using the FWHM values as a characterisation of the spray widths, it can be compared to the values determined during the spray shape analysis experiments. The values shown in Table 5.5 are for the ambient air temperature case. The values of the FWHM of the Gaussian velocity fits are larger compared to the image intensity based method by about 14% to 32%. This difference in magnitude between the two techniques is common, as the PDA technique is more reliable in capturing the highly unsteady edge compared to light scattering based methods [205]. The overall trends, however, are the same in this case. The width, generated by the blends PM1, PM2 and PM3 do not change notably. By increasing the ethanol content the spray cone becomes larger and reaches a maximum for blend PM7 with 85% ethanol. This means that the observation of the previous chapter is also reflected in the Phase Doppler measurements.

In order to further compare the spray structures of the different fuel blends and to look more extensively into potential similarities and differences between them, a more detailed statistical analysis of the droplet velocities and diameters was performed. For this purpose the steady spray phase of each centerline position described in Figure 5.12, was

divided into three windows looking at the beginning, the middle and the end of the injection. The intention is to assess if the spray changes over the course of an injection, which might not be reflected in the mean values. The first window was between 0.8 ms and 1.0 ms, the second between 1.4 ms and 1.6 ms and the third between 1.9 ms and 2.1 ms. A graphical representation of the time segments is shown in Figure 5.15.

Table 5.5: *Comparison of the spray width based on the Gaussian velocity fits and the values calculated from the intensity analysis in chapter 5.1.*

fuel	FWHM, mm	avg. width chapter 5.1, mm	delta [*], %
PM1	4.98	3.41	31.48
PM2	4.67	3.55	23.89
PM3	4.72	3.52	25.34
PM5	4.80	3.97	14.24
PM7	5.48	4.23	22.84

[*)] difference relative to FWHM

For each fuel blend the extracted data was accumulated and processed separately. The time signal of the droplet size was compared and scatter plots correlating the velocity with droplet size of every droplet were generated. The latter shows the connection between the droplet size and the carried momentum, which is expressed in the velocity. Generally, larger droplets should retain a higher momentum and hence show larger velocities at the probe volume. The results for blend PM1 is presented are Figure 5.16.

The majority of the droplets form a cluster between 0-20 µm and 75-175 ms^{-1}. Only very few droplets have smaller velocities and larger sizes than this. Comparing the three extraction windows there are no apparent differences. This means that the droplet characteristics do not change between the beginning and the end of the injection process, neither in size nor in velocity for this fuel. The same behavior was found for the other blends. None of them showed any noticeable changes of the droplet sizes and velocities over the course of the injection.

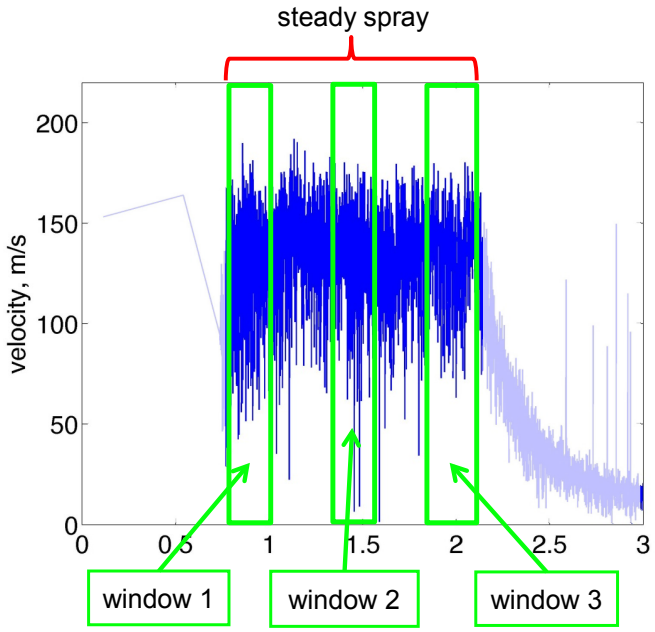


Fig. 5.15 *Illustration of the three windows that were extracted from each time series corresponding to the droplet distributions at the beginning, the mid and the end of the injection. The three windows are highlighted in green.*

To further compare the behavior of different blends, the same type of plots was compiled for each centerline point. Because there was no change within the steady state phase of any observed spray, the entire recording duration – as shown in Figure 5.12 – was used. The different scatterplot correlations between size and velocity are shown in Figure 5.17. Additionally, the Weber Numbers for all droplets were calculated (cf. Equation 2.1) and correlated with the droplet size (Figure 5.18).

Despite the detailed depiction of the centerline droplet characteristics presented, there are no noticeable differences between the different fuel blends, similar to the radial profiles of the mean droplet velocities, AMDs and SMDs. The majority of the droplets of all blends have sizes between 0 and 20 µm and velocities between 75 and 175 ms^{-1}. Even blend PM7, which shows slightly different values across the spray, does not show any differences in these plots. The same can be concluded for the Weber Numbers that are below $2.5x10^4$ for all blends, which are values that can be found for these types of sprays, when the absolute droplet velocity is considered [206]. Additionally, the Weber Number

based on the slip velocity between the air and the spray droplets can be calculated [207]. Assuming that droplets of a size smaller than 5 µm follow the flow the air velocity can be approximated by their mean droplet velocity. This value can then be subtracted from the measured droplet velocity and the slip velocity based Weber Number can be calculated. These plots are shown in Figure 5.19. Again, all fuels have almost identical values with the majority of droplets below 1000. The presented Weber Number values mean that the same level atomization of the spray is occurring in all cases.

Combining the information of all plots shown in this chapter it can be seen that there are no differences observable in the spray structure of the investigated blend with the very mild exception of PM7 that generated a slightly wider spray cone with marginally lower velocities and bigger droplets.

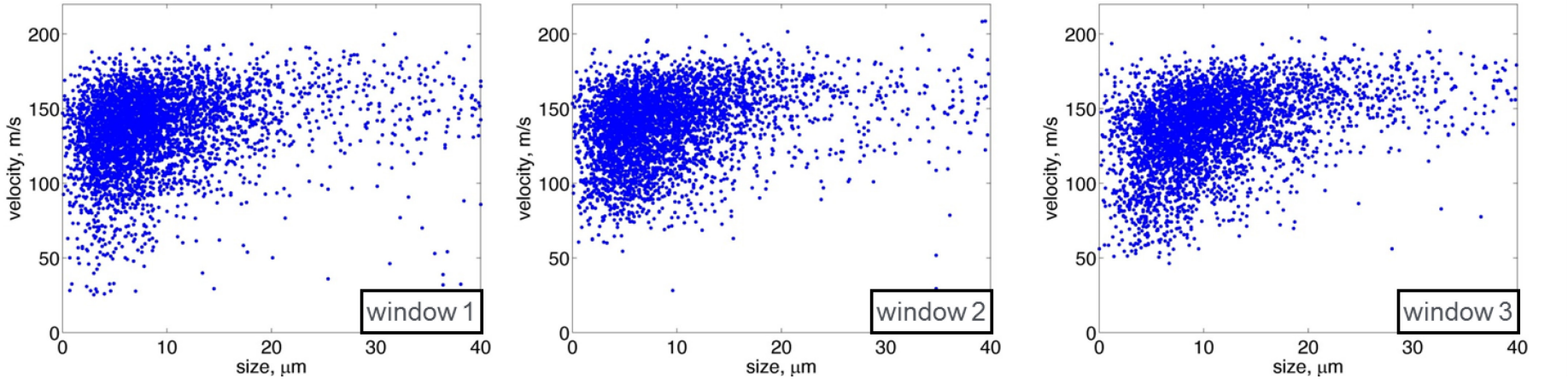


Fig. 5.16 *Scatter plots of the correlation between the droplet size and velocity of the three extracted windows for the centreline point of fuel blend PM1 at ambient temperature and 150 bar rail pressure.*

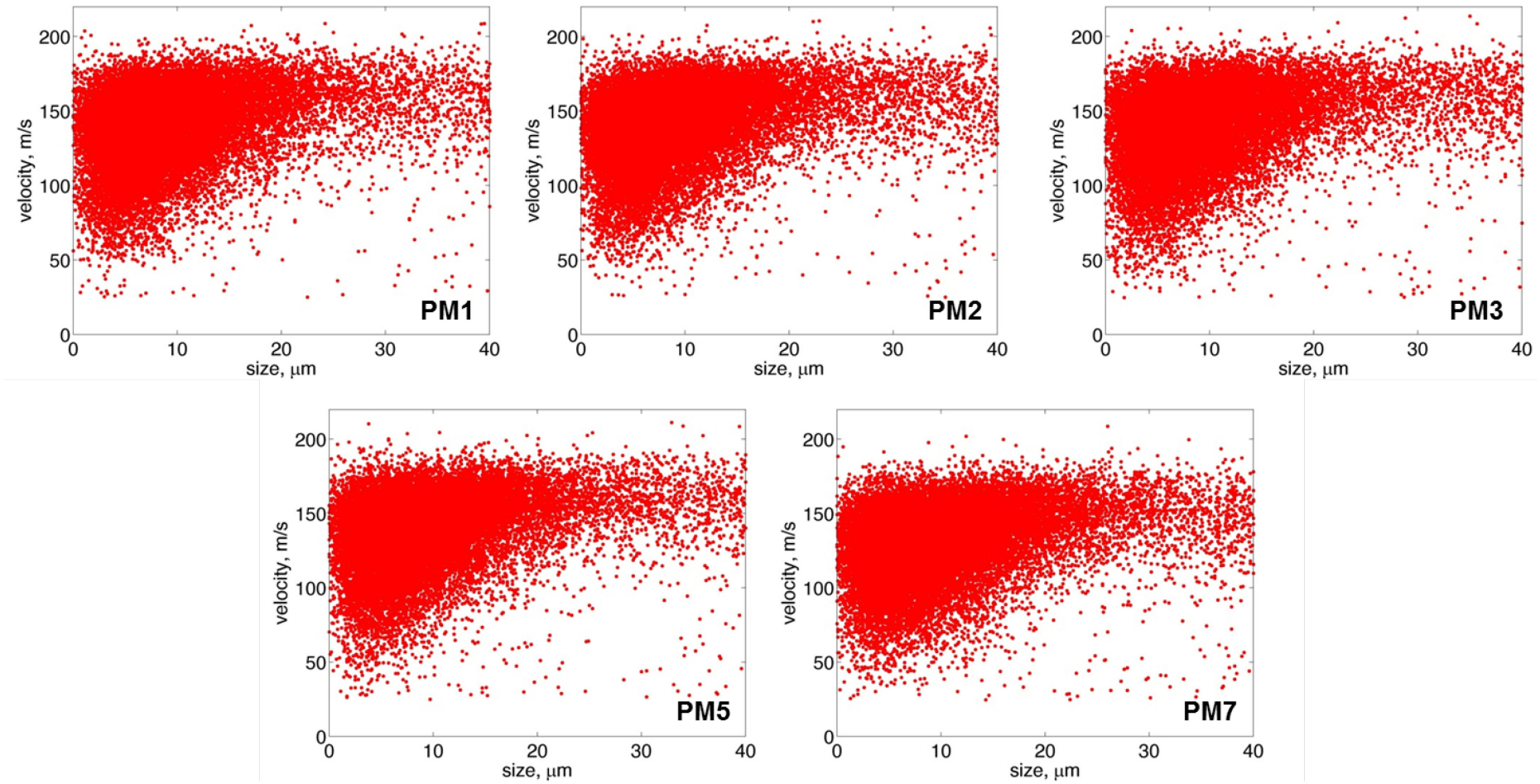


Fig. 5.17 *Scatter plots of the correlation between the droplet size and velocity for the centreline point of all fuel blends at ambient temperature and 150 bar rail pressure.*

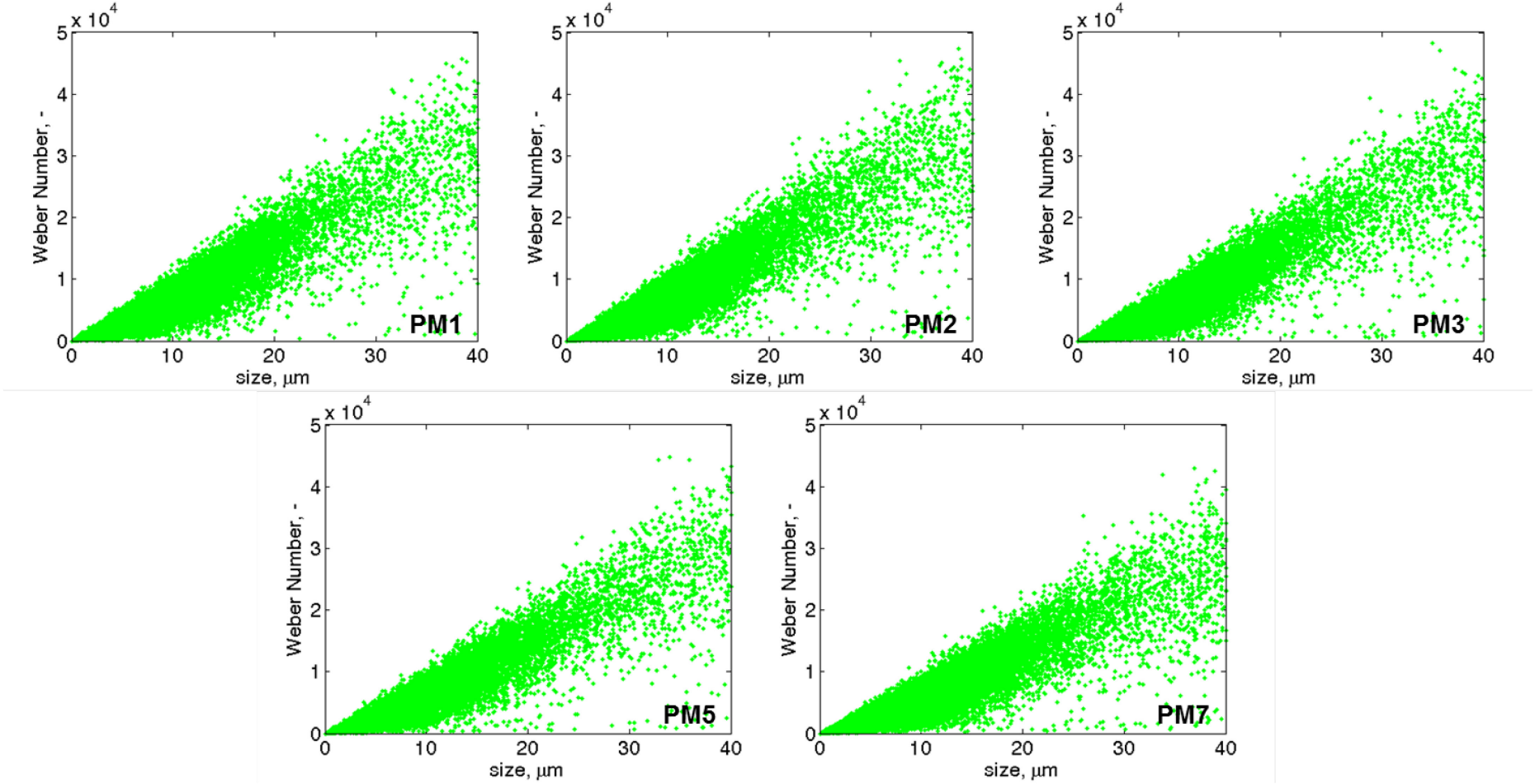


Fig. 5.18 *Scatter plots of the correlation between the droplet size and Weber Number of the centreline point for all fuel blends at ambient temperature and 150 bar rail pressure.*

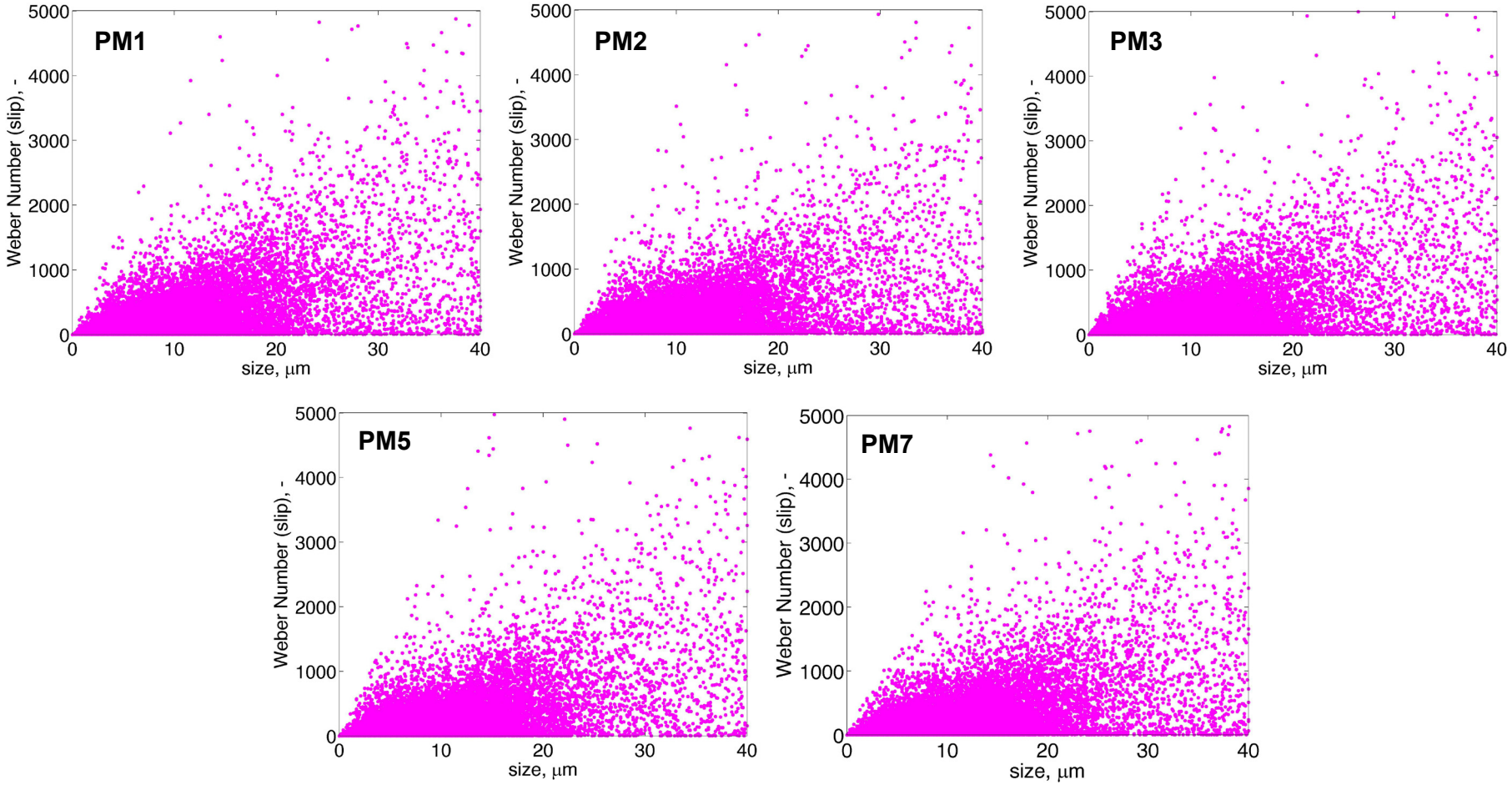


Fig. 5.19 *Scatter plots of the correlation between the droplet size and Weber Number based on the approximated slip velocity between the air and the spray droplets of the centreline point for all fuel blends at ambient temperature and 150 bar rail pressure.*

5.3 Analysis of the liquid deposit formed by the impinging spray in the injection chamber

After the spray pattern analysis and the droplet size and velocity measurements, the experimental setup was modified to accommodate the technique presented in chapter 4 to quantify the liquid deposits of the impinging sprays on the rough metal surface. The results of the preceding experiments showed strong similarities between the sprays with nearly identical droplet distributions. Some differences were observed in the qualitative analysis of the liquid deposit on the glass plate (chapter 5.1), *e.g.* increasing ethanol content promotes the evaporation of the fuel film.

For the experiments of the impinging fuel sprays with the rough metal plate, seven fuel blends were selected in the first run. These were PM2, PM3, PM5, PM6 and PM7 from the physical matrix as well as A and E from the chemical matrix. All blends were injected at 150 bar into the chamber at ambient air temperature with the plate at temperatures of 120 °C and 160 °C. The air temperatures measured above the plate were around 50 °C for the lower plate temperature and 90 °C for the higher. Each measurement was repeated five times for each blend and condition, and mean images as well as mean deposit volumes were calculated from these, analogous to the results presented in chapter 4.5. From the image series, the extent and the local thickness of the fuel deposit can be obtained. An example of this is shown in Figure 5.20.

The initial PM2 fuel film on the surface of the impingement plate appears almost circular with a slight deformation on the right edge (Figure 5.20a). The measured thickness looks fairly even but on the left side there is a darker region that roughly corresponds to the point where the spray impinges on the plate. This observation agrees with the finding of the qualitative deposit analysis on the glass plate in chapter 5.1, where the film is less pronounced on the side where the spray impinges on the surface. Most of the initial deposit thickness is between 2 and 3 µm. As time progresses, the liquid film is evaporating (Figure 5.20b) and changes its shape. The film in the area that was perceived as thinner in the initial frame has almost completely evaporated by 10 ms after VEOI and a “hole” is created in the deposit. Additionally, the film is beginning to evaporate from the lower right

border. The entirety also becomes more inhomogeneous with a dark horseshoe shaped area that originates from the evaporated spot on the left forming an arch that goes anti-clockwise through the film. The processes are emphasised over time (Figure 5.20c), with an increasing black area, where the spray had originally impinged and growing gaps throughout the film. Also the overall thickness is decreasing noticeably. This behaviour continues with time and most of the deposit disappears (Figure 5.20e). More or less only the top left rim of the deposit remains at this stage. At 33 ms after VEOI (Figure 5.20f), there is only a very small fraction of the initial deposit left and the fuel has evaporated almost completely.

In the analysis of the time series of the other fuel blends, similar non-homogeneous evaporation behaviours over time were observed, where gaps are formed in the film by regions that evaporate faster than others. The magnitude of these deposits, however, was vastly different between the fuel blends. Figure 5.21 shows a comparison of the maximum fuel film area and thickness measured for each of the blends.

With this comparison it becomes obvious that there are great differences between the fuel blends in the context of wall wetting and fuel deposit formation. Fuel PM3, in comparison to PM2, produces liquid deposits that are much larger in size and thickness. Even though the basic shape is similar, with a rounded boundary at the left side and a deformed right side, the PM3 film exceeds PM2 distinctively, so much in fact that it is the largest and thickest deposit of all blends investigated. Additionally, the former shows spatter marks on the right side, most likely generated by the moving droplets and flow of the adhered liquid during the injection. These marks are characteristic for PM3 and cannot be observed for any other fuel at such a magnitude. Furthermore, large regions of this deposit reach thicknesses of 7 µm, which is not the case for other blends. Despite these unique properties, the characteristic thinner region on the left side, where the spray collides with the surface, also exists here. Switching to the deposit of fuel PM5 more similarities to PM2 are obvious. Both the area as well as the thickness are very comparable between them.

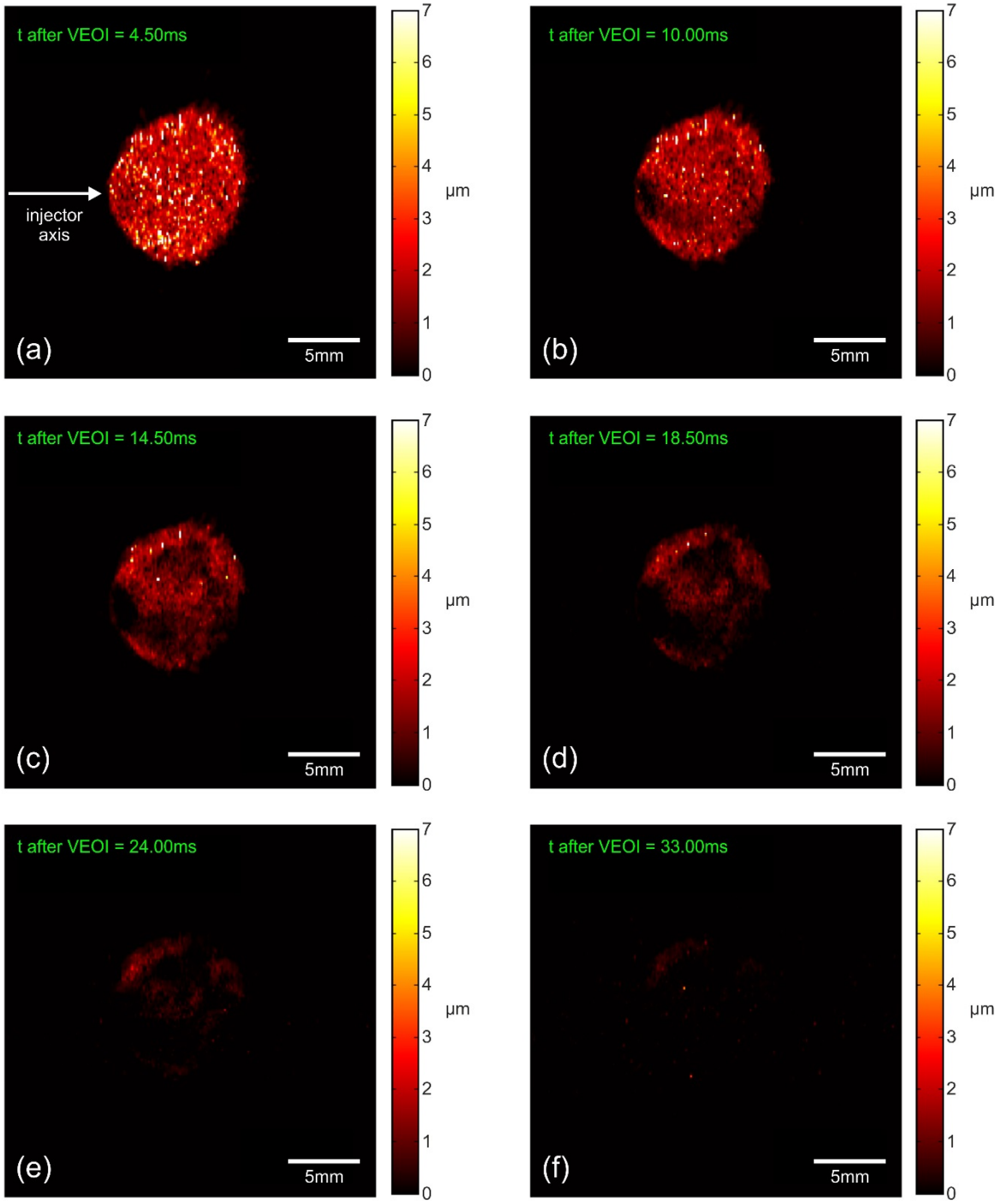


Fig. 5.20 *Extracted frames of the processed recording of the fuel deposit on the rough metal impingement plate for blend PM2 with a time stamp showing the time after the visible end of injection. The images represent the calculated mean from five repeated recordings for the measurements with a plate temperature of 120 °C and 150 bar rail pressure.*

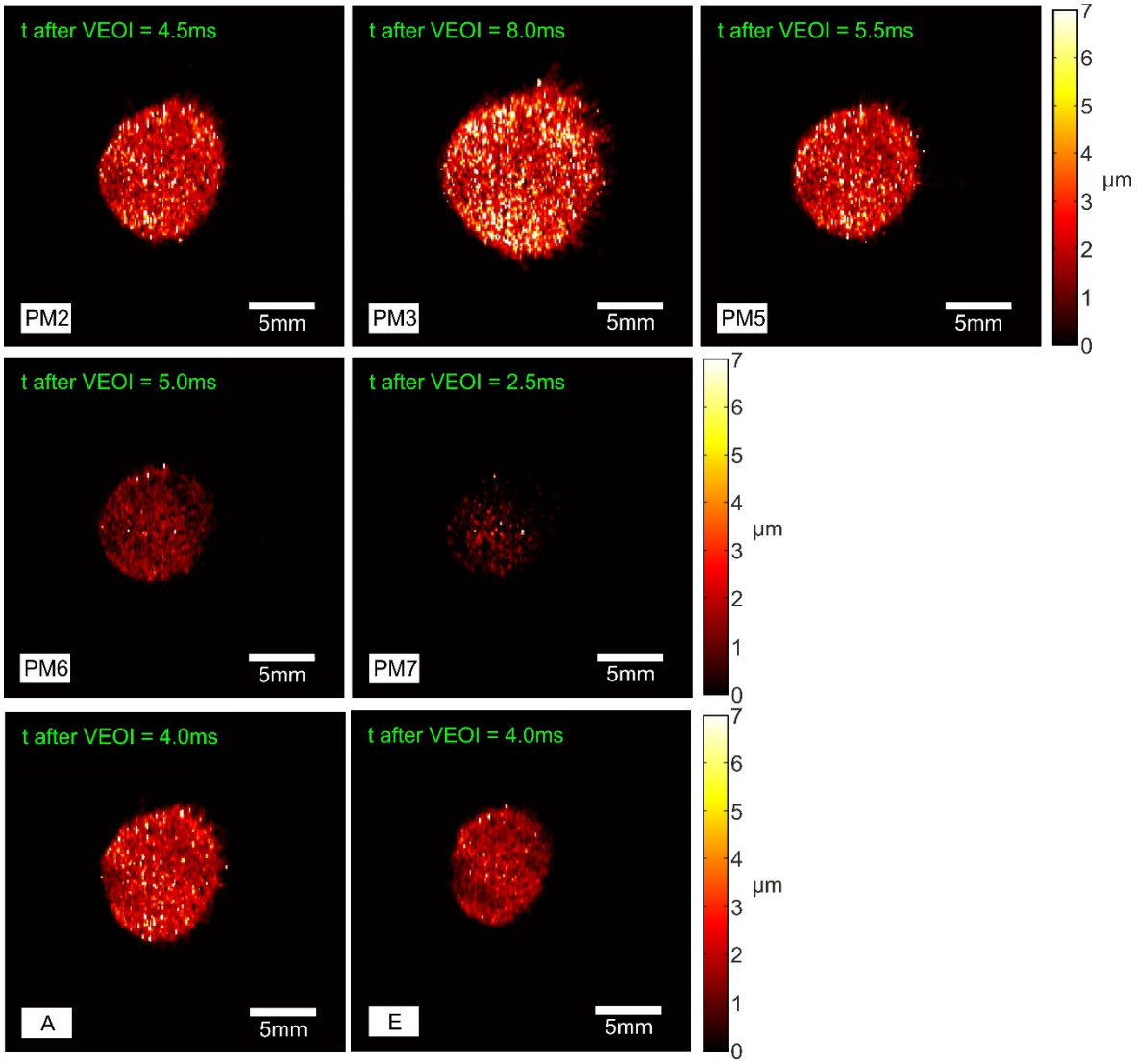


Fig. 5.21 *Maximum mean fuel deposit of each blend for a plate temperature of 120 °C and 150 bar rail pressure, with the corresponding time after VEOI. Note that the time is different for each fuel blend.*

If one compares PM5, PM6 and PM7, a drastic reduction in the deposit can be seen. These three represent the fuel axis with increasing ethanol content in the physical matrix, where PM5 has 20%, PM6 50% and PM7 85% ethanol in its blend. While PM5 is comparable to PM2, the difference in this case is 15%, ethanol has a noteworthy impact on the deposit when going from 20% to 50%: the area of the deposit is reduced by about 30% and the thickness is between 1 to 2 µm instead of 3 to 4 µm. Once 85% ethanol content is reached,

the deposit is reduced to such an extent that it becomes almost non-existent relative to the other blends. This is by far the smallest and thinnest fuel film observed during all measurements with a plate temperature of 120 °C.

The two deposits of the chemical matrix are similar to PM2 and PM5 in shape rather than to PM6 and PM7. Blend A produces a larger and thicker fuel film than blend E, which is about 30% smaller. The former reaches thicknesses of around 3 µm and the latter of around 2 µm. The deposit of blend E also seems more uneven with a more progressive evaporation.

Overall it is striking that, despite the large difference between the blends all deposits show a distinct darker area where the spray meets with the plate and the left side of the deposit is usually more rounded than the right side.

In order to further elaborate on the evaporation rate behaviour of all blends and their differences, later frames of each mean image time series were analysed. Figure 5.22 shows images of the partially evaporated deposit for every blend. The images were selected in a way that the remaining fuel was at a similar level in all cases, with thicknesses around 2 µm.

The inhomogeneous evaporation described in the image series of PM2 (Figure 5.20) is reflected in the behaviour of all blends. In particular the darker region seen in the initial deposit corresponding to the collision area of the spray, is evaporating the fastest. The resulting gap in the film propagates towards the lower right side in all cases. At the same time, additional parts that are no longer covered by fuel appear in the top right. Looking at the time scale it becomes again evident that the different blends behave differently in the wall wetting. To reach the stage of the deposits shown in Figure 5.22, blend PM3 requires by far the longest with 93 ms after VEOI and blend PM7 the shortest with 4.5 ms after VEOI. The latter is just a single frame after the maximum deposit. The second fastest evaporation of the physical matrix blend is occurring for PM6 with less ethanol, followed by PM2 and PM5. The two chemical matrix blends are again closer to PM2 and PM5 rather than PM6 and PM7. Between them, E takes less time to reach this level than A.

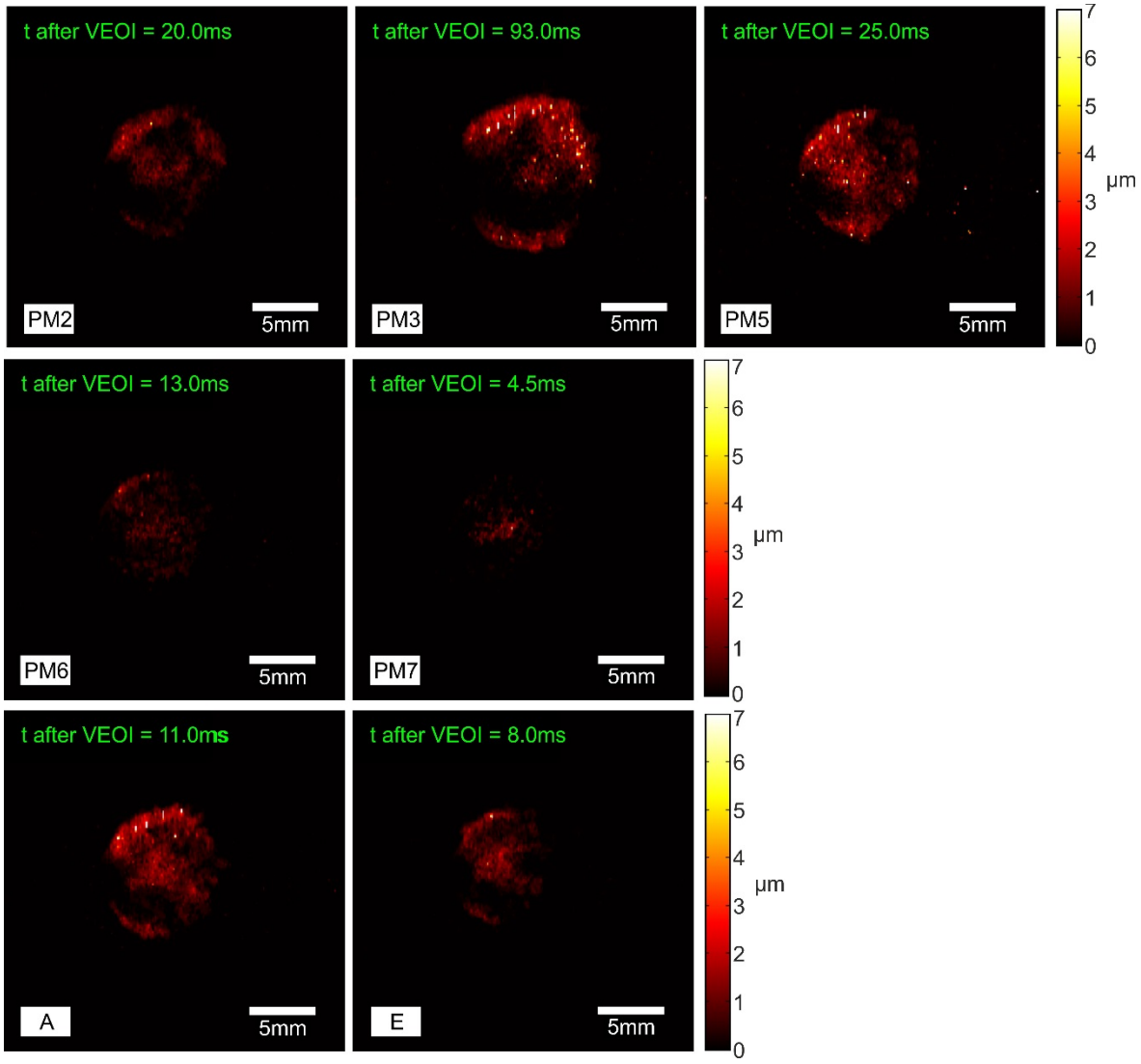


Fig. 5.22 *Partially evaporated mean fuel deposit of each blend for a plate temperature of 120 °C and 150 bar rail pressure, with the corresponding time after VEOI.*

As described in chapter 3.1.4 the same measurements and processing steps were done for a plate temperate of 160 °C to see the impact of surface temperature on the liquid deposit and its evaporation. Figure 5.23 displays the overview of the maximum fuel deposit for each blend with the higher temperature similar to what was presented in Figure 5.21 for the lower plate temperature. Please note that the scale of the thickness is lower than for the 120 °C case.

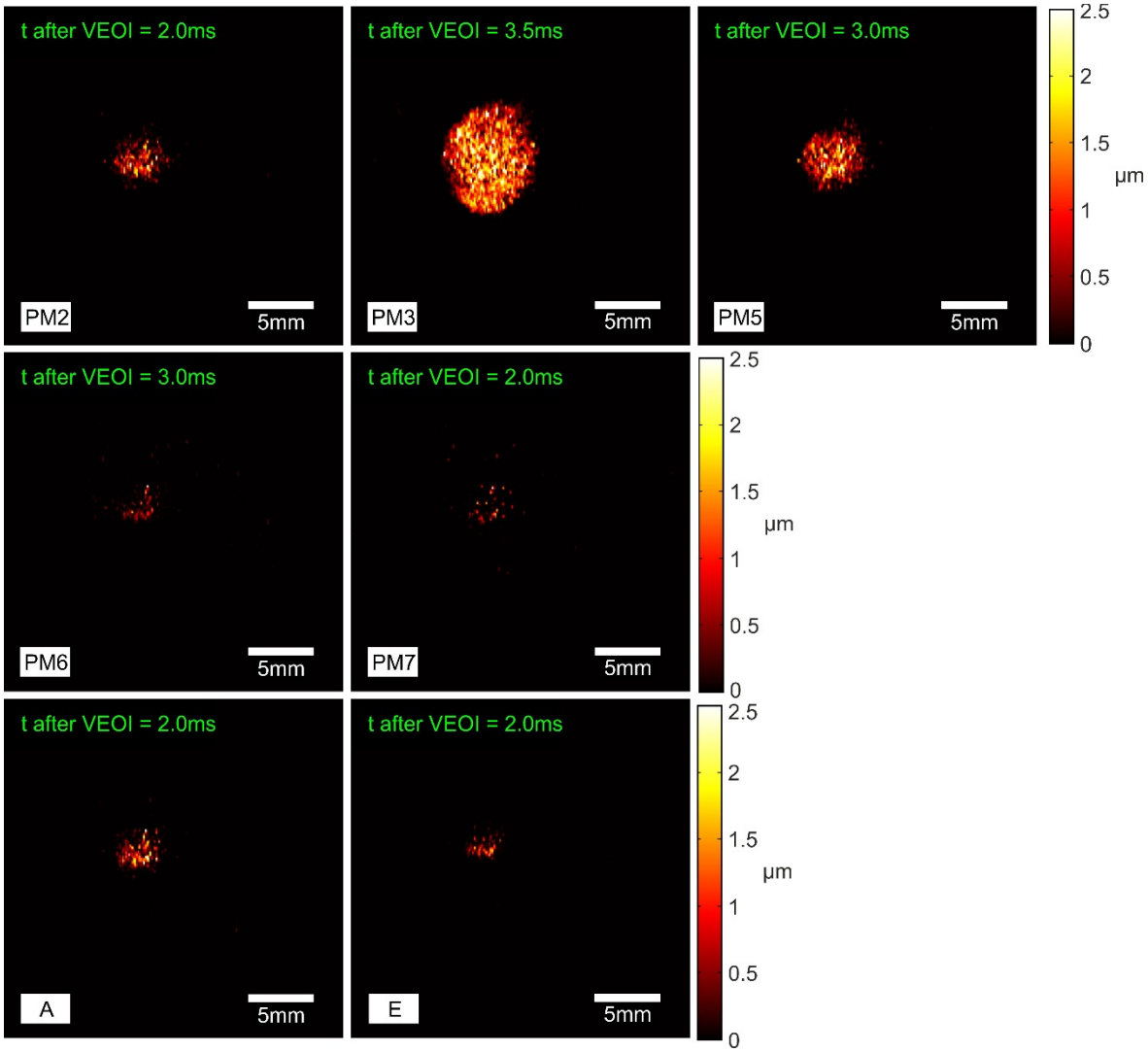


Fig. 5.23 *Maximum mean fuel deposit of each blend for a plate temperature of 160 °C and 150 bar rail pressure, with the corresponding time after VEOI.*

To begin with, the extent of the fuel deposit and the corresponding thickness is greatly reduced at all cases. However, the relative trends observed at the lower temperature measurements are reproduced here. PM3 produces by far the largest fuel film with the highest local film thickness, which is around 2 µm. Although this value is less than a third of what was seen at 120 °C it is still significantly larger than for the other blends. Fuel PM2 and PM5 are much smaller in comparison with thicknesses lower than 1 µm for the most part. Between PM5, PM6 and PM7 and their increasing ethanol content, the film gets reduced further, which is comparable with the lower temperature measurements. In this

case, however, the differences between PM6 and PM7 are less distinct and their maximum deposit in these images seems to be closer together. The two chemical matrix blends behave again more closely to PM2 and PM5 rather than the other three. The deposit of blend A is slightly larger than of blend E.

With all the observations and conclusions made it becomes obvious that the relative behaviour between the fuel blends does not change significantly, but the overall extent reduces drastically by increasing the surface temperature from 120 to 160 °C.

To further deepen these implications the deposit volume over time was calculated from the time series of all fuels and both plate temperatures. This provides a quantitative comparison between the blends and of how they might behave in a direct injection engine. Figure 5.24 shows the fuel deposit volume over time for the blends measured on the plate at 120 °C.

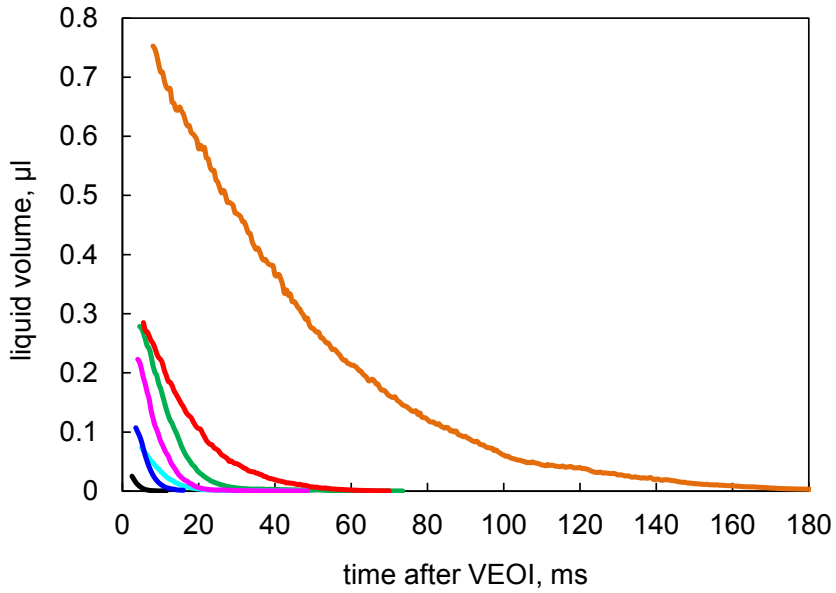


Fig. 5.24 *Mean fuel deposit over time, calculated from the image time series of all seven blends for the plate temperature 120 °C and 150 bar rail pressure, for PM2 (—), PM3 (—), PM5 (—), PM6 (—), PM7 (—), A (—) and E (—).*

The trends observed in the plan view film analysis are also reflected here, with large differences in the deposit volume and evaporation time. The most striking blend is again PM3, which deposits the largest amount of fuel by far. The initial volume reaches almost 0.8 µl and it takes close to 180 ms to evaporate. The other fuel blends are much closer together with PM2 and PM5 starting with almost the same value for the volume. The former, however, takes less time to evaporate, which is most likely to be attributed to its smaller T90. Identical to observations of the plan view film, the liquid deposit volume is reduced with increasing ethanol content for PM6 and PM7. The latter produces the smallest volume and requires the shortest time to evaporate of all blends investigated. The range between the two extremes is more than an order of magnitude, both for the volume and the time required to evaporate. When comparing the two blends from the chemical matrix with each other it becomes clear that blend A deposits about twice as much fuel on the plate as blend E, which is also the case for the time required to evaporate. Overall, it is evident that a larger liquid volume usually leads to a larger evaporation time among the two groups of blends, with the only exception of PM2. Furthermore, all trends described for the plan view film analysis are represented in this plot.

Comparing the results of the 120 °C plate temperature with the 160 °C case (Figure 5.25) it is noticeable that the time and the length scale has reduced drastically by about a factor of 10. The maximum volumes for the larger plate temperature are of the same order as the smallest values of the lower plate temperature. The succession of deposited volume is the same as for the lower temperature, with PM3 producing the largest numbers and PM7 the smallest overall. The gap between PM3 and the rest of the blends is also similarly large. A slightly different behaviour can be observed for PM2 and PM5 which are more distinct for the higher temperature plate. There is about a factor of two between them in maximum volume, while previously their values were close to identical. It shall be noted that the deposits created by PM2, PM6, PM7, A and E are extremely small and are very close to the limit of the experimental setup. Because of this, their absolute values of the volume need to be considered more cautiously.

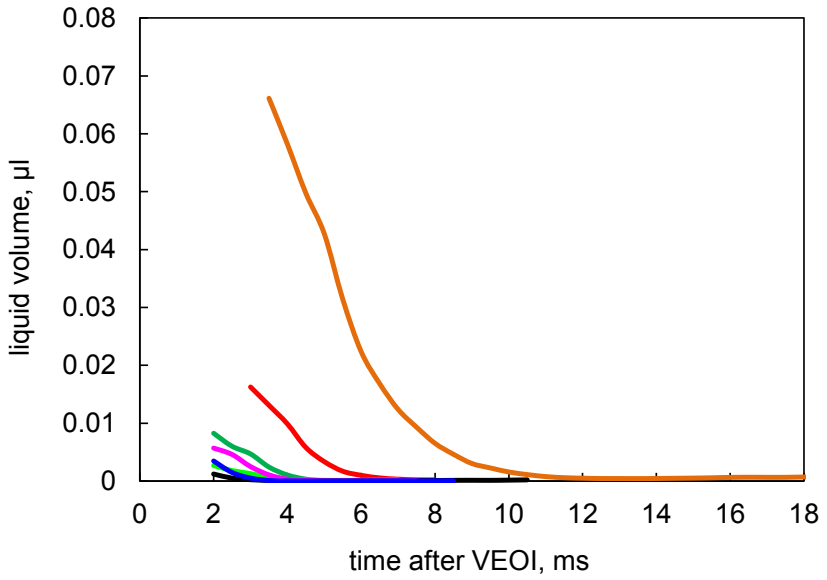


Fig. 5.25 *Mean fuel deposit over time, calculated from the image time series of all seven blends for the plate temperature 160 °C and 150 bar rail pressure, for PM2 (—), PM3 (—), PM5 (—), PM6 (—), PM7 (—), A (—) and E (—).*

In order to evaluate the magnitude of fluctuations between each measurement series, the standard deviation of the liquid film thickness was calculated for all blends. These are presented as individual plots in Figure 5.26 for the lower plate temperature and in Figure 5.27 for the higher.

The standard deviations for all cases of 120 °C are reasonably small and of a similar magnitude relative to the mean value. The fluctuations reduce and converge with the mean volume once the film becomes smaller. They are increasing for the plate temperature of 160 °C and become irregularly shaped. Fuels PM6, A and E exhibit larger deviations at early times. This is most likely due to the droplet cloud above the deposit immediately at the end of the injection. Also, the signal recorded is much smaller for the higher temperature case and smaller deposits caused by these blends.

In general, it was noticed during the analysis of the deposits that a larger film generated by a blend with a lower evaporation rate requires more time to generate a stable signal of the liquid deposit because of the remaining droplet cloud above the film, which is blocking the line of sight of the camera and remains there slightly longer.

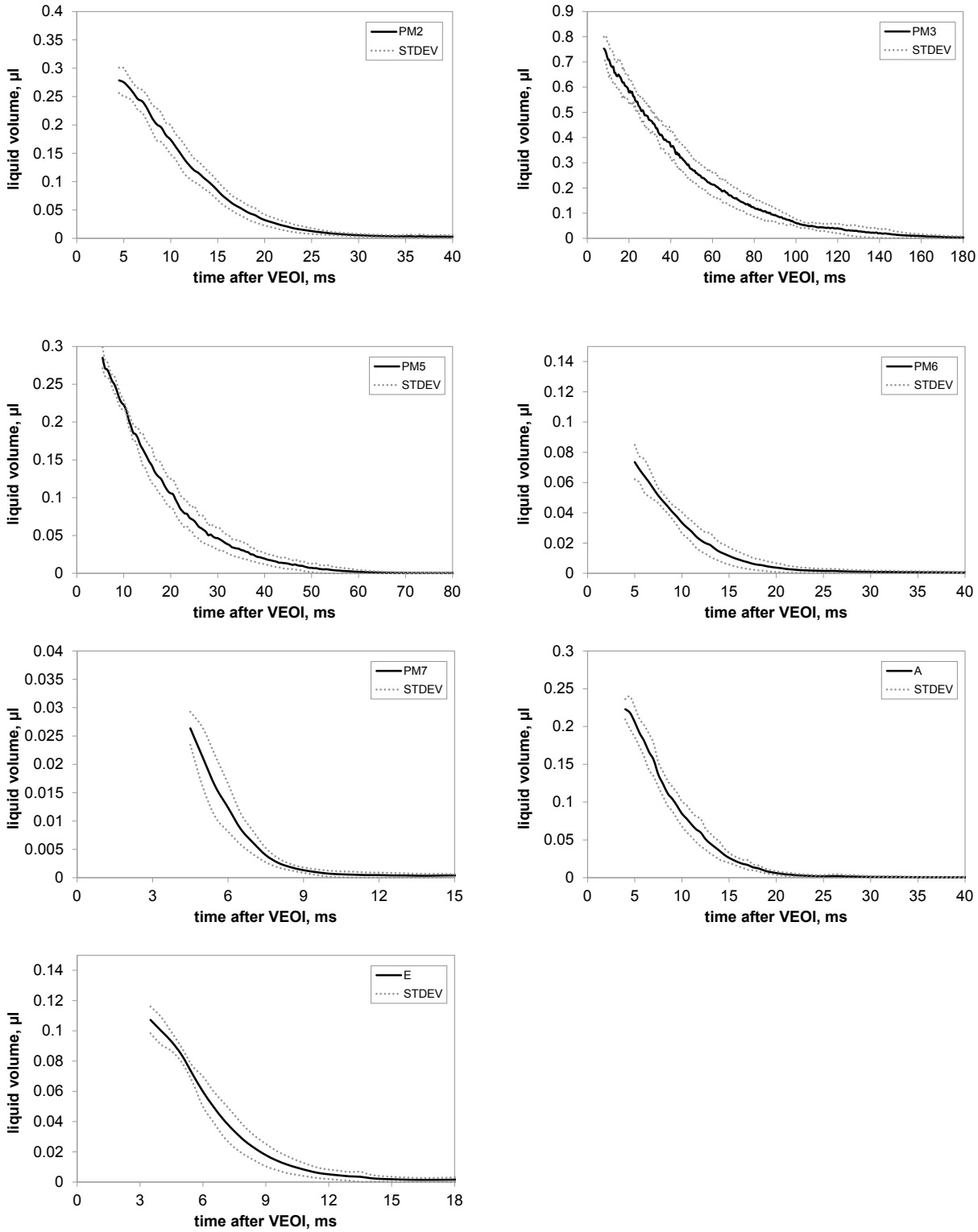


Fig. 5.26 *Mean deposit and standard deviation of each fuel blend for a plate temperature of 120 °C and 150 bar rail pressure as a function of time. The axes are scaled separately for each blend.*

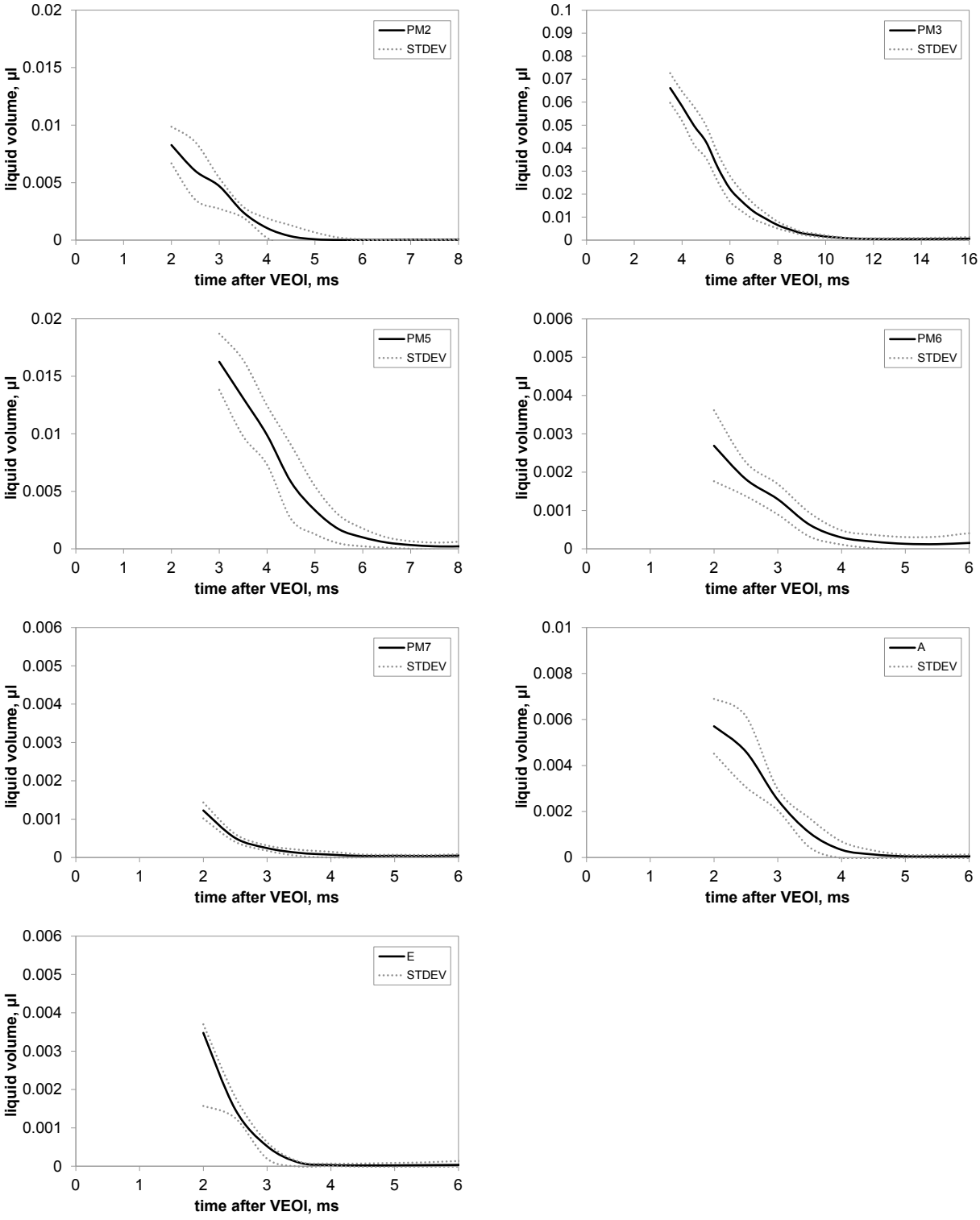


Fig. 5.27 *Mean deposit and standard deviation of each fuel blend for a plate temperature of 160 °C and 150 bar rail pressure as a function of time. The axes are scaled separately for each blend.*

In order to further characterise the evaporation behavior of the fuels, a decay coefficient for each fuel blend and temperature can be determined. This is done by fitting a function describing the exponential rate of evaporation to each time plot. This rate of evaporation is defined as

$$E(t) = E_0 \cdot e^{-t/\tau} \tag{5.2}$$

where E_0 is the maximum fuel deposit, and τ is the decay coefficient. At the time τ, the remaining fuel volume equals $(1/e) \cdot E_0 = 0.3679\ E_0$ or 36.79% of the maximum deposit. Consequently, 3τ refers to the time when 95.02% (resulting from $1/e^3$) of the initial deposit has evaporated. Figure 5.28 illustrates this relation in an example.

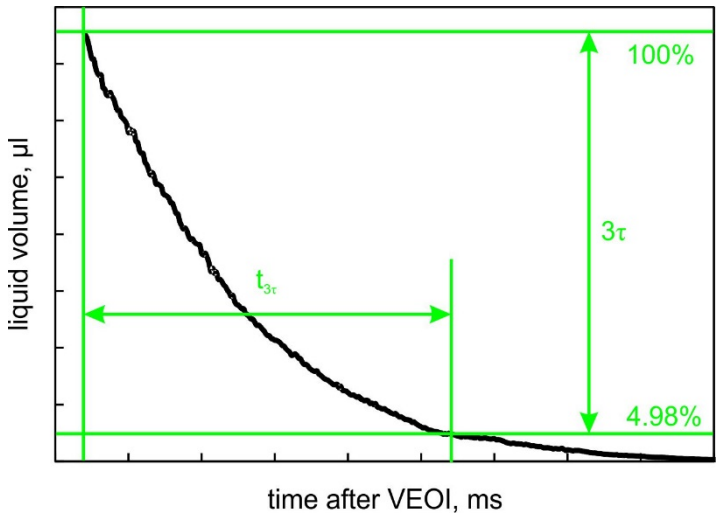


Fig. 5.28 *Example of a time plot and representation of the decay time* $t_{3\tau}$ *and coefficient* 3τ.

Additionally, the deposit mass can be calculated by the measured volume and the density of the liquid listed in Tables 3.1 and 3.2. This mass can then be related to the total injection mass. The latter was calculated by using an approximation based on reference measurements on this particular injector with n-heptane. These measurements yielded an injected fuel mass of 2.46 µg with its density of 0.684 gcm^{-3} at an injection pressure of

100 bar and 1.5 ms injection time. These numbers can be used in Equation 3.1 to calculate a ratio factor between all fuel blends, replacing the lower heating value with the injection time and relating all values to n-heptane and the listed properties instead of PM4. The numbers of n-heptane used here were provided by Nissan Motor Company Limited. for this work.

The results of the maximum deposit mass alongside the injection mass and the deposit decay times for both plate temperatures are listed in Table 5.6. In addition the calculated injection mass, a series of measurements were performed with blend PM3 to measure the mass manually. This blend was chosen as it showed the lowest evaporation rate of all fuels investigated. During these experiments the fuel from different numbers of injections were collected in a vial and sealed with paraffin films (Parafilm M, Bemis NA). From these, the cumulative mass was measured and, through a linear fit, the mass per injection was calculated. For PM3 a mass of 3.9 µg was found, which only deviates by about 10% from the calculated value.

Table 5.6: *Respective decay time $t_{3\tau}$, fuel injection mass, maximum deposit mass, and percentage of deposited fuel for all fuel blends.*

fuel	$t_{3\tau}$, 120 °C, ms	$t_{3\tau}$, 160 °C, ms	Injection mass, µg	max. deposit 120 °C, µg	max. deposit 160 °C, µg	rel. deposit 120 °C, %	rel. deposit 160 °C, %
PM2	23.40	3.43	4.38	0.208	0.00615	4.75	0.14
PM3	123.87	6.31	4.34	0.568	0.0498	13.09	1.15
PM5	40.24	3.97	4.59	0.215	0.0123	4.68	0.27
PM6	16.61	3.33	5.32	0.0564	0.00206	1.06	0.04
PM7	4.89	1.00	6.29	0.0196	0.000946	0.31	0.02
A	16.29	3.02	4.38	0.169	0.00433	3.86	0.10
E	9.57	1.63	4.21	0.0811	0.00264	1.9	0.06

With a value of 123.87 ms, blend PM3 at a plate temperature of 120 °C has the longest decay time by a significant margin, compared to the rest of the fuels. The fast evaporation of the smallest deposit generated by PM7 is also reflected in the decay time with 4.89 ms,

which equates to a factor of 25 between them. The fastest evaporating chemical matrix blend E takes still twice as long. Blends PM2, PM6 and A share similar values. Increasing the surface temperature by 40 °C has a striking impact on the decay time which was also observed for the plan view film and the volume over time. Throughout, the decay time gets reduced drastically. In the case of PM3 with the highest T90 the reduction is more than an order of magnitude. Based on the observations of the single component fuels in chapter 4.5 and their behaviour towards surface temperatures can also be applied here. Once the plate temperature is at, or above, the boiling temperature – or in this case the T90 of the fuel – the evaporation gets accelerated rapidly. The smallest changes in the decay time are found for the blends that already show small values in the lower temperature case. PM7 has the smallest relative reduction by a factor of less than 5. This makes sense in the context of distillation temperatures. PM7 has the smallest T90 of all, which is already surpassed by 40 °C with the lower plate temperature. A further increase to 160 °C has less of an effect because the evaporation is increasing less with temperature once the T90 is passed notably. This was also observed by Stanglmaier *et al.* [65] in their droplet experiments.

The calculated injection mass is around 4.4 µg for blends with small ethanol content. The only real exceptions are PM6 and PM7 with 50% and 85% ethanol respectively. Because of the lower heating value of ethanol compared to gasoline, the required injection time and as such injection mass is increased to maintain the same fuel to air ratio in a direct injection engine (cf. Table 3.1, Table 3.2 and Table 3.3). If one compares the injection mass with the deposit mass at 120 °C, it can be seen that PM3 deposits by far the largest amount relative to its injection mass at 13.09%. The values for PM2 and PM5 are less than half of that and in the case of PM7 only 0.31% is actually deposited. In relative terms blend A deposits twice as much as blend E, which is almost as much as PM2 and PM5. These observations match the trends of the decay time pretty well as well as the conclusions of the plan view film analysis and the deposit volume over time. The fraction of the deposited mass at 160 °C becomes much smaller, as expected. The values are all under 1%, with the exception of PM3. In fact the deposited mass becomes so small, that despite the trend of the 120 °C case being preserved, it could be argued as almost non-existent for all blends except for PM3. Additionally, what little gets deposited

evaporates within 4 ms after VEOI, which illustrates very well that higher surface temperatures are to be preferred if one wants to minimise wall wetting and all the drawbacks associated with it.

To further investigate the influence of the T90 property on the wall wetting behaviour, it was decided to perform a second set of experiments to include PM1 into this study. The associated experiments were performed at a much later stage with the same fuel blends that were stored for over two years, which is why they are not included in the results presented above. Also, it was decided to retest blends PM1 and PM3 to provide a reference. The evaporation curves of the deposited volume over time for the second run can be found in Figure 5.29 (120 °C plate temperature) and Figure 5.30 (160 °C plate temperature).

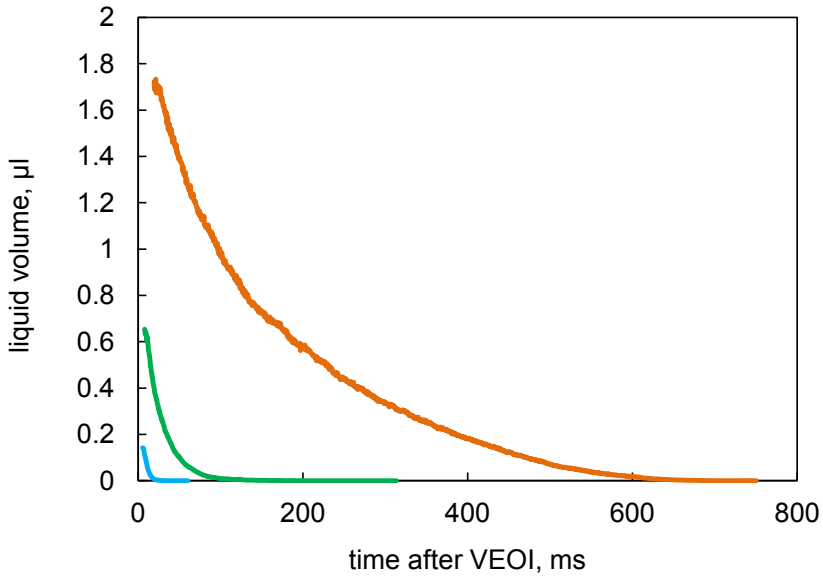


Fig. 5.29 *Mean fuel deposit over time for PM1 (—), PM2 (—) and PM3 (—) that is based on a second set of measurements with the plate temperature 120 °C and 150 bar rail pressure.*

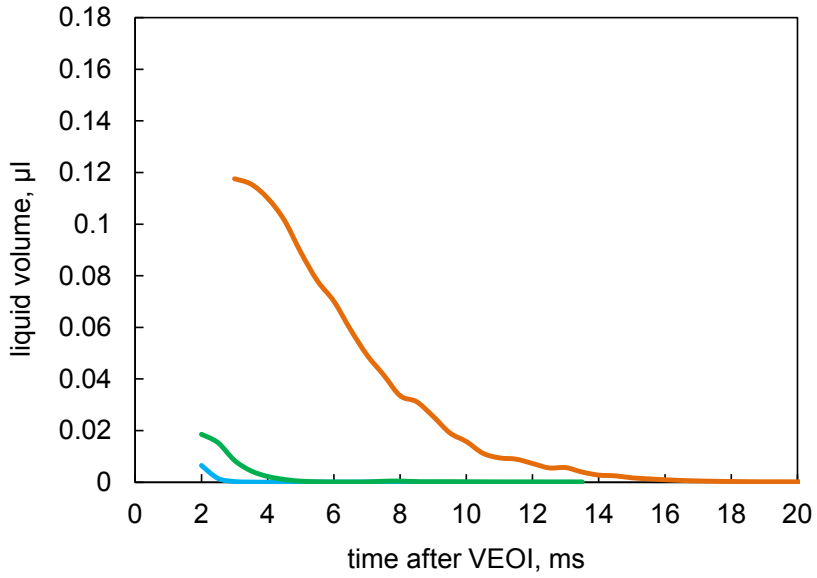


Fig. 5.30 *Mean fuel deposit over time for PM1 (—), PM2 (—) and PM3 (—) that is based on a second set of measurements with the plate temperature 160 °C and 150 bar rail pressure.*

As can be seen for the lower temperature cases, both PM2 and PM3 are behaving differently than before and produce about twice the volume after injection. In addition the evaporation time is also significantly increased by 2-3 times. Most likely this is caused by fuel aging over the two years of storage. All canisters were sealed air tight, but oxidisation or decomposition of some components cannot be ruled out completely. For this reason the results of the second set of experiments will be evaluated separately. Despite the described change, however, the relationship between PM2 and PM3 remains the same with a significantly larger deposit volume for the latter. Also, the relative evaporation time remains the same. Blend PM1 with the smallest T90 of this group produces a deposit that is not only smaller, but also evaporates faster than the two others. Both, the volume and the time scale follow the same trend for all blends. An increase of the T90 by about 30 °C leads to three times larger volume and evaporation time from PM1 to PM2 and from PM2 to PM3 respectively. The overall volume is almost ten times larger for PM3 compared to PM1 and the evaporation takes more than 40 times longer. When the plate temperature is increased to 160 °C all values are reduced drastically, as was the case in the first run. Also,

the blends come closer together both in volume and time, especially in the case of PM1 and PM2 which have a T90 well under the plate temperature. PM3 is again less affected by this change because of its high T90. By combining all these observations it is fair to assume that the relationship between the blends was still intact during the second run of the measurements, despite the change in the absolute values. For this reason the data obtained here will also be used evaluate the influence of the physical properties of the blends on wall wetting.

The results presented in this chapter show the huge impact fuel properties and operating conditions can have on the liquid deposit in direct injection engines. These parameters show a large potential for further optimisations in the future.

5.4 Summary and conclusions

The focus of the work presented was to investigate and evaluate the impact of fuel properties and operating conditions on the extent of liquid fuel deposits similar to those found on the piston surface or cylinder liner in gasoline direct injection engines. The experiments were performed in a dedicated injection chamber that was designed for this project and allowed for recreating desired engine conditions at an easier to control environment with better accessibility.

The tests carried out were under three different headings. The first set of experiments was looking at the spray structure with shadowgraphic recordings of the spray in non-impinging and impinging configurations. All fuel blends provided for this work were used in this phase and at the same time different air temperatures, fuel rail pressures and plate temperatures were investigated. These comprised pressures of 50 bar and 150 bar, plate temperatures of ambient, 80 °C, 200 °C and the individual T90 temperature of the blend. The air temperature was either ambient or adjusted to 80 °C. Five recordings with a rate of 15 kHz were obtained for each fuel blend and conditions. The images without an impingement plate were used to evaluate the spray shape and the recordings with the plate provided data on the fuel deposition and film evaporation process. In order

to synchronize the time series of each fuel and condition, every recording was evaluated and a visible start of injection (VSOI) and a visible end of injection (VEOI) were defined. From the difference between the two values the visible injection time (VIT) could be calculated. It was found that the VSOI was the same for all recordings, despite the injection pressure changes, most likely due to the temporal resolution provided by the 15 kHz recordings being too small to resolve the subtle changes. The VEOI was mainly determined by the set injection time that was calculated based on the rail pressure and lower heating value of the blend. The observed differences between the set injection time and the VIT were around 5 % and most likely caused by inertia of the injector needle and the stagnant liquid. During measurements that did not have a fixed vessel temperature, the air temperature above the plate was monitored. This property was affected by heat transfer from the hot plate to the surrounding air and as such is a function of the set value. The recorded values were usually around 50 °C for the 80 °C plate temperature and 90 °C for the 200 °C plate.

From the recordings of the free spray, images of the mean and standard deviation of the fluctuations of the image intensities were compiled. These were evaluated regarding the spray shape and droplet number density. From the images presented, horizontal intensity lines were extracted and, with a fitting algorithm, the width of each spray was calculated at 45 mm downstream of the nozzle, which corresponded to the plate distance of the impingement experiments. These steps were repeated for both rail pressures and, in addition, the spray widths of the experiments with the impingement plate and ambient air temperature were also calculated.

The recordings with the installed plate were used to look at the shape and extent of the deposit right after VEOI and at later points in time. In this way the differences in the evaporation behavior could also be evaluated for the different blends. The main findings of these experiments are presented below.

- The spray structure of PM1, PM2 and PM3 looked almost identical. They all showed small cone angles with high intensities caused by large droplet densities, despite an increase of T90 by 60 °C between them, which means that this property

does not have an effect on the spray shape. The surface tension and viscosity of these blends was similar, which could be the reason for this observation.

- With increasing ethanol content the spray becomes wider and less dense. This was especially the case for PM7 with 85% ethanol that produced the widest spray cone and the smallest apparent spray density. PM7 also had the largest viscosity of all blends investigated.
- The sprays at 50 bar rail pressure looked notably less dense and had larger droplet patterns. This was caused by poorer atomization related to the reduced pressures, which was also shown by other groups.
- Within the group of chemical matrix blends no clear trend was observed. Blend A produced the largest spray of all fuels including the ones from the physical matrix. The spray of blend F was the most compact of this group and looked similar to PM1-PM3.
- The calculated width of the spray at 45 mm downstream of the nozzle was varying between 3 and 4.2 mm at 150 bar rail pressure and 80 °C air temperature. PM7 showed the largest value in comparison and the overall trend of wider sprays with higher ethanol content was also seen. Reducing the fuel pressure led to only slightly smaller values and the trend of the ethanol blends was lost. Comparing the 150 bar results to the data obtained from the ambient air temperature sprays showed larger values throughout with blend A being the only exception. This illustrates that an increasing cylinder temperature in the volume promotes spray evaporation and can assist in the minimization of particulate emissions even before wall wetting occurs. This parameter could potentially be adjusted by changing the coolant flow rate or temperature.
- Overall, the differences between the blends were very subtle and not as drastic as one might expect, given the large range of T90 and ethanol content between the blends. Only blend PM7 showed notable differences in the spray structure.
- The liquid deposit on the glass surface at 80 °C was fairly similar between the different blends close after the VEOI. The ethanol blends produces slightly larger

films, most likely as a consequence of their wider sprays. No real differences between the blend from the chemical matrix was observed.

- At 5 ms after VEOI the blends were partially evaporated which lead to fuel films that looked the thinnest in the case of PM7 as well as A and F. The rest of the blends looked less even with a more pronounced film on the right side in the direction of the spray and away from the initial impact. This was caused by the momentum that was introduced by the angled spray and was also described by other groups.
- Increasing the surface temperature led to beginning droplet formation in the film after VEOI and blends PM7, A and E produced more pronounced films, which again stress the importance of this property.
- The shape of the films became quite similar for all blends when the surface temperature was adjusted to the respective T90.
- At 200 °C all fuels showed increased evaporation, which also highlights the importance of the plate temperature as a factor to minimize wall wetting. The differences between the blends, however, were less visible for this condition.

In the second part, fuels PM1, PM2, PM3, PM5 and PM7 were selected to undergo droplet size and velocity characterizations with a Phase Doppler Anemometer. A radial profile though the centreline was obtained for these blends 45 mm downstream of the nozzle and without a plate installed. In order to obtain representative data of the steady state spray without effects of the leading or the trailing edge, time signals obtained by the PDA were evaluated and the data was filtered between a lower and an upper time limit. Mean values of the droplet velocity and size were calculated as well as the corresponding standard deviations. To further see if the spray properties drift over the course of the injection, three different time windows were extracted from the signal and evaluated separately. This was done by looking at the droplet size over time and with scatter plots correlating the individual droplet velocity with the size. Additionally the Weber Number was also correlated with the droplet size. The findings of these analyses are listed in the following paragraphs.

- The radial profiles appeared almost identical for all sprays with the highest velocities at the centre and the lowest at the spray border. The same was seen for droplet sizes. The former was reaching velocities of about 140 ms^{-1} and sizes of almost 10 µm. These values were about halved at the outside of the spray due to momentum losses between the liquid and the air in the chamber. The calculated Sauter diameters were about twice as large as the arithmetic mean values.
- The differences between the blends were extremely small, both of the velocity and size profiles. The only slight exception was PM7 that produced marginally smaller speeds and larger diameters than the rest. Given the drastically increased ethanol content of PM7 one might expect a larger change, which was not confirmed through any of the PDA measurements.
- Gaussian fits were used to calculate the maxima of the droplet size and velocity of each spray as well as the synthetic spray width. These values were compared to the width based on the high speed images and showed a discrepancy of up to 30% in magnitude. However, the trends described in the previous section were also reflected here.
- The in depth analysis of the spray beginning, mid and end sections provided additional information that greatly supports the conclusions of all blends producing the same structure of the spray. Even when merging all data together in plots, showing the entirety of the spray, no differences were found.
- These conclusions combined with the findings of the spray visualization demonstrate that any notable differences in particulate emissions measured in engine tests can only be caused by the wall wetting behavior and not by the spray shape or structure itself.

In the last part of this study the novel measurement technique for liquid film thickness measurements, described in chapter 4, was used to quantify the liquid deposits generated by the impinging spray on a rough metal surface. Blends PM2, PM3, PM5, PM6, PM7, A and E were investigated here. In a later run, the data was expanded to PM1 to obtain more information about the influence of T90. From five recordings of each blend and condition,

instantaneous plan view film thicknesses were compiled, analysed and compared. The data stored in these images was also used to calculate the cumulative deposit volume over time for the blends at 120 °C and 160 °C plate temperatures. Based on these a decay time and deposit mass were calculated from which the latter was related to the calculated injection mass. The findings and conclusions of these investigations are listed below.

- The fuel deposit was fairly even and usually had a circular shape with a slight deformation on the right side. The region corresponding to the immediate contact area of the impinging spray was less thick than the rest.
- Evaporation of the film did not occur homogeneously and began from the left side where the spray hit the plate.
- The different blends generated deposits of a wide range. PM3 produced the largest and thickest fuel film and PM7 the smallest and thinnest. Fuels PM2 and PM5 behaved similarly. The positive influence of ethanol on the deposit minimization was also seen here with a clear correlation between ethanol content and fuel film for PM5 to PM7. This trend confirms the positive effect of alcohol as a fuel supplement. Chemical matrix blend A produced a larger and thicker deposit than blend E.
- From the time series analysis, it became apparent that the evaporation time is significantly different between the blends.
- Increasing the plate temperature by 40 °C led to drastically reduced wall wetting. Both the size and the thickness values were much smaller, even though the relative differences found in the lower temperature measurements were also present here. Blends PM6 and PM7 in particular produced almost no deposit at all.
- These findings were supported by the quantitative analysis of the deposit volumes with PM3 being the largest by far and again illustrate the potential of an increased surface temperature inside the engine cylinder to minimize particulate emissions. However, increased temperatures could lead to a reduced volumetric efficiency of the engine.
- The general order of the deposit volume also followed the evaporation time. Overall, larger deposits led to longer evaporation times.

- The increased plate temperature reduced the scales of both the deposit volume and time, by an order of magnitude, while maintaining the relation between the blends. This is similar to the observations in the first part of this study, during which larger glass surface temperatures also reduced the extent of the fuel film and increased the evaporation notably.
- The deposited mass relative to the calculated injection mass varied greatly between the blends. From the PM3 spray about 13% was found on the plate and from PM7 only 0.3% at 120 °C. This range again shows the great potential of ethanol's usability as a fuel supplement not only to increase the amount of biofuel but also to further minimize the wall wetting and as such the particulate emissions.
- The relative deposit mass was much below 1% for the larger plate temperature, again with the exception of PM3. Under these conditions is could be argued that there is no deposit to be found for these blends and that under such an operating condition no real increase in particulate emissions due to fuel film is to be expected.

The trends of the spray impingement measurements are summarised in Figure 5.31. Within the physical matrix a reduction in ethanol content and an increase of the distillation properties (T90) has a promoting effect on wall wetting. Based on this work, the worst case fuel would have only very little ethanol content and a large T90, which is represented in this study by fuel blend PM3. A recommendation to reduce the particulate emissions associated with the ignition of the liquid fuel films on a piston surface or a cylinder liner would be to reduce or substitute some of the heavier components in the fuel with ones that have a lower boiling temperature. Also, the addition of gasoline substitutes like ethanol or similar alcohols is to be preferred. Even though the energy density of these liquids is lower than for regular gasoline and with that an increased injection mass is required, the blends with high alcohol content produce very little fuel deposits and promote deposit evaporation at the same time. Additionally, the boiling temperature of such a component is usually lower than for gasoline and also more likely below the surface temperature inside the cylinder during a wider range of engine operating points. This is especially interesting, as the potential of an increased surface temperature relative to the boiling temperature of the

fuel seems to be the best parameter to minimise wall wetting in general. With the literature presented in chapter 2.2.3 it becomes obvious that these properties are very beneficial for reaching an optimal evaporation of the injected fuel and, eventually, for the reduction of particulate emissions.

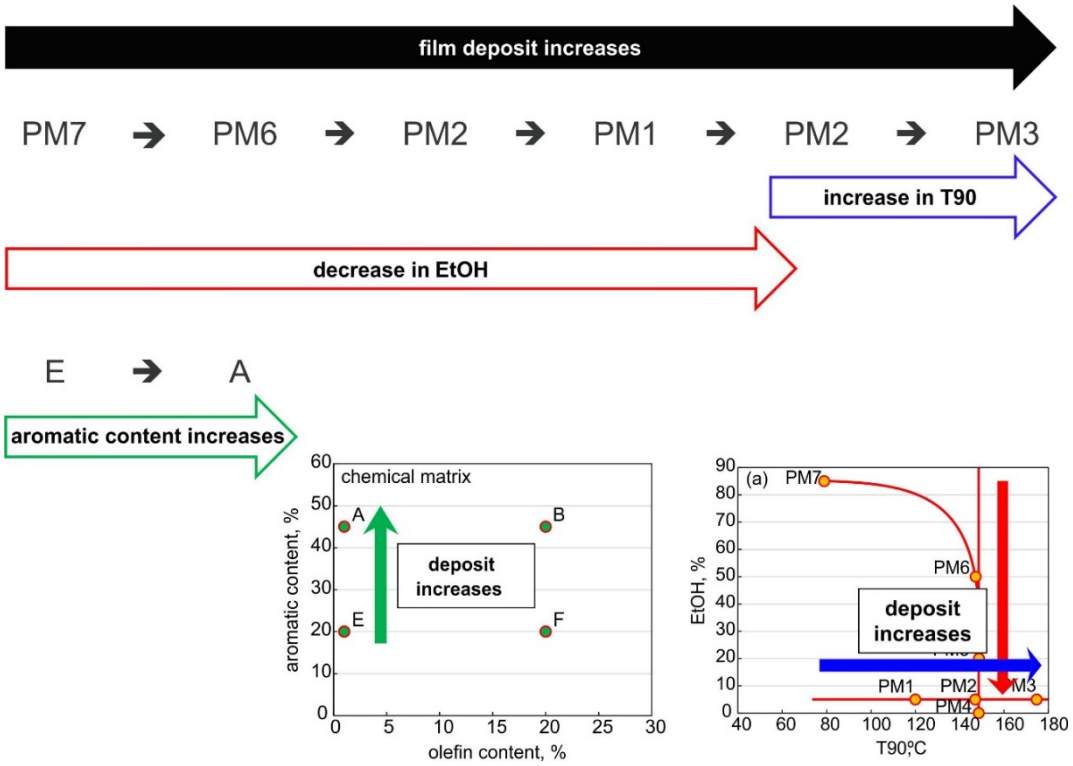


Fig. 5.31 *Summary of the trends found during the film thickness measurements of the impinging sprays on a rough metal plate.*

Chapter 6

Effect of injector fouling on spray characteristics

In this part, the process of injector fouling was studied in order to evaluate the effect that it has on the resulting spray characteristics from GDI injectors. The changes in the spray characteristics can potentially influence the combustion process in the engine and might lead to increased particulate formation that results in increased engine-out emissions. Different fuel blends were used to deliberately create deposits of different extents in test engines (IAV Automotive Engineering). After a fixed cycle, the original fuels were replaced with a blend utilising a detergent additive. In this way, it was possible to reverse most of the negative effects observed during the dirty-up cycle. The intention of the current study was to quantify whether the spray pattern from different injectors, *i.e.* new, after fouling and after cleaning, changes and discuss potential links to engine operation.

For this investigation, the injector deposits were analysed visually with a microscope and correlated with exhaust emission measurements. It was also used to verify the cleaning effect of the detergent blend on the nozzles of the injector. Based on the findings, a selection of injectors was tested in the modified injection chamber, described in chapter 3.2.1 to obtain data on the spray pattern and how it differs between fouled, cleaned and a new injectors.

In the first section of this chapter, the experienced drift in particulate emissions due to injector fouling will be presented and discussed alongside photographs of the deposits. These will be compared to the measurements of the engine tests with the detergent blend. After this, the analysis procedure of the spray pattern of the selected injectors will be presented and the findings will be discussed and compared.

6.1 Formation of injector fouling and its impact on particulate emissions during the run in test engines

A total number of 48 injectors were used for the test procedures in the engines, during which engine performance and emissions data was recorded. The tests were split into two parts, a dirty-up and a clean-up phase. The former was run for about five hours and showed a significant increase in the particulate emissions: the latter lasted about nine hours. The data presented in this chapter was provided by IAV Automotive Engineering for this work, as a collaborative effort.

A brief overview of the blends tested and how they performed regarding the emissions of particulate numbers can be seen in Figure 6.1. During the dirty-up phase, all of the blends showed a significant increase in particulate numbers. The only exceptions were Fuel B and Fuel C which did not show any drift at all over this period of time. Fuel C, the blend with the added detergent, already shows the effectiveness of such an additive to avoid increased emissions associated with injector fouling in direct injection engines from the beginning. Most other blends produced a similar emissions drift, with Fuel A showing the largest drift of all.

Notable is that the increase in particulate emissions happens very early after the start of the cycle for Fuel E, while Fuel A and D show a lag phase until about 90 min into the test. Fuel E also has a very strong increase in numbers right at the beginning, which seems to ease off towards a steady production of emissions. The increase of the two latter does not taper-off as much throughout the dirty-up phase, especially for Fuel D, which

shows almost a linear increase. The dirt-up phase was performed twice to produce two sets of fouled injectors.

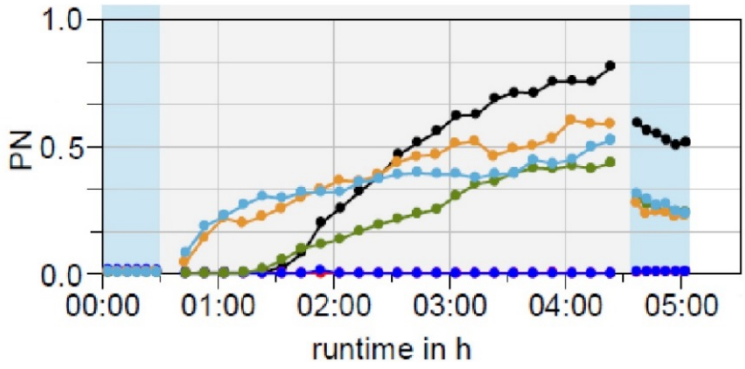


Fig. 6.1 *Relative drift of engine out particulate numbers during the dirty-up phase for blends Fuel A (●), Fuel B (●), Fuel C (●), Fuel D (●) and Fuel E (●,●). The latter fuel was run twice in this phase. Zero PN equals to the basic emissions level of new injectors. The blue bands correspond to start-up and shutdown phases of the test. This data was provided by Shell Global Solutions.*

After completing this cycle, the engine was switched to Fuel C (the fuel with the detergent) and one of each set of the fouled injectors was run in the clean-up phase. Additionally, one set that were previously run with Fuel E, were treated with Fuel F in this phase. The monitored particulate numbers over the course of nine hours in this cycle can be seen in Figure 6.2.

A cleaning effect induced through Fuel C can be observed immediately after switching the blend. After about two hours the injectors previously fouled with Fuel E reach emission levels of a clean injector, followed by Fuel D, which requires about four hours. However, both sets of injectors showed the same drift in the dirty-up phase, which demonstrates that the detergent additive has a different effectiveness on different deposits. Of all injectors, the ones fouled with Fuel A requires the longest cleaning time by far. Only after about 7 hours did the emission levels fall back to the level of the clean injector case.

The set of injectors that was treated with Fuel F in this cycle showed a small initial reduction but their relative particulate number stabilises over time at a constant level. The injectors that were run with Fuel A and Fuel C in the dirty-up phase do not show any change in particulate emissions, as expected from their previous behavior.

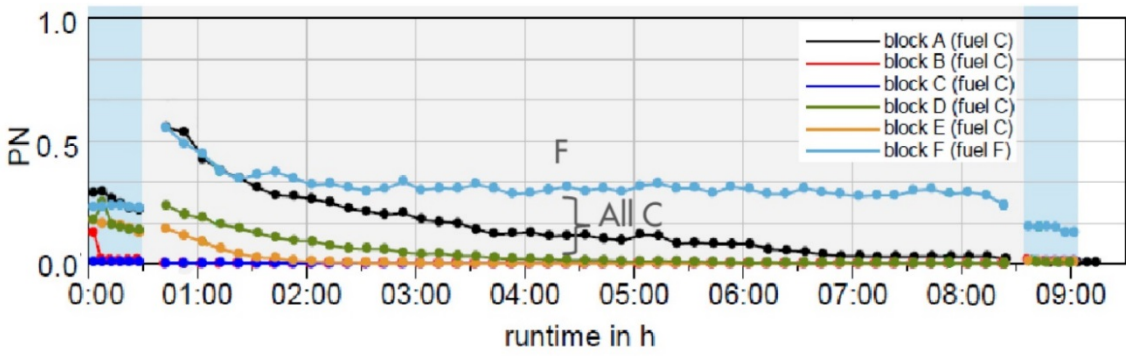


Fig. 6.2 *Relative drift of engine out particulate numbers during the clean-up phase for injectors previously fouled with blends Fuel A (•), Fuel B (•), Fuel C (•), Fuel D (•) and Fuel E (•,•). All injectors were run with Fuel C during this part, with the exception of one set of Fuel E that was exposed to Fuel F (•) here. Zero PN equals to the basic emissions level of new injectors. The blue bands correspond to start-up and shutdown phases of the test. This data was provided by Shell Global Solutions.*

Additional analyses of the hydrocarbon, carbon monoxide and NO_x emissions did not show any significant changes during both phases. Also, there was no drift of the injection width and fuel trim observed. From the data presented it can be inferred that the particulate number drift can be reversed by switching to a fuel with the detergent additive.

After completing a test phase, the injectors were removed from the engine and examined with a microscope to analyse the extent of the deposits. The findings from the micrographs, combined with the emissions data, were used as a basis to select injectors for the spray structure study in the following experiments. Figure 6.3 shows a detailed comparison of an injector that was run with Fuel A during the dirty-up phase, next to a

clean injector. The injectors from this particular cycle represent the worst case of all, both in particulate emissions drift and deposit build-up on the injector tip.

These photographs provide a good impression of the extent of the deposits found during the engine test. The entire surface of the injector tip (Figure 6.3-a2) is covered with solid combustion products that are concentrated around the nozzles. However, the deposits do not appear homogeneous over the entire area. It looks as though the fouling is stronger at the top side, which corresponds to the predominant direction of the sprays. This means that the degree of fouling can be promoted by the angle of the spray relative to the injector and that a spray perpendicular to the surface, as is the case for hole #3, reduces this effect. Around the five nozzles of the injector fouling is most severe (Figure 6.3-b2). The build-up of combustion deposits is thick, especially right in the centre, with a mostly dark colour. Additionally, the deposit forms lumps around the nozzles. In this image it can also be seen that fouling is occurring inside the nozzle with a pattern that is made of streaks. These two shapes are most probably caused by the flow direction of the fuel during and after injection. The fast moving droplets inside the nozzle form stripes along the deposit while passing by and the liquid that sticks to the tip after injection forms more spherical shapes. From the close-up view of the injector nozzle (Figure 6.3-c2) is can be seen that the circular shape of the well all around the nozzle hole and the hole itself is affected by deposits. Both diameters are reduced notably which could have a negative impact on the spray formation during injection. Additionally, the residual combustion products can act as a sponge due to their porous nature and promote injector fouling even more [193]. The side view (Figure 6.3-d2) shows that the deposits also affect the sides of the injector tip, which are also exposed in the engine cylinder. The build-up at the centre of the injector tip is very dominant and the conical shape of the clean tip (Figure 6.3-d1) much less recognizable as compared to the clean injector.

Figure 6.4 shows the comparison between the injector that was run with Fuel A and one that was run with Fuel D. The latter produced notably less of a particulate emissions drift during dirty-up.

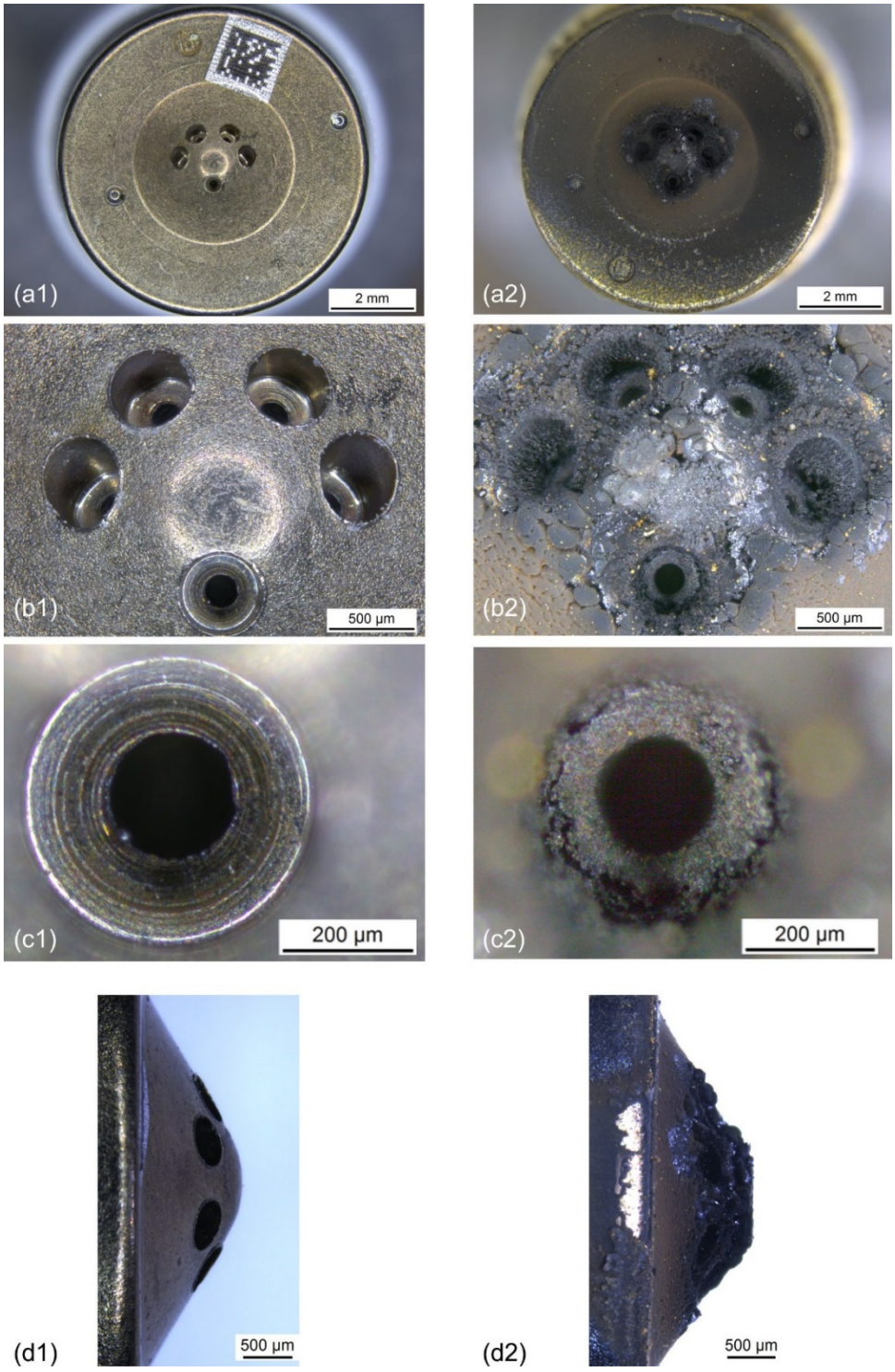


Fig. 6.3 *Comparison of micrographs from an injector that was run with Fuel A (a1-d1) in the dirty-up phase and a clean injector (a2-d2), with detailed pictures of both injector tips (a1, a2), all injector nozzles (b1, b2), a single injector nozzle close-up view (c1, c2) and the side views (d1,d2). The photographs were provided by IAV Automotive Engineering.*

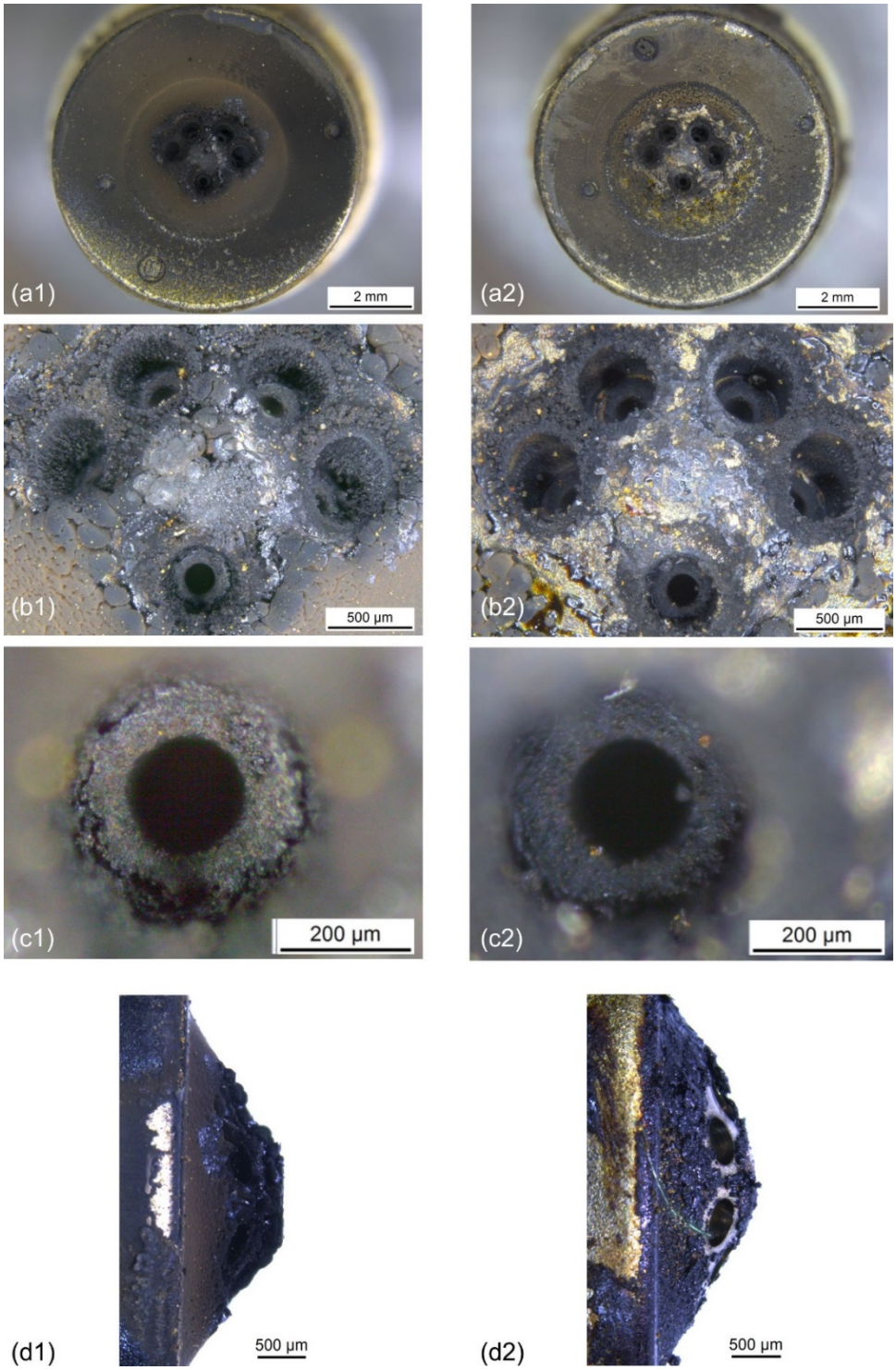


Fig. 6.4 *Comparison of micrographs from an injector that was run with Fuel A (a1-d1) in the dirty-up phase and an injector that was run with Fuel D (a2-d2), with detailed pictures of both injector tips (a1, a2), all injector nozzles (b1, b2), a single injector nozzle close-up view (c1, c2) and the side views (d1,d2). The photographs were provided by IAV Automotive Engineering.*

First, it is apparent that the overall level of fouling is lower for Fuel D compared to Fuel A. The surface of the injector tip is covered in a less dense layer of combustion products that has gaps showing the metal surface (Figure 6.4-a2). The regions around the injector nozzle are notably less fouled compared to the Fuel A injector (Figure 6.4-b2). Parts of the metal surface are not covered by the deposits and the overall shape is smoother. The lumps that formed on the Fuel A injector are not present here. The level of fouling is increasing inside the actual nozzles compared to the tip, but the overall thickness is again smaller compared to Fuel A. Parts of the metal surface remain uncovered, especially around the bottom edge of the nozzle well. The nozzle exit itself seems to be covered (Figure 6.4-c2), but the apparent reduction of the diameter is smaller. The conical shape of the injector tip is much better preserved for the Fuel D injector (Figure 6.4-d2) and it appears that parts of the deposit were detaching during engine operation leaving the metal surface between the nozzles exposed.

Comparing a Fuel C injector to the Fuel D case (Figure 6.5), the effectiveness of the detergent on preventing fouling becomes visible. The surface of the injector tip is covered much less in combustion deposits (Figure 6.5-a2) and most of the metal can be seen. The area in and around the nozzles does not seem to be affected by a deposit at all (Figure 6.5-b2) and only the centre and the outside of the tip are covered in a thin layer that appears to be smoother compared to the Fuel D injector. The nozzle exit (Figure 6.5-c2) is not affected as well and the diameter seems unchanged. However, the side views of both injectors (Figure 6.5-d1 and Figure 6.5-d2) appear more similar. Both show a thin layer of combustion products that have gaps, most likely formed by continuous break-off of the solid residuals.

The observations made here are also valid for the other injectors of the respective set, with only minor differences. This means that the extent of the fouling correlates very well with the measured engine-out emissions.

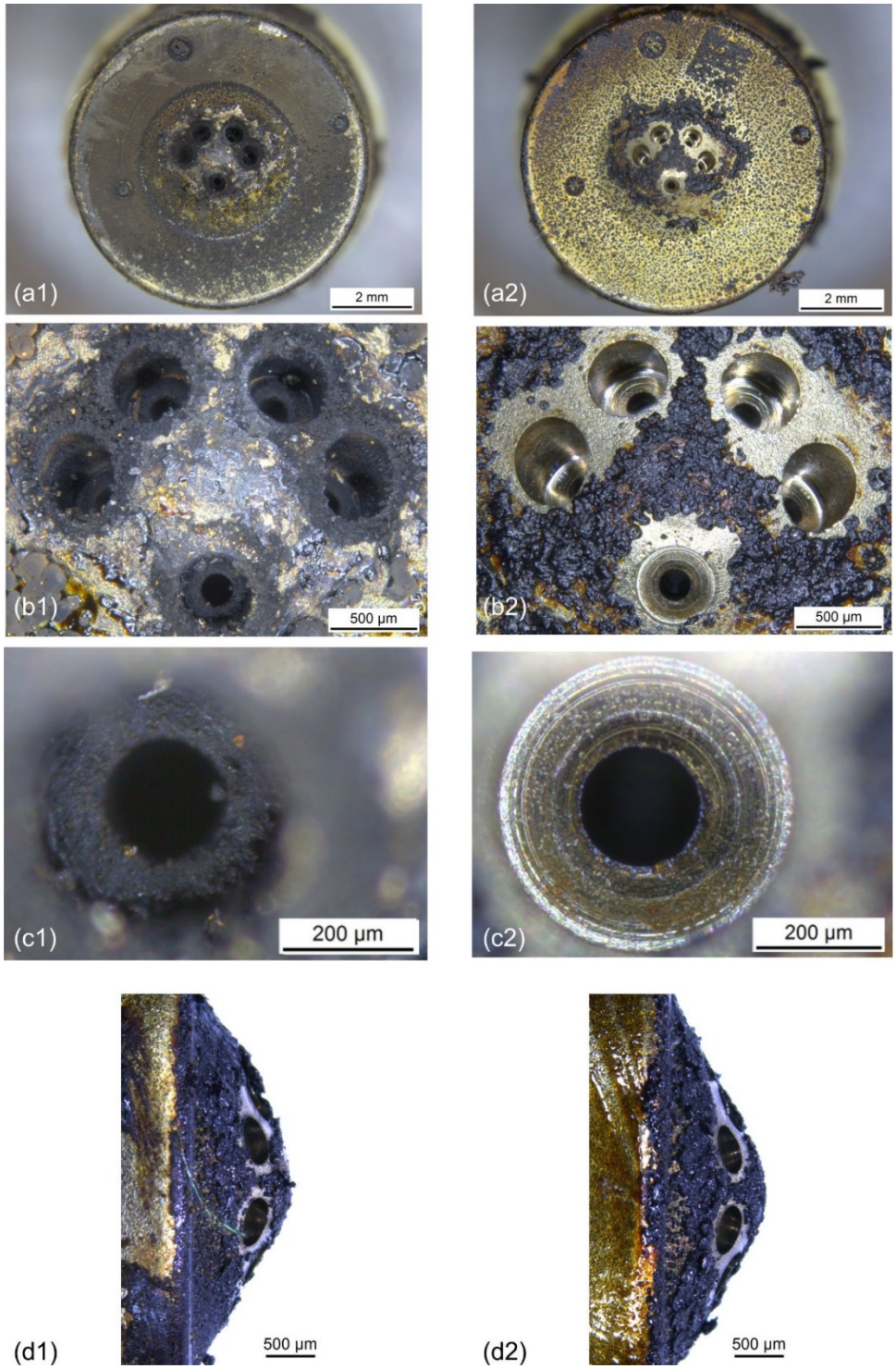


Fig. 6.5 *Comparison of micrographs from an injector that was run with Fuel D (a1-d1) in the dirty-up phase and an injector that was run with Fuel C (a2-d2), with detailed pictures of both injector tips (a1, a2), all injector nozzles (b1, b2), a single injector nozzle close-up view (c1, c2) and the side views (d1, d2). The photographs were provided by IAV Automotive Engineering.*

After switching to the detergent blend, a similar appearance of the cleaned-up injector to the case that was run only with Fuel C is to be expected. Figure 6.6 shows a comparison between the injector that was run with Fuel A during dirty-up and one that was subsequently cleaned with Fuel C from the same cylinder.

The cleaned injector shares a strong resemblance with the injector that was run with Fuel C in the dirty-up phase. Large parts of the injector tip surface were free from the combustion deposits (Figure 6.6-a2) with the highest efficiency of cleaning at the bottom half. The area inside and around the nozzles is almost completely free from the deposits (Figure 6.6-b2) and the fouling on the injector tip was also reduced significantly. The nozzle exit itself (Figure 6.6-c2) shows no real signs of fouling anymore and a possible effect on the spray pattern due to the reduction in diameter should be reversed. The side view (Figure 6.6-d2) shows that larger parts of the deposits have broken off and the conical shape of the tip is restored to a large extent.

Overall, this example illustrates why a reversal of the emissions drift was observed once the fouled injectors were used with the detergent fuel. The photographs presented also show where the spray directly interacts with the surface of the injector. Areas that were cleaned the best are very likely exposed to fast moving droplets, or liquid streams, that remove the solid residuals more efficiently. The results of the injector cleaning for the other cases looked similar to this, yielding the same conclusions.

Based on this data, one injector from the dirty-up phase with Fuel A was selected to be tested in the injection chamber. The corresponding injector from the same cylinder that was treated in the clean-up phase was also chosen. These two were then compared to a clean injector as a reference.

The procedures used during the dirty-up phase are similar to what was reported previously by Aradi *et al.* [185] and Joedicke *et al.* [191] in their engine tests.

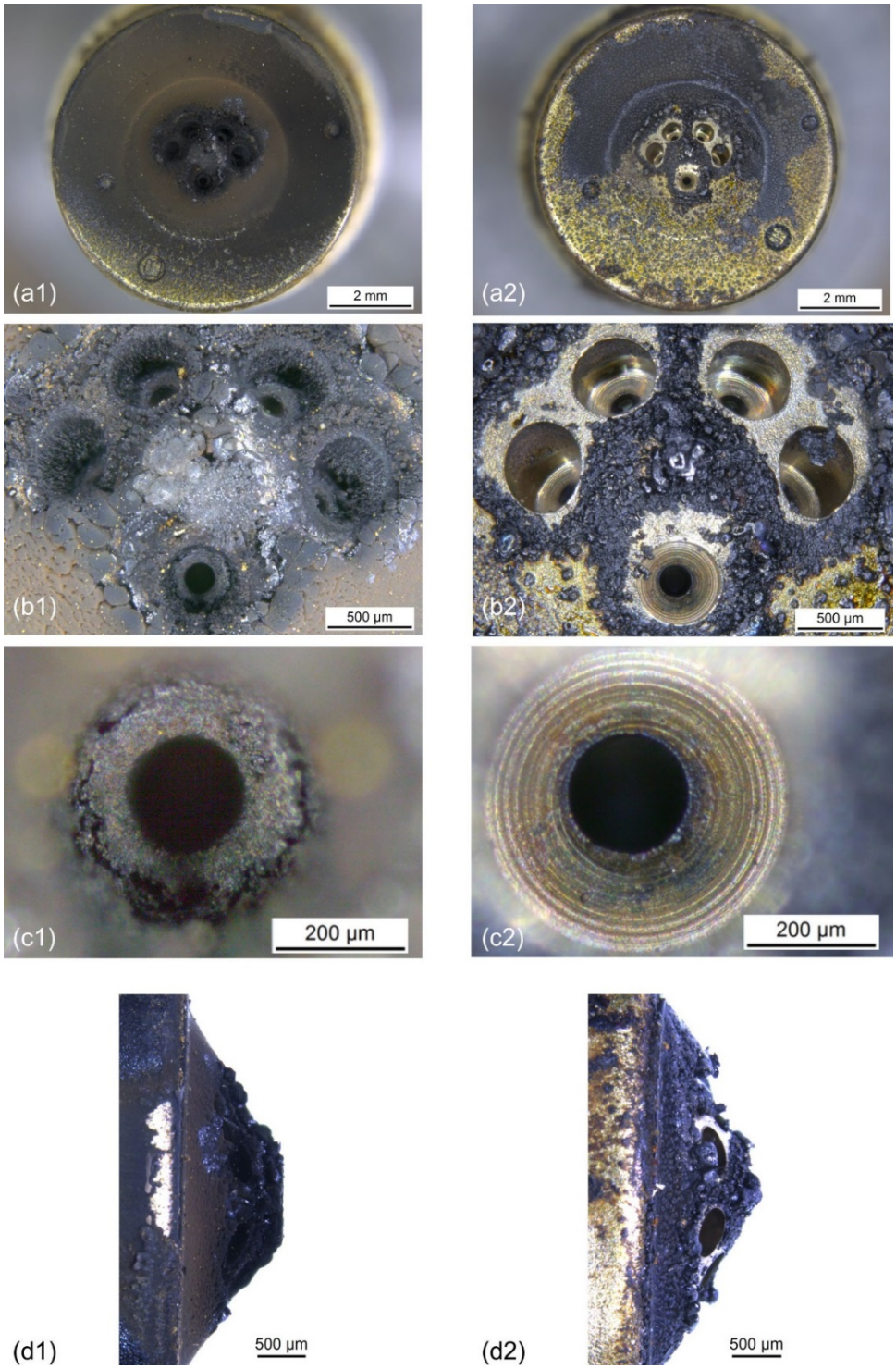


Fig. 6.6 *Comparison of micrographs from an injector that was run with Fuel A (a1-d1) in the dirty-up phase and one with Fuel C afterwards (a2-d2), with detailed pictures of both injector tips (a1, a2), all injector nozzles (b1, b2), a single injector nozzle close-up view (c1, c2) and the side views (d1,d2). The photographs were provided by IAV Automotive Engineering.*

6.2 Analysis of the spray pattern of clean and fouled injectors

From the three injectors that were selected, large number of injections was recorded and mean and standard deviation images were calculated. In a first step, it was determined how many injections would be necessary to produce a representative mean image, which would provide reliable information about the difference between sprays, when comparing injectors. For this purpose a series of 50 injections was recorded for the clean injector. Mean images from the first 5, 10, 15, 20 and finally all 50 injections were calculated 1.05 ms after triggering the injector and are shown in Figure 6.7. By this time, the spray was fully developed and had a stable appearance.

The spray shape shown in the mean image intensity calculated from 5 injections shows strong wrinkling at the border of the jets, especially for the two sprays at the top. This indicates strong fluctuations between injections that have not yet averaged out in the mean using this number of images. When calculating the average based on 10 injections, these instabilities are notably reduced and the spray border seems much smoother. This trend remains in the mean image calculated from 15 injections. Now, the spray border becomes more regular. Once the number of raw images exceeds 15, no significant improvement in the mean image can be observed. This means that a minimum of 15 injections is necessary to produce a reliable mean image based on the clean spray. This criterion is important if one would need to minimize the amount of repetitions and, as such, the storage required for these measurements. However, it was decided that, for all following mean intensity and standard deviation of intensity images, 50 injections were to be used. This would provide enough of a safety margin to account for increased fluctuations that could be possible in the case of fouled injectors. The intention was to maximize the reliability of the data.

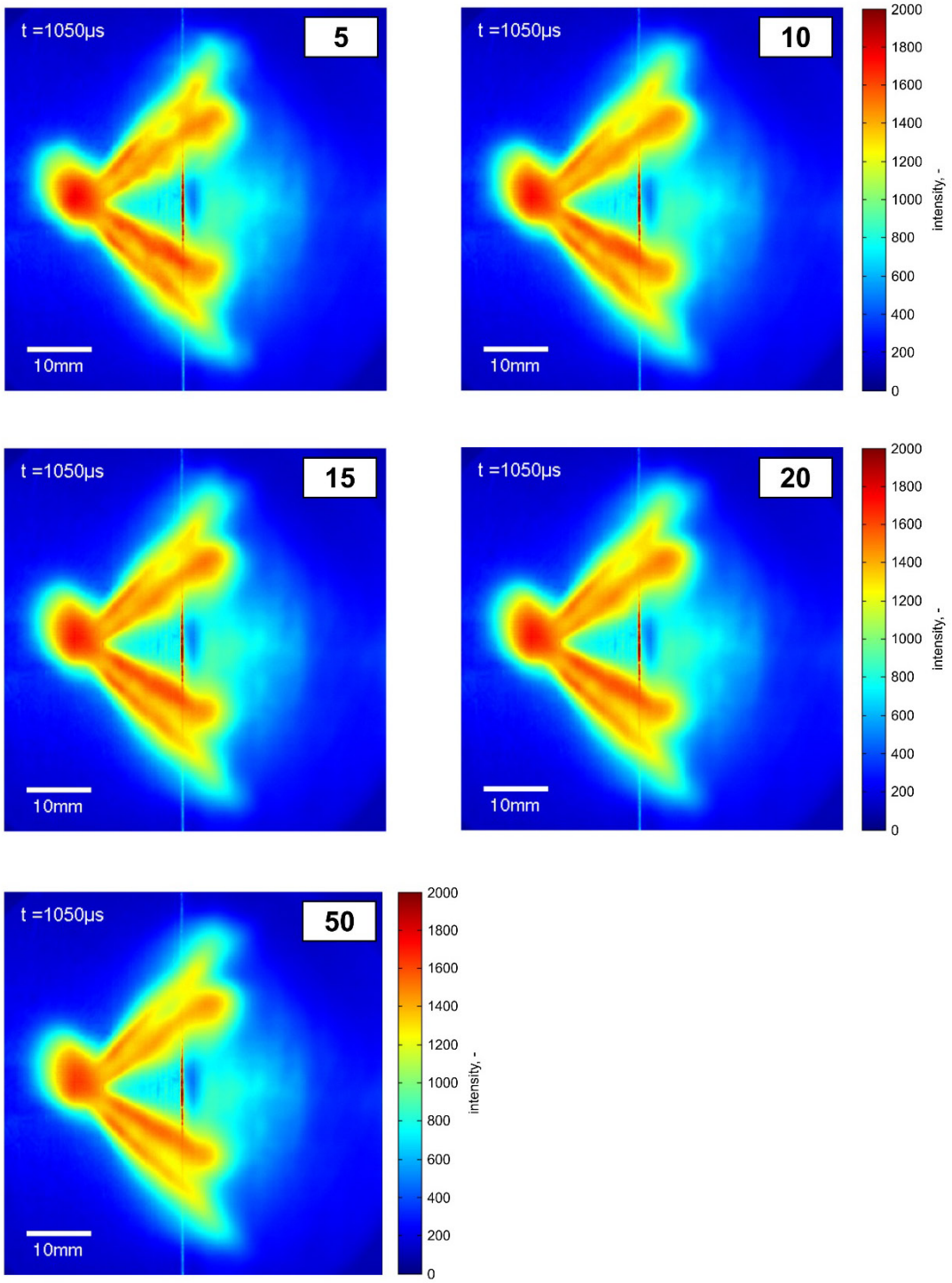


Fig. 6.7 *Mean images of the spray from the clean injector based on 5, 10, 15, 20 and 50 injections.*

Please note that the background of the spray does not appear dark, but has intensities larger than 0. This is caused by scattered light from the spray that is reflected by the aluminum injector holder, once the spray is illuminated. Additionally, the apparent "centerline" that cuts the image vertically is a result from the step that was machined into the injector holder to reduce weight. Further efforts were made to minimize the background noise by coating the surface of the holder with black paint.

With the results of this test in mind, time series from the three injectors were recorded. Figure 6.8 shows extracted frames from the mean image time series of the clean injector. The field of view of all recordings was chosen in such a way that the injector tip is close the left border, but centered vertically.

In the first couple of frames of the recording, essentially no spray is visible (Figure 6.8a). This is due to the delay between injector triggering and the needle lift together with the time required for fuel to travel through the nozzles. This is something that was also observed during the experiments with the single-hole model injector in the wall wetting experiments. About 0.35 ms into the recording, the spray appears and all five jets are immediately visible (Figure 6.8b). Over time the spray grows as it propagates away from the injector (Figure 6.8c), until it reaches a steady shape that is maintained until the end of the injection process (Figure 6.8d). Once the needle closes, the individual jets separate from the nozzles, but the droplets continue to travel outwards (Figure 6.8e). A faint cloud of droplets remains suspended in the air above the glass plate, which takes rather long to vanish (Figure 6.8f).

The overall direction of the jets differs depending on the nozzle angle. The single jet on the left side of the injector tip in the frame was pointed almost directly downward and, as such, hits the glass plate first. The other four jets faced outwards, away from the injector and were distributed symmetrically between the top and the bottom half of the frame. The absolute intensities depicted in the images correlate with the droplet number and are a measure of how dense the spray is. The spray from hole #3 (cf. Figure 3.13) shows the largest intensity of all jets. The outside jets at the top and the bottom (from hole #2 and #4) appear thinner and longer than the adjacent ones that are closer to the centre. Also they are penetrating slightly deeper. The front of the two jets on the inside at the top

and the bottom (from hole #1 and hole #5) are more rounded with larger intensities than the other two.

The time series of the dirty and the cleaned-up injectors were analysed in the same way. Extracted mean frames, which are representative of all three time series, is shown in Figure 6.9 with the corresponding standard deviation images underneath. The intensity values are absolute in both cases, but the colour bar is scaled differently with a smaller range in case of the latter.

Compared to the spray pattern of the clean injector, the fouled injector spray produces jets that are notably thinner. Also, they are penetrating slightly deeper. Especially, the two jets on the outside (from hole #2 and hole #4) become very narrow and less intense towards their leading edges. Additionally, the spacing between the adjacent jets is increased and the most forward regions of the jets from hole #1 and hole #5 are less pronounced. The shape and intensity of the single jets that are directed downwards do not differ that much from each other. The deeper penetration could be the result of the reduced nozzle diameter due to deposits in and around it, as reported from the microscope photographs. Assuming a similar pressure drop, a smaller orifice would lead to an increased velocity and as such increased droplet momentum and penetration distance over time.

The cleaned-up injector produces the most diffuse spray of the three. All jets have a larger cone angle and are wider with the smallest penetration. Additionally, the recorded intensities in the centre of the downward jet from hole #3 have the largest values of all images. This means the differences of the spray pattern between the sprays of the fouled and the cleaned-up injector are larger than between the fouled and the clean, based on this analysis.

Looking at the scattered light fluctuations in the spray generated by the clean injector, which is illustrated in the standard deviation image, one can see that the largest values are found at the boundaries of the jets and especially at their leading edges. The values reach around 250 as a maximum, but only in a very small region of the jets from hole #1 and hole #5. Similar to this, the fluctuations observed in the corresponding jets of the fouled injector fluctuate the most also in these regions, but reach values over 300. This

means that there are slightly stronger variations in the leading edge of the spray from the fouled injector. The cleaned-up injector that produced the most diffuse spray also produces the most fluctuations in the two central jets. This would indicate that the broader appearance of the spray seen in the mean image is mainly due to larger movement, or flapping, of the jet from these holes. Even though the magnitude of the standard deviation is not much different in all cases, the area that shows increased values is the largest for the cleaned-up injector.

In order to assess if there is a drift of the spray pattern over time, three time series of 500 injections each were recorded for all three injectors. From these series, mean images of the first and the final 50 injections were compiled, similar to those presented in Figure 6.9. Extracted frames from these can be seen side by side in Figure 6.10.

All images demonstrate clearly that there is no visible change between the first and the last 50 injections, which consequently means that there is no change of the nozzle shape and so both, no "mechanical" cleaning nor additional build-up of the deposit are occurring, caused by the injection process without combustion. Effectively, this means that the injector performance is not affected over the course of such a long term test. This is an important factor because the measurements would be skewed if this were not the case and it would be difficult to maintain the trends observed at the beginning of the measurements throughout the duration of this project.

In order to analyse the differences of the sprays more deeply, a relative planar intensity change was derived as an additional criterion. This was done by calculating the pixel-by-pixel intensity difference between the means of the dirty and of the clean, as well as between the means of the dirty and of the cleaned-up injector sprays. Both results were then divided, pixel-by-pixel by the mean intensity of the dirty injector. The results can be seen in Figure 6.11.

The values of these relative differences are plotted between -1 and 1. The black regions mean that the two mean sprays have the same local intensity, while the red region corresponds to areas where there is no spray visible in the image of the dirty injector. The green regions illustrate the opposite, with the spray visible only in the image of the dirty injector.

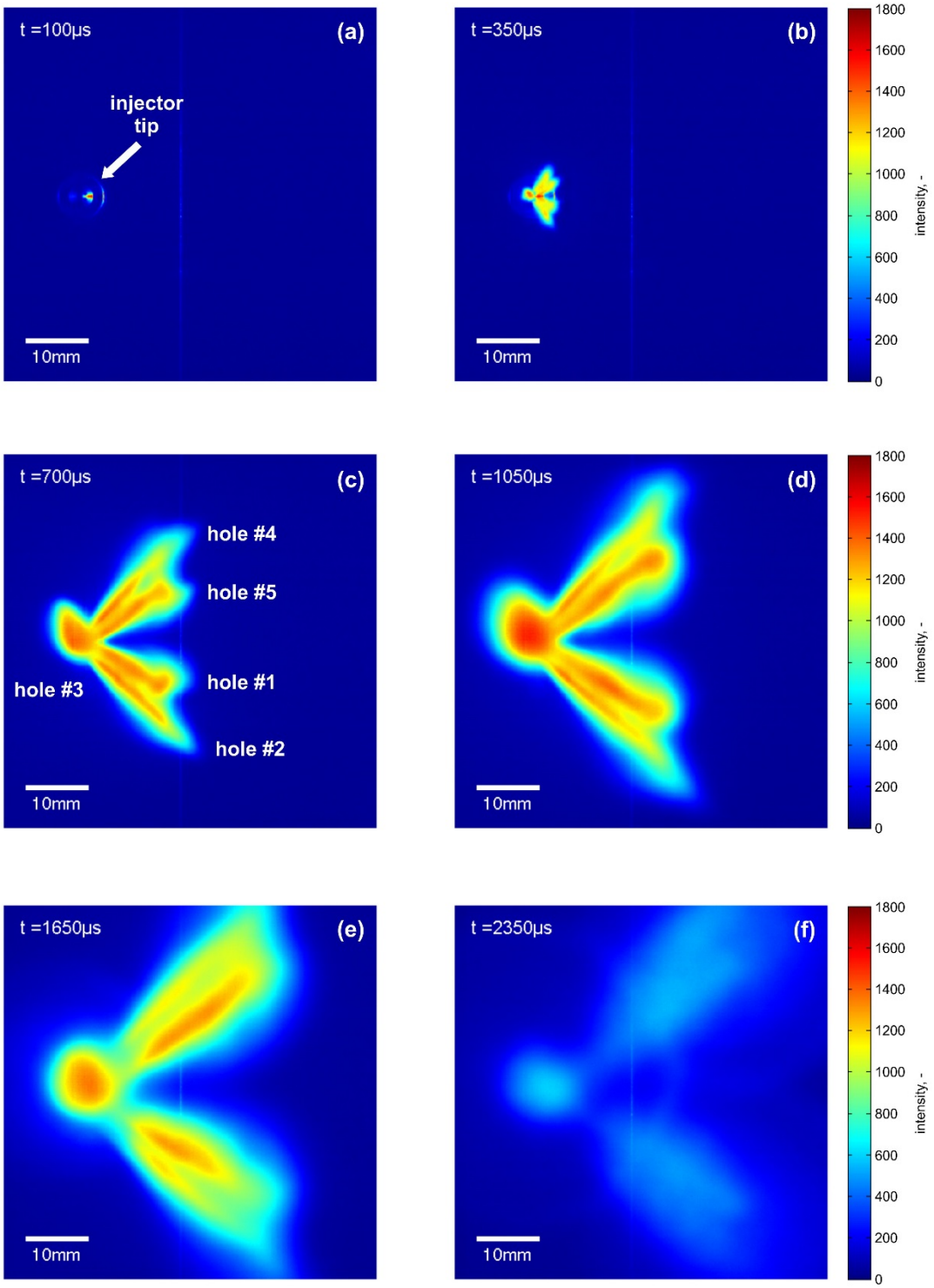


Fig. 6.8 *Extracted frames from the mean scattering intensity time series of the clean injector. The timestamp corresponds to the time after triggering the injector.*

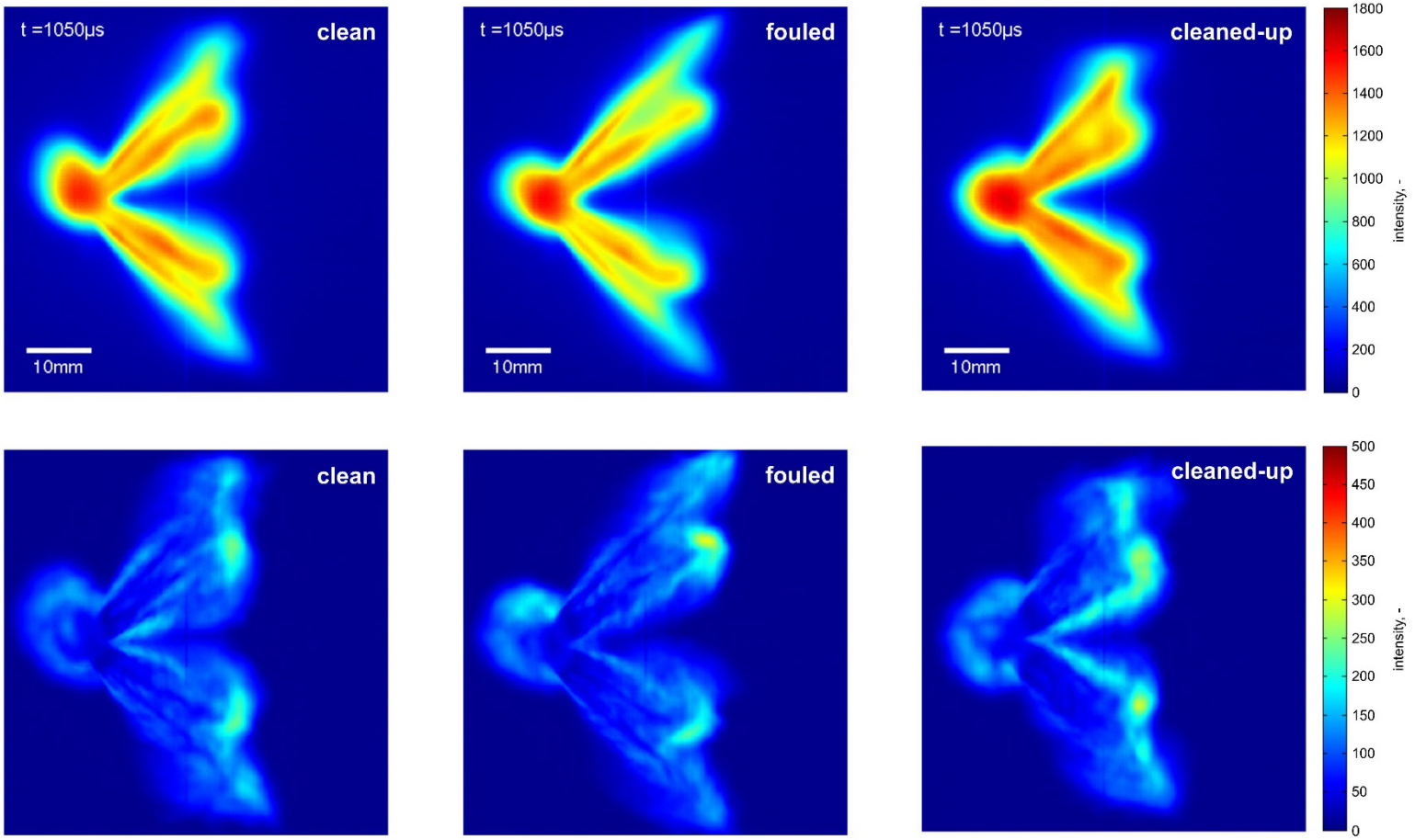


Fig. 6.9 *Comparison of the spray pattern between the clean, the fouled (Fuel A) and the cleaned-up (Fuel C) injector. The top row shows the extracted mean image and the bottom row the corresponding standard deviation.*

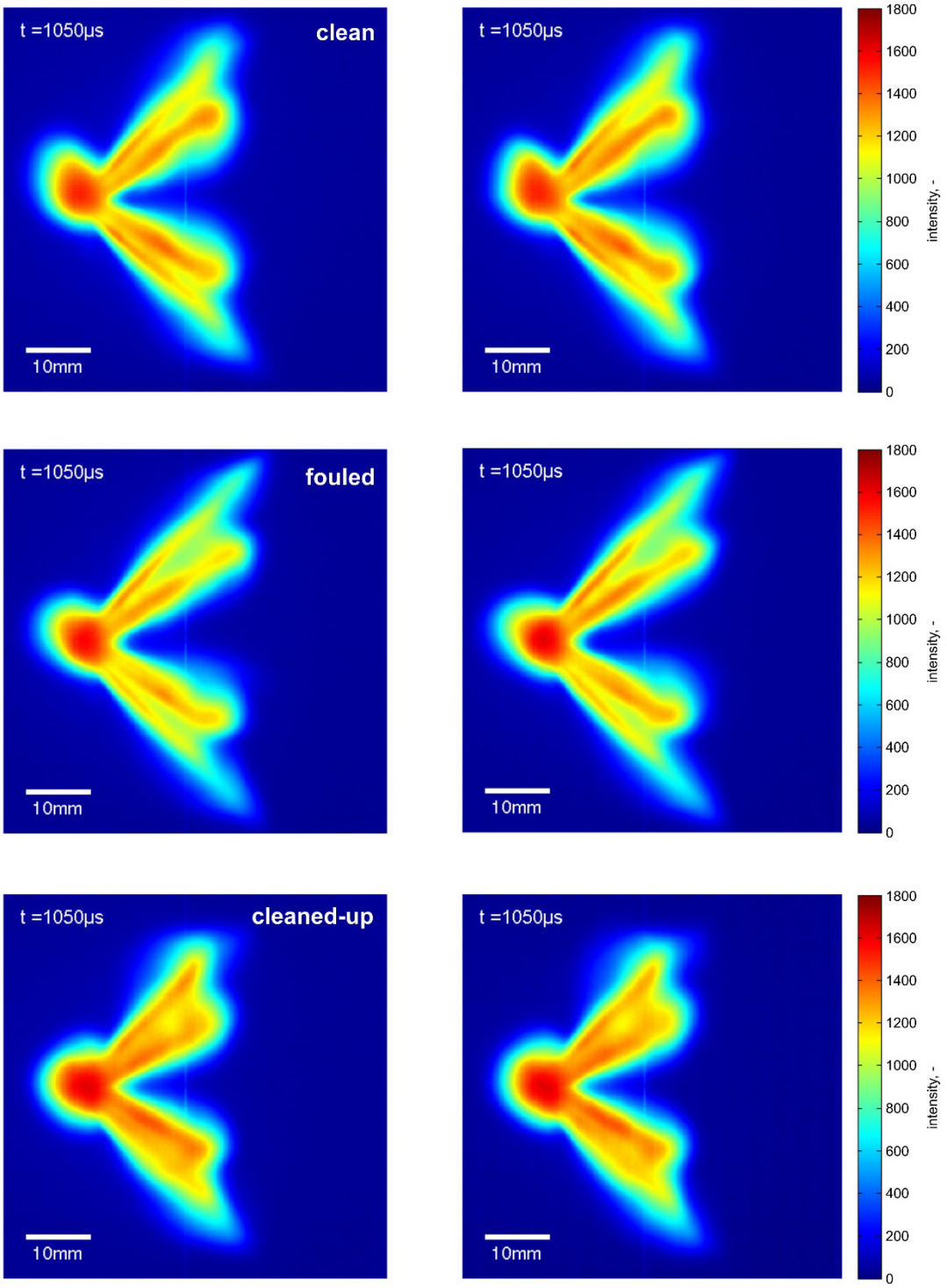


Fig. 6.10 *Comparison of mean scattering intensity images calculated from the first 50 (left column) and the last 50 (right column) injections of a 500 injection series.*

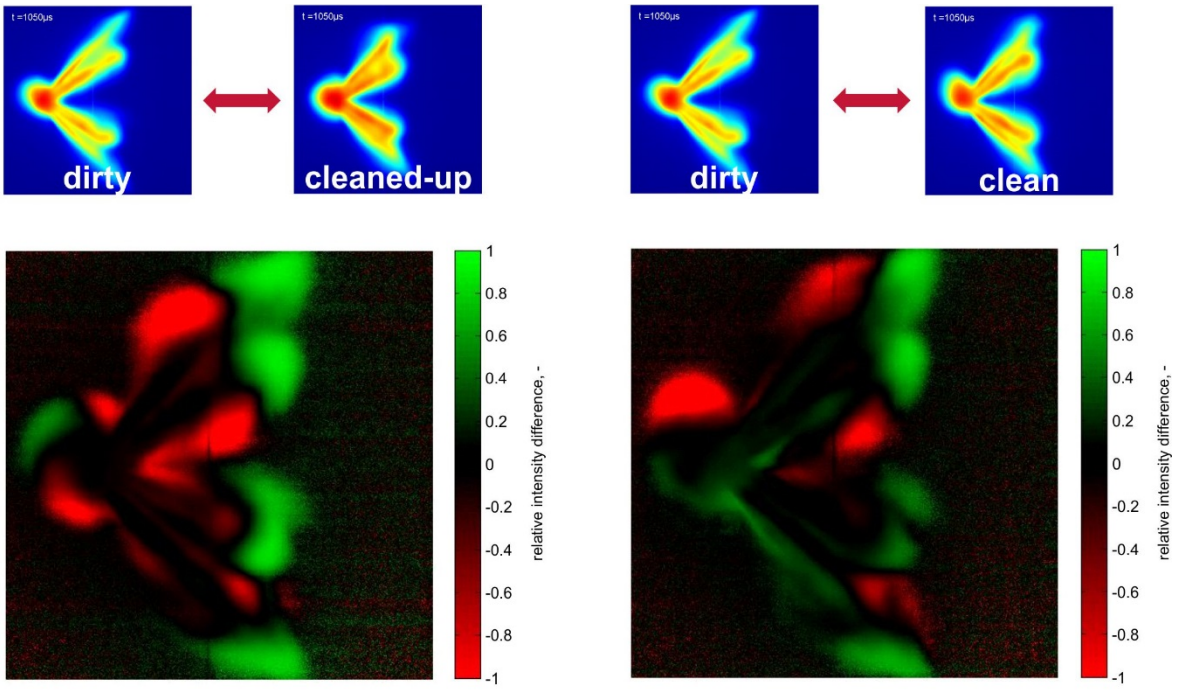


Fig. 6.11 *Relative differences between the dirty and the cleaned-up injector sprays (left side) and the dirty and clean injector sprays (right side). Black corresponds to the same local intensity in both images, green to higher and red to lower intensities in the mean spray image of the dirty injector.*

These two images illustrate the differences between the three injectors more clearly. Between the dirty and the cleaned-up injector the penetration of the former is larger, which is represented in the green regions on the right hand side. This is the case for all angled jets and the differences are rather pronounced. On the other hand, the large red regions in the centre, especially at the jet boundaries of hole #4 and hole #5 mean that the cleaned-up injector produces a much wider spray than the fouled counterpart. This reflects the observations seen in the previous comparison of the two mean time series very well. The two jets from hole #3 are more similar. The spray from the dirty injector is shaped slightly more towards the top left, but both overlap reasonably well.

In the planar difference between the fouled and the clean injector similar, but less pronounced trends can be observed. The jets of the dirty injector are also penetrating deeper than the clean jets, but the differences are slightly less strong, which results in

smaller green regions. Especially the two jets of the bottom half are less different. The sprays of the clean injector also appear wider in the center of the image and the top border. Overall, the spray pattern of the clean injector seems to be shifted slightly more upwards. This is also the case for the downward jet (hole #3), that is more distinct towards the top side. The trends observed in the relative intensity image of the fouled and the cleaned-up injector are still seen here. The jets of the fouled injector are the most compact with the smallest cone angle and the deepest penetration depth.

These findings clarify the differences seen in the evaluation of the mean spray patterns. The cleaned-up and the clean injector sprays are more similar than the fouled and the clean injector, which means that injector fouling does not only cause a significant drift in particulate emissions but also has a noticeable impact on the spray pattern. Both of these phenomena seem to be interconnected.

As an additional tool to analyse the sprays and to work out their differences, a proper orthogonal decomposition (POD) was performed on all series. This was done following the instruction and examples by Chen *et al.* [208]–[210] and Liu *et al.* [211]. The intention was to decompose the intensities seen in the mean spray images into structures containing the most energy or significance. The mean images can be used to see overall differences, but they do not include information on how these structures are formed inside the spray nor on how significant they are.

With this tool it is possible to compare shapes that occur the most during the 50 repetitions. This is achieved by decomposing the images into in different eigenmodes, sorted by the magnitude of their eigenvalue. A larger eigenvalue means that the corresponding eigenmode contains a more relevant shape or structure that eventually contributes to the mean image. Ultimately, it means that these spray structures contain the most fluctuating energy of the spray. The eigenmodes are sorted by descending energy content, which, in this case also means with descending occurrence probability. With the applied processing steps, the first eigenmode resembles the mean image and will not be discussed here as it mostly a mean to verify the applied analytics. The second eigenmode, followed by the third show the most significant and representative spray structures. Based on the cumulative eigenvalues these two contain more than 90% of the complete

information found in the mean image. Because of this, they can be used as an additional tool to compare the sprays of the three injectors. Figure 6.12 shows the second and the third eigenmode of all three sprays.

The spray of the clean injector is formed by a dominant green region in the centre of the second eigenmode. The leading spray edges of the two upper and lower jets seem rather similar with mostly red regions. Overall the patterns of the second eigenmode appear quite symmetrical between the top and the bottom half. This is in contrast to the second eigenmode of the fouled injector spray, which appears much more uneven. The dominant green region in the centre of the clean injector is missing here completely and the two top and bottom sprays also are not symmetrical. The upper half consists of larger structures, especially close to the leading edge. The second eigenmode of the cleaned-up spray seems to be a mixture of the other two, carrying a combination of both attributes. There is a green region in the centre, but the extent is smaller than for the clean injector. Also the top and the bottom half appears quite symmetrical albeit with opposite colours between them.

The third eigenmodes paint a similar picture. The clean injector produces a pattern that is relatively even and covers almost the entire spray similar to what is shown in the mean image. The spatial extents of the individual regions are also relatively small. The third eigenmode of the dirty injector is much more pronounced towards the leading edges of the jets with very wide structures. The centre and the left part of the jets is almost not represented here, which means that there is no variability in that region. Similar to the first eigenmode, the cleaned-up injector lies again in-between the other two with a dominant part towards the right side but also with structures around the centre of the image.

By decomposing the images with POD in this way, it becomes clearer where the similarities and differences between the three injectors lie. All three sprays are different from each other with the clean and the fouled injector forming two opposing extremes. The spray of the cleaned-up injector has attributes of both but seems more similar to the clean injector. This is in conjunction with the observation of the mean spray image analysis and the calculated relative differences.

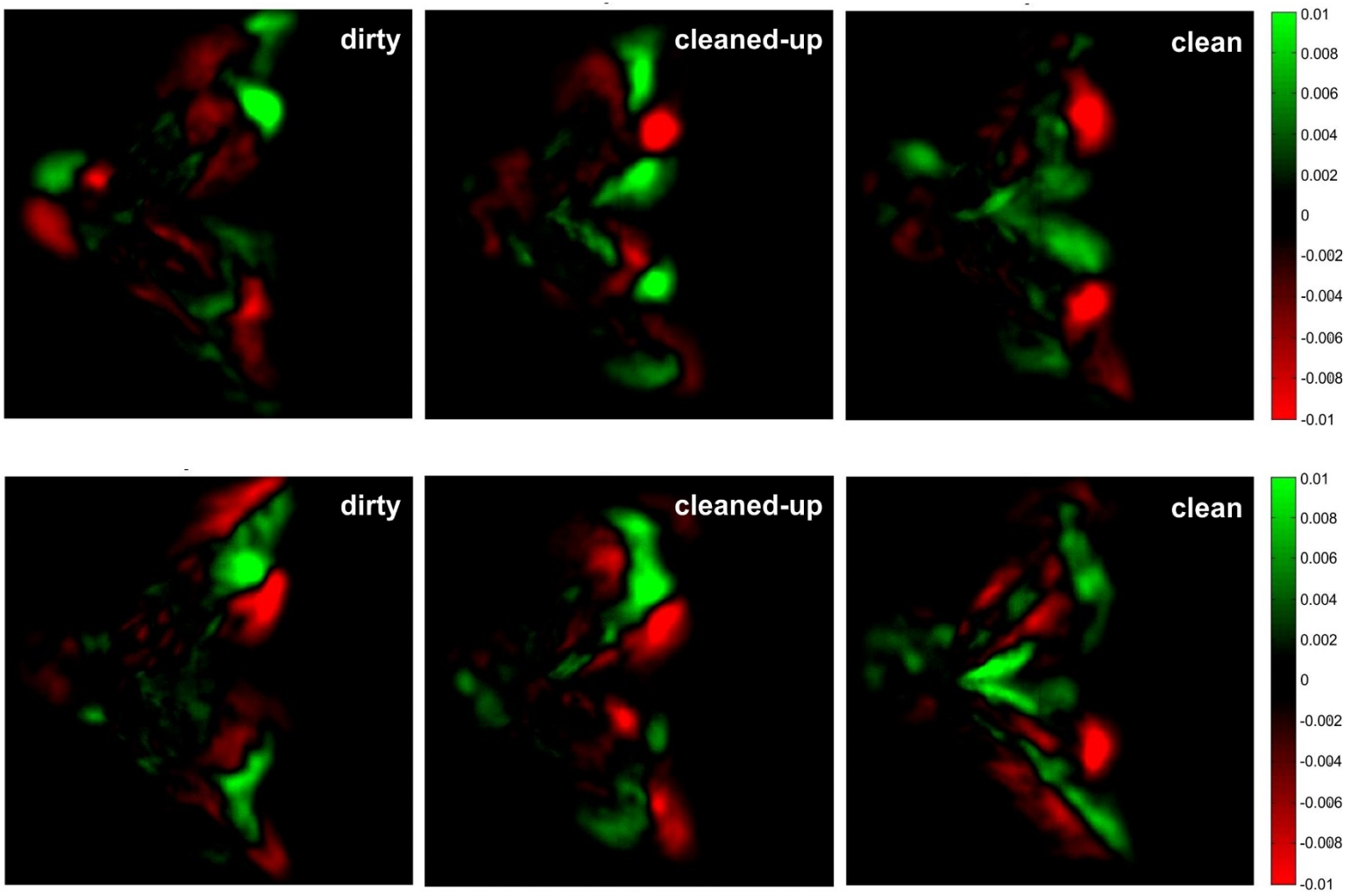


Fig. 6.12 *Second eigenmode (top row) and third eigenmode (bottom row) of the sprays generated by the three injectors.*

Despite the described differences of the clean, fouled and cleaned-up injectors, the sprays also differ in their structure in a way that is associated with manufacturing tolerances. This becomes evident when the presented mean spray pattern of the cleaned-up injector is compared to preliminary measurements of the second, unused, injector that was available. The two images can be seen in Figure 6.13. Please note that the image of the second clean injector was performed without the dark background, which is why the absolute intensity values should not be compared, but only the qualitative spray shape.

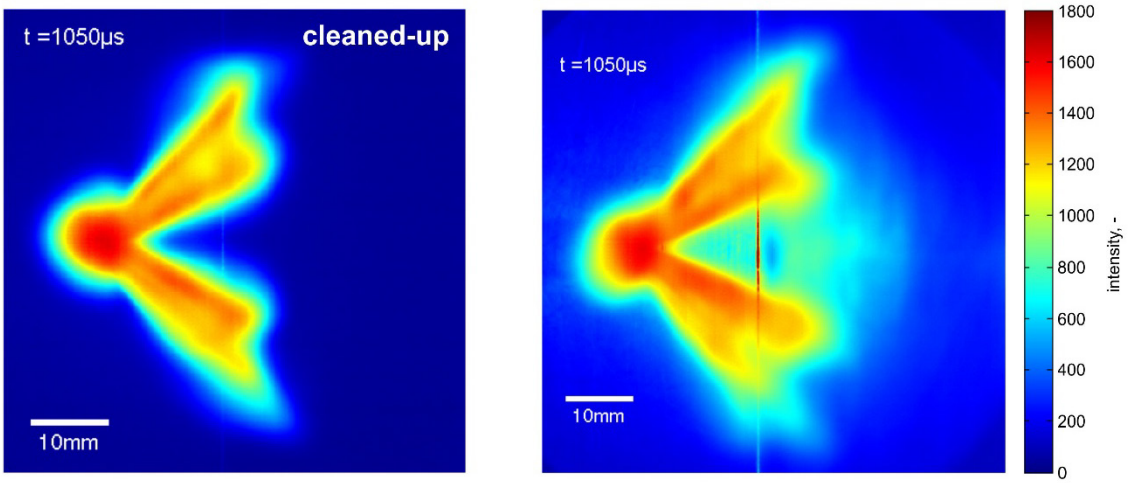


Fig. 6.13 *Comparison between the cleaned-up injector (left) and the second clean injector (right).*

These two spray patterns share a strong similarity with their diffuse jets, especially in the top half of the images. In a more general context, this leads to the conclusions that there are production differences between injectors that should not be neglected for future investigations of the impact that fouling has on the spray. It is necessary to distinguish between these two factors, which will require modifications in future experimental procedures.

Please note that the results presented are to be understood as preliminary data. By the time of submission of this thesis for examination only three injectors could be analysed regarding their spray pattern, which represents only a small fraction of the available

injectors from the engine experiments. Due to time constraints, the worst fouling case was selected to provide a first insight into this matter and to help develop experimental and analytical procedures for the ongoing investigation. Also, findings with additional clean injectors (not shown here) from a newer batch have revealed that there are significant differences in the injector performance between production runs and that newer injectors cannot be used to potentially increase the statistical reliability of the clean injector reference patterns. For this reason it was decided to mechanically clean the selected injector injectors and repeat the presented measurements. In this way a better comparison can be performed which should provide an assessment, of how much manufacturing tolerances affect the spray pattern.

6.3 Summary and conclusions

The intention of the work presented in this chapter was to look at the injector fouling process and how it affects particulate emissions in direct injection engines. The intention was to deliberately foul injectors that would be used to study what effect combustion product deposits have on engine performance and how it can be explained by changes in the spray structure. Additionally, some of the fouled injectors were treated with a detergent fuel that was counteracting the fouling process and reverting the emissions drift that was previously observed. Examining both types of injectors and comparing them to a clean reference yielded information about the reasons for the observed change in engine performance.

In a first step, injectors were used in test engines in a defined dirty-up cycle with different fuel blends. Constant monitoring of the particulate emissions showed a significant increase over the course of five hours. Two identical sets of four injectors, one for each cylinder of the engine, were produced in this phase. One of each sets was then treated with a blend containing a detergent additive in a clean-up cycle. Over time, the increased emissions level previously measured were reduced.

One dirty injector, representing the largest change in engine-out particulates, the corresponding cleaned-up injector and a clean reference injector were selected for tests in the modified injection chamber. The recorded time series of the spray patterns were analysed and compared through mean and standard deviation images. Additionally, relative differences were calculated and proper orthogonal decomposition was applied. The findings and conclusions are listed below.

Emissions measurements during the dirty-up phase of the engine experiments showed a drastic increase of more than an order of magnitude in all tests, expect for one main grade fuel and the blend containing the detergent.

- The emissions drift occurred at different rates: in some cases after slightly more than 30 minutes a change was observed, while others required around 90 minutes. This indicates that the actual mechanism of injector deposit formation must be different depending on the composition of the fuel. This was also described by other research groups [185], [188], [189].
- Running fouled injectors in a clean-up cycle completely negated the previously observed emissions drift. The reduction in particulates was observed almost immediately after switching to the detergent blend. This behavior is similar to the work by Aradi *et al.* [186], [187], and shows the potential of such fuel additives to not only maintain a low level of emissions but also reduce a possible negative effect caused by injector fouling.
- Microscopic imaging was used to evaluate the extent of deposits for each case and large differences were observed. The blend that produced the biggest emissions drift also showed the highest level of fouling and the blend which produced almost no drift produced very little deposits in comparison.
- In preliminary tests it was established that the recording of a minimum of 15 injections was necessary to produce reliable mean spray images.
- The comparison between the mean images of the fouled, cleaned-up and unused injector showed differences of the spray pattern. The fouled injector produced the narrowest jets that penetrated the most. This was most likely due to the reduction of the injector nozzle diameter that was observed in the microscopy images.

- A test run of 500 injection did not show any drift of the spray patterns for all three injectors, which shows that there is no mechanical cleaning or deposition visible for these tests. This was reassuring as a possible change in the fouling level of an injector would have skewed the results and potentially questioned the validity of the findings.
- Additional calculations of the relative differences between the injectors confirmed the trends that were observed in the mean image time series
- Proper orthongonal decomposition was used as a tool to further deepen the analysis of the similarities and differences. The second and the third eigenmode of the spray patterns showed that the clean and the dirty injector sprays are, in fact, different and that the spray of the cleaned-up lies in between.
- A comparison of the spray pattern of the cleaned-up injector with the second clean injector illustrated that there are more similarities between these two sprays compared to the first clean injector. This stresses the fact that there are production tolerances between individual injectors that need to be taken into account to evaluate the spray patterns. For this reason the three injectors will be cleaned mechanically from all deposits and measured again to see the relative changes before and after. This should provide the most reliable data and insight into the effect of injector fouling on the fuel spray.

The data presented from this study is to be understood as preliminary. The measurements and analytical procedures were used to determine if there are differences in the spray patterns observable and they build the foundation for the ongoing investigations. The results have shown that there are, in fact, differences between the three injector stages (fouled, cleaned-up, clean), but that these are “convoluted” to some extent with the manufacturing tolerances between injectors. Adding additional clean injectors to improve upon the statistical reliability of the reference sprays was not an option as the patterns produced by newer batches of nominally identical injectors were varying too much. This is why it was decided to proceed with the mechanical cleaning of the injectors presented to obtain more significant information about the changes caused by fouling.

Once these steps are completed, spray droplet analyses with Phase Doppler and liquid deposit measurements will be performed, similar to those presented in the first part of this thesis. By combining all the data that would be gathered at the end, a deeper insight into the mechanism and effects of injector fouling will be obtained.

Chapter 7

Conclusions and suggestions for future work

The concept of gasoline direct injection provides large potentials for the ongoing optimisation of the modern internal combustion engine. However, due to the shift of the injection from the air manifold into the combustion chamber, new challenges arise that were previously a non-factor. Depending on the engine operation, an interaction between the spray and the piston top or the cylinder surface cannot be avoided and the phenomenon of wall wetting occurs. Because of a short cycle time between injection and ignition this can lead to rich diffusion flames, called pool fires, which increase the engine emissions significantly. This is especially of concern for all OEMs as emissions legislations, such as EURO6 and LEV III, demand increasingly stricter limits by these engines. Additionally, these pool fires lead to combustion residues inside the cylinder that increase wear of the engine.

Another challenge that gained attention in recent years is injector fouling. This process describes the deposition of combustion products inside and around the injector nozzle. Because the injector is mounted inside the combustion chamber it is directly exposed to the flame, something that is not occurring in common port fuel injection engines. Literature shows several negative examples and the issues associated with this

phenomenon, such as a reduction of injector lifetime and an increase in engine-out emissions. The latter is of particular concern and also linked to the wall wetting issue, which poses additional challenges to fulfil modern emissions legislations.

The focus of the work presented was to investigate the process of wall wetting and how it can be minimised by adjusting fuel composition and engine operating parameters. Additionally, the application of ethanol as a fuel supplement was investigated in this context. With the knowledge gained and the experimental expertise that was developed, the process of injector fouling was studied in a second experiment and how it affects the spray patterns of multi-hole injectors. For both parts, novel measurement and processing procedures were developed to allow for a better insight into the underlying processes and to provide suggestions on future opportunities to optimise modern gasoline direct injection engines.

For the analysis of liquid deposits caused by fuel sprays found in gasoline direct injection engines a novel measurement technique was developed that allowed to record high resolution data of 2D liquid films on a rough metal plate similar to what would be found inside the combustion engine. Common techniques that were applied in the past usually require several compromises such as the addition of proxies that alter the physical or chemical composition of the fuel or do not yield reliable data over a longer period of time. Additionally, it would be difficult to find a substance that would work equally well with the large variety of fuel blends, that was subject of the investigations presented. Using different types of proxies for different blends would drastically increase the amount of calibration work necessary for such a parametric study. Other optical techniques that do not require proxies, such as interferometry usually only yield 1D information of the liquid deposit and do not have a large enough temporal resolution to capture the highly non-stationary process of liquid film deposition and evaporation. The very recent application of the Refractive Index Matching method overcomes most of these drawbacks but requires the use of a glass surface which does not share the same thermal properties as the metal used in engines. With the newly developed measurement technique presented it is possible to recreate the conditions inside the cylinder much more closely. The signal is also independent from changes of temperature and pressure, which opens it up to a large range

of experimental boundary conditions. The physical principle depends on the change of light scattering behaviour of the roughened metal surface once liquid is present, which can be related to the actual film thickness. In order to do so a calibration procedure was established and the post processing steps were developed to generate the 2D information about the local deposit film thickness with large temporal resolution. With this it was possible for the first time to quantify wall wetting under a range of boundary condition that resemble these found inside the engine cylinder at different operating points very closely.

To verify the experimental setup and the data processing a series of single component fuels were selected and tested inside the chamber. They were chosen in a way that the influence of the boiling temperature of the fuel in relation to the surface temperature of the impingement plate could be investigated. It was found that the boiling temperature is in fact the most dominating property of the liquid that determines the extent of the liquid deposit and the evaporation time. By matching the surface temperature with the respective boiling temperature of the liquid it was possible to collapse the time signals of the deposit volume. This is rather remarkable and illustrates very well the importance of the cylinder surface temperature as an optimisation parameter to avoid the occurrence of liquid deposits and rich pool fires during the combustion cycle.

With this in mind a series of 11 fuel blends with changing physical and chemical properties was investigated under a wide range of conditions to see what parameters affect the spray shape, droplet size and velocities and wall wetting. The first step was to investigate how the spray cone is affected if the boiling temperature, represented by T90, and the ethanol content is increased. Also, the olefin and aromatic content of blends was of interest. Different injection pressures, air temperatures and plate temperatures were considered here. From the free spray images there were only smaller differences observed, but a very large ethanol content increased the spray width notably. This was also reflected in the liquid deposit on a heated glass impingement plate that showed small differences and similar trends of the spray widths. These findings were meant as a criterion to select a number of fuel blends for additional more profound measurements.

Between the selected blends no significant difference was found in the droplet analysis through Phase Doppler Anemometry. All fuels produced the same velocity and

size cross profiles. Additional detailed statistical analyses at the centreline also showed strong similarities between the blends. In conjunction with the results of the preceding experiments, this led to the conclusion that potential differences in the engine performance by the different fuel blends could not be explained by the spray structure, but must be dominated by the individual wall wetting characteristics.

For this reason the novel measurement technique to quantify fuel films on a rough metal surface was applied and the deposit formation between the blends was studied very carefully. A total of eight blends were selected and two different engine operating conditions were simulated by adjusting the plate temperature. The results of the 2D evolution of the liquid deposits showed that the films do not evaporate homogeneously and that the area that is interacting directly with the spray is covered by a thinner layer. The differences of the deposits between the blends were large, and the positive effect of ethanol on the reduction of wall wetting both on a spatial and temporal scale was significant. This was confirmed by the cumulative deposit volume over time. The changes between the worst and the best case was more than an order of magnitude, with the blend that contained 85% ethanol producing the least amount of fuel deposit by far. This trend was also seen in the deposit mass relative to the total injection mass that was the smallest for this blend. These results mean that using ethanol is not only a favourable choice to increase the level of biofuels in a blend, but also to minimise the particulate emission that are produced in pool fires. An increase of the surface temperature by 40 °C also had a remarkable effect. Both the volume and the time scale could be reduced by an order of magnitude pretty much for all blends. Under these conditions the worst blend behaved almost as well as the best blend at the lower temperature point. This clearly shows that this parameter has the most impact of all investigated in this study. Changing the surface temperature could also be implemented in existing engine designs relatively easily by adjusting the coolant temperature and performance. Additionally, the lower boiling temperature of ethanol would be also beneficial here. The measurements with the blend containing 85% ethanol did not produce a noticeable deposit at this point and as such should not produce increased levels of particulate emissions in the engine. With the understanding that the extent of the liquid deposit directly correlated with the increase of particulate emissions the rig and

methodology presented provide a cost and time efficient option to evaluate new fuel blends and determine their usability in GDI engines even before actual engine tests that are usually much more complex and time consuming. This setup could become a vital tool for OEMs and petrochemical companies for the development of new fuel and injection concepts to further optimise the concept of direct injection and evaluate the level of emissions in the future.

In the second part of this work, that was looking at injector fouling and how it affects the spray shape of three injectors, one clean, one fouled and one cleaned-up, were investigated out of a group of 50 injectors. Some of these injectors underwent a deliberate fouling process with different fuel blends after which they showed varying levels of combustion deposits on the surface of their tips. Some of the fouled injectors were treated with a detergent blend in the engine that cleaned-off the deposits over time. The fouling phase resulted in an emissions drift that correlated with the level of injector deposits and was reverted during the clean-up phase with the detergent as the combustion products were removed from the nozzles over time.

The selected fouled injector and the corresponding clean-up version represented the worst case scenario of these engine cycles and were compared to the clean and unused model in the modified injection chamber. The spray pattern of the three injectors were different and the fouling led to smaller spray cones and increased penetration depth due to a decreased nozzle diameter. A possibly increased wall wetting due to the faster moving spray would explain the measured increase in particulate emissions. The spray of the cleaned-up injector was the most diffuse, even more so than the clean injector. This was most likely caused by production tolerances between these. When comparing the spray pattern of the cleaned-up injector with the second clean injector it could be seen that these share more similarities. Nevertheless, none of the tested injector reached the same level of penetration and small cone angles as the fouled one.

Additional, calculations of the relative spray differences between the dirty and cleaned-up as well as between the dirty and clean injector revealed more details about the effects of injector fouling. The largest changes were seen in the leading spray edge that

was much more progressed for the dirty injector, while the sides of the jets were less developed at the same time.

To further the analysis of the sprays, proper orthogonal decomposition was applied to the image series. Although this method is not novel on its own, it has not been applied to these types of spray patterns before. The deconstruction of the spray patterns into the most significant structures showed that the cleaned-up spray behaves like a mixture of the clean and the fouled injector, combining characteristics of both. This is something that was not obvious from the mean image comparison.

The results of the injector fouling study were meant as the foundation for the following analyses. They were used to assess the level of differences that can be observed in the spray structures between the types of injectors. The continuation of this study in the future will yield a large number of data points that can be compared with each other and will provide an even more detailed insight into the process of injector fouling and how it impacts its performance.

Based on the conclusions of the studies recommendation for future work shall be given. These are split into groups that cover the developed measurement technique, the fuel spray and deposit measurements as well as the injector fouling study.

<u>Development of a measurement technique to quantify liquid deposits on a rough metal surface:</u>

The measurement technique that was developed specifically to measure the deposition of fuel on a surface already shows great potential for a wide range of applications. During the establishment of the calibration procedure it became apparent that there is a level dependency of the signal and measurement range towards the camera and light source angles. Generally, smaller angles shift the sensitivity towards thinner films and larger angles towards thicker. The chosen angle was a compromise between optical accessibility and expected film thicknesses and has proven to be very reliable. Additional

characterisation of these parameters, however, would make the technique more robust and potentially increase the range of application.

The calibration process itself is still depending on the actual setup and needs to be performed *in-situ*. By gaining a more profound understanding of the relation between the set angles of the light source and the camera it might be possible to create a more abstract calibration correlation that can be applied to different setups without the need for a recalibration. Additionally, the application of the technique in a metal test engine is not given immediately and a calibration inside the engine would require a large effort. By using an endoscope and performing a calibration outside of the engine it would be possible to study wall wetting in the actual environment.

The chosen distance between the light source, camera and specimen would allow for a large range of injection chamber designs where different types of injectors could be tested under even more conditions. For example, the wall wetting of common rail Diesel injectors could be investigated at cylinder pressures and temperatures that are commonly found in these engines, with a similar setup. It would also be possible to investigate the effect of combustion deposits on the piston surface on the wall wetting behaviour. As mentioned this is one of the negative effects of fuel deposits that persist in the combustion phase. The changed surface properties due to carbon layers could be investigated, and how it affects fuel film build-up and evaporation. The porous layer most likely captures unburnt hydrocarbons and changes the level of emissions even more. This sort of investigation could also prove useful in a similar fashion to test the interaction between the engine lubricant and the fuel and how the surface changes its behaviour over time. It would even be possible to extend this type of investigations and include different surface treatments or coatings that change the wettability of the fuel and as such the fuel film generation.

The material that was chosen for this technique was stainless steel. It was necessary to use this over aluminium which is the material used to build the engine block and piston, because of its larger hardness. So far it was not possible to create similar surface roughnesses that were used here with such a soft material. Maybe with different manufacturing techniques and extensive testing it might be possible to use this and other metals to recreate engine conditions even more realistically.

The influence of the surface roughness on the wall wetting would be another factor that could be investigated in the future. Usually, the surface quality is specified by the OEM and meeting these specifications is rather costly. Correlations between the evaporation rate and the structure of the piston surface could result in a potential reduction of these costs, for example if an increased roughness leads to faster evaporation.

Additionally, the surface roughness determines the measurement range. Effectively, this means that operating conditions that create very large deposits could be captured with a rougher surface, while very small and thin deposits could be quantified with a smoother. This way the measurement range would be increased even further.

The results of the single component fuel showed the influence of the surface temperature on the deposition and evaporation behaviour of liquid films. By investigating a larger number of surface temperatures an actual *in-situ* characterisation of the evaporation rate of these potential fuel supplements could be created. When these are expanded to binary mixtures or fuels with component numbers of a higher order the differences in the evaporation behaviour could be studied. This is important as research by other groups has shown that fuel injectors and wall wetting should not be studied through single component fuel surrogates. These liquids show a fundamentally different evaporation at various operating conditions as there is no interaction between lighter and heavier components that would occur in real fuels. Phenomena like these could be quantified with the developed technique without requiring single droplet generators that would also decrease the closeness to reality.

Outside of engine research, the technique could also be applied to other fields, such as in aeronautic engineering. It could be used to investigate prefilming atomisers and study how the actual film thickness on the surface of the injector influences the atomisation process during break-up of the liquid.

Also, liquid deposition is a very large field of research in the chemical industry. This includes for example liquid film coating processes, different kinds of thin layer resins and polymers, drying processes, printing of circuit boards or the even how ink is distributed and absorbed by different types of paper and polymer in a printing process. It would be possible to modify the measurement technique to accommodate the requirements

that these processes would have. Essentially, the application for any chemical process where thin liquid films are present on solid surfaces would be conceivable.

Study of spray pattern and wall wetting from fuel sprays generated by an injector typical for gasoline direct injection engines:

The study has shown that both fuel composition and engine parameters have a big impact the wall wetting for a given injector.

Even though the results of the spray pattern analysis did not yield drastic changes between the different blends a continuation of these experiments would be beneficial. The number of blends of the physical matrix could be expanded and even other alcohols that are relevant as gasoline substitutes could be added. It would also be of interest how larger changes in surface tension and viscosity would change the shape of the spray.

The comparison between two different ambient air temperatures in the injector chamber showed that larger values reduce the width of the spray by promoting the evaporation of the droplet cloud. A dedicated study of this parameter over a larger range of engine conditions and maybe beyond the boiling temperature would provide more information on how the spray itself can be affected. With an optimised atomisation and evaporation process wall wetting could be further reduced already at the stage before spray impingement. Also other groups have observed that sprays can collapse under certain conditions. Additional studies like this would help to find out the operating limits of novel fuel blends. This could even be combined with measurements of the hot glass plate which would most likely change the mass transfer significantly as is also determined by the heat transfer from the air to the film.

The results of Phase Doppler Anemometry did not show large changes between the investigated blends under ambient conditions. For future research this could be extended to measurement with heated air inside the chamber. The observed change in the spray width during the high speed imaging already indicated the effect of hot air and could be quantified with droplet size and velocity statistics.

Furthermore, the formation of secondary droplets close to the plate surface would be of interest. The high speed recordings showed a cloud that moved closely along the surface of the plate with relatively large velocities. It can be assumed that some of these leave the impingement plate and do not contribute to the liquid film. Inside an engine, these would be confined by the cylinder wall and possibly form secondary deposits. This phenomenon could be assessed not only by characterising the secondary droplets, but also by equipping the impingement plate with side walls that prevent droplets from leaving the specimen. This concept could also be applied to the film thickness measurements by adding rough plates on the side. With multiple cameras and light sources the impingement process study could be expanded to the entirety of the cylinder and provide an even better insight into potential improvements. Measuring the secondary droplets on heated plates could further expand this concept.

Study of injector fouling and its impact on the spray pattern of multi-hole injectors:

The preliminary data presented already illustrates the differences in the spray shape that are caused by deposits forming inside and around injector nozzles. The number of injectors that were compared will be increased in the future. This way the trends that were described can be solidified.

Additionally, the investigations will be expanded with measurements of the liquid deposit. This is most likely the defining factor that is causing the observed drift in particulate emissions. In the first project the reliability of the measurement technique presented was proven and the information obtained about the deposit volume and mass would give a detailed insight into the consequences of injector fouling.

An analysis of the droplet size and velocity statistics will also be done with Phase Doppler Anemometry measurements. It is possible that the atomisation efficiency is changed by the reduction of the nozzle diameter and possibly in a different amount for the individual jets.

On a larger scheme of injector fouling it would be interesting to study a series of injectors over the course of a fouling cycle. This could be started with the complete

characterisation of clean injectors that will be subsequently treated in engine cycles similar to the ones used in this study. The process could be interrupted and the spray could be measured at different stages of the fouling. This way the actual process could be characterised even more and the fouling rate by different fuel blends would be assessed. The same could be applied to the clean-up phase and possibly combined with different blends that utilise detergent additives.

Summarising the findings and the conclusions that were drawn it can be said that the work presented builds a good foundation for future research. This includes both, the measurement techniques that were developed and applied as well as the parameters studied. The suggestions for future work could be used to expand the data gathered and would widen the catalogue of suggestions to continue the optimisation of the gasoline direct injection engine design. A continued effort to work closely with industry partners would provide additional ideas and concepts that could be incorporated not only long term, but also within a generation of engines. This way it will be possible to overcome not only the present but also future challenges that the ever-changing automotive industry is facing.

Bibliography

[1] R. van Basshuysen and U. Spicher, *Gasoline Engine with Direct Injection: Processes, Systems, Development, Potential*. Wiesbaden: Springer Verlag, 2009.

[2] C. Queiroz and E. Tomanik, "Gasoline Direct Injection Engines - A Bibliographical Review," in *SAE Technical Paper*, 1997.

[3] E. Stevens and R. Steeper, "Piston wetting in an optical DISI engine: fuel films, pool fires, and soot generation," *SAE Tech. Pap. Ser.*, no. 2001–01–1203, 2001.

[4] J. Li, R. D. Matthews, R. H. Stanglmaier, C. E. Roberts, and R. W. Anderson, "Further Experiments on the Effects of In-Cylinder Wall Wetting on HC Emissions from Direct Injection Gasoline Engines," in *SAE Technical Paper*, 1999.

[5] A. Montanaro, L. Allocca, D. Ettorre, T. Lucchini, F. Brusiani, and G. Cazzoli, "Experimental Characterization of High-Pressure Impinging Sprays for CFD Modeling of GDI Engines," *SAE Int. J. Engines*, vol. 4, pp. 747–763, 2011.

[6] A. Montanaro, S. Malaguti, and S. Alfuso, "Wall Impingement Process of a Multi-Hole GDI Spray: Experimental and Numerical Investigation," in *SAE Technical Paper*, 2012.

[7] S. Hochgreb, "Liquid Fuel Impingement on the Piston Bowl of a Direct-Injection, Spark-Ignited (DISI) Engine under Stratified Operation," in *SAE Technical Paper*, 2001.

[8] F. Zhao, M.-C. Lai, and D. . Harrington, "Automotive spark-ignited direct-injection gasoline engines," *Prog. Energy Combust. Sci.*, vol. 25, no. 5, pp. 437–562, Oct. 1999.

[9] M. C. Drake and T. D. Fansler, "Piston Fuel Films as a Source of Smoke and Hydrocarbon Emissions from a Wall-Controlled Spark-Ignited Direct-Injection Engine," *SAE Tech. Pap. Ser.*, no. 2003–01–0547, 2003.

[10] X. He, M. A. Ratcliff, and B. T. Zig, "Effects of Gasoline Direct Injection Engine Operating Parameters on Particle Number Emissions," *Energy & Fuels*, vol. 26, no. 4, pp. 2014–2027, 2012.

[11] S. Malaguti and S. Fontanesi, "CFD Investigation of Fuel Film Formation Within a GDI Engine Under Cold Start Cranking Operation," *Proc. 2009 Spring Tech. Conf. ASME Int. Combust. Engine Div.*, pp. 555–562, 2009.

[12] F. Zhao, M.-C. Lai, and D. L. Harrington, "Automotive spark-ignited direct-injection gasoline engines," *Prog. Energy Combust. Sci.*, vol. 25, no. 5, pp. 437–562, 1999.

[13] R. H. Stanglmaier, J. Li, and R. D. Matthews, "The Effect of In-Cylinder Wall Wetting Location on the HC Emissions from SI Engines," in *SAE Technical Paper*,

1999.

[14] J. Li, Y. Huang, T. F. Alger, R. D. Matthews, and M. J. Hall, "Liquid fuel impingement on in-cylinder surfaces as a source of hydrocarbon emissions from direct injection gasoline engines," *J. Eng. GAS TURBINES POWER-TRANSACTIONS ASME*, vol. 123, no. 3, pp. 659–668, Jul. 2001.

[15] B. D. Stojkovic, T. D. Fansler, M. C. Drake, and V. Sick, "High-speed imaging of OH* and soot temperature and concentration in a stratified-charge direct-injection gasoline engine," *Proc. Combust. Inst.*, vol. 30, no. 2, pp. 2657–2665, 2005.

[16] C. L. Myung and S. Park, "Exhaust nanoparticle emissions from internal combustion engines: A review," *Int. J. Automot. Technol.*, vol. 13, no. 1, pp. 9–22, Jan. 2012.

[17] Y. Kim, Y. Kim, S. Jun, K. H. Lee, S. Rew, D. Lee, and S. Park, "Strategies for Particle Emissions Reduction from GDI Engines," in *SAE Technical Paper*, 2013.

[18] S. Zhang and W. McMahon, "Particulate Emissions for LEV II Light-Duty Gasoline Direct Injection Vehicles," *SAE Int. J. Fuels Lubr.*, vol. 5, pp. 637–646, 2012.

[19] D. E. Hall and C. J. Dickens, "Measurement of the Number and Size Distribution of Particles Emitted from a Gasoline Direct Injection Vehicle," in *SAE Technical Paper*, 1999.

[20] F. Xu and R. Stone, "The Effects of Hot Air Dilution and an Evaporation Tube (ET) on the Particulate Matter Emissions from a Spray Guided Direct Injection Spark Ignition Engine," in *SAE Technical Paper*, 2012.

[21] R. I. Crane, L. Rubino, C. Arcoumanis, S. E. Golunski, J. M. McNamara, S. Poulston, and R. R. Rajaram, "Strategies for Gasoline Particulate Emission Control - A 'Foresight Vehicle' Project," in *SAE Technical Paper*, 2002.

[22] Health and Safety Executive, *Using nanomaterials at work*, vol. 272, no. Published 2013. 2013.

[23] C. Cheng, a E. Porter, K. Muller, K. Koziol, J. N. Skepper, P. Midgley, and M. Welland, "Imaging carbon nanoparticles and related cytotoxicity," *J. Phys. Conf. Ser.*, vol. 151, p. 012030, 2009.

[24] L. A. Sgro, P. Sementa, B. M. Vaglieco, G. Rusciano, A. D'Anna, and P. Minutolo, "Investigating the origin of nuclei particles in {GDI} engine exhausts," *Combust. Flame*, vol. 159, no. 4, pp. 1687–1692, 2012.

[25] A. Überall, R. Otte, P. Eilts, and J. Krahl, "A literature research about particle emissions from engines with direct gasoline injection and the potential to reduce these emissions," *Fuel*, vol. 147, pp. 203–207, 2015.

[26] M. Fatouraie, M. Wooldridge, and S. Wooldridge, "In-Cylinder Particulate Matter and Spray Imaging of Ethanol/Gasoline Blends in a Direct Injection Spark Ignition Engine," *SAE Int. J. Fuels Lubr.*, vol. 6, pp. 1–10, 2013.

[27] W. Piock, G. Hoffmann, A. Berndorfer, P. Salemi, and B. Fusshoeller, "Strategies Towards Meeting Future Particulate Matter Emission Requirements in Homogeneous Gasoline Direct Injection Engines," *SAE Int. J. Engines*, vol. 4, pp. 1455–1468, 2011.

[28] F. Köpple, P. Jochmann, A. Kufferath, and M. Bargende, "Investigation of the Parameters Influencing the Spray-Wall Interaction in a GDI Engine - Prerequisite for the Prediction of Particulate Emissions by Numerical Simulation," *SAE Int. J. Engines*, vol. 6, pp. 911–925, 2013.

[29] F. Köpple, D. Seboldt, P. Jochmann, A. Hettinger, A. Kufferath, and M. Bargende, "Experimental Investigation of Fuel Impingement and Spray-Cooling on the Piston of a GDI Engine via Instantaneous Surface Temperature Measurements," *SAE Int. J.*

Engines, vol. 7, pp. 1178–1194, 2014.

[30] T. W. Chan, E. Meloche, J. Kubsh, R. Brezny, D. Rosenblatt, and G. Rideout, "Impact of Ambient Temperature on Gaseous and Particle Emissions from a Direct Injection Gasoline Vehicle and its Implications on Particle Filtration," *SAE Int. J. Fuels Lubr.*, vol. 6, pp. 350–371, 2013.

[31] B. A. VanDerWege and S. Hochgreb, "Effects of Fuel Volatility and Operating Conditions on Fuel Sprays in DISI Engines: (2) PDPA Investigation," in *SAE Technical Paper*, 2000.

[32] H. Sandquist, I. Denbratt, F. Owrang, and J. Olsson, "Influence of Fuel Parameters on Deposit Formation and Emissions in a Direct Injection Stratified Charge SI Engine," in *SAE Technical Paper*, 2001.

[33] D. C. Arters and M. J. Macduff, "The Effect on Vehicle Performance of Injector Deposits in a Direct Injection Gasoline Engine," in *SAE Technical Paper*, 2000.

[34] F.-Q. Zhao, M.-C. Lai, and D. L. Harrington, "A Review of Mixture Preparation and Combustion Control Strategies for Spark-Ignited Direct-Injection Gasoline Engines," in *SAE Technical Paper*, 1997.

[35] D. D. Brehob, J. E. Fleming, M. Haghgooie, and R. A. Stein, "Stratified-Charge Engine Fuel Economy and Emission Characteristics," in *SAE Technical Paper*, 1998.

[36] M. Alperstein, G. H. Schafer, and F. J. Villforth, "Texaco's Stratified Charge Engine - Multifuel Efficient, Clean, and Practical," in *SAE Technical Paper*, 1974.

[37] T. D. Fansler, D. L. Reuss, V. Sick, and R. N. Dahms, "Combustion instability in spray-guided stratified-charge engines: A review," *Int. J. Engine Res.*, vol. 16, no. 3, pp. 260–305, 2015.

[38] J. Milpied, N. Jeuland, G. Plassat, S. Guichaous, N. Dioc, A. Marchal, and P. Schmelzle, "Impact of Fuel Properties on the Performances and Knock Behaviour of a Downsized Turbocharged DI SI Engine - Focus on Octane Numbers and Latent Heat of Vaporization," *SAE Int. J. Fuels Lubr.*, vol. 2, pp. 118–126, 2009.

[39] M. Amann and D. Ouwenga, "Engine Parameter Optimization for Improved Engine and Drive Cycle Efficiency for Boosted, GDI Engines with Different Boosting System Architecture," in *SAE Technical Paper*, 2014.

[40] W. Bandel, G. K. Fraidl, P. E. Kapus, H. Sikinger, and C. N. Cowland, "The Turbocharged GDI Engine: Boosted Synergies for High Fuel Economy Plus Ultra-low Emission," in *SAE Technical Paper*, 2006.

[41] Y. Huang, G. Hong, X. Cheng, and R. Huang, "Investigation to Charge Cooling Effect of Evaporation of Ethanol Fuel Directly Injected in a Gasoline Port Injection Engine," in *SAE Technical Paper*, 2013.

[42] F.-Q. Zhao, M.-C. Lai, and D. L. Harrington, "The Spray Characteristics of Automotive Port Fuel Injection-A Critical Reviews," in *SAE Technical Paper*, 1995.

[43] S. T. Chin and C.-F. F. Lee, "Numerical investigation of the effect of wall wetting on hydrocarbon emissions in engines," *Proc. Combust. Inst.*, vol. 29, no. 1, pp. 767–773, 2002.

[44] W. Anderson, J. Yang, D. D. Brehob, J. K. Vallance, and R. M. Whiteaker, "Understanding the Thermodynamics of Direct Injection Spark Ignition (DISI) Combustion Systems: An Analytical and Experimental Investigation," in *SAE Technical Paper*, 1996.

[45] E. Kasseris and J. B. Heywood, "Charge Cooling Effects on Knock Limits in SI DI Engines Using Gasoline/Ethanol Blends: Part 1-Quantifying Charge Cooling," in *SAE Technical Paper*, 2012.

[46] E. W. Kaiser, W. O. Siegl, D. D. Brehob, and M. Haghgooie, "Engine-Out Emissions from a Direct-Injection Spark-Ignition (DISI) Engine," in *SAE Technical Paper*, 1999.

[47] B. Liang, Y. Ge, J. Tan, X. Han, L. Gao, L. Hao, W. Ye, and P. Dai, "Comparison of PM emissions from a gasoline direct injected (GDI) vehicle and a port fuel injected (PFI) vehicle measured by electrical low pressure impactor (ELPI) with two fuels: Gasoline and M15 methanol gasoline," *J. Aerosol Sci.*, vol. 57, pp. 22–31, Mar. 2013.

[48] M. M. Maricq, "Chemical characterization of particulate emissions from diesel engines: A review," *J. Aerosol Sci.*, vol. 38, no. 11, pp. 1079–1118, 2007.

[49] T. V Johnson, "Vehicular Emissions in Review," *SAE Int. J. Engines*, vol. 5, pp. 216–234, 2012.

[50] T. Johnson, "Vehicular Emissions in Review," *SAE Int. J. Engines*, vol. 7, pp. 1207–1227, 2014.

[51] D. W. Stanton and C. J. Rutland, "Modeling Fuel Film Formation and Wall Interaction in Diesel Engines," in *SAE Technical Paper*, 1996.

[52] F. Schulz and J. Schmidt, "Infrared thermography based fuel film investigations Institute of Fluid Dynamics and Thermodynamics," *whcih ICLASS*, 2012.

[53] A. L. N. Moreira, A. S. Moita, and M. R. Panão, "Advances and challenges in explaining fuel spray impingement: How much of single droplet impact research is useful?," *Prog. Energy Combust. Sci.*, vol. 36, no. 5, pp. 554–580, 2010.

[54] D. Salters, P. Williams, A. Greig, and D. Brehob, "Fuel Spray Characterisation within an Optically Accessed Gasoline Direct Injection Engine Using a CCD Imaging System," in *SAE Technical Paper*, 1996.

[55] C. Arcoumanis, M. Gavaises, and B. French, "Effect of Fuel Injection Processes on the Structure of Diesel Sprays." SAE International, 1997.

[56] C. Bai and A. D. Gosman, "Development of Methodology for Spray Impingement Simulation," in *SAE Technical Paper*, 1995.

[57] R. Lindgren and I. Denbratt, "Modeling Gasoline Spray-Wall Interactions and Comparison to Experimental Data," in *SAE Technical Paper*, 2004.

[58] R. Lindgren and I. Denbratt, "Modelling Gasoline Spray-wall Interaction -a Review of Current Models," in *SAE Technical Paper*, 2000.

[59] L. Zigan, M. Ammon, I. Schmitz, M. Wensing, A. Leipertz, and V. Gupta, "Investigation of Fuel Effects on Spray Atomization and Evaporation Studied for a Multi-hole DISI Injector with a Late Injection Timing," *SAE Int. J. Fuels Lubr.*, vol. 5, pp. 254–264, 2011.

[60] C. X. Bai, H. Rusche, and A. D. Gosman, "Modeling of gasoline spray impingement," *At. SPRAYS*, vol. 12, no. 1–3, pp. 1–27, 2002.

[61] C. Mundo, M. Sommerfeld, and C. Tropea, "On the modeling of liquid sprays impinging on surfaces," *At. SPRAYS*, vol. 8, no. 6, pp. 625–652, 1998.

[62] J. Senda and H. G. Fujimoto, "Multidimensional Modeling of Impinging Sprays on the Wall in Diesel Engines," *Appl. Mech. Rev.*, vol. 52, no. 4, pp. 119–138, Apr. 1999.

[63] S. Chandra and C. T. Avedisian, "On The Collision of a Doplet With a Solid-Surface," *Proc. R. Soc. LONDON Ser. A-MATHEMATICAL Phys. Eng. Sci.*, vol. 432, no. 1884, pp. 13–41, Jan. 1991.

[64] B. S. Gottfried, C. J. Lee, and K. J. Bell, "The leidenfrost phenomenon: film boiling of liquid droplets on a flat plate," *Int. J. Heat Mass Transf.*, vol. 9, no. 11, pp. 1167–1188, 1966.

[65] R. H. Stanglmaier, C. E. Roberts, and C. A. Moses, "Vaporization of Individual Fuel Drops on a Heated Surface: A Study of Fuel-Wall Interactions within Direct-Injected Gasoline (DIG) Engines," in *SAE Technical Paper*, 2002.

[66] C. Mundo, M. Sommerfeld, and C. Tropea, "Droplet-wall Collisions - Experimental Studies of the Deformation and Breakup Process," *Int. J. Multiph. FLOW*, vol. 21, no. 2, pp. 151–173, Apr. 1995.

[67] J. D. Naber and R. D. Reitz, "Modeling Engine Spray/Wall Impingement," in *SAE Technical Paper*, 1988.

[68] Z. Han, Z. Xu, and N. Trigui, "Spray/wall interaction models for multidimensional engine simulation," *Int. J. Engine Res.*, vol. 1, no. 1, pp. 127–146, 2000.

[69] J. E. Ketterer and W. K. Cheng, "On the Nature of Particulate Emissions from DISI Engines at Cold-Fast-Idle," *SAE Int. J. Engines*, vol. 7, pp. 986–994, 2014.

[70] C. Stovell, R. D. Matthews, B. E. Johnson, H. Ng, and B. Larsen, "Emissions and Fuel Economy of a 1998 Toyota with a Direct Injection Spark Ignition Engine," in *SAE Technical Paper*, 1999.

[71] H. Sandquist, R. Lindgren, and I. Denbratt, "Sources of Hydrocarbon Emissions from a Direct Injection Stratified Charge Spark Ignition Engine," in *SAE Technical Paper*, 2000.

[72] E. Stevens and R. Steeper, "Piston Wetting in an Optical DISI Engine: Fuel Films, Pool Fires, and Soot Generation," in *SAE Technical Paper*, 2001.

[73] M. C. Drake, T. D. Fansler, A. S. Solomon, and G. A. Szekely, "Piston Fuel Films as a Source of Smoke and Hydrocarbon Emissions from a Wall-Controlled Spark-Ignited Direct-Injection Engine," in *SAE Technical Paper*, 2003.

[74] I. B. Oliveira and S. Hochgreb, "Detailed Calculation of Heating, Evaporation, and Reaction Processes of a Thin Liquid Layer of Hydrocarbon Fuel," in *SAE Technical Paper*, 2000.

[75] M. E. Drake, M.C. , Fansler, T.D. , and Rosalik, "Quantitative high-speed imaging of piston fuel films in direct-injection engines using a refractive-index- matching techniquee," *ILASS-02 – 15th Annu. Conf. Liq. At. Spray Syst. Madison, WI*, 2002.

[76] T. D. Fansler, M. C. Drake, B. Stojkovic, and M. E. Rosalik, "Local fuel concentration, ignition and combustion in a stratified charge spark combustion in a stratified charge spark ignited direct injection engine: Spectroscopic, imaging and pressure-based measurements," *Int. J. Engine Res.*, vol. 4, no. 2, pp. 61–86, 2003.

[77] R. Ortmann, S. Arndt, J. Raimann, R. Grzeszik, and G. Würfel, "Methods and Analysis of Fuel Injection, Mixture Preparation and Charge Stratification in Different Direct Injected SI Engines," in *SAE Technical Paper*, 2001.

[78] Q. Jiao and R. D. Reitz, "The Effect of Operating Parameters on Soot Emissions in GDI Engines," *SAE Int. J. Engines*, vol. 8, pp. 1322–1333, 2015.

[79] J. P. Szybist, A. D. Youngquist, T. L. Barone, J. M. Storey, W. R. Moore, M. Foster, and K. Confer, "Ethanol Blends and Engine Operating Strategy Effects on Light-Duty Spark-Ignition Engine Particle Emissions," *ENERGY & FUELS*, vol. 25, no. 11, pp. 4977–4985, Nov. 2011.

[80] D. Sabathil, A. Koenigstein, P. Schaffner, J. Fritzsche, and A. Doehler, "The Influence of DISI Engine Operating Parameters on Particle Number Emissions," in *SAE Technical Paper*, 2011.

[81] A. Velji, K. Yeom, U. Wagner, U. Spicher, M. Rossbach, R. Suntz, and H. Bockhorn, "Investigations of the Formation and Oxidation of Soot Inside a Direct Injection Spark Ignition Engine Using Advanced Laser-Techniques," in *SAE Technical Paper*, 2010.

[82] L. C. R. Johansen and S. Hemdal, "In cylinder visualization of stratified combustion of {E85} and main sources of soot formation," *Fuel*, vol. 159, pp. 392–411, 2015.
[83] S. Oh, S. Lee, Y. Choi, K.-Y. Kang, J. Cho, and K. Cha, "Combustion and Emission Characteristics in a Direct Injection LPG/Gasoline Spark Ignition Engine," in *SAE Technical Paper*, 2010.
[84] A. J. Giovanetti, J. A. Ekchian, J. B. Heywood, and E. F. Fort, "Analysis of Hydrocarbon Emissions Mechanisms in a Direct Injection Spark-Ignition Engine," in *SAE Technical Paper*, 1983.
[85] J. Li, Y. Huang, T. F. Alger, R. D. Matthews, M. J. Hall, R. H. Stanglmaier, C. E. Roberts, W. Dai, and R. W. Anderson, "Liquid Fuel Impingement on In-Cylinder Surfaces as a Source of Hydrocarbon Emissions From Direct Injection Gasoline Engines," *J. Eng. Gas Turbines Power*, vol. 123, no. 3, pp. 659–668, Dec. 2000.
[86] Y. Huang, T. Alger, R. D. Matthews, and J. Ellzey, "The Effects of Fuel Volatility and Structure on HC Emissions from Piston Wetting in DISI Engines," in *SAE Technical Paper*, 2001.
[87] Y. Huang, R. D. Matthews, J. Ellzey, and W. Dai, "Effects of Fuel Volatility, Load, and Speed on HC Emissions Due to Piston Wetting," in *SAE Technical Paper*, 2001.
[88] P. Pierre, M. Castagné, G. Corde, G. Eyssavel, and A. Floch, "Analysis of HC Emissions on Single Cylinder During Transient Conditions," in *SAE Technical Paper*, 2004.
[89] V. S. Costanzo and J. B. Heywood, "Effect of In-Cylinder Liquid Fuel Films on Engine-Out Unburned Hydrocarbon Emissions for an SI Engine," in *SAE Technical Paper*, 2012.
[90] R. E. Chase, G. J. Duszkiewicz, J. F. O. Richert, D. Lewis, M. M. Maricq, and N. Xu, "PM Measurement Artifact: Organic Vapor Deposition on Different Filter Media," in *SAE Technical Paper*, 2004.
[91] K. Ehara, C. Hagwood, and K. J. Coakley, "Novel method to classify aerosol particles according to their mass-to-charge ratio—Aerosol particle mass analyser," *J. Aerosol Sci.*, vol. 27, no. 2, pp. 217–234, 1996.
[92] J. S. Olfert and N. Collings, "New method for particle mass classification—the Couette centrifugal particle mass analyzer," *J. Aerosol Sci.*, vol. 36, no. 11, pp. 1338–1352, 2005.
[93] P. A. Baron and K. Willeke, *Aerosol measurement: principles, techniques, and applications*. New York: Wiley, 1993.
[94] H. Burtscher, "Physical characterization of particulate emissions from diesel engines: a review," *J. Aerosol Sci.*, vol. 36, no. 7, pp. 896–932, 2005.
[95] S. C. Wang and R. C. Flagan, "Scanning electrical mobility spectrometer," *J. Aerosol Sci.*, vol. 20, no. 8, pp. 1485–1488, 1989.
[96] C. Van Gulijk, J. C. M. Marijnissen, M. Makkee, J. A. Moulijn, and A. Schmidt-Ott, "Measuring diesel soot with a scanning mobility particle sizer and an electrical low-pressure impactor: performance assessment with a model for fractal-like agglomerates," *J. Aerosol Sci.*, vol. 35, no. 5, pp. 633–655, 2004.
[97] S. J. Harris and M. M. Maricq, "Signature size distributions for diesel and gasoline engine exhaust particulate matter," *J. Aerosol Sci.*, vol. 32, no. 6, pp. 749–764, 2001.
[98] J. Keskinen, K. Pietarinen, and M. Lehtimäki, "Electrical low pressure impactor," *J. Aerosol Sci.*, vol. 23, no. 4, pp. 353–360, 1992.
[99] M. Marjamäki, J. Keskinen, D.-R. Chen, and D. Y. H. Pui, "Performance Evaluation of the Electrical Low-Pressure Impactor (ELPI)," *J. Aerosol Sci.*, vol. 31, no. 2, pp.

249–261, 2000.
[100] M. Kasper, A. Keller, J. Paul, K. Siegmann, and H. C. Siegmann, "Photoelectron spectroscopy without vacuum: nanoparticles in gas suspension," *J. Electron Spectros. Relat. Phenomena*, vol. 98–99, pp. 83–93, 1999.
[101] M. Lapuerta, O. Armas, and A. Gómez, "Diesel Particle Size Distribution Estimation from Digital Image Analysis," *Aerosol Sci. Technol.*, vol. 37, no. 4, pp. 369–381.
[102] M. Zielinski, H. Römmelt, and G. Fruhmann, "Ambient air soot concentrations in Munich public transportation systems," *Sci. Total Environ.*, vol. 196, no. 2, pp. 107–110, 1997.
[103] S. Schraml, S. Dankers, K. Bader, S. Will, and A. Leipertz, "Soot temperature measurements and implications for time-resolved laser-induced incandescence (TIRE-LII)," *Combust. Flame*, vol. 120, no. 4, pp. 439–450, 2000.
[104] C. Crua, D. A. Kennaird, and M. R. Heikal, "Laser-induced incandescence study of diesel soot formation in a rapid compression machine at elevated pressures," *Combust. Flame*, vol. 135, no. 4, pp. 475–488, 2003.
[105] R. Viskup, "In-situ Laser Induced Incandescence technique for measurement of full stream fast transient soot emissions in real-time," *Measurement*, vol. 58, pp. 429–440, 2014.
[106] S. J. Gregg and K. S. W. Sing, *Adsorption, surface area, and porosity*. Academic Press, 1991.
[107] U. Baltensperger, H. W. Gäggeler, D. T. Jost, M. Emmenegger, and W. Nägeli, "Continuous background aerosol monitoring with the epiphaniometer," *Atmos. Environ. Part A. Gen. Top.*, vol. 25, no. 3, pp. 629–634, 1991.
[108] I. M. Khan, C. H. T. Wang, and B. E. Langridge, "Coagulation and combustion of soot particles in diesel engines," *Combust. Flame*, vol. 17, no. 3, pp. 409–419, 1971.
[109] J. Ristimäki, A. Virtanen, M. Marjamäki, A. Rostedt, and J. Keskinen, "On-line measurement of size distribution and effective density of submicron aerosol particles," *J. Aerosol Sci.*, vol. 33, no. 11, pp. 1541–1557, 2002.
[110] C. Farron, N. Matthias, D. E. Foster, M. Andrie, R. Krieger, P. Najt, K. Narayanaswamy, A. Solomon, and A. Zelenyuk, "Particulate Characteristics for Varying Engine Operation in a Gasoline Spark Ignited, Direct Injection Engine," in *SAE Technical Paper*, 2011.
[111] R. Daniel, G. Tian, H. Xu, and S. Shuai, "Ignition timing sensitivities of oxygenated biofuels compared to gasoline in a direct-injection {SI} engine," *Fuel*, vol. 99, pp. 72–82, 2012.
[112] H. Oh, C. Bae, J. Park, and J. Jeon, "Effect of the Multiple Injection on Stratified Combustion Characteristics in a Spray-Guided DISI Engine," *Soc. Automot. Eng.*, 2011.
[113] A. N. Johansson, S. Hemdal, and P. Dahlander, "Experimental Investigation of Soot in a Spray-Guided Single Cylinder GDI Engine Operating in a Stratified Mode," in *SAE Technical Paper*, 2013.
[114] T. Alger, Y. Huang, M. Hall, and R. D. Matthews, "Liquid Film Evaporation Off the Piston of a Direct Injection Gasoline Engine," in *SAE Technical Paper*, 2001.
[115] J. Serras-Pereira, P. G. Aleiferis, D. Richardson, and S. Wallace, "Spray Development, Flow Interactions and Wall Impingement in a Direct-Injection Spark-Ignition Engine," in *SAE Technical Paper*, 2007.
[116] F. Schulz, J. Schmidt, A. Kufferath, and W. Samenfink, "Gasoline Wall Films and Spray/Wall Interaction Analyzed by Infrared Thermography," *SAE Int. J. Engines*,

vol. 7, pp. 1165–1177, 2014.
[117] S. Taniguchi, K. Yoshida, and Y. Tsukasaki, "Feasibility Study of Ethanol Applications to A Direct Injection Gasoline Engine," in *SAE Technical Paper*, 2007.
[118] P. Price, B. Twiney, R. Stone, K. Kar, and H. Walmsley, "Particulate and Hydrocarbon Emissions from a Spray Guided Direct Injection Spark Ignition Engine with Oxygenate Fuel Blends," in *SAE Technical Paper*, 2007.
[119] J. M. E. Storey, T. L. Barone, J. F. Thomas, and S. P. Huff, "Exhaust Particle Characterization for Lean and Stoichiometric DI Vehicles Operating on Ethanol-Gasoline Blends," in *SAE Technical Paper*, 2012.
[120] J. M. Storey, T. Barone, K. Norman, and S. Lewis, "Ethanol Blend Effects On Direct Injection Spark-Ignition Gasoline Vehicle Particulate Matter Emissions," *SAE Int. J. Fuels Lubr.*, vol. 3, pp. 650–659, 2010.
[121] F. Catapano, S. Di Iorio, M. Lazzaro, P. Sementa, and B. M. Vaglieco, "Characterization of Ethanol Blends Combustion Processes and Soot Formation in a GDI Optical Engine," in *SAE Technical Paper*, 2013.
[122] R. A. Sobotowski, A. D. Butler, and Z. Guerra, "A Pilot Study of Fuel Impacts on PM Emissions from Light-Duty Gasoline Vehicles," *SAE Int. J. Fuels Lubr.*, vol. 8, pp. 214–233, 2015.
[123] K. Aikawa, T. Sakurai, and J. J. Jetter, "Development of a Predictive Model for Gasoline Vehicle Particulate Matter Emissions," *SAE Int. J. Fuels Lubr.*, vol. 3, no. 2, pp. 610–622, 2010.
[124] P. Sementa, B. M. Vaglieco, and F. Catapano, "Thermodynamic and optical characterizations of a high performance {GDI} engine operating in homogeneous and stratified charge mixture conditions fueled with gasoline and bio-ethanol," *Fuel*, vol. 96, pp. 204–219, 2012.
[125] M. A. Costagliola, L. De Simio, S. Iannaccone, and M. V Prati, "Combustion efficiency and engine out emissions of a S.I. engine fueled with alcohol/gasoline blends," *Appl. Energy*, vol. 111, pp. 1162–1171, 2013.
[126] X. He, J. C. Ireland, B. T. Zigler, M. A. Ratcliff, K. E. Knoll, T. L. Alleman, and J. T. Tester, "The Impacts of Mid-level Biofuel Content in Gasoline on SIDI Engine-out and Tailpipe Particulate Matter Emissions," in *SAE Technical Paper*, 2010.
[127] R. Daniel, H. Xu, C. Wang, D. Richardson, and S. Shuai, "Gaseous and particulate matter emissions of biofuel blends in dual-injection compared to direct-injection and port injection," *Appl. Energy*, vol. 105, pp. 252–261, 2013.
[128] C. Wang, H. Xu, J. M. Herreros, J. Wang, and R. Cracknell, "Impact of fuel and injection system on particle emissions from a GDI engine," *Appl. Energy*, vol. 132, pp. 178–191, 2014.
[129] L. Chen and R. Stone, "Measurement of Enthalpies of Vaporization of Isooctane and Ethanol Blends and Their Effects on PM Emissions from a GDI Engine," *ENERGY & FUELS*, vol. 25, no. 3, pp. 1254–1259, Mar. 2011.
[130] L. Chen, R. Stone, and D. Richardson, "A study of mixture preparation and PM emissions using a direct injection engine fuelled with stoichiometric gasoline/ethanol blends," *Fuel*, vol. 96, pp. 120–130, 2012.
[131] H. Zhao, R. Stone, and L. Zhou, "Analysis of the particulate emissions and combustion performance of a direct injection spark ignition engine using hydrogen and gasoline mixtures," *Int. J. Hydrogen Energy*, vol. 35, no. 10, pp. 4676–4686, 2010.
[132] F. Leach, R. Stone, and D. Richardson, "The Influence of Fuel Properties on Particulate Number Emissions from a Direct Injection Spark Ignition Engine," in

SAE Technical Paper, 2013.
[133] C. Wang, H. Xu, J. M. Herreros, T. Lattimore, and S. Shuai, "Fuel Effect on Particulate Matter Composition and Soot Oxidation in a Direct-Injection Spark Ignition (DISI) Engine," *Energy & Fuels*, vol. 28, no. 3, pp. 2003–2012, 2014.
[134] Y. Sukegawa and K. Oryoji, "3D Modeling of Particulate Matter from Spark Ignition Engines," *SAE Int. J. Engines*, vol. 8, pp. 419–425, 2015.
[135] C. V Naik, L. Liang, K. Puduppakkam, and E. Meeks, "Simulation and Analysis of In-Cylinder Soot Formation in a Gasoline Direct-Injection Engine Using a Detailed Reaction Mechanism," in *SAE Technical Paper*, 2014.
[136] F. Steimle, A. Kulzer, H. Richter, D. Schwarzenthal, and C. Romberg, "Systematic Analysis and Particle Emission Reduction of Homogeneous Direct Injection SI Engines," in *SAE Technical Paper*, 2013.
[137] E. Hecht, *Optics*. San Francisco: Addison-Wesley Longman, Incorporated, 2002.
[138] T. Ohyama, K. Endoh, A. Mikami, and Y. H. Mori, "Optical interferometry for measuring instantaneous thickness of transparent solid and liquid films," *Rev. Sci. Instrum.*, vol. 59, no. 9, pp. 2018–2022, 1988.
[139] S.-W. Kim and G.-H. Kim, "Thickness-Profile Measurement of Transparent Thin-Film Layers by White-Light Scanning Interferometry," *Appl. Opt.*, vol. 38, no. 28, pp. 5968–5973, 1999.
[140] N. Borgetto, C. Galizzi, F. André, and D. Escudié, "A thickness measurement technique based on low-coherence interferometry applied to a liquid film with thermal gradient," *Exp. Therm. Fluid Sci.*, vol. 34, no. 8, pp. 1242–1246, 2010.
[141] F. Gao, H. Muhamedsalih, and X. Jiang, "Surface and thickness measurement of a transparent film using wavelength scanning interferometry.," *Opt. Express*, vol. 20, no. 19, pp. 21450–6, 2012.
[142] X. Jiang, K. Wang, F. Gao, and H. Muhamedsalih, "Fast surface measurement using wavelength scanning interferometry with compensation of environmental noise," *Appl. Opt.*, vol. 49, no. 15, pp. 2903–2909, 2010.
[143] S. K. Debnath, M. P. Kothiyal, J. Schmit, and P. Hariharan, "Spectrally resolved phase-shifting interferometry of transparent thin films: sensitivity of thickness measurements.," *Appl. Opt.*, vol. 45, no. 34, pp. 8636–40, 2006.
[144] X. S. Wang and H. H. Qiu, "Fringe probing of liquid film thickness of a plug bubble in a micropipe," *Meas. Sci. Technol.*, vol. 16, no. 2, pp. 594–600, 2005.
[145] A. Kariyasaki, Y. Yamasaki, M. Kagawa, T. Nagashima, A. Ousaka, and S. Morooka, "Measurement of Liquid Film Thickness by a Fringe Method," *Heat Transf. Eng.*, vol. 30, no. 1–2, pp. 28–36, 2009.
[146] M. Kuhner and E. Sackmann, "Ultrathin hydrated dextran films grafted on glass: Preparation and characterization of structural, viscous, and elastic properties by quantitative microinterferometry," *Langmuir*, vol. 12, no. 20, pp. 4866–4876, 1996.
[147] G. Wiegand, K. R. Neumaier, and E. Sackmann, "Microinterferometry: Three-Dimensional Reconstruction of Surface Microtopography for Thin-Film and Wetting Studies by Reflection Interference Contrast Microscopy (RICM)," *Appl. Opt.*, vol. 37, no. 29, pp. 6892–6905, 1998.
[148] I. B. Ozdemir and J. H. Whitelaw, "An Optical Method for the Measurement of Unsteady Film Thickness," *Exp. Fluids*, vol. 13, no. 5, pp. 321–331, 1992.
[149] C. Schulz and V. Sick, "Tracer-LIF diagnostics: quantitative measurement of fuel concentration, temperature and fuel/air ratio in practical combustion systems," *Prog. Energy Combust. Sci.*, vol. 31, no. 1, pp. 75–121, Jan. 2005.
[150] A. C. Eckbreth, *Laser Diagnostics for Combustion Temperature and Species*.

Amsterdam: Gordon and Breach Publishers, 1996.
[151] M. Alonso, P. J. Kay, P. J. Bowen, R. Gilchrist, and S. Sapsford, "A laser induced fluorescence technique for quantifying transient liquid fuel films utilising total internal reflection," *Exp. Fluids*, vol. 48, no. 1, pp. 133–142, 2010.
[152] T. Fujikawa, Y. Hattori, M. Koike, K. Akihama, T. Kobayashi, and S. Matsushita, "Quantitative 2-D fuel distribution measurements in a direct-injection gasoline engine using laser-induced fluorescence technique," *JSME Int. J. Ser. B-Fluids Therm. Eng.*, vol. 42, no. 4, pp. 760–767, 1999.
[153] Y. Cheng, K. Deng, and T. Li, "Measurement and simulation of wall-wetted fuel film thickness," *Int. J. Therm. Sci.*, vol. 49, no. 4, pp. 733–739, 2010.
[154] I. Duewel, J. Schorr, P. Peuser, P. Zeller, J. Wolfrum, and C. Schulz, "Spray diagnostics using an all-solid-state Nd:YAlO3 laser and fluorescence tracers in commercial gasoline and diesel fuels," *Appl. Phys. B*, vol. 79, no. 2, pp. 249–254, 2004.
[155] R. Domann and Y. Hardalupas, "Spatial distribution of fluorescence intensity within large droplets and its dependence on dye concentration," *Appl. Opt.*, vol. 40, no. 21, pp. 3586–3597, 2001.
[156] M. Davy, P. Williams, D. Han, and R. Steeper, "Evaporation characteristics of the 3-pentanone-isooctane binary system," *Exp. Fluids*, vol. 35, no. 1, pp. 92–99, 2003.
[157] D. Greszik, H. Yang, T. Dreier, and C. Schulz, "Laser-based diagnostics for the measurement of liquid water film thickness," *Appl. Opt.*, vol. 50, no. 4, pp. A60–A67, 2011.
[158] I. K. Kabardin, V. G. Meledin, I. a. Eliseev, and V. V. Rakhmanov, "Optical measurement of instantaneous liquid film thickness based on total internal reflection," *J. Eng. Thermophys.*, vol. 20, no. 4, pp. 407–415, 2011.
[159] C. H. Hidrovo and D. P. Hart, "Emission reabsorption laser induced fluorescence (ERLIF) film thickness measurement," *Meas. Sci. Technol.*, vol. 12, no. 4, pp. 467–477, 2001.
[160] A. A. Mouza, N. A. Vlachos, S. V. Paras, and A. J. Karabelas, "Measurement of liquid film thickness using a laser light absorption method," *Exp. Fluids*, vol. 28, no. 4, pp. 355–359, 2000.
[161] B. Commoner and D. Lipkin, "The Application of the Beer-Lambert Law to Optically Anisotropic Systems," *Science (80-.).*, vol. 110, no. 2845, pp. 41–43, 1949.
[162] H. Yang, D. Greszik, T. Dreier, and C. Schulz, "Simultaneous measurement of liquid water film thickness and vapor temperature using near-infrared tunable diode laser spectroscopy," *Appl. Phys. B*, vol. 99, no. 3, pp. 385–390, 2010.
[163] G. M. Hale and M. R. Querry, "Optical Constants of Water in the 200-nm to 200-micrometer Wavelength Region," *Appl. Opt.*, vol. 12, no. 3, pp. 555–563, 1973.
[164] Q. Lu, N. V Suryanrayana, and C. Christododoulu, "Film Thickness Measurement with an Ultrasonic Transducer," *Exp. Therm. Fluid Sci.*, vol. 7, no. 4, pp. 354–361, 1993.
[165] P. C. Pedersen, Z. Cakareski, and J. C. Hermanson, "Ultrasonic monitoring of film condensation for applications in reduced gravity," *Ultrasonics*, vol. 38, no. 1–8, pp. 486–490, 2000.
[166] M. W. E. Coney, "The theory and application of conductance probes for the measurement of liquid film thickness in two-phase flow," *J. Phys. E.*, vol. 6, no. 9, p. 903, 1973.
[167] T. Fukano, "Measurement of time varying thickness of liquid film flowing with high

speed gas flow by a constant electric current method (CECM)," *Nucl. Eng. Des.*, vol. 184, no. 2–3, pp. 363–377, 1998.
[168] P. Seleghim and E. Hervieu, "Direct imaging of two-phase flows by electrical impedance measurements," *Meas. Sci. Technol.*, vol. 9, no. 9, pp. 1492–1500, 1998.
[169] M. R. Ozgu, J. C. Chen, and N. Eberhardt, "A capacitance method for measurement of film thickness in two-phase flow," *Rev. Sci. Instrum.*, vol. 44, no. 12, pp. 1714–1716, 1973.
[170] J. F. Klausner, L. Z. Zeng, and D. M. Bernhard, "Development of a film thickness probe using capacitance for asymmetrical two-phase flow with heat addition," *Rev. Sci. Instrum.*, vol. 63, no. 5, pp. 3147–3152, 1992.
[171] M. C. Fansler, T.D., Drake, "Optical Diagnostics Applied to Spark-Ignited Direct-Injection Engine Development," *5. Int. Symp. fuer Verbrennungsdiagnostik, Baden-bad.*, 2002.
[172] B. Yang and J. Ghandhi, "Measurement of Diesel Spray Impingement and Fuel Film Characteristics Using Refractive Index Matching Method," *SAE Tech. Pap. Ser.*, no. 2007–01–0485, 2007.
[173] D. Maligne and G. Bruneaux, "Time-Resolved Fuel Film Thickness Measurement for Direct Injection SI Engines Using Refractive Index Matching," *SAE Tech. Pap. Ser.*, no. 2011–01–1215, 2011.
[174] T. Stach, J. Schlerfer, and M. Vorbach, "New Generation Multi-hole Fuel Injector for Direct-Injection SI Engines - Optimization of Spray Characteristics by Means of Adapted Injector Layout and Multiple Injection," in *SAE Technical Paper*, 2007.
[175] N. Mitroglou, J. M. Nouri, Y. Yan, M. Gavaises, and C. Arcoumanis, "Spray Structure Generated by Multi-Hole Injectors for Gasoline Direct-Injection Engines," in *SAE Technical Paper*, 2007.
[176] L. Marchitto, S. Merola, C. Tornatore, and G. Valentino, "Experimental Study on the Spray Atomization of a Multi-hole Injector for Spark Ignition Engines Fuelled by Gasoline and n-Butanol," in *SAE Technical Paper*, 2014.
[177] P. G. Aleiferis and Z. R. van Romunde, "An analysis of spray development with iso-octane, n-pentane, gasoline, ethanol and n-butanol from a multi-hole injector under hot fuel conditions," *Fuel*, vol. 105, pp. 143–168, 2013.
[178] H. Li, C. Li, X. Ma, P. TU, H. Xu, S.-J. Shuai, and A. Ghafourian, "Numerical Study of DMF and Gasoline Spray and Mixture Preparation in a GDI Engine," in *SAE Technical Paper*, 2013.
[179] M. Behringer, P. Aleiferis, D. OudeNijeweme, and P. Freeland, "Spray Formation from Spark-Eroded and Laser-Drilled Injectors for DISI Engines with Gasoline and Alcohol Fuels," *SAE Int. J. Fuels Lubr.*, vol. 7, pp. 803–822, 2014.
[180] R. Lindgren, M. Skogsberg, H. Sandquist, and I. Denbratt, "The Influence of Injector Deposits on Mixture Formation in a DISC SI Engine," in *SAE Technical Paper*, 2003.
[181] M. Kinoshita, A. Saito, S. Matsushita, H. Shibata, and Y. Niwa, "A Method for Suppressing Formation of Deposits on Fuel Injector for Direct Injection Gasoline Engine," in *SAE Technical Paper*, 1999.
[182] D. C. Arters, E. A. Bardasz, E. A. Schiferl, and D. W. Fisher, "A Comparison of Gasoline Direct Injection Part I - Fuel System Deposits and Vehicle Performance," in *SAE Technical Paper*, 1999.
[183] H. Xu, C. Wang, X. Ma, A. K. Sarangi, A. Weall, and J. Krueger-Venus, "Fuel injector deposits in direct-injection spark-ignition engines," *Prog. Energy Combust. Sci.*, vol. 50, pp. 63–80, 2015.

[184] P. S. Von Bacho, J. Galante-Fox, and D. W. Sant, "Development of a Robust Injector Design for Superior Deposit Resistance," in *SAE Technical Paper*, 2005.
[185] A. A. Aradi, B. Imoehl, N. L. Avery, P. P. Wells, and R. W. Grosser, "The Effect of Fuel Composition and Engine Operating Parameters on Injector Deposits in a High-Pressure Direct Injection Gasoline (DIG) Research Engine," in *SAE Technical Paper*, 1999.
[186] A. A. Aradi, W. J. Colucci, H. M. Scull, and M. J. Openshaw, "A Study of Fuel Additives for Direct Injection Gasoline (DIG) Injector Deposit Control," in *SAE Technical Paper*, 2000.
[187] A. A. Aradi, J. Evans, K. Miller, and A. Hotchkiss, "Direct Injection Gasoline (DIG) Injector Deposit Control with Additives," in *SAE Technical Paper*, 2003.
[188] T. Ashida, Y. Takei, and H. Hosi, "Effects of Fuel Properties on SIDI Fuel Injector Deposit," in *SAE Technical Paper*, 2001.
[189] K. Noma, T. Noda, T. Ashida, R. Kamioka, K. Hosono, T. Nishida, A. Kameoka, K. Koseki, M. Watanabe, K. Takahashi, S. Koide, T. Suzuki, H. Fukui, M. Hirose, S. Ohta, Y. Notsuki, and K. Tsuboi, "A Study of Injector Deposits, Combustion Chamber Deposits (CCD) and Intake Valve Deposits (IVD) in Direct Injection Spark Ignition (DISI) Engines," in *SAE Technical Paper*, 2002.
[190] R. J. DuMont, J. A. Evans, D. P. Feist, W. M. Studzinski, and T. J. Cushing, "Test and Control of Fuel Injector Deposits in Direct Injected Spark Ignition Vehicles," in *SAE Technical Paper*, 2009.
[191] A. Joedicke, J. Krueger-Venus, P. Bohr, R. Cracknell, and D. Doyle, "Understanding the Effect of DISI Injector Deposits on Vehicle Performance," in *SAE Technical Paper*, 2012.
[192] H. W. Carlisle, R. W. Frew, J. R. Mills, A. A. Aradi, and N. L. Avery, "The Effect of Fuel Composition and Additive Content on Injector Deposits and Performance of an Air-Assisted Direct Injection Spark Ignition (DISI) Research Engine," in *SAE Technical Paper*, 2001.
[193] A. Berndorfer, S. Breuer, W. Piock, and P. Von Bacho, "Diffusion Combustion Phenomena in GDi Engines caused by Injection Process," in *SAE Technical Paper*, 2013.
[194] P. S. Von Bacho, J. K. Sofianek, J. M. Galante-Fox, and C. J. McMahon, "Engine Test for Accelerated Fuel Deposit Formation on Injectors Used in Gasoline Direct Injection Engines," in *SAE Technical Paper*, 2009.
[195] M. Raffel, C. E. Willert, S. T. Wereley, and J. Kompenhans, *Particle Image Velocimetry: A Practical Guide*. Heidelberg: Springer, 2007.
[196] F. Durst, *Fluid Mechanics - An Introduction to the Theory of Fluid Flows*. Berlin Heidelberg: Springer-Verlag, 2008.
[197] H.-E. Albrecht, N. Damaschke, M. Borys, and C. Tropea, *Laser Doppler and Phase Doppler Measurement Techniques*. Berlin Heidelberg: Springer-Verlag Berlin Heidelberg New York, 2003.
[198] J. Weickert, "A review of nonlinear diffusion filtering," in *Scale-Space Theory in Computer Vision SE - 1*, vol. 1252, B. Haar Romeny, L. Florack, J. Koenderink, and M. Viergever, Eds. Springer Berlin Heidelberg, 1997, pp. 1–28.
[199] J. Weickert, B. M. T. H. Romeny, and M. A. Viergever, "Efficient and reliable schemes for nonlinear diffusion filtering," *Image Process. IEEE Trans.*, vol. 7, no. 3, pp. 398–410, 1998.
[200] S. Pfadler, F. Beyrau, and A. Leipertz, "Flame front detection and characterization using conditioned particle image velocimetry (CPIV)," *Opt. Express*, vol. 15, no. 23,

pp. 15444–15456, 2007.
[201] "NIST Chemisrty Webbook," *NIST Standard Reference Database Number 69*. [Online]. Available: http://webbook.nist.gov/chemistry/.
[202] J. Park, X. Xie, K.-S. Im, H. Kim, M.-C. Lai, J. Yang, Z. Han, and R. W. Anderson, "Characteristics of Direct Injection Gasoline Spray Wall Impingement at Elevated Temperature Conditions," in *SAE Technical Paper*, 1999.
[203] A. Montanaro, M. Costa, U. Sorge, and L. Allocca, "GDI Spray-Wall Interaction with Numerical Characterization: Wall Temperature Influence," in *SAE Technical Paper*, 2015.
[204] V. Semião, P. Andrade, and M. da Graça Carvalho, "Spray characterization: Numerical prediction of Sauter mean diameter and droplet size distribution," *Fuel*, vol. 75, no. 15, pp. 1707–1714, 1996.
[205] J. W. Powell, "A Quantitative Assessment of Droplet Sizes in Atmospheric and Engine Environments," University of Illinois at Urbana-Champaign, 2009.
[206] G. Zhang and D. L. S. Hung, "Temporal investigations of transient fuel spray characteristics from a multi-hole injector using dimensionless analysis," *Exp. Therm. Fluid Sci.*, vol. 66, pp. 150–159, 2015.
[207] K. K. Kuo, *Recent Advances in Spray Combustion: Spray combustion measurements and model simulation*. Michigan: American Institute of Aeronautics and Astronautics, Inc., 1996.
[208] H. Chen, D. L. Reuss, D. L. S. Hung, and V. Sick, "A practical guide for using proper orthogonal decomposition in engine research," *Int. J. ENGINE Res.*, vol. 14, no. 4, pp. 307–319, Aug. 2013.
[209] H. Chen, D. L. Reuss, and V. Sick, "On the use and interpretation of proper orthogonal decomposition of in-cylinder engine flows," *Meas. Sci. Technol.*, vol. 23, no. 8, Aug. 2012.
[210] H. Chen, D. L. Reuss, and V. Sick, "Analysis of misfires in a direct injection engine using proper orthogonal decomposition," *Exp. Fluids*, vol. 51, no. 4, pp. 1139–1151, Oct. 2011.
[211] K. Liu and D. C. Haworth, "Development and Assessment of POD for Analysis of Turbulent Flow in Piston Engines," in *SAE Technical Paper*, 2011.